MEASUREMENTS OF THE NEUTRON LONGITUDINAL SPIN ASYMMETRY A_1 AND FLAVOR DECOMPOSITION IN THE VALENCE QUARK REGION

A Dissertation
Submitted to
the Temple University Graduate Board

In Partial Fulfillment
of the Requirements for the Degree
DOCTOR OF PHILOSOPHY

---

by
David Flay
August 2014

Examining Committee Members:

Zein-Eddine Meziani, Department of Physics, Advisory Chair
C. J. Martoff, Department of Physics
Jim Napolitano, Department of Physics
Bernd Surrow, Department of Physics
Leonard Gamberg, External Member, Penn State University-Berks

ABSTRACT

The current data for the nucleon-virtual photon longitudinal spin asymmetry A_1 on the proton and neutron have shown that the ratio of the polarized-to-unpolarized down-quark parton distribution functions, $\Delta d/d$, tends towards -1/2 at large x, in disagreement with the perturbative QCD prediction that $\Delta d/d$ approaches 1 but more in line with constituent quark models. As a part of experiment E06-014 in Hall A of Jefferson Lab, double-spin asymmetries were measured in the scattering of a longitudinally polarized electron beam of energies 4.74 and 5.89 GeV from a longitudinally and transversely polarized ^{3}He target in the deep inelastic scattering and resonance region, allowing for the extraction of the neutron asymmetry A_1^n and the ratios $\Delta d/d$ and $\Delta u/u$. We will discuss our analysis of the data and present results for A_1 and g_1/F_1 on both ^{3}He and the neutron, and the resulting quark ratios for the up and down quarks in the kinematic range of $0.2 < x < 0.6$ and $2 < Q^2 < 5\,\mathrm{GeV}^2$ for our deep inelastic scattering data. Invoking duality, we also extract A_1^n and g_1^n/F_1^n in the resonance region, characterized by $0.6 < x < 0.8$ and $3.3 < Q^2 < 7\,\mathrm{GeV}^2$. Our measurements are compared to the world data and various theoretical models and more recent predictions using the Dyson-Schwinger Equation approach. We also present analysis of the unpolarized cross section data, which contributes to the g_1 spin structure function and eventually the a_2 matrix element, an x^2-weighted moment of g_1. The extracted a_2 data are compared to a Lattice QCD calculation.

DEDICATION

for my mother

ACKNOWLEDGEMENTS

First and foremost, I would like to thank Zein-Eddine Meziani for giving me the opportunity to work as a part of his research group and be a part of the Jefferson Lab Hall A E06-014 experiment. His guidance and encouragement have been invaluable over the years in teaching me to be the physicist I have grown to become, and I am grateful for all that I have learned from him.

I would also like to thank the spokespeople of the experiment, including Seonho Choi, Zein-Eddine Meziani, Xiaodong Jiang and Brad Sawatzky for their efforts in the planning and guidance of the experiment. Additionally, I want to thank the numerous run coordinators and shift workers, Hall A staff, and the accelerator division for all their efforts in allowing for the completion of the experiment with high-quality data, despite the various hurdles that had to be overcome.

I want to thank the other Ph. D. students that worked on the experiment, Matt Posik and Diana Parno, for all their hard work and perseverance not only during the experiment when monitoring the detector systems, but also during the analysis stage to ensure that everything was done thoroughly and correctly. I also want to thank Patricia Solvignon, Karl Slifer, J.-P. Chen, Elaine Schulte, Whitney Armstrong, Huan Yao, Vincent Sulkosky, Kalyan Allada, Chiranjib Dutta, Xin Qian and Jin Huang for all of the insightful and helpful conversations at various points throughout the experiment and analysis process; I have learned a lot from each of them, and I am thankful for their generosity and their friendship.

I would like to thank my undergraduate professors at Manhattan College. In particular, Louis Uffer for piquing my interest in physics so as to inspire me to study physics beyond the undergraduate level. I also want to thank Gregory Dorata, Bruce Liby, Rostislav Konoplich, Joseph Capitani and Sezar Fesjian for all of their guidance and invigorating courses that they taught. I am grateful for their encouragement and support.

Thank you to my family and friends for all of their support. In particular, my mother Conni, brother George, sister Maggie, sister-in-law Emily, step-father Bobby and grandmother Fannie for all of their encouragement and support over the years. I certainly could not have done it without them.

CONTENTS

LIST OF FIGURES

LIST OF TABLES

CHAPTER 1

INTRODUCTION

1.1 The Structure of Matter

One of the most fundamental questions that scientists have tried to answer is "what is matter made of?" It was believed prior to 1897 that atoms were the most basic, indivisible building blocks of matter. However, in that year, J. J. Thompson discovered the negatively charged electron. This changed the way the atom was viewed, and sparked further investigation into its structure. In 1911, Ernest Rutherford discovered the nucleus when scattering alpha particles from a thin gold foil. With the observation of the backward scattering of the alpha particles, it was determined that the atom was composed of mostly empty space with a dense core at the center, called the *nucleus*. This piqued the interest as to what makes up the nucleus, and protons and neutrons were discovered thereafter. In particular, J. Chadwick's discovery of the neutron was rewarded with a Nobel prize. Protons and neutrons are the particles that make up the nucleus, and are collectively called *nucleons*.

With the discovery of nucleons, the interest then turned to understanding their structure. In 1956, W. McAllister and R. Hofstadter published experimental results of elastic scattering of electrons from a hydrogen target, revealing that the proton has internal structure [1]. Hofstader's work on electron scattering from nuclei and discoveries concerning nucleon structure resulted in a Nobel prize in 1961. In 1964, Gell-Mann [2] (and independently) Zweig [3] proposed a theory that nucleons are composed of pointlike particles called *quarks*. These quarks were postulated to have spin-1/2, a fractional electric charge, and came in three different types called *flavors*, known as up (u), down (d) and strange (s). Their fractional charges are 2/3, -1/3 and -1/3, respectively. Combinations of different flavors of quarks yields protons and neutrons, which belong to the type of particles called *baryons* (built up from three quarks) and mesons (a quark and an anti-quark). These two groups of particles are categorized as *hadrons*.

1.2 Early Electron Scattering Experiments

The first electron scattering experiment that showed that nucleons are composed of quarks took place at the Stanford Linear Accelerator Center (SLAC). The experiment [4, 5] consisted of scattering a high-energy electron beam from a hydrogen target, measuring the scattered electron. These measurements allow for the study of the internal structure of the target. The electrons interact with the target through the electromagnetic force, mediated by a *virtual* photon*.

The kinematics of the experiment consisted of beam energies E from 7 to 17 GeV and scattering angles θ of 6° to 10°. Cross sections were measured for Q^2 values up to 7.4 GeV^2†. The square of the four-momentum of the virtual photon, Q^2, is a measure of the resolution of the experiment. Figure 1.1 shows the ratio of the measured cross section to the Mott cross section (which describes electron scattering from a point particle) is plotted as function of Q^2 for a scattering angle of $\theta = 10°$, for invariant mass W = 2–3.5 GeV‡. A curve is also displayed for elastic scattering of electrons (e) from protons (p).

It is clear from Figure 1.1 that as the invariant mass increases, the dependence of the cross section on the resolution $\left(Q^2\right)$ decreases. The lack of structure in the cross section or "flatness" indicates that the particles the electrons are scattering from—the quarks—are particles without structure, or *pointlike*.

The results of the SLAC experiment lead to the postulation from J. Bjorken that electron scattering cross sections are dependent upon a single variable x, later labeled *Bjorken-x*. The variable x is a dimensionless quantity, defined as $x \equiv Q^2/(2M\nu)$, where M is the mass of the target nucleon, and $\nu = E - E'$, the energy lost by the electron in the scattering process. This x-dependence (and independence of Q^2) is known as *scaling* [6], which will be discussed in more detail in Section 1.4.5.1. Such scaling behavior lead to Feynman's model, where protons are described in terms of pointlike constituents called *partons* at the time, and later known to be quarks. Feynman's *Quark Parton Model* (QPM) (Sect. 1.4.5.2) described electron deep inelastic scattering data well and was an excellent complement to the theories of Gell-Mann *et al*. concerning the quarks and how they describe the properties of the proton. However, as new and unexpected experimental results were obtained, new questions arose which required a refined approach to the QPM and also the formulation of a new theory to describe the new data.

*In electron scattering processes, it is this virtual photon—not the electron—that probes the nucleon. It carries a fraction of the momentum of the incident electron and transfers it to the nucleon. More details about the virtual photon follow in Section 1.4.2.2.

†Natural units where $\hbar = c = 1$ are used throughout this thesis.

‡The invariant mass is the mathematical combination of the energy and momentum of the particle or system of particles in question, and is independent of the inertial frame of reference. See Section 1.4.2.2.

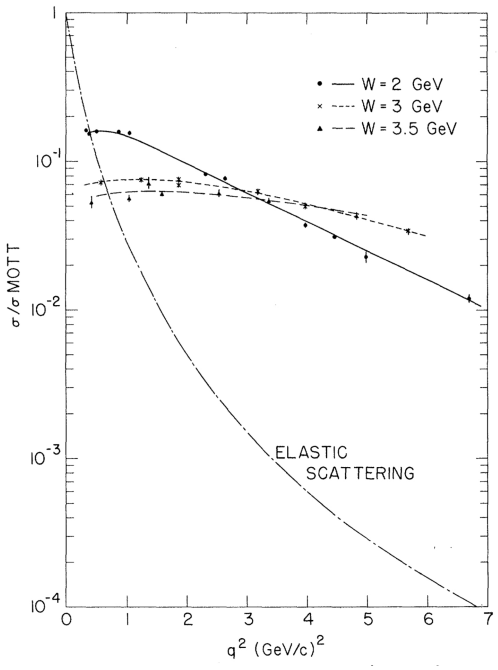

Figure 1.1: The ratio of the measured cross section σ to the Mott cross section σ_{Mott} for a scattering angle of 10° as a function of Q^2 for $W = 2$, 3 and 3.5 GeV. The elastic curve is also shown. Figure reproduced from [5].

1.3 Quantum Chromodynamics

While the QPM was successful in describing various aspects of hadrons in terms of quarks, it had its limitations. For instance, it could not explain how only *half* of the nucleon's momentum comes from the constituent quarks. The concept of how quarks were bound together via the strong force to form a nucleon—called *confinement*—is another topic of great interest. Confinement is accounted for by introducing the concept of quarks possessing *color* charge. There are three different types of color: red, blue and green. The mathematics of color charge dictates that hadrons, composed of these color-charged quarks, are in fact colorless; that is, hadrons are in color singlet states. This effectively describes how quarks cannot be observed directly. From a theoretical standpoint, one approach of implementing confinement is through defining gauge fields on a discrete lattice in Euclidean space-time*.

While quarks are bound inside the nucleon, there is a possibility for them to behave like free particles. This is the concept of *asymptotic freedom*, which corresponds to how quarks behave when the nucleon is probed via a virtual photon at large momentum transfers ($Q^2 > 1\,\text{GeV}^2$) and large invariant mass $W > 2\,\text{GeV}$, which characterizes the so-called *deep*

*This sub-field of particle physics is called lattice QCD [7, 8].

inelastic scattering regime*. Asymptotic freedom was described by D. Gross, F. Wilczek and D. Politzer, utilizing non-abelian quantum field theory. This was soon followed by Quantum Chromodynamics (QCD), which is a theory of the strong interaction, describing how the quarks and gluons bind together, forming hadrons. It is called *chromo*dynamics since it is a field theory that describes the *color* interactions [9–11].

QCD follows the formalism of Quantum Electrodynamics (QED), which has a coupling constant α that describes the strength of the electromagnetic interaction; in QCD, the coupling constant α_s gives the strength of the strong (color) interaction. The concept of asymptotic freedom can be described in the framework of QCD. Since the strength of the quark interactions are small at large Q^2, corresponding to probing the nucleon at small distance scales, this results in α_s being small. As a result, a perturbative approach can be taken in the mathematical description of the interactions, with α_s as the expansion parameter. This kinematic regime is called *perturbative* QCD or just pQCD. On the other hand, when Q^2 is small (probing the nucleon at large distances), pQCD is no longer applicable; the coupling constant α_s is large, and the interactions between quarks are very strong. This is referred to as the *non*-perturbative QCD regime. The functional form of the QCD coupling constant is shown in Figure 1.2.

We now turn to examining the structure of the nucleon in the context of QCD. In particular, we investigate how the quark spins contribute to the nucleon spin and how this spin content is determined via electron scattering.

*Deep inelastic scattering (DIS) will be discussed in further detail in Sections 1.4.2.2 and 1.4.5.

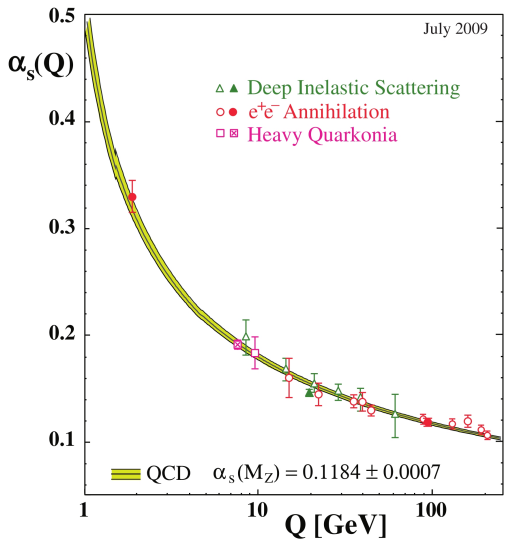

Figure 1.2: The QCD coupling constant α_s as a function of $Q = \sqrt{Q^2}$. The curves represent QCD predictions for the combined world average value of α_s. M_Z is the rest mass of the Z^0 boson. Open triangles and squares are from next-to-leading order (NLO) QCD calculations; open circles are based on next-to-next-to-leading order (NNLO) calculations; Filled in symbols are from N3O QCD calculations. The cross-filled square is from lattice QCD. Figure reproduced from [12].

1.4 Nucleon Structure

1.4.1 Nucleon Spin

Spin is an intrinsic property of quarks and nucleons. Despite numerous theoretical models and experiments conducted to understand the origin of spin, not much is known for certain.

On the theoretical front, Ellis and Jaffe [13] predict the contribution of the quarks' spin to that of the nucleon to be $\sim 58\%$, excluding the components due to the gluons and the orbital angular momentum. The sea quark* contribution is also assumed to be zero.

In order to probe the spin structure of the nucleon through electron scattering, polarized electrons *and* polarized nucleon targets are needed. The first polarized electron-polarized proton experiments were carried out at SLAC, called E80 [14, 15] and E130 [16, 17]. They focused on the measurement of spin-dependent asymmetries in inclusive† DIS of longitudinally polarized electrons scattering from a longitudinally polarized proton target.

*Sea quarks refer to quark-anti-quark (q-$\bar{q}$) pairs that appear due to pair-production and disappear in annihilation processes in the nucleon. The lightest quarks are most probable, u, d and s quarks. Heavier flavors like charm, bottom and top are less likely in nucleons.

†Inclusive means that only the scattered electron was measured, while the recoiling target fragment was not measured.

The results of the experiments, despite their limited kinematic range and relatively low precision by modern standards, supported the identification of quarks with partons such that nearly all of the proton spin was composed of the spins of the valence (non-sea) quarks, and that the other possible sources of angular momentum could be neglected.

This picture of the nucleon spin was changed drastically however, with the results from the European Muon Collaboration (EMC) experiment [18, 19]. Instead of scattering polarized electrons from polarized protons, the EMC experiment used polarized muons, and measured their spin asymmetry. The results gathered here disagreed greatly with the predictions of Ellis and Jaffe, as it was found that the quark spin makes up only a small fraction of the nucleon spin. Such results were later confirmed by CERN's SMC and SLAC's E142 and E143 experiments. The combination of EMC and SLAC E143 data showed that the spin contribution from the valence and sea quarks was only $12\% \pm 17\%$ [19] of the total proton spin of 1/2. This big disagreement between theory and experiment is referred to as the *nucleon spin crisis*.

The big question now is "where is the spin?" Inside the nucleon, there is also the presence of gluons, which also have spin (ΔG). The gluons and quarks have orbital angular momentum, $\mathcal{L}_G$ and $\mathcal{L}_q$, respectively. Including the contribution from of the *helicities* of the valence and sea quarks $\left(\sum_q \Delta q\right)$, the nucleon spin may be written as:

$$\frac{1}{2} = \sum_q \frac{1}{2}\Delta q + \mathcal{L}_q + \Delta G + \mathcal{L}_G. \tag{1.1}$$

The form of Equation 1.1 was originally given by Jaffe and Manohar [20]; an alternative form is given by Ji [21], where the spin of the nucleon may be expressed in the form:

$$\frac{1}{2} = \sum_q \frac{1}{2}\Delta q + L_q + J_G. \tag{1.2}$$

In both forms, $\sum_q \Delta q = \Delta\Sigma$ is understood to be the contribution due to the helicities of valence and sea quarks. Current measurements show $\Delta\Sigma$ to be $\sim$ 30–35% [22]. The definition of the quark orbital angular momentum, given as L_q or $\mathcal{L}_q$, for the two equations is not equivalent. In Equation 1.2, L_q contains a covariant derivative and is necessarily sensitive to gluonic degrees of freedom. In Equation 1.1, $\mathcal{L}_q$ is defined such that a covariant derivative is not present. Because of this, the interpretation of the two forms of the quark orbital angular momentum is not the same; recently, the difference between the two forms has been described as due to a torque on the struck quark in final state interactions [23]. Experimentally, $J_q = (1/2)\Delta\Sigma + L_q$ may be accessed through deeply-virtual Compton scat-

tering or deeply virtual meson production*; in extracting L_q from such measurements, the experimental value of $(1/2)\Delta\Sigma$ would need to be subtracted. The quantity ΔG is interpreted as the contribution due to the gluon spin in Equation 1.1, and has been measured to be $\sim$ 20% [25]. Under the interpretation of Ji, J_G cannot be cleanly separated into its spin and orbital components [21]. It is clear that when discussing the spin content of the nucleon, one has to take care to indicate which convention is being used. A more thorough discussion may be found in the literature [26–34].

1.4.2 Methods of Probing the Nucleon

When investigating the structure of the nucleon, particle scattering proves to be a vital tool. With the size of the nucleus being on the order of 2–15 femtometers (1 fm = 10^{-15} m) and the nucleon being smaller than that (the proton's charge radius is $\sim$0.877 fm [35]), conventional tools of classical physics like X-rays and microscopes are not capable of probing the substructure of these objects. In scattering processes between two particles, however, measurements of how often the interaction takes place, the types of particles produced and their kinematics—the energies, momenta and angles—allows one to determine the nature of the interaction and describe the structure of the target.

In this section we outline the two broad sub-fields of particle scattering used to probe nucleus and nucleon structure.

1.4.2.1 Hadronic Collisions

The first scattering method we consider is *Drell-Yan* [36]. It consists of hadron-hadron collisions, where the two hadrons are accelerated to high energies in opposite directions (towards one another) so that they collide. A quark inside one of the incident hadrons annihilates with an anti-quark from the other hadron. This produces a virtual photon, which typically decays into an electron-positron or muon-antimuon pair at large energies relative to the hadrons involved in the collision. Due to this process consisting of interactions between quarks and anti-quarks, Drell-Yan processes are sensitive to the sea quark distribution and even gluons [37, 38]. However, the desired yields tend to be small relative to those for the hadronic final states. Low-luminosity beams limit the precision with which measurements may be made using the Drell-Yan processes.

*In this interaction, a virtual photon is absorbed by a nucleon target, and a real photon or meson is released into the final state and the target nucleon remains intact. The theoretical description is given in terms of generalized parton distributions (GPDs) [24]. Different combinations of polarized electron beams and targets allows for access to different GPDs.

For the second method, we have lepton scattering. Since the work in this dissertation is done for an experiment that utilized electrons, we will focus on electrons as our leptons; however, the general theory is necessarily true for other leptons, like muons.

1.4.2.2 Electron Scattering

In electron scattering, the electrons are accelerated to high energies and scatter from a nuclear or nucleon target. In practice, the target is typically at rest. The electron interacts with the target by exchanging a so-called virtual photon with the target object, where its energy and momentum are transferred to the target. An advantage of lepton scattering is that the interaction at the scattering vertex (where the photon is exchanged) is described by QED, which simplifies the mathematics. The electromagnetic nature of the interaction also results in the process being a "clean" probe into the structure of the nucleon, where the QCD Physics is contained entirely in the description of the nucleon and is not convoluted with the scattering process itself.

To describe the process more quantitatively, consider Figure 1.3. The incident and scattered electron has the four-momenta $k = (E, \vec{k})$ and $k' = (E', \vec{k}')$, respectively. The target has a four-momentum of $p = (E_T, \vec{p})$. The virtual photon exchanged between the incident electron and the target is described by the four-momentum $q = (\nu, \vec{q})$. If the incident electron has enough energy, the target can break up into a number of distinct hadrons; otherwise, the nucleus or nucleon would remain intact. In the latter case, the recoiling target object would have a four-momentum p' in the final hadronic state. Electron scattering data is presented and discussed in terms of a number of invariant variables, namely ν, y, Q^2, W and x. Starting with ν, we first consider q. Since the four-momentum at each vertex is conserved, we can define q in terms of the incoming and outgoing electron four-momenta:

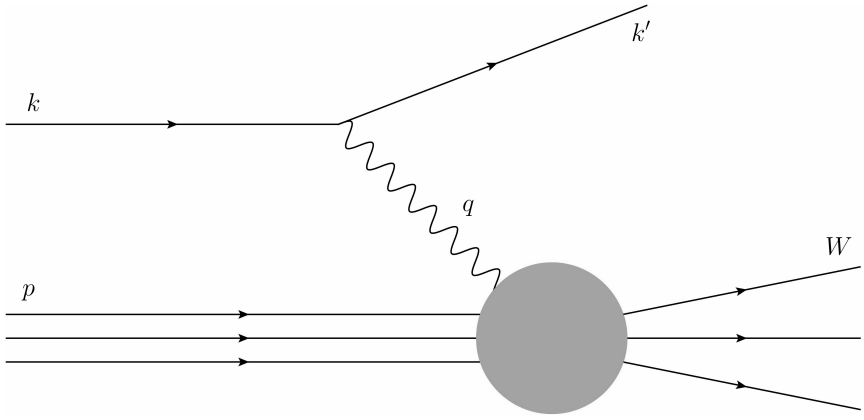

Figure 1.3: Lowest-order Feynman diagram of inclusive electron-nucleon scattering, $en \to eX$.

$$q = k - k' = (E - E', \vec{k} - \vec{k}') = (\nu, \vec{q}), \tag{1.3}$$

where ν can be defined in an invariant form:

$$\nu \equiv p \cdot q / M, \tag{1.4}$$

with M being the mass of the nucleon. In the target rest frame, $p = (M, \vec{0})$, so Equation 1.4 reduces to $\nu = E - E'$, and is known as the *electron energy loss*. A related invariant term, called the *fractional energy loss* is defined as:

$$y \equiv \frac{p \cdot q}{q \cdot k} = \frac{E - E'}{E}. \tag{1.5}$$

There are two distinct situations considering the energy and momentum exchanged between the electron and the target, represented by q. If $q^2 = 0$, then the photon is real. If $q^2 \neq 0$, then the photon is off its mass shell, and therefore does not necessarily behave like a regular photon; hence, it is referred to as a *virtual* photon. In this case, it carries a "borrowed" quantity of energy for a small period of time, satisfying the Heisenberg uncertainty principle [39]. In computing q^2, it is less than zero. For convenience, we define a positive quantity Q^2:

$$Q^2 \equiv -q^2 = 4EE' \sin^2(\theta/2), \tag{1.6}$$

where θ is the scattering angle of the electron in the laboratory frame and we have neglected the electron mass.

Shifting our focus to the hadronic side of Figure 1.3, there are two possibilities for the final state: there is one object (the target remains intact) or several, determined by the energy with which the target is probed. Furthermore, the overall interaction may be described by two general terms: *exclusive* or *inclusive* scattering. In the case of exclusive scattering, the scattered electron *and* a final-state hadron is detected. For inclusive scattering, only the scattered electron is detected in the final state.

Inclusive scattering can be represented as $en \rightarrow eX$, where e is the electron, n is the target nucleon and X is the final (unmeasured) hadronic state. In the context of an unmeasured final hadronic state, we can define the invariant mass of the system, W:

$$W^2 \equiv (q + p)^2 = M^2 + 2M\nu - Q^2. \tag{1.7}$$

where W^2 defines the final hadronic state X which could consist of any of the multitude of particle states for a given combination of ν and Q^2 values.

Finally, we come to the variable x. It is defined in terms of the other invariants ν and Q^2 as:

$$x \equiv \frac{Q^2}{2p \cdot q} = \frac{Q^2}{2M\nu}. \tag{1.8}$$

The simplest interpretation of x comes in the infinite momentum frame, where the nucleon is traveling with a large momentum along $\vec{q}$. In this frame, the active quark in the interaction (struck by the virtual photon) carries the momentum fraction x of the nucleon momentum [39].

1.4.3 The Scattering Cross Section

In electron scattering, the description of the target particle is realized in terms of the *scattering cross section*, denoted as $d^2\sigma/(dE'd\Omega)$. Experimentally, it describes the *probability* of scattering with an energy $(E', E' + dE')$ into a solid angle $d\Omega$; thus, it can be seen as an intrinsic strength of the interaction. The units of the quantity work out to be those of area (cm^2), hence the name *cross section*. It displays a strong dependence on ν and Q^2, as shown in Figure 1.4, which represents a cross section of inclusive electron scattering from a light nucleus. Note that Q^2 effectively defines the spatial resolution of the virtual photon that probes the target (cf. the frequency of a real photon used in an X-ray image or a microscope, which defines the spatial resolution of the image). With this in mind while examining Figure 1.4, one can define different regimes of scattering based on the ν and Q^2 dependence, each with their own unique dynamics.

In the region of low ν and Q^2, we have *elastic scattering*. The spatial resolution is not high enough to see the target's composition. The target nucleus stays intact and recoils coherently in the scattering interaction. For a nuclear target, the momentum transferred to the target is shared equally among all nucleons. The invariant mass of the system is given as $W^2 = M_T^2$, where M_T is the mass of the (nucleus or nucleon) target.

When ν is larger than the binding energy of the nucleon in the nucleus, the nucleus breaks apart as a result of the interaction. The electron effectively scatters elastically from a nucleon, which is ejected from the nucleus. This is called *quasi-elastic scattering*. Unlike the elastic case, the nucleons in the nuclear medium are *not* at rest in the laboratory frame. The nucleons carry an initial momentum of $\sim$ 55–250 MeV due to their motion in the nucleus, behaving like a Fermi gas [41, 42]. This so-called Fermi motion leads to a broadening of the quasi-elastic peak, located at $\nu = Q^2/(2M)$, with M being the nucleon mass, and ν is the energy loss due to elastic scattering from a free nucleon. The invariant mass of the system is given as $W^2 = M^2$.

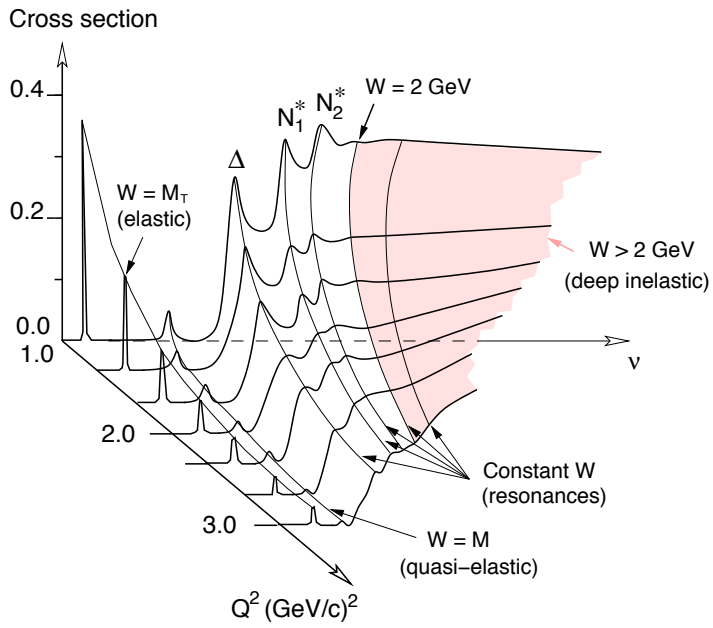

Figure 1.4: Inclusive electron scattering cross section from a light nuclear target. Figure reproduced from [40].

As ν and Q^2 increase further such that $1.2 < W < 2\,\text{GeV}$, we come to the *resonance region*, where we explore the substructure of the nucleon. In this energy range, it is the quarks that make up the nucleon absorbing the energy of the virtual photon, leading to (unstable) excited states of the nucleon called nucleon resonances. The most prominent resonance occurs at $W = 1.232\,\text{GeV}$, known as the Δ resonance. Higher resonances are also possible at $W > 1.4\,\text{GeV}$, but are difficult to discern from one another, as their peaks and tails tend to overlap.

In the region for $W > 2\,\text{GeV}$, ν and Q^2 become large enough so that the quarks can be resolved inside the nucleon. This region is known as the *deep inelastic scattering* (DIS) region. In this case, the electron is scattering from an asymptotically free quark (or anti-quark) in the nucleon. The smooth cross section in Figure 1.4 at large ν and Q^2 indicates the large number of multiparticle states which are accessible via a large combination of ν and Q^2 values.

1.4.3.1 Scattering Formalism

In this section we give a mathematical description of the DIS cross section for electrons scattering from a nucleon target. The process can be represented by the contraction of

two tensors*. We can describe the lepton vertex of Figure 1.3 with the tensor $L_{\mu\nu}$, and in a similar fashion we can represent the hadron vertex by a tensor $W^{\mu\nu}$. Assuming one photon exchange between the incident electron and the target nucleon, one can write the differential cross section for detecting a scattered electron in the energy range $(E', E'+dE')$ in a solid angle of $d\Omega$ in the laboratory frame as:

$$\frac{d^2\sigma}{d\Omega dE'} = \frac{\alpha^2}{2Mq^4}\frac{E'}{E}L_{\mu\nu}W^{\mu\nu}, \tag{1.9}$$

where α is the electromagnetic structure constant, $\sim 1/137$; M is the mass of the nucleon in GeV; q is the four-momentum transfer to the target; E' is the scattered electron energy in GeV; E is the incident electron energy in GeV; $L_{\mu\nu}$ is the leptonic tensor, and $W^{\mu\nu}$ is the hadronic tensor. The leptonic tensor is understood from quantum electrodynamics and may be written in terms of the Dirac γ matrices and Dirac electron spinors u and $\bar{u} = u^\dagger\gamma^0$:

$$L_{\mu\nu}\left(k,s;k',s'\right) = \left[\bar{u}\left(k',s'\right)\gamma_\mu u\left(k,s\right)\right]^*\left[\bar{u}\left(k',s'\right)\gamma_\nu u\left(k,s\right)\right], \tag{1.10}$$

where the electron spinors are functions of the incident and scattered electron four-momenta k and k', respectively, as well as their spin four-vectors s and s'. We can separate $L_{\mu\nu}$ into symmetric and antisymmetric components under the interchange of the μ and ν indices, which will prove to be useful shortly:

$$L_{\mu\nu}\left(k,s;k',s'\right) = L^{(S)}_{\mu\nu}\left(k;k'\right) + iL^{(A)}_{\mu\nu}\left(k,s;k'\right) + L^{'(S)}_{\mu\nu}\left(k,s;k',s'\right) + iL^{'(A)}_{\mu\nu}\left(k;k',s'\right). \tag{1.11}$$

The individual symmetric (S) and anti-symmetric (A) terms are written as:

$$\begin{aligned}
L^{(S)}_{\mu\nu}\left(k;k'\right) &= k_\mu k'_\nu + k'_\mu k'_\nu - g_{\mu\nu}\left(k\cdot k' - m^2\right), && (1.12)\\
L^{(A)}_{\mu\nu}\left(k,s;k'\right) &= m\varepsilon_{\mu\nu\alpha\beta}s^\alpha\left(k-k'\right)^\beta, && (1.13)\\
L^{'(S)}_{\mu\nu}\left(k,s;k',s'\right) &= \left(k\cdot s'\right)\left(k'_\mu s_\nu + s_\mu k'_\nu - g_{\mu\nu}k'\cdot s\right) - \left(k\cdot k' - m^2\right)\left(s_\mu s'_\nu + s'_\mu s_\nu - g_{\mu\nu}s\cdot s'\right)\\
&+ \left(k'\cdot s\right)\left(s'_\mu k_\nu + k_\mu s'_\nu\right) - \left(s\cdot s'\right)\left(k_\mu k'_\nu + k'_\mu k_\nu\right), && (1.14)\\
L^{'(A)}_{\mu\nu}\left(k;k',s'\right) &= m\varepsilon_{\mu\nu\alpha\beta}s'^\alpha\left(k-k'\right)^\beta, && (1.15)
\end{aligned}$$

where ε is the Levi-Civita symbol, evaluated to +1 for cyclic permutations of ε_{0123}, and -1 for reverse-cyclic permutations like ε_{3210}. Upon summing Equation 1.10 over s' and

*For this discussion, we will follow the work of Anselmino *et al.* [43].

averaging over s, we obtain the unpolarized leptonic tensor $2L^{(S)}_{\mu\nu}$. Summing over just the final spin states s' yields the combination $2L^{(S)}_{\mu\nu} + 2iL^{(A)}_{\mu\nu}$.

The hadronic tensor $W^{\mu\nu}$ contains QED and QCD physics, and therefore is not as well-known as $L_{\mu\nu}$. However, we can still define it in terms of symmetric and anti-symmetric components in a similar fashion to what was done for the leptonic tensor:

$$W_{\mu\nu}(q;P,S) = W^{(S)}_{\mu\nu}(q;P) + iW^{(A)}_{\mu\nu}(q;P,S), \tag{1.16}$$

where q is the four-momentum transfer, P is the four-momentum of the target nucleon and S is its spin four-vector. The symmetric and anti-symmetric components are written as:

$$\begin{aligned}
\frac{1}{2M}W^{(S)}_{\mu\nu}(q;P) &= \left(-g_{\mu\nu} + \frac{q_\mu q_\nu}{q^2}\right) W_1\left(P\cdot q, q^2\right) \\
&+ \left[\left(P_\mu - \frac{P\cdot q}{q^2}q_\mu\right)\left(P_\nu - \frac{P\cdot q}{q^2}q_\nu\right)\right]\frac{W_2\left(P\cdot q, q^2\right)}{M^2} \qquad (1.17) \\
\frac{1}{2M}W^{(A)}_{\mu\nu}(q;P,S) &= \varepsilon_{\mu\nu\alpha\beta}q^\alpha\Bigg\{MS^\beta G_1\left(P\cdot q, q^2\right) \\
&+ \left[(P\cdot q)S^\beta - (S\cdot q)P^\beta\right]\frac{G_2\left(P\cdot q, q^2\right)}{M}\Bigg\}. \qquad (1.18)
\end{aligned}$$

Here, we have introduced the spin-averaged *structure functions* W_1 and W_2, which appear in the symmetric component, and the spin-dependent structure functions G_1 and G_2, which appear in the anti-symmetric component of $W_{\mu\nu}$. These structure functions effectively parameterize the unknown internal hadronic structure [39].

Utilizing Equations 1.9, 1.10 and 1.16, the cross section may be written as:

$$\frac{d^2\sigma}{d\Omega dE'} = \frac{\alpha^2}{2Mq^4}\frac{E'}{E}\left[L^{(S)}_{\mu\nu}W^{\mu\nu(S)} + L'^{(S)}_{\mu\nu}W^{\mu\nu(S)} - L^{(A)}_{\mu\nu}W^{\mu\nu(A)} - L'^{(A)}_{\mu\nu}W^{\mu\nu(A)}\right]. \tag{1.19}$$

The individual terms in the square brackets of Equation 1.19 are in general, measurable quantities. Experimentally, they can be investigated by considering different combinations of initial- and final-state lepton and hadron spin polarizations. For example, the unpolarized cross section is obtained by averaging over the initial spin states and summing over the final spin states, yielding the $L^{(S)}_{\mu\nu}W^{\mu\nu(S)}$ term:

$$\frac{d^2\sigma^{\text{unpol.}}}{d\Omega dE'} = \frac{1}{4}\sum_{s,s',S}\frac{d^2\sigma}{d\Omega dE'}\left(k,s;k',s'\right) = \frac{\alpha^2}{2Mq^4}\frac{E'}{E}2L^{(S)}_{\mu\nu}W^{\mu\nu(S)}, \tag{1.20}$$

whereas the difference of cross sections that have opposite target spins gives the combination of the anti-symmetric terms:

$$\sum_{s'}\left[\frac{d^2\sigma}{d\Omega dE'}\left(k,s,P,-S;k',s'\right)-\frac{d^2\sigma}{d\Omega dE'}\left(k,s,P,S;k',s'\right)\right]=\frac{\alpha^2}{2Mq^4}\frac{E'}{E}4L^{(A)}_{\mu\nu}W^{\mu\nu(A)}. \tag{1.21}$$

It should be noted that, in practice, experimentally it is typically easier to control the incident spins s and S, while not measuring the final spins s' and S'. This tends to limit the experimental investigation of the hadronic tensor.

1.4.4 Nucleon Structure Functions

Consider scattering unpolarized electrons from point-like, unpolarized spin-1/2 particles that are infinitely heavy with a charge of +1. In this case, energy conservation would give $E'=E$ and the cross section would be given by:

$$\left(\frac{d\sigma}{d\Omega}\right)_{\text{Mott}}=\frac{\alpha^2\cos^2(\theta/2)}{4E^2\sin^4(\theta/2)}, \tag{1.22}$$

with θ being the scattering angle of the electron. This quantity is known as the *Mott cross section*. However, since the nucleon is a composite object and is not infinitely massive, the cross section is more complicated than that seen in Equation 1.22, and is given by (cf. Equation 1.20):

$$\frac{d^2\sigma^{\text{unpol.}}}{d\Omega dE'}=\left(\frac{d\sigma}{d\Omega}\right)_{\text{Mott}}\left[W_2\left(\nu,Q^2\right)+2\tan^2(\theta/2)\,W_1\left(\nu,Q^2\right)\right], \tag{1.23}$$

where we have expressed the structure functions W_1 and W_2 in terms of ν, using $P\cdot q=M\nu$. We see from Equation 1.23 that the internal structure of the nucleon effectively augments the Mott cross section with the inclusion of structure functions. These functions parameterize how the nucleon structure deviates from a point particle, which is explicitly seen in their dependence on the energy scale, Q^2.

1.4.4.1 Unpolarized Structure Functions

By convention, the structure functions W_1 and W_2 are replaced by the structure functions F_1 and F_2, and also expressed in terms of the Bjorken-x variable and Q^2. They are defined as:

$$F_1\left(x,Q^2\right) = MW_1\left(\nu,Q^2\right) \tag{1.24}$$

$$F_2\left(x,Q^2\right) = \nu W_2\left(\nu,Q^2\right). \tag{1.25}$$

The use of x instead of ν arises because of the phenomenon of Bjorken scaling, which will be discussed in detail in Section 1.4.5.1. In essence, in the limit of large ν and Q^2 at fixed x, the structure functions $F_{1,2}$ lose a lot of their dependence on Q^2 and may be expressed as functions of x alone. In this limit, F_1 may be related to F_2 in a simple fashion.

Utilizing the expressions of $W_{1,2}$ in terms of $F_{1,2}$, the unpolarized cross section is expressed as:

$$\frac{d^2\sigma^{\text{unpol.}}}{d\Omega dE'} = \left(\frac{d\sigma}{d\Omega}\right)_{\text{Mott}}\left[\frac{1}{\nu}F_2\left(\nu,Q^2\right) + 2\tan^2\left(\theta/2\right)\frac{1}{M}F_1\left(\nu,Q^2\right)\right]. \tag{1.26}$$

For experiments that use targets that are not nucleons ($A \neq 1$), there are two conventions for expressing the quantities F_1 and F_2. The first is *per nucleon*, written as F_1/A and F_2/A. The second is *per nucleus*, where the structure functions are reported without dividing by A. The latter representation is used in this dissertation.

1.4.4.2 Polarized Structure Functions

We have seen how F_1 and F_2 allow one to access the symmetric part of the hadronic tensor (Eqn. 1.26). In a similar way, G_1 and G_2 gives access to the antisymmetric part of the hadronic tensor. First, we rewrite $G_{1,2}$ in terms of $g_{1,2}$, to follow the conventional representation (comparable to F_1 and F_2):

$$g_1\left(x,Q^2\right) = M^2\nu G_1\left(\nu,Q^2\right) \tag{1.27}$$

$$g_2\left(x,Q^2\right) = M\nu^2 G_2\left(\nu,Q^2\right). \tag{1.28}$$

In order to learn more about g_1 and g_2, we consider the experiment of scattering longitudinally polarized electrons (with their spins parallel or anti-parallel to their momentum) from polarized nucleons, which are at rest. Again, we follow the description in Anselmino *et al.* [43]. The spin four-vectors s for the electron and S for the target may be written as:

$$s^\mu_\uparrow = -s^\mu_\downarrow = \frac{1}{m}\left(|k|, E\hat{k}\right) \quad \text{and} \quad S^\mu = \left(0,\hat{S}\right), \tag{1.29}$$

where $\hat{k} = \vec{k}/|k|$; $\uparrow$ indicates that the electron spin is parallel to its momentum, $\downarrow$ indicates an anti-parallel electron spin.

Consider the cross section for the target spin aligned in one direction, and when it is flipped, keeping the electron spin direction fixed*. The difference of these two cross sections is written as:

$$\begin{aligned} \frac{d^2\sigma^{\uparrow,S}}{d\Omega dE'} - \frac{d^2\sigma^{\uparrow,-S}}{d\Omega dE'} &= -\frac{4\alpha^2}{Q^2}\frac{E'}{E}\Big[\left(E\cos\beta + E'\cos\Theta\right)\frac{1}{M\nu}g_1\left(x,Q^2\right) \\ &+ 2EE'\left(\cos\Theta - \cos\beta\right)\frac{1}{M\nu^2}g_2\left(x,Q^2\right)\Big], \end{aligned} \tag{1.30}$$

where β is the angle between the incident electron momentum $\vec{k}$ and the target spin $\vec{S}$ and Θ is the angle between the scattered electron momentum $\vec{k}'$ and $\vec{S}$, written as:

$$\cos\Theta = \sin\theta\sin\beta\cos\phi + \cos\theta\cos\beta. \tag{1.31}$$

The electron scattering angle is θ, which is the angle between $\vec{k}$ and $\vec{k}'$; ϕ is the angle between the electron scattering plane ($\vec{k}$,$\vec{k}'$) and the polarization plane ($\vec{k}$,$\vec{S}$). see Figure 1.5.

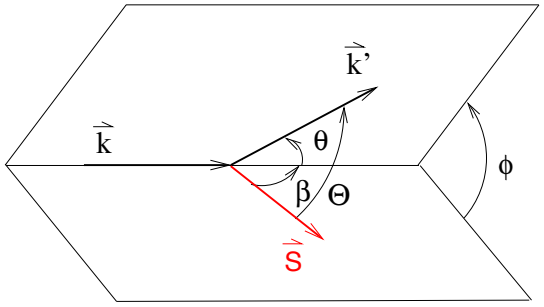

Figure 1.5: The kinematics of polarized electron-nucleon scattering. Figure reproduced from [40].

The two special cases we are interested in are when the target spin is parallel to the electron spin and when the target spin is perpendicular to the electron spin. When the target spin and electron spins are parallel, $\beta = 0$ and $\Theta = \theta$ and the cross section difference is given as:

*Alternatively, one could flip the electron spins and keep the target spin fixed, which would give the same result; it is the *relative* spin between the electron and target that matters.

$$\frac{d^2\sigma^{\downarrow,\Uparrow}}{d\Omega dE'} - \frac{d^2\sigma^{\uparrow,\Uparrow}}{d\Omega dE'} = \frac{4\alpha^2}{Q^2}\frac{E'}{\nu E}\left[\left(E + E'\cos\theta\right) g_1\left(x,Q^2\right) - 2Mxg_2\left(x,Q^2\right)\right]. \quad (1.32)$$

When the target spin is perpendicular to the electron spin, $\beta = \pi/2$ and $\Theta = \arccos\left(\sin\theta\cos\phi\right)$, and the cross section difference is written as:

$$\frac{d^2\sigma^{\downarrow,\Rightarrow}}{d\Omega dE'} - \frac{d^2\sigma^{\uparrow,\Rightarrow}}{d\Omega dE'} = \frac{4\alpha^2}{Q^2}\frac{E'^2}{\nu E}\sin\theta\left[g_1\left(x,Q^2\right) + \frac{2ME}{\nu}g_2\left(x,Q^2\right)\right]. \quad (1.33)$$

1.4.5 Interpretation

Up until now in the discussion, the unpolarized structure functions F_1 and F_2 and the polarized structure functions g_1 and g_2 have served to parameterize the unknown structure of the nucleon, simplifying our equations. In this section, we take a closer look at the physical meaning of the structure functions and how they describe the physics of the interactions inside the nucleon.

1.4.5.1 Bjorken Scaling

When probing an object of finite size, the measurement will depend upon the spatial resolution of our probe; in the case of electron scattering, this is the momentum transferred to the target squared, Q^2. If we consider the case where we increase Q^2 so that we can resolve the internal structure of the nucleon, the quarks will become visible. At this point, the inelastic electron-nucleon scattering may be seen as elastic scattering from a single quark (Fig. 1.6), while the other quarks remain undisturbed. Considering that quarks are point-like particles, increasing the resolution Q^2 will no longer affect the interaction.

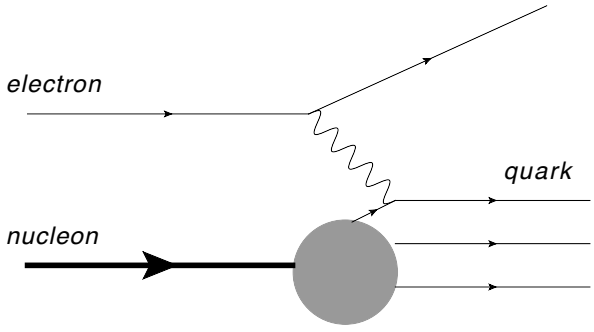

Figure 1.6: Lowest-order electron-quark scattering.

In the limit where $Q^2 \to \infty$ and $\nu \to \infty$, with $x = Q^2/(2M\nu)$ fixed (the Bjorken limit), the phenomenon where experimental observables lose their Q^2-dependence is known as *Bjorken scaling* [44]. As a result, the structure functions depend upon a single variable x. Furthermore, the F_2 structure function can be related to the F_1 structure function by the *Callan-Gross relation* [45]:

$$F_2(x) = 2xF_1(x). \tag{1.34}$$

1.4.5.2 The Quark-Parton Model

The Quark-Parton Model (QPM) is a model which allows us to connect the quark behavior to the structure functions. In this model, the interaction is described by incoherent scattering of virtual photons from free partons (quarks and anti-quarks) inside the nucleon, which holds in the limit where Q^2 is large enough to resolve the internal structure of the nucleon ($Q^2 > M^2$).

For convenience, we consider the infinite momentum reference frame, where the nucleon moves along the $\hat{z}$-axis with infinite momentum. In this frame, the target momentum is much larger than its mass*, and the three-momentum of the quark may be written as $\vec{p} = x\vec{P} + \vec{p}_T$, where P is the nucleon momentum, and p_T is the transverse quark momentum. At short interaction times, p_T is considered negligible. Hence, the momentum of the quark is given as $p = xP$, a fraction x of the nucleon momentum.

At this point, the structure functions may be written in terms of parton distribution functions (PDFs). If we define $q(x)$ as the probability of finding a quark q with momentum fraction x in a nucleon, we can express the unpolarized PDF as:

$$q(x) = q^{\uparrow}(x) + q^{\downarrow}(x). \tag{1.35}$$

The $\uparrow$ and $\downarrow$ indicate that the quark is polarized parallel or anti-parallel to the parent nucleon's polarization. For the unpolarized structure functions F_1 and F_2, we then have:

$$F_1(x) = \frac{1}{2}\sum_i e_i^2 q_i(x) \tag{1.36}$$

$$F_2(x) = x\sum_i e_i^2 q_i(x), \tag{1.37}$$

*Because of this, we can safely neglect target mass effects [46].

where e_i is the electromagnetic charge of the i^{th} quark, which arises because the quark-virtual photon coupling is electromagnetic. The equation for F_2 follows from the Callan-Gross relation.

The polarized structure functions may be expressed in terms of the PDFs in a similar manner. This time, we consider the polarized PDF, which is the difference of the polarized quark distributions:

$$\Delta q(x) = q^{\uparrow}(x) - q^{\downarrow}(x). \tag{1.38}$$

In an analogous fashion to F_1, the polarized structure function g_1 is given as:

$$g_1(x) = \frac{1}{2}\sum_i e_i^2 \Delta q_i(x), \tag{1.39}$$

where we see that g_1 is effectively the sum over the helicity distributions $\Delta q = q^{\uparrow} - q^{\downarrow}$ for all quark flavors i. The spin structure function g_2 has no clear interpretation in the parton model, as it necessarily describes the transverse spin structure of the nucleon, which vanishes in the QPM. To gain an understanding of g_2, we have to examine the interactions that occur between gluons and quarks which bind the nucleon together (Sect. 1.4.5.4).

1.4.5.3 Scaling Violation

The scaling behavior presented in Section 1.4.5.1 is only true in the limit of infinite Q^2 and ν. At finite values of Q^2 and ν, it is only an approximation. In reality, the quarks participating in the interaction with the electron may radiate gluons before or after scattering, shown in Figure 1.7. Such processes result in an infinite cross section, and can only be treated properly when all other processes of the same order are considered. These gluonic radiative corrections result in the cross section acquiring a logarithmic Q^2 dependence. As a result, the Q^2 dependence manifests itself in the structure functions. Such a dependence is seen in Figure 1.8, showing the F_2 structure function over many orders of magnitude in both x and Q^2.

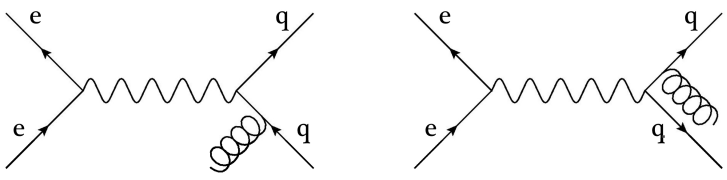

Figure 1.7: Lowest order gluon radiation in electron-quark scattering. Figure reproduced from [47].

As a result of the scaling violation, we re-cast the PDFs and the structure functions (Eqn. 1.36, 1.37 and 1.39) in terms of both x and Q^2. In particular, the definition of the PDF is now $q^{\uparrow(\downarrow)}(x,Q^2)$: this is the probability of finding a quark q with its polarization parallel (anti-parallel) to its parent nucleon's polarization with momentum fraction x *when viewed at an energy scale* $Q = \sqrt{Q^2}$.

The physical interpretation tied to scaling violation is that structure functions at low Q^2 are dominated by three *valence* quarks "dressed" by sea quarks (manifesting as q-$\bar{q}$ pairs) and gluons. As Q^2 is increased, the resolving power increases, allowing for sensitivity to the "bare" quarks and gluons which make up the nucleon.

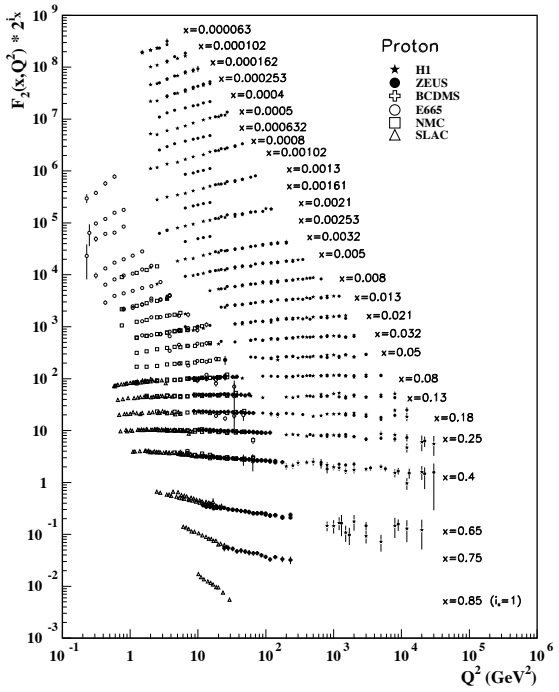

Figure 1.8: Scaling violation in the F_2 structure function. In order to visually separate the data, the F_2 data were multiplied by 2^{i_x}, with $1 \leq i_x \leq 28$ being the x bin number. H1 and ZEUS data are positron-proton collider experiments. All other data are from lepton scattering from fixed proton targets. The SLAC data used an electron beam, while BCDMS, E665 and NMC used a muon beam. Figure reproduced from [35].

1.4.5.4 The Operator Product Expansion

The QPM provides a *probabilistic* interpretation for the deep inelastic structure functions in the limit of $Q^2 \to \infty$. To understand structure functions (and ultimately cross sections) at finite Q^2 however, another approach is needed. The *Operator Product Expansion* (OPE) [48]

allows for this by seperating the perturbative component from the non-perturbative component in the formalism, where *moments* of structure functions may be computed.

The key concept of the OPE is to consider the product of two *local* quark (or gluon) operators $\mathcal{O}_a(x)\mathcal{O}_b(0)$, where we consider the limit of $x \to 0$:

$$\lim_{x\to 0} \mathcal{O}_a(x)\mathcal{O}_b(0) = \sum_k c_{abk}(x)\mathcal{O}_k(0),$$

where the coefficient functions c_{abk} are the Wilson coefficients and contain the perturbative part; non-perturbative effects become important for distances much larger than x [46]. The non-perturbative components manifest in $\mathcal{O}_k(0)$, which contribute to the cross section on the order of $x^{-n}(Q/M)^{2-D-n}$. The exponents D and n are the (mass) dimension and spin of the operator, respectively. The nucleon mass is given by M and $Q = \sqrt{Q^2}$. The *twist* of the operator t is defined by:

$$t \equiv D - n. \tag{1.40}$$

At large Q^2, $t = 2$ terms dominate in the OPE; at low Q^2, higher-twist ($t > 2$) operators become important. In particular, the g_2 structure function gives us insight into higher-twist effects.

The work of Wandzura and Wilczek [49] showed that (ignoring quark mass effects) g_2 can be separated into a purely twist-2 term and a higher-twist term:

$$g_2(x,Q^2) = g_2^{\mathrm{WW}}(x,Q^2) + \bar{g}_2(x,Q^2), \tag{1.41}$$

where $g_2^{\mathrm{WW}}(x,Q^2)$ is a pure twist-2 term, which can be expressed entirely in terms of g_1:

$$g_2^{\mathrm{WW}} = -g_1(x,Q^2) + \int_x^1 dy \frac{g_1(y,Q^2)}{y}, \tag{1.42}$$

and $\bar{g}_2(x,Q^2)$ is a twist-3 term that contains quark-gluon correlations [49]. With the knowledge of the twist-2 function g_1, the higher-twist component of g_2 may be isolated. This makes g_2 a useful measure of higher-twist effects in non-perturbative QCD, as g_2 contributes at leading order to the experimental asymmetry $A_\perp$ (Ch. 2).

1.5 Dissertation Outline

The rest of this dissertation is outlined as follows: in Chapter 2, we discuss a number of models used to describe and interpret the A_1 data. In Chapter 3, we outline the setup used for the E06-014 experiment, including the hardware components and analysis software. In Chapter 4, the calibration procedures for a number of the sub-detectors is presented. Chapter 5 gives a detailed description of the data analysis for particle identification, efficiency studies and simulations for the Left High-Resolution Spectrometer (LHRS) and the BigBite spectrometer, along with the analysis required to extract unpolarized cross sections from the LHRS data, and double-spin asymmetries from the BigBite data that ultimately leads to obtaining A_1^n, the matrix element a_2^n, and the flavor-separated ratios $(\Delta u + \Delta\bar{u})/(u + \bar{u})$ and $(\Delta d + \Delta\bar{d})/(d + \bar{d})$. Chapter 6 presents the results for A_1^n, a_2^n and flavor-separated ratios for the up and down quarks compared to existing world data. We present concluding remarks in Chapter 7.

CHAPTER 2

A_1: THE VIRTUAL PHOTON-NUCLEON ASYMMETRY

In this chapter, we will discuss the virtual photon-nucleon asymmetry, A_1. In Section 2.1.1, it is described in terms of virtual photon cross sections. In Section 2.1.2, it is written in terms of the spin structure functions which gives some insight into the spin structure of the nucleon. The experimental measurement of A_1 is discussed in Section 2.2. Various models are discussed in Section 2.4, and in Section 2.3 the current world data is presented.

2.1 Defining the A_1 and A_2 Spin Asymmetries

2.1.1 Virtual Photon Cross Sections

When scattering electrons from nucleons, the interaction is mediated by an exchange of *virtual* photons with four-momentum q. Each of these particles carry spin, and plays a role in affecting the probability (or cross section) of the scattering interaction.

The difference between a virtual photon and a real photon is that real photons have $q^2 = 0$, whereas for virtual photons, $q^2 \neq 0$. Another important difference is that while real photons have two possible polarization states perpendicular to its momentum, virtual photons can be polarized longitudinally or transversely relative to its momentum $\vec{q}$, resulting in three possible polarization states. This plays a role in the computation of the cross section involving virtual photons and nucleons.

To determine the cross section of the nucleon that absorbs the virtual photon, the virtual photon flux must be treated correctly. For real photons, the flux is $4M\nu$, with M being the nucleon mass. It turns out that the flux factor for virtual photons is arbitrary [39]. The Hand convention [50] is typically utilized, which yields a flux in the laboratory-frame of

$4M[\nu - Q^2/(2M)]$. Using this, the photoabsorption cross section for a nucleon target may be written as:

$$\frac{d\sigma}{dE'd\Omega} = \Gamma\left(\varepsilon\sigma_L + \sigma_T\right), \tag{2.1}$$

where $\sigma_{L,T}$ corresponds to cross sections where the virtual photon is polarized longitudinally or transversely with respect to its momentum. The virtual photon flux factor Γ is:

$$\Gamma = \frac{\alpha\left[\nu - Q^2/(2M)\right]}{2\pi^2 Q^2}\frac{E'}{E}\frac{1}{1-\varepsilon}, \tag{2.2}$$

where E is the electron beam energy, E' is the scattered electron energy and ε is the ratio of the virtual photon's longitudinal to transverse polarization. It is expressed as:

$$\varepsilon = \left[1 + 2\left(1+\gamma^2\right)\tan^2\frac{\theta}{2}\right]^{-1}, \tag{2.3}$$

and θ is the electron scattering angle and $\gamma^2 = (2Mx)^2/Q^2$. The cross sections σ_L and σ_T in Equation 2.1 contain information describing the hadronic vertex, much like the unpolarized structure functions F_1 and F_2. Due to this, these cross sections can be expressed in terms of σ_T and σ_L [39]:

$$\sigma_T \equiv \frac{4\pi^2\alpha}{\nu - Q^2/(2M)}\frac{1}{M}F_1\left(\nu, Q^2\right) \tag{2.4}$$

$$\sigma_L \equiv \frac{4\pi^2\alpha}{\nu - Q^2/(2M)}\left[\left(1+\frac{\nu^2}{Q^2}\right)\frac{1}{\nu}F_2\left(\nu, Q^2\right) - \frac{1}{M}F_1\left(\nu, Q^2\right)\right]. \tag{2.5}$$

From these equations, a relationship between F_1 and F_2 can be determined:

$$F_1\left(x, Q^2\right) = \frac{F_2\left(x, Q^2\right)\left(1+\gamma^2\right)}{2x\left[1 + R\left(x, Q^2\right)\right]}, \tag{2.6}$$

with $R = \sigma_L/\sigma_T$. In the Bjorken limit, it can be seen that $\sigma_L \to 0$, and Equation 2.6 reduces to the Callan-Gross relation (cf. Equation 1.34).

Let us consider a scattering interaction where the nucleon is longitudinally polarized, while the virtual photon is circularly polarized with a helicity of ± 1. There then arises two possible helicity-dependent cross sections for a given nucleon polarization, denoted as $\sigma_{3/2}$ and $\sigma_{1/2}$. The subscripts denote the projection of the total spin of the virtual photon-nucleon system along the direction of the virtual photon momentum [40, 51]. When the virtual photon spin is parallel (anti-parallel) to the nucleon spin, they add to 3/2 (1/2), see Figure 2.1. From these two cross sections, the A_1 *asymmetry* is formed as:

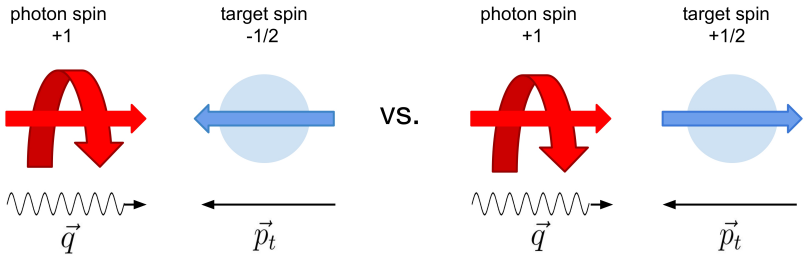

Figure 2.1: The two cases of spin projections for the virtual photon and target nucleon in the definition of the A_1 spin asymmetry.

$$A_1 \equiv \frac{\sigma_{1/2} - \sigma_{3/2}}{\sigma_{1/2} + \sigma_{3/2}}, \tag{2.7}$$

where the ratio of the difference of cross sections to their sum is called an asymmetry.

Another spin asymmetry that may be formed in terms of these virtual photon cross sections is the A_2 asymmetry, defined as:

$$A_2 \equiv \frac{2\sigma_{LT}}{\sigma_{1/2} + \sigma_{3/2}}. \tag{2.8}$$

This asymmetry arises as an interference between the longitudinal and transverse virtual photon-nucleon scattering amplitudes, which is manifested in the cross section σ_{LT} [52], and is defined as:

$$\sigma_{LT} \equiv \frac{4\pi^2\alpha}{M\left(\nu - Q^2/(2M)\right)} \frac{\sqrt{Q^2}}{\nu} \left[g_1\left(x, Q^2\right) + g_2\left(x, Q^2\right)\right]. \tag{2.9}$$

There exists no physical interpretation of σ_{LT} that is comparable to that for the cross sections $\sigma_{1/2}$ and $\sigma_{3/2}$. The A_2 asymmetry is bounded by a function of A_1 and the ratio $R = \sigma_L/\sigma_T$, known as the Soffer Bound [53]:

$$A_2(x, Q^2) \leq \sqrt{\frac{R(x, Q^2)}{2}\left[1 + A_1(x, Q^2)\right]}. \tag{2.10}$$

2.1.2 Spin Structure Functions

The spin asymmetries A_1 and A_2 may be written in terms of the spin structure functions g_1 and g_2:

$$A_1 = \frac{g_1(x,Q^2) - \gamma^2 g_2(x,Q^2)}{F_1(x,Q^2)} \tag{2.11}$$

$$A_2 = \frac{\gamma\left[g_1(x,Q^2) + g_2(x,Q^2)\right]}{F_1(x,Q^2)}. \tag{2.12}$$

At large Q^2*, $A_1 \approx g_1/F_1$. This can be seen by where $\gamma^2 \to 0$ as $Q^2 \to \infty$. A more physical argument on the quark level that describes this is as follows: if the spin of the virtual photon is anti-parallel to that of the quark, then the virtual photon can be absorbed and the quark spin is flipped; however, if the spins are *parallel*, then the absorption of the virtual photon is forbidden, since the total projection of the spins along $\vec{q}$ is 3/2 and the quark is a spin-1/2 particle. The mathematical form of the approximation can be illustrated using this physical interpretation in the following: for the case where the spins of the nucleon and virtual photon are parallel ($\sigma_{3/2}$), then the quark that *can* absorb the virtual photon has its spin anti-parallel to the nucleon spin. This translates to: $\sigma_{3/2} \sim \sum_i e_i^2 q_i^{\downarrow}(x)$. A similar argument may be made for the $\sigma_{1/2}$ case where only quarks with spins parallel to the parent nucleon can absorb virtual photons. Thus, we have: $\sigma_{1/2} \sim \sum_i e_i^2 q_i^{\uparrow}(x)$. Rewriting A_1 in terms of these approximations, we obtain:

$$A_1 \sim \frac{\sum_i e_i^2 \left[q_i^{\uparrow}(x) - q_i^{\downarrow}(x)\right]}{\sum_i e_i^2 \left[q_i^{\uparrow}(x) + q_i^{\downarrow}(x)\right]} = \frac{\sum_i e_i^2 \Delta q_i(x)}{\sum_i e_i^2 q_i(x)} = \frac{g_1(x)}{F_1(x)}. \tag{2.13}$$

As seen above, the A_1 asymmetry is a ratio of structure functions, and as a result there is not necessarily any Q^2 dependence. This is because g_1 and F_1 follow the same Q^2 evolution described by the DGLAP equations [54–56] which tends to cancel in the ratio, leading to A_1 being roughly Q^2 independent. This is reflected in experimental data [57] on the proton and neutron, shown in Figure 2.2.

*That is, for Q^2 large relative to the nucleon mass.

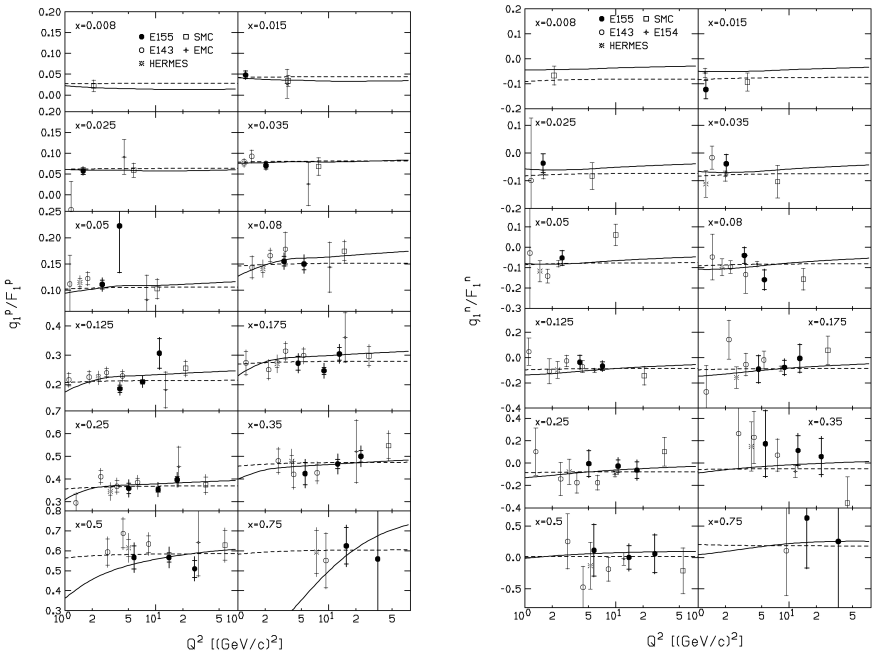

(a) g_1/F_1 for the proton (b) g_1/F_1 for the neutron

Figure 2.2: Q^2 evolution for g_1/F_1 for the proton (a) and neutron (b). Figures reproduced from [57].

2.2 Measuring A_1 and A_2

2.2.1 Electron Asymmetries

Due to the difficulty associated with aligning the virtual photon spin along the direction of the nucleon spin, another approach is utilized to measure A_1 and A_2; it consists of aligning the incident *electron* spin along the direction of the nucleon spin. The extraction of the *electron asymmetries* allows for the determination of A_1 and A_2. The electron asymmetries are given as:

$$A_{\parallel} \equiv \frac{\sigma^{\downarrow\Uparrow} - \sigma^{\uparrow\Uparrow}}{\sigma^{\downarrow\Uparrow} + \sigma^{\uparrow\Uparrow}} = \frac{1-\varepsilon}{(1-\varepsilon R)W_1}\left[M\left(E+E'\cos\theta\right)G_1 - Q^2 G_2\right] \tag{2.14}$$

$$A_{\perp} \equiv \frac{\sigma^{\downarrow\Rightarrow} - \sigma^{\uparrow\Rightarrow}}{\sigma^{\downarrow\Uparrow} + \sigma^{\uparrow\Uparrow}} = \frac{(1-\varepsilon)E'}{(1-\varepsilon R)W_1}\left[MG_1 + 2EG_2\right]\cos\theta, \tag{2.15}$$

where $\uparrow$ ($\downarrow$) indicates the electron spin parallel (anti-parallel) to its momentum and $\Uparrow$ ($\Downarrow$) indicates the target spin parallel (anti-parallel) to the electron beam momentum. The $\Leftarrow$ ($\Rightarrow$) indicates the target spin perpendicular to the beam momentum, pointing to the left

(right) of the beam line*. The benefit of measuring asymmetries is that the systematic uncertainties of cross sections tends to cancel in the ratio.

Since $A_\parallel$ and $A_\perp$ are functions of the unpolarized structure functions F_1 and F_2 and the polarized structure functions g_1 and g_2, the comparison of experimental results to theory becomes somewhat complicated. To simplify things, the relation of F_2 to F_1 via the ratio R may be exploited to yield [58]:

$$\frac{g_1}{F_1} = \frac{1}{d'}\left(A_\parallel + \tan\frac{\theta}{2}A_\perp\right) \tag{2.16}$$

$$\frac{g_2}{F_1} = \frac{y}{2d'}\left(-A_\parallel + \frac{E+E'\cos\theta}{E'\sin\theta}A_\perp\right) \tag{2.17}$$

where d' is:

$$d' = \frac{(1-\varepsilon)(2-y)}{y(1+\varepsilon R)}. \tag{2.18}$$

After some algebra, electron asymmetries may be written as [59]:

$$A_\parallel = D\,(A_1 + \eta A_2) \tag{2.19}$$

$$A_\perp = d\,(A_2 - \eta A_1)\,. \tag{2.20}$$

From Equations 2.19 and 2.20, we obtain for A_1 and A_2:

$$A_1 = \frac{1}{D(1+\eta\xi)}A_\parallel - \frac{\eta}{d(1+\eta\xi)}A_\perp \tag{2.21}$$

$$A_2 = \frac{\xi}{D(1+\eta\xi)}A_\parallel + \frac{1}{d(1+\eta\xi)}A_\perp, \tag{2.22}$$

where D is the virtual photon depolarization factor. The kinematic factors D, η, d and ξ are defined as:

*The sign convention that determines these directions will be discussed in Section 5.5.

$$D = \frac{E - \varepsilon E'}{E(1+\varepsilon R)} \tag{2.23}$$

$$\eta = \frac{\varepsilon\sqrt{Q^2}}{E - \varepsilon E'} \tag{2.24}$$

$$d = D\sqrt{\frac{2\varepsilon}{1+\varepsilon}} \tag{2.25}$$

$$\xi = \eta\frac{1+\varepsilon}{2\varepsilon}. \tag{2.26}$$

Equations 2.21 and 2.22 allow us to compute A_1 and A_2 directly from the measured electron spin asymmetries.

2.3 World Data

Experimental measurements for A_1 have been conducted by a number of collaborations from SLAC, CERN, DESY and Jefferson Lab covering a large range in x and Q^2 using various targets, including the proton, neutron, deuterium and ^{3}He. These data are plotted in Figure 2.3. In Table 2.1, we summarize the existing measurements.

Table 2.1: Existing measurements of A_1.

Experiment	Target	Observable	x Coverage	Q^2 Coverage $\left(\mathrm{GeV}^2\right)$
SLAC E142 [60]	^{3}He	$A_1^n, A_1^{^3\mathrm{He}}$	$0.03 \lesssim x \lesssim 0.6$	2
SLAC E143 [51]	NH_3, ND_3	A_1^n, A_1^p, A_1^d	$0.024 \lesssim x \lesssim 0.75$	$0.5 \sim 10$
SLAC E154 [61]	^{3}He	A_1^n	$0.014 \lesssim x \lesssim 0.7$	$1 \sim 17$
SLAC E155 [62, 63]	NH_3	A_1^p, A_1^d	$0.014 \lesssim x \lesssim 0.9$	$1 \sim 40$
HERMES [64–67]	H, ^{2}H, ^{3}He	$A_1^n, A_1^p, A_1^d, A_1^{^3\mathrm{He}}$	$0.023 \lesssim x \lesssim 0.6$	$1 \sim 15$
SMC [68]	NH_3,C_4H_9OH,C_4D_9OH	A_1^p, A_1^d	$0.003 \lesssim x \lesssim 0.7$	$1 \sim 60$
EMC [18, 19]	NH_3	A_1^p	$0.01 \lesssim x \lesssim 0.7$	$3.5 \sim 29.5$
COMPASS [69, 70]	NH_3	A_1^p, A_1^d	$0.004 \lesssim x \lesssim 0.7$	$1 \sim 100$
JLab E99-117 [71]	^{3}He	$A_1^n, A_1^{^3\mathrm{He}}$	$0.327 < x < 0.601$	$2.7 \sim 4.8$
JLab E01-012 [72]	^{3}He	$A_1^{^3\mathrm{He}}$	$0.4 \lesssim x \lesssim 0.9$	$1 \sim 3.6$
JLab CLAS EG1b [73]	NH_3,ND_3	A_1^p, A_1^d	$0.175 < x < 0.575$	$1 \sim 4$

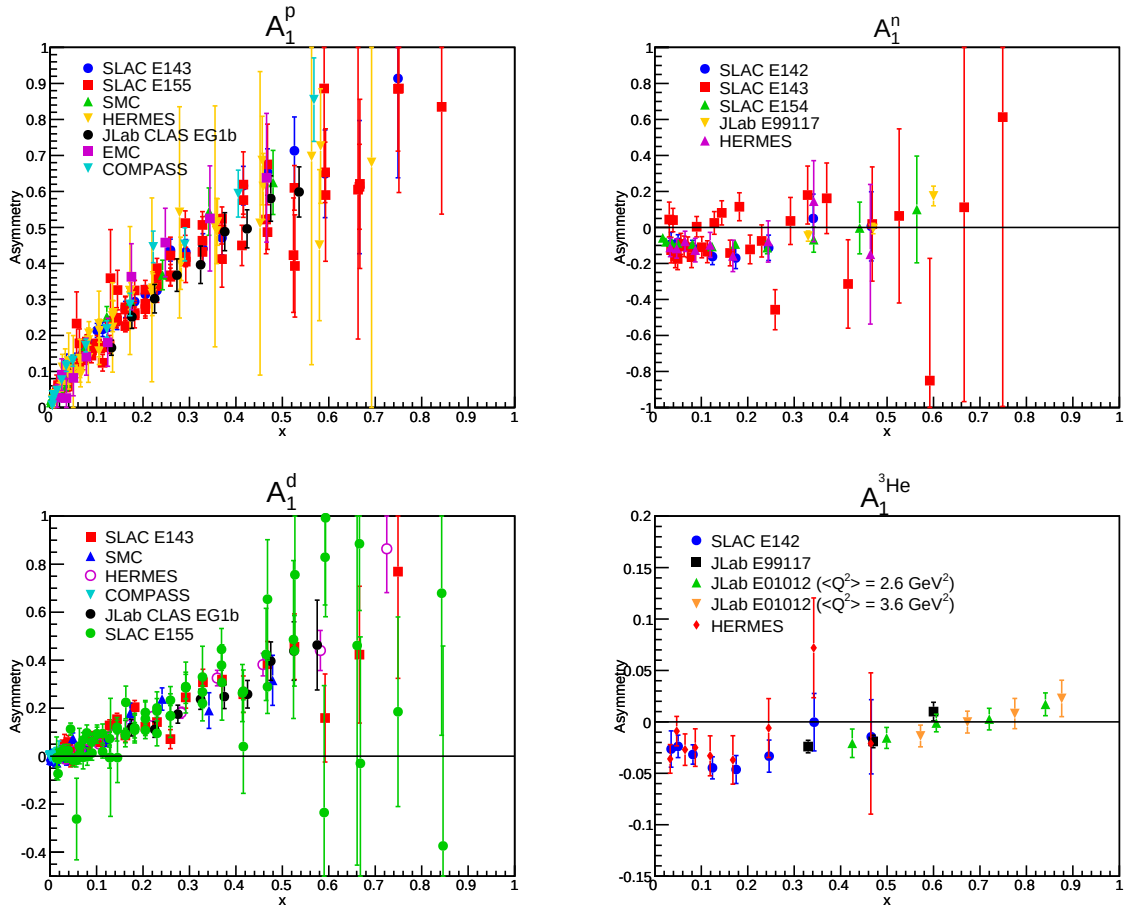

Figure 2.3: The world data on A_1 for the proton, neutron, deuteron and ^{3}He.

2.4 Models

In this section, we discuss the various theoretical models that can be used to describe A_1. In Section 2.4.1, we discuss SU(6) symmetric models, while in Section 2.4.2 we discuss mechanisms that break SU(6) symmetry. In Section 2.4.3 we discuss perturbative QCD calculations in two forms, without and with orbital angular momentum included. In Section 2.4.4, a statistical quark model is presented. Duality is discussed in Section 2.4.5, while chiral soliton models are examined in Section 2.4.6. Instanton models are presented in Section 2.4.7, and bag model calculations are discussed in Section 2.4.8. Finally, Dyson-Schwinger Equation treatments are presented in Section 2.4.9.

When the various models are compared to data, we focus on A_1^n. In the figures to follow, we intentionally leave out the results from SLAC E143 due to their large errors in the large x ($\gtrsim 0.4$) region.

2.4.1 SU(6)

2.4.1.1 Constituent Quarks

Constituent quarks have the same conserved charges and quantum numbers as the fundamental QCD quarks, but have effective masses that are larger than those used in pQCD calculations (current quarks). A qualitative description of constituent quarks corresponds to valence (current) quarks being "dressed" by clouds of q-$\bar{q}$ pairs and gluons, where the quark gains an effective mass of $\approx 300\,\text{MeV}$.

Despite the ambiguity concerning the mechanism by which current quarks become dressed in QCD, it is an accepted model due to its success in describing hadronic physics data in the low-energy regime; in particular, hadron spectroscopy and structure [74].

2.4.1.2 Non-Relativistic Constituent Quark Model

In the non-relativistic constituent quark model (CQM), the nucleon is described by a symmetric SU(6) wave function in both the constituent quark and current quark basis. The six degrees of freedom correspond to spin and isospin (2), and flavor (3). Spin and isospin are equal to 1/2, and orbital angular momentum of the quarks is neglected. If we consider a neutron that is polarized along the $+\hat{z}$ direction, its wave function is given by [75]:

$$\begin{aligned} |n\uparrow\rangle &= \frac{1}{\sqrt{2}}\left|d\uparrow(ud)_{S=0,S_z=0}\right\rangle \\ &+ \frac{1}{\sqrt{18}}\left|d\uparrow(ud)_{S=1,S_z=0}\right\rangle - \frac{1}{3}\left|d\downarrow(ud)_{S=1,S_z=1}\right\rangle \\ &- \frac{1}{3}\left|u\uparrow(dd)_{S=1,S_z=0}\right\rangle - \frac{\sqrt{2}}{3}\left|u\downarrow(dd)_{S=1,S_z=1}\right\rangle, \end{aligned} \tag{2.27}$$

where the quarks in the parentheses are in a diquark state, and their total spin is denoted by S and the $\hat{z}$-projection is given by S_z. The equivalent wave function for the proton may be obtained by interchanging u and d in Equation 2.27. When SU(6) is considered a perfect symmetry, diquark states for which $S = 0$ and 1 contribute equally [76]. Additionally, combining the calculated total probability of finding each quark in a given spin state and assuming that the virtual photon absorption cross section is equal to the sum of those for the three constituent quarks, predictions for A_1^p, A_1^n, $\Delta u/u$ and $\Delta d/d$ are given as [75]:

$$A_1^p = \frac{5}{9}, \quad A_1^n = 0, \quad \frac{\Delta u}{u} = \frac{2}{3}, \quad \text{and} \quad \frac{\Delta d}{d} = -\frac{1}{3}. \tag{2.28}$$

We can examine SU(6) symmetry through the ratio of F_2^n/F_2^p in the valence quark region:

$$R^{np} \equiv \frac{F_2^n}{F_2^p} = \frac{u(x)+4d(x)}{4u(x)+d(x)}. \tag{2.29}$$

If SU(6) symmetry were true, then $R^{np} = 2/3$ because the relation $u(x) = 2d(x)$ holds when comparing valence quark distributions in the proton and neutron. Experimental data from SLAC [77–79] has shown that $R^{np} \neq 2/3$, see Figure 2.4. This indicates that SU(6) symmetry is broken [76, 80]. As a result, more complicated models for A_1 must be considered.

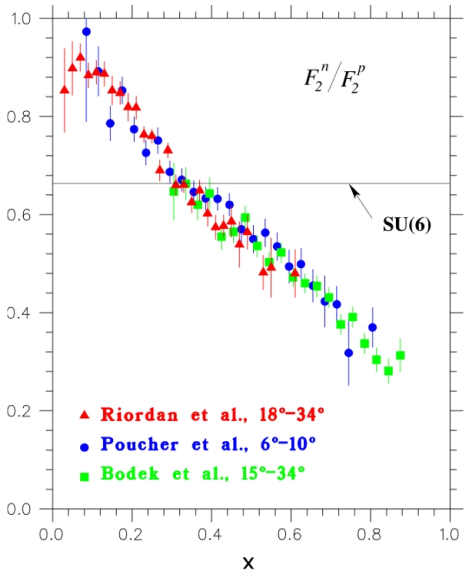

Figure 2.4: The world data on F_2^n/F_2^p from SLAC [77–79]. We note here how the data are in stark contrast to the SU(6) prediction of 2/3. Plot reproduced from [40].

2.4.2 SU(6) Breaking and Hyperfine Perturbed CQM

With SU(6) symmetry known to be broken, the SU(6) approach can be extended to include hyperfine (or chromomagnetic) interactions between the quarks in the diquark state, described by the equation [81]:

$$H_{hyp}^{ij} = A_{ij}\left\{\frac{8\pi}{3}\vec{S}_i\cdot\vec{S}_j\delta^3(\vec{r}_{ij}) + \frac{1}{r_{ij}^3}\left[3\left(\vec{S}_i\cdot\hat{r}_{ij}\right)\left(\vec{S}_j\cdot\hat{r}_{ij}\right) - \vec{S}_i\cdot\vec{S}_j\right]\right\}, \tag{2.30}$$

where $A_{ij} = 2\alpha_s/(3m_im_j)$ and $m_{i,j}$ is the mass of the i^{th} and j^{th} quarks, respectively. To

zeroth order, nucleons are S-wave particles, so the only term that remains is the first term, the Fermi contact term*. In the nucleon rest frame, this term *raises* the energy of $S = 1$ diquark states and *lowers* the energy of $S = 0$ diquark states [81], making the first term in Equation 2.27, $|d^{\uparrow}(ud)_{S=0,S_z=0}\rangle$, more stable and hence is the dominant term in the momentum distribution as $x \to 1$.

Allowing for relativistic motion of quarks in a constituent quark framework reduces the contribution of the quarks' spin to that of the nucleon, called quenching. This effect can be described as a probability for a spin-flip (i.e., a spin-up quark flipping to spin-down, and vice-versa), $c_A(x)$:

$$c_A(x) = nx(1-x)^n. \tag{2.31}$$

Equation 2.31 needs to vanish at low and high x, as is evident by inspection. The parameter n is bounded by $2 < n < 4$ to provide the necessary amount of relativistic quenching†. A parameterization of the ratio $d(x)/u(x)$ is also made:

$$\frac{d(x)}{u(x)} = \kappa(1-x) \text{ for } x \to 1 \text{ and } 0.5 < \kappa < 0.6. \tag{2.32}$$

In the model, a pair of identical quarks is in an $S = 1$ state, while u-d pairs are in mixtures of $S = 0$ and $S = 1$ states [81]. Up quarks have a larger energy than down quarks on average‡, yielding a higher probability of finding an up quark at high x compared to finding a down quark. An immediate consequence of this is that $d/u \to 0$ as $x \to 1$. A result of these assumptions and parameterizations is that at $x = 1$, we have:

$$A_1^p = 1, \quad A_1^n = 1, \quad \frac{\Delta u}{u} = 1, \quad \text{and} \quad \frac{\Delta d}{d} = -\frac{1}{3}. \tag{2.33}$$

The predictions from this model are presented in Figure 2.5, which plots the world data on A_1^n from SLAC E142 [60] and E154 [82], HERMES [64], and JLab E99-117 [71] compared to the relativistic SU(6) model [81], given by the shaded band. The band indicates all possible combinations of n and κ (Eqns. 2.31 and 2.32). The model also predicts that:

$$\lim_{x\to 1} \frac{F_2^n}{F_2^p} = \frac{1}{4}, \tag{2.34}$$

which agrees with the data shown in Figure 2.4.

*This term is responsible for the ∼300 MeV difference between the nucleon and Δ masses [81].
†This means that the "relativistic SU(6)" spin distributions can satisfy the Bjorken sum rule [81].
‡Note that the PDFs we refer to here are those in the *proton*.

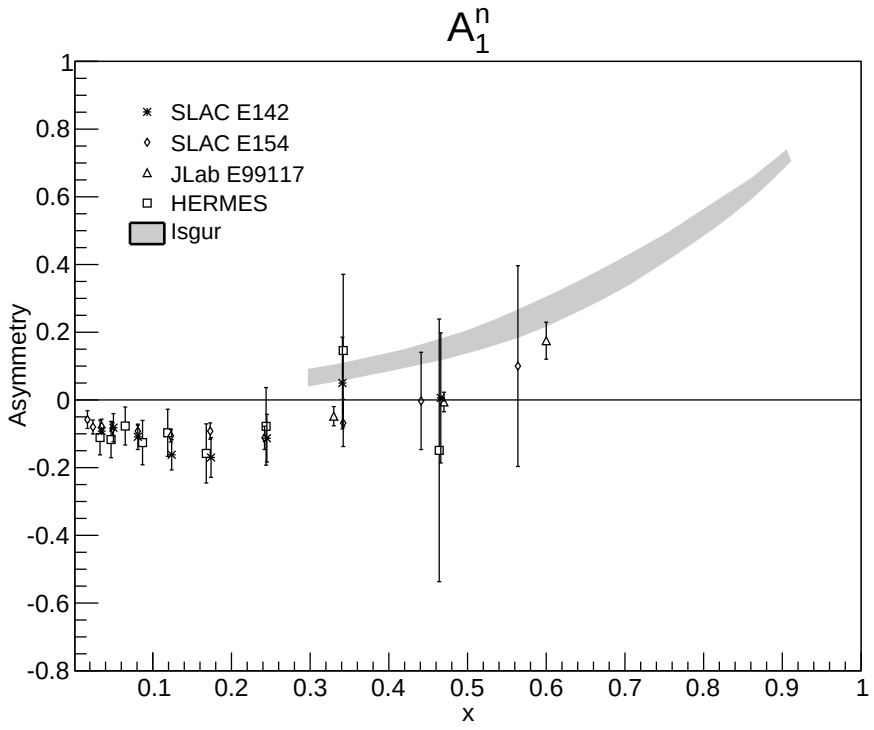

Figure 2.5: The world data on A_1^n from SLAC E142 [60] and E154 [82], HERMES [64], and JLab E99-117 [71] compared to the relativistic SU(6) model [81]. The shaded band indicates all possible combinations of n and κ, see text.

2.4.3 Perturbative QCD

Modeling the nucleon in the valence region can be approached in a perturbative manner, where incorporating some assumptions concerning the underlying physics leads to predictions about A_1 and the polarized-to-unpolarized PDF ratios. In this section, we highlight two of the main approaches used in the pQCD framework.

2.4.3.1 Hadron Helicity Conservation

The first approach concerns the work of Farrar *et al.* [83, 84], where they assume that the orbital angular momentum of quarks is zero. It then follows that there are two possible processes when the virtual photon probes the nucleon: the quarks in the diquark state can have their spins anti-aligned ($S = 0$) or aligned ($S = 1$). In the $S = 0$ state, these quarks exchange a transversely polarized gluon, and both spins are flipped, to conserve angular momentum; in the $S = 1$ state, the quarks exchange a *longitudinally* polarized gluon, and there is no spin-flip, due to angular momentum conservation. The ratio of the small momentum of the quark-pair to the large momentum of the longitudinally polarized gluon suppresses this

mode relative to the $S = 0$ state. As a result, as $x \to 1$, the struck quark must carry the helicity of the nucleon. This is called *hadron helicity conservation* (HHC).

Brodsky, Burkardt and Schmidt (BBS) performed a fit to the g_1 data available at the time, which included SLAC E142 and the SMC experiment at CERN, requiring HHC in the large x region [85]. This yielded parameterizations for the helicity-dependent quark distributions, from which the unpolarized and polarized PDFs can be constructed. Later, the group of Leader, Siderov and Stamenov (LSS) expanded upon the BBS parameterization by implementing Q^2-evolution and directly fitting A_1 data, and not derived measurements of g_1; this parameterization is known as the LSS (BBS) fit. The fits, as compared to world data on A_1^n, are plotted in Figure 2.6 at $Q^2 = 4\,\mathrm{GeV}^2$.

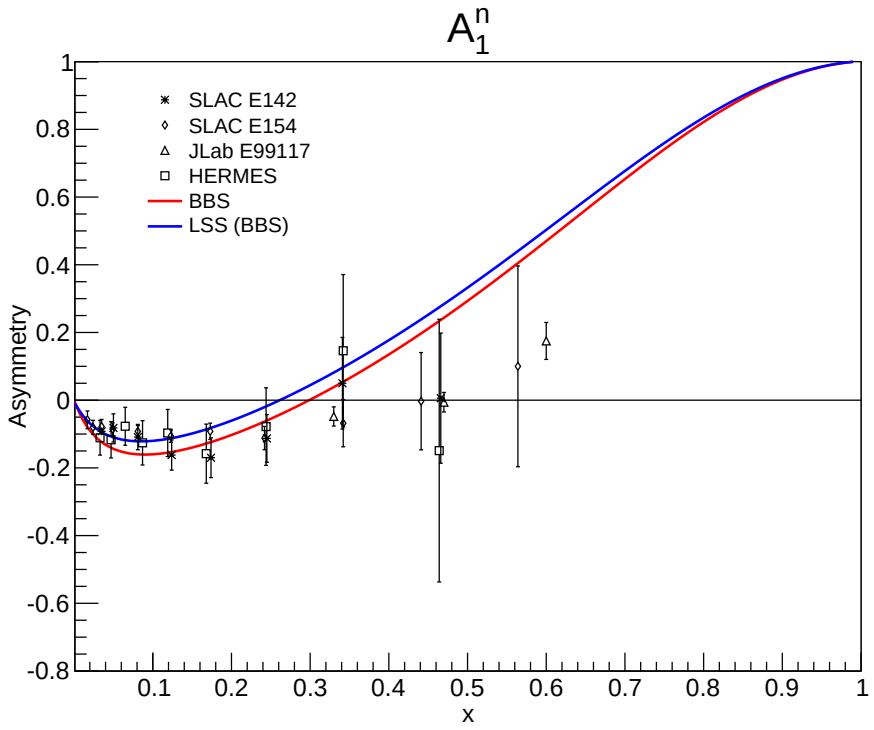

Figure 2.6: The world data [60, 64, 71, 82] on A_1^n compared to the BBS [85] and LSS (BBS) [86] parameterizations, which require hadron helicity conservation. Both models are evaluated at $Q^2 = 4\,\mathrm{GeV}^2$.

The predictions under HHC for A_1, $\Delta u/u$ and $\Delta d/d$ in the limit of $x \to 1$ are given as:

$$A_1^p = 1, \quad A_1^n = 1, \quad \frac{\Delta u}{u} = 1, \quad \text{and} \quad \frac{\Delta d}{d} = 1. \tag{2.35}$$

2.4.3.2 Orbital Angular Momentum of Quarks

A more realistic picture of the quarks in the nucleon is to allow for non-zero quark orbital angular momentum. This intrinsically violates the underlying assumptions of HHC, where angular momentum is transferred between the helicity of the struck quark and the orbital angular momentum.

Unfortunately, the available polarized data is limited at large Q^2 and W^2, compared to the wealth of unpolarized data; consequently, the $1/Q^2$ dependence of the polarized data cannot be ignored. To circumvent the problem, the LSS group made fits [87] at leading and next-to-leading order (NLO) in Q^2 *without* the constraints imposed by HHC, and is plotted in Figure 2.7 against the world data on A_1^n for $Q^2 = 2.5$ and $10\,\mathrm{GeV}^2$. These are the most up-to-date predictions of g_1^n/F_1^n for which the target mass and higher-twist corrections (that are scaled by $1/Q^2$) are accounted for.

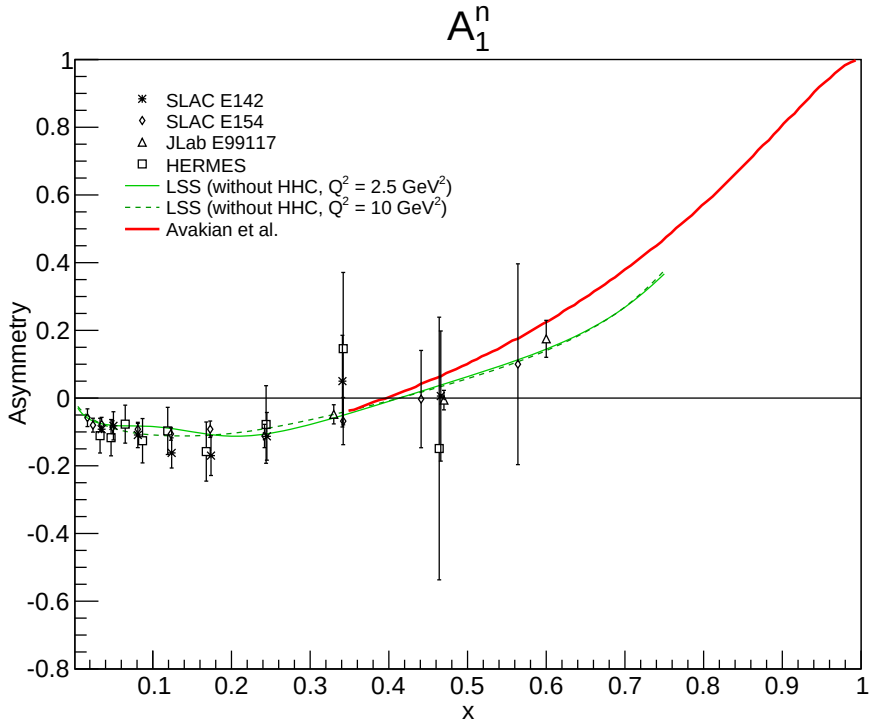

Figure 2.7: The world data [60, 64, 71, 82] on A_1^n compared to the LSS [87] parameterization at $Q^2 = 2.5\,\mathrm{GeV}^2$ (solid green) and $10\,\mathrm{GeV}^2$ (dashed green), which require does not require HHC. Also plotted is the Avakian *et al.* [88] model, which explicitly includes orbital angular momentum, and is evaluated at $Q^2 = 4\,\mathrm{GeV}^2$.

A pQCD calculation that explicitly includes Fock states with non-zero quark orbital angular momentum was developed by Avakian *et al.* [88]. These Fock states enhance helicity-flip amplitudes by logarithmic factors. In particular, at large x, the positive helicity

state (quark spin aligned with the nucleon spin) scales like $(1-x)^3$, whereas the negative helicity state scales as $(1-x)^5\log^2(1-x)$. This has a large effect on the behavior of the down quark distributions, in particular $\Delta d/d$ (Fig. 2.14). The Avakian *et al.* parameterization is also shown in Figure 2.7, plotted for $Q^2 = 4\,\mathrm{GeV}^2$. We see here that the LSS and Avakian *et al.* fits do better in describing the data compared to the parameterizations that require HHC, suggesting the importance of quark orbital angular momentum in the spin structure of the nucleon.

2.4.4 Statistical Model

A statistical mechanical approach may be used to describe nucleon structure; here, we describe the formalism developed by Bourrely *et al.* [89]. The nucleon is seen as a gas of massless partons in equilibrium at a given temperature in a finite volume, where a parton's distribution $p(x)$ at an input energy scale Q_0^2 is given by:

$$p(x) \propto \frac{1}{\exp\left(\frac{x-X_{0p}}{\bar{x}}\right) \pm 1}, \tag{2.36}$$

where the plus sign in the denominator is used for Fermi-Dirac distributions, for describing quarks and anti-quarks; the negative sign is used for Bose-Einstein distributions, to describe the gluons. The variable X_{0p} is a constant, comparable to a thermodynamical potential for the parton p, and $\bar{x}$ is a *universal* temperature for all partons. The parton distribution also contains a diffractive term*, which is not featured in other models of A_1. Based on this parameterization, a global NLO QCD analysis is performed for both unpolarized and polarized DIS data to obtain the best set of parameters, of which there are only eight.

The chiral nature of QCD yields two properties of the potential in this model: the first being that the potential of a quark with helicity h is opposite of that for an anti-quark of helicity -h. The second property is that the potential for gluons is zero. From the DIS data, it is seen that the u quark dominates compared to the d quark; this affects the relative strength of the potentials of the up and down quarks, where the up quark potential is greater than that of the down quark. The consequences of this leads to the predictions of A_1, $\Delta u/u$ and $\Delta d/d$ in the limit of $x \to 1$ to be [90]:

$$A_1^p = 0.80, \quad A_1^n = 0.30, \quad \frac{\Delta u}{u} = 0.77, \quad \text{and} \quad \frac{\Delta d}{d} = -0.35. \tag{2.37}$$

How the model performs compared to the world data on A_1^n is illustrated in Figure 2.8, where the model is evaluated at $Q^2 = 4\,\mathrm{GeV}^2$. Since the model is focused on the global

*The so-called "diffractive term" adjusts the PDFs so as to obtain better agreement with data towards the low x region, and is a consequence of pomeron universality [89].

behavior of partons, it turns out to be a good approximation in the low-x region, where the sea quarks and gluons dominate. Towards larger values of $x \gtrsim 0.6$, the features of valence quarks become the most prominent. The model shows decent agreement with the data in this range, and it will be interesting to see how the predictions shown at large x will compare to results expected from approved experiments in the 12 GeV era of JLab, where measurements are proposed to measure A_1^n in the DIS regime up to $x \sim 0.8$ with high precision [91, 92].

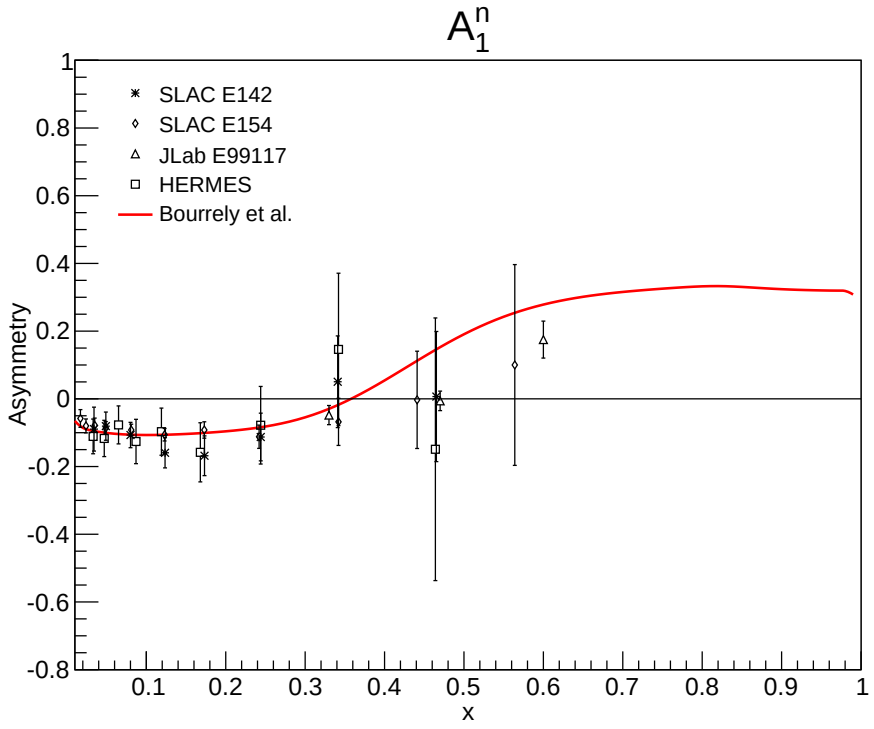

Figure 2.8: The world data [60, 64, 71, 82] on A_1^n compared to the statistical quark model [89, 90] evaluated at $Q^2 = 4\,\mathrm{GeV}^2$.

2.4.5 Quark-Hadron Duality

The concept of duality was established by Bloom and Gilman [93, 94], which demonstrated that data for the unpolarized structure function F_2 at low W (corresponding to resonance data) follows a global scaling curve for *high* W—that is, for DIS data—on average. This is written mathematically as:

$$\int_{x_1(W_1,Q^2)}^{x_2(W_2,Q^2)} dx F_2^{\mathrm{res}}(x,Q^2) = \int_{x_1(W_1,Q^2)}^{x_2(W_2,Q^2)} dx F_2^{\mathrm{DIS}}(x,Q^2), \tag{2.38}$$

where F_2^{res} corresponds to measurements of F_2 at $W \lesssim 2\,\text{GeV}$ and corresponds to relatively low Q^2, whereas F_2^{DIS} corresponds to measurements of F_2 for $W > 2\,\text{GeV}$, at comparatively high Q^2, and are evolved to the Q^2 of the resonance data. The integral may be conducted over the entire resonance region, which describes *global duality*, as portrayed in Equation 2.38; on the other hand, the integral can be performed over restricted regions in W, which is known as *local duality*.

High-luminosity data from JLab Hall C in the past ten years has shown 10% agreement with global duality for unpolarized structure functions down to $Q^2 \sim 0.5\,\text{GeV}^2$, and that local duality is upheld for the three most prominent resonances [95]. Elsewhere, experiments at DESY [96] and JLab Hall B [73, 97] have shown that global duality is satisfied for proton and deuteron *polarized* structure functions down to $Q^2 = 1.7\,\text{GeV}^2$, but *local* duality is violated up to $Q^2 \sim 5\,\text{GeV}^2$ [97]. Another JLab experiment in Hall A [72] found that global duality held for g_1 on the neutron and ^{3}He down to $Q^2 = 1.8\,\text{GeV}^2$.

Under the assumption that local duality is true, it allows for establishing a connection between the behavior of DIS structure functions in the limit of $x \to 1$ with elastic form factors at large Q^2 [98]. With local duality, one can use measured structure functions in the resonance region at large ξ* to extract elastic form factors [99]; or the reverse may be done, where elastic electromagnetic form factors at large Q^2 can be used to deduce the large x behavior of DIS structure functions. Such an approach is model independent, since duality is a phenomenological observation. It turns out that duality is in agreement with the pQCD prediction that $A_1 \to 1$ as $x \to 1$ [98].

In applying duality to observables, it has been motivated largely by phenomenology and is not well understood in a strict theoretical sense. Despite this, theorists have implemented finite-energy sum rules in terms of moments of structure functions, which allows for the mixing of contributions from all scattering regimes; this leads to duality given that Bjorken-scaling is not violated strongly [99]. Another approach is to combine quark-hadron duality with different methods of SU(6) symmetry breaking. For a given mechanism of SU(6) symmetry breaking used, different resonances (e.g., states for $s = 3/2$) can be suppressed in the large x region. For a specific mode, the relative strength for each resonance may be determined by imposing the condition that the calculations reproduce local duality. With the formalism in place, predictions for observables may be made; in particular, Figure 2.9 shows A_1^n plotted with the world data along with results obtained from three different approaches: suppressed transitions for helicity of $3/2$ (red); suppressed resonances with spin $3/2$ (blue); and finally suppressed resonances with symmetric wave functions (magenta).

*The variable ξ is the elastic analog to x in DIS, incorporating target mass corrections. Section 5.9.3.2 addresses target mass corrections for our measurements.

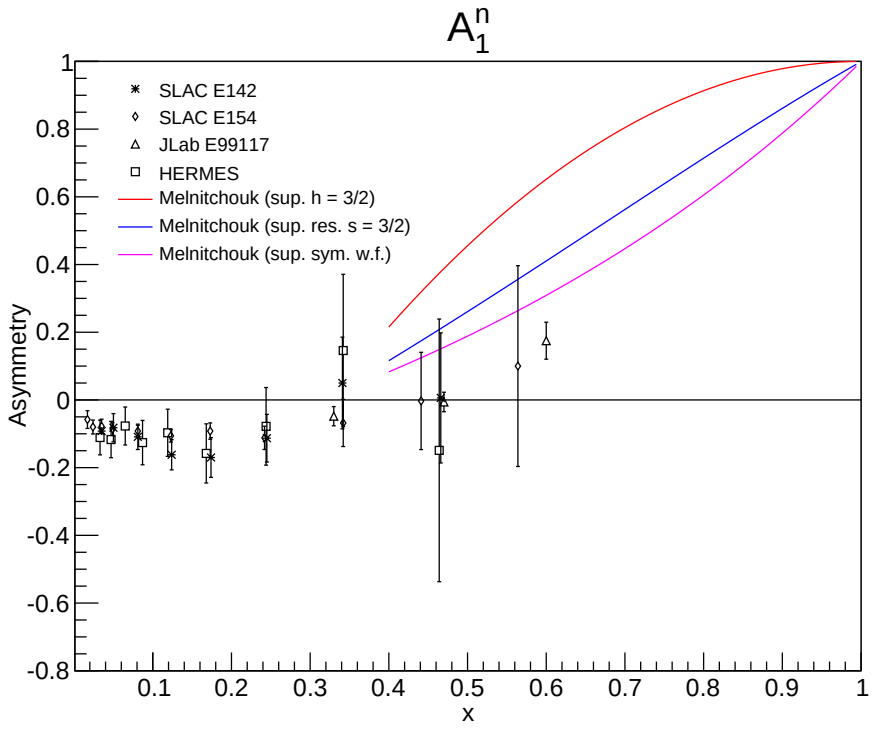

Figure 2.9: The world data [60, 64, 71, 82] on A_1^n compared to calculations from Melnitchouk [98] for suppression of different quantities: transitions of helicity $3/2$ (red); resonances with spin $3/2$ (blue); and finally, resonances with symmetric wave functions (magenta).

Future work for testing duality includes an approved experiment at Jefferson Lab in the 12 GeV era [92], where measurements of A_1 and g_1 on the neutron are planned in the resonance and DIS regions covering $0.4 \leq x \leq 0.7$.

2.4.6 Chiral Soliton Models

The chiral soliton framework is used in the low-energy, non-perturbative regime, where the assumptions and calculations of pQCD are not valid. Here, we discuss chiral symmetry breaking, and how the nucleon is modeled as an object known as a chiral soliton.

2.4.6.1 Chiral Symmetry Breaking

The QCD Lagrangian written using N_f massless flavors is known to have a *global* symmetry under unitary flavor transformations which mixes states of left- and right-handed quark fields according to $U_L(N_f) \times U_R(N_f)$ rotations, referred to as *chiral* symmetry [100]. If chiral symmetry was an exact symmetry, then a degeneracy in parity of all states for otherwise equal quantum numbers would be expected. However, in nature, this does not

occur; mass differences (splittings) between states of the same quantum numbers but *opposite* parities are large. For example, the mass of the ρ vector meson and axial meson a_1 is $1260 - 770 \approx 500\,\text{MeV}$. Additionally, the mass difference between the nucleon and its parity partner, the $N(1535)$ resonance, is $\approx 600\,\text{MeV}$; this difference in mass is too large to be explained by the small masses of current-quarks*. The *chiral condensate*, or "order parameter," gives an indication of how strongly chiral symmetry is broken; it is on the order of a few hundred MeV [100]. Due to its size compared to the mass of the nucleon, it can be seen that it has a sizable effect on the dynamical structure of the nucleon.

To treat the nucleon under the formalism of chirality, one can generalize QCD to an arbitrary large number of colors, N_C [101–103]. This allows for a perturbative approach at low energies, taking $1/N_C$ as the expansion parameter. This leads to a description of the nucleon in an effective theory of infinitely many weakly-interacting mesons and glueballs, which bind the valence quarks together in the nucleon. Even though $N_C = 3$ in nature, the theory (utilizing large N_C) has been successful in describing the mass splittings in the baryon octet and decuplet, in agreement with the data to within 1% [104].

2.4.6.2 Baryons as Chiral Solitons

According to the general parameters laid out above, there are a number of approaches in formulating the nucleon as a chiral soliton. One particular description utilized by a number of groups [105–108] follows from the Nambu-Jona-Lasinio (NJL) model [109, 110], where hadronic currents are described by quark degrees of freedom which are functionals of solitonic meson fields. The dynamics are governed by a $U(1) \times SU(2)_L \times SU(2)_R$ chiral symmetry. In such a model, baryons are viewed as "mesonic lumps," compared to the quark-parton model, where baryons are composites of nearly non-interacting, point-like quarks [105]. In these NJL-type models, the mean-field quark wave functions—immersed in a background consisting of a chiral soliton—is a representation of a non-trivial coupling of spin and isospin; this is in stark contrast to bag models, which describe baryons in terms of direct products of spin and isospin states [105, 106]. Another approach on the market [111] is to assume that spontaneous chiral symmetry breaking arises due to *instantons*, which are non-perturbative vacuum fluctuations of the gluon fields; this has the effect of delocalizing quark wave functions. This approach preserves the original chiral symmetry of $SU(N_f)_L \times SU(N_f)_R$, but breaks the axial $U(1)$ symmetry. This instanton-based approach has been extended to $N_f = 3$, and used to make predictions concerning the nucleon structure functions [112, 113].

*The mass of the up, down and strange quarks are $m_u \sim 4\,\text{MeV}$, $m_d \sim 7\,\text{MeV}$, and $m_s \sim 150\,\text{MeV}$. These mass differences explicitly break chiral symmetry, to a large degree.

Predictions for A_1^n from two chiral soliton model approaches are compared to the world data in Figure 2.10. In the NJL-type calculation from Weigel *et al.* [105, 106] (red), the ratio g_1^n/F_1^n is computed at $Q^2 = 3\,\mathrm{GeV}^2$. We note here that this is a pure model calculation, with no influence from fitting world data. A model from Cloët *et al.* [114] is shown in green, where their approach utilizes a modified NJL model and confinement is simulated by eliminating unphysical thresholds for nucleon decay into quarks. Nucleon states are obtained by solving the Faddeev equation in the quark-diquark approximation where scalar and axial-vector diquark states are included. The instanton approach by Wakamatsu *et al.* [112, 113] at $Q^2 = 2.7\,\mathrm{GeV}^2$ is also presented and is given by the blue curve.

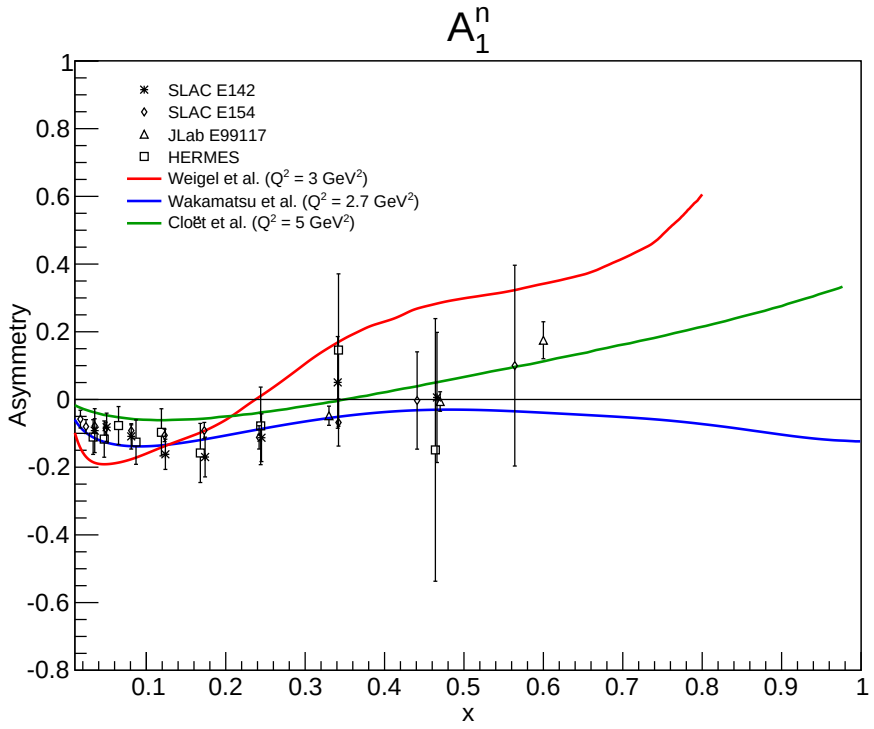

Figure 2.10: The world data [60, 64, 71, 82] on A_1^n compared to a chiral soliton model from Weigel *et al.* [105, 106] (red) an instanton-based model from Wakamatsu *et al.* [112, 113] (blue), and a modified NJL model from Cloët *et al.* [114] (green).

2.4.7 Instanton Model

As briefly introduced in Section 2.4.6, instantons are non-perturbative vacuum fluctuations of the gluon fields. This random ensemble is seen to bind quarks at zero energy [111]. Delocalization* arises due to the quantum-mechanical overlap of the quark wave functions,

*Delocalization means that an infinite number of helicity flips occur; this generates the dynamical mass of quarks—that is, delocalization corresponds to dynamical chiral symmetry breaking [111].

and quarks can move between instantons. Such transitions cause quarks to flip their helicity or chirality, leading to quark depolarization inside the nucleon. This description has been introduced to explain the observed violation of the Ellis-Jaffe sum rule, sometimes referred to as the so-called "spin crisis" [115] (Sect. 1.4.1).

The effects of the quark-quark and quark-gluon interactions induced by instantons have been estimated in an instanton liquid model by Kochelev [115]. It was found that these *q*-*q* and *q*-*g* interactions reduce the quarks' spin contributions to the nucleon, and carry an x-dependence. Furthermore, it gives a reasonable violation of the Ellis-Jaffe sum rule on the proton, describing the decrease of g_1^p in the large x region.

The understanding of the neutron g_1 is very sensitive to the intricacies of SU(6) symmetry breaking, but is not discussed in [115]; however, if a similar negative effect on the neutron spin due to the *q*-*q* and *q*-*g* interactions is a fair estimate, then there is a possibility of A_1^n being near zero and potentially negative in the large x region.

2.4.8 Bag Model

In the bag model formalism, the hadron is treated as a finite region of space in which the strong fields are confined (MIT bag model) [116]. In this region, (i.e., the *bag*), massless quarks can move quasi-freely and relativistically but are confined to the bag via boundary conditions; in particular, outside the bag, the quarks are infinitely massive.

In the fundamental description, quarks move in their own orbit and do not interact with the other quarks. This was later extended by Schreiber *et al.* [117] in a three-dimensional bag, where other interactions, like one-gluon exchange (i.e., the color hyperfine interaction) between quarks are included. Predictions were made for $2xg_1/F_2$ for the proton; in the Bjorken limit, where the Callan-Gross relation is expected to hold, the ratio should reduce to $g_1/F_1 = A_1$.

Although one-gluon exchange is an improvement in the model, there are other effects that should be considered. As seen in Section 2.4.6 and Section 2.4.7, we need to consider the effects instantons have on the bag. To investigate this, Song and McCarthy [118] introduced generalized spin-dependent effects via an explicit symmetry-breaking parameter. This allows for predictions of $2xg_1/F_2$ for the proton and neutron.

A problem with the bag model approach is that chiral symmetry is explicitly broken on the surface of the bag. To circumvent this issue, a meson cloud is coupled to the quarks at the surface of the bag. This approach is known as the *cloudy bag model* [119, 120]. The meson cloud is composed largely of pions; other mesons have larger masses, and therefore any corrections due to their presence would be comparatively smaller than those due to pions [121].

According to the cloudy bag model, the proton spin puzzle is somewhat of a non-issue [122], in that experiment and theory agree that $\approx 35\%$ of the nucleon spin is carried by the valence quarks. Theoretically speaking, the valence quarks need to be treated in a relativistic fashion, which is intrinsically incorporated into the original MIT bag model. Also, it is predicted that the pion cloud has to have its net spin *opposite* to that of the *bare* nucleon*. Furthermore, introducing one-gluon exchange further reduces the valence quark spin.

Investigations of the behavior of g_1^p with and without pion cloud effects have been presented by Boros and Thomas [123]; also a part of the effort are predictions of A_1^n where hyperfine interactions are considered [124]. The calculations *without* pion corrections [125] are presented in Figure 2.11 compared to the world data.

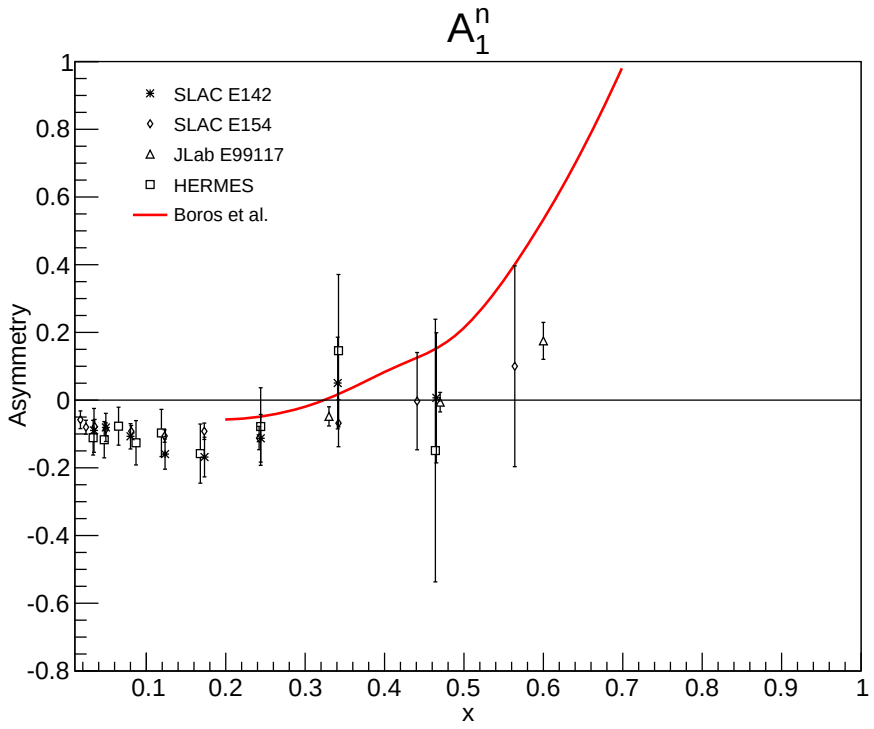

Figure 2.11: The world data [60, 64, 71, 82] on A_1^n compared to the bag model from Boros *et al.* [123].

2.4.9 Dyson-Schwinger Equation Treatments

A recent treatment by Roberts *et al.* [126] analyses the strong interaction via the Dyson-Schwinger Equations (DSEs). In particular, the calculation is carried out on the domain of

*A bare nucleon is one that is not dressed with pions.

$x \simeq 1$ where the nucleon elastic form factors can be connected to predictions of the large-x behavior PDFs via a Pioncaré covariant Faddeev amplitude. In the construction of the Faddeev equation, Roberts *et al.* employ a dressed-quark propagator of two different types for the calculations: one where the mass term is momentum independent, and the other where the mass term carries a momentum dependence. This yields two different sets of results, referred to as *contact* and *realistic*, respectively.

These calculations were not extended to $x \neq 1$, as Roberts *et al.* argue that on the domain of $x \simeq 1$, the interpretation of PDFs is unambiguous, in that they inform how interactions between dressed-quarks and -gluons create hadron bound states and how such interactions arise from QCD [126].

The results of the calculations reveal the importance of non-pointlike diquark correlations within the nucleon. Unlike other models (in particular, CQM) where point-like diquark correlations are inserted "by hand," *non*-pointlike diquark correlations arise naturally as a consequence of dynamical chiral symmetry breaking [126]. In the contact framework, the predictions at $x = 1$ for A_1, $\Delta u/u$ and $\Delta d/d$ are given as:

$$A_1^p = 0.88, \quad A_1^n = 0.34, \quad \frac{\Delta u}{u} = 0.88, \quad \text{and} \quad \frac{\Delta d}{d} = -0.33, \quad \text{(contact)} \tag{2.39}$$

and in the realistic picture:

$$A_1^p = 0.59, \quad A_1^n = 0.17, \quad \frac{\Delta u}{u} = 0.65, \quad \text{and} \quad \frac{\Delta d}{d} = -0.26 \quad \text{(realistic)}. \tag{2.40}$$

2.5 Flavor Decomposition

The partons that make up the nucleon consist of the valence quarks, corresponding to the up and down quarks, the sea quarks (which includes the strange quarks), anti-quarks, and finally, there are gluons. A PDF is the probability of finding a given parton with momentum fraction x at a resolution (or energy scale) of Q^2. Such an interpretation allows for understanding the roles of these distributions in the nucleon when comparing the different quark flavors as a function of x, as shown in Figure 2.12, at $Q^2 = 4\,\text{GeV}^2$. The distributions are from the fits of the CTEQ-JLab (CJ12) [127] collaboration. We see that the valence up and down quarks dominate in the large x region, which is known as the *valence quark region*; it is a relatively simple region to model theoretically under the formalism of pQCD to predict structure functions, asymmetries (like A_1) and PDFs; however, in the low x region, the perturbative framework breaks down and does not do well in describing the physics.

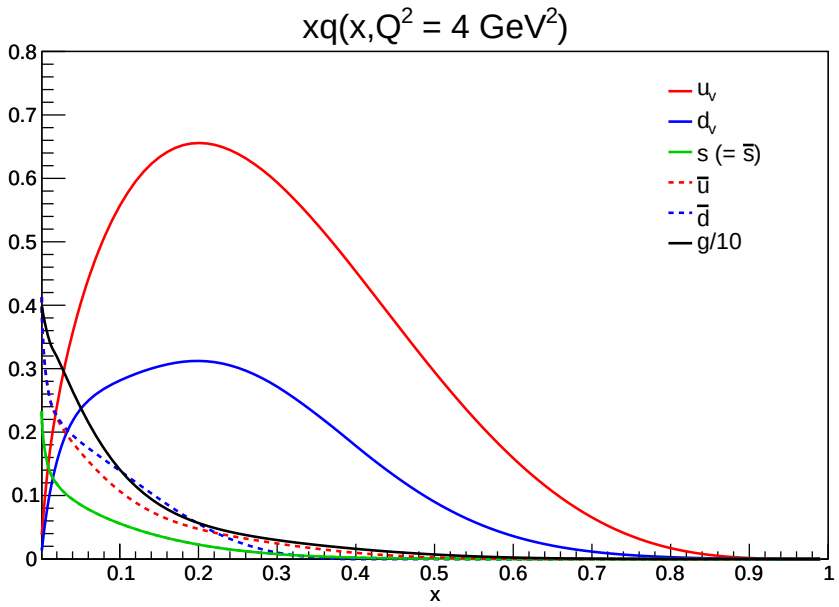

Figure 2.12: Unpolarized valence (solid) and sea (dashed) PDFs for $Q^2 = 4\,\mathrm{GeV}^2$. The distributions are from the CJ12 [127] parameterization. The gluon distribution is scaled down by a factor of 10.

Utilizing *isospin* symmetry, one can combine the data from proton and (effective) neutron targets to extract spin-dependent information on the individual quark flavors, Such an analysis is known as *flavor decomposition*. In the valence region, we can ignore strange quarks for the time being. Combining the equations for g_1 and F_1, we can obtain:

$$\frac{g_1^p}{F_1^p} = \frac{4\Delta u + \Delta d + 4\Delta\bar{u} + \Delta\bar{d}}{4u + d + 4\bar{u} + \bar{d}} \tag{2.41}$$

$$\frac{g_1^n}{F_1^n} = \frac{4\Delta d + \Delta u + 4\Delta\bar{d} + \Delta\bar{u}}{4d + u + 4\bar{d} + \bar{u}}, \tag{2.42}$$

where the neutron equation is obtained from isospin symmetry; that is, $u \leftrightarrow d$ in the g_1^p/F_1^p ratio yields g_1^n/F_1^n. Under the formalism of the QPM and assuming the strange quark contribution is small in the valence quark region, $x \gtrsim 0.3$, combining these two equations for g_1^p/F_1^p and g_1^n/F_1^n gives expressions for the up and down quarks:

$$\frac{\Delta u + \Delta\bar{u}}{u + \bar{u}} = \frac{4}{15}\frac{g_1^p}{F_1^p}\left(4 + \frac{d + \bar{d}}{u + \bar{u}}\right) - \frac{1}{15}\frac{g_1^n}{F_1^n}\left(1 + 4\frac{d + \bar{d}}{u + \bar{u}}\right) \tag{2.43}$$

$$\frac{\Delta d + \Delta\bar{d}}{d + \bar{d}} = \frac{4}{15}\frac{g_1^n}{F_1^n}\left(4 + \frac{u + \bar{u}}{d + \bar{d}}\right) - \frac{1}{15}\frac{g_1^p}{F_1^p}\left(1 + 4\frac{u + \bar{u}}{d + \bar{d}}\right), \tag{2.44}$$

where the ratio of the down-to-up quark distributions is typically defined as R^{du}, and arises from data on F_2^n/F_2^p from experiments using proton or deuteron targets; however, in the large x region, the deuteron target data tends to have large uncertainties due to nuclear corrections [127]. In this valence quark region, $R^{du} \approx d/u$. The PDF ratios as shown in Equations 2.43 and 2.44 can be obtained from measurements of g_1^p/F_1^p and g_1^n/F_1^n, along with utilizing a parameterization of the ratio R^{du}. The world data for R^{du} is given in Figure 2.13.

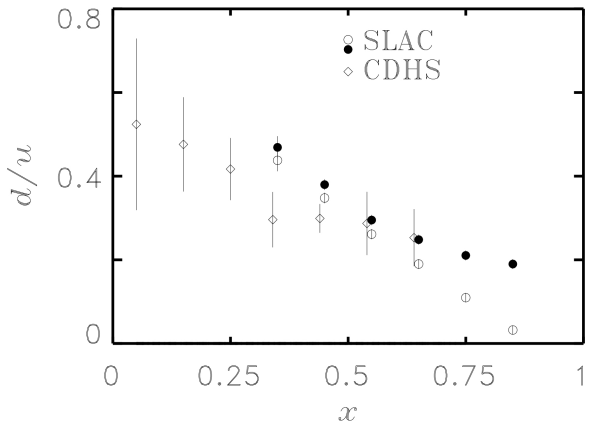

Figure 2.13: The world data for R^{du} from SLAC for proton and deuteron targets. The open circles indicate the use of on-shell calculations for the deuteron, while the solid circles use an off-shell model. The open diamonds indicate measurements taken with a neutrino beam, which are insensitive to nuclear effects, by the CDHS collaboration [128]. Figure reproduced from [129]

The PDF ratios in Equations 2.43 and 2.44 are quantities that include contributions from *all* quark types; that is, it includes contributions from the valence and sea quarks. Theoretical predictions are often given in terms of the valence quarks only, so a proper comparison of experimental results to those of theory entails understanding how much the experimentally-extracted result that includes sea quarks to those that don't include sea quarks. To illustrate how the PDF ratio for valence quarks is extracted from data, we follow the work of X. Zheng [40]. We denote valence quarks as q_V and sea quarks as q_S. We note that $q_S = \bar{q}$; with this in hand, we can see that for unpolarized and polarized PDFs:

$$q + \bar{q} = q_V + q_S + \bar{q} = q_V + 2\bar{q} \tag{2.45}$$

$$\Delta q + \Delta\bar{q} = \Delta q_V + \Delta q_S + \Delta\bar{q} = \Delta q_V + 2\Delta\bar{q}. \tag{2.46}$$

Then using Equations 2.45 and 2.46, we have:

$$\frac{\Delta q_V}{q_V} = \frac{\Delta q_V + 2\Delta\bar{q}}{q_V + 2\bar{q}} \cdot \frac{q_V + 2\bar{q}}{q_V} \cdot \frac{\Delta q_V}{\Delta q_V + 2\Delta\bar{q}}, \tag{2.47}$$

rewriting this, we obtain:

$$\frac{\Delta q_V}{q_V} = \frac{\Delta q_V + 2\Delta\bar{q}}{q_V + 2\bar{q}} \left(1 + \frac{2\bar{q}}{q_V}\right) \left(1 + \frac{2\Delta\bar{q}}{\Delta q_V}\right)^{-1}. \tag{2.48}$$

Now, the fraction in the last term is multiplied by q_V/q_V, and both sides of the equation are multiplied by $\left(1 + \frac{2\Delta\bar{q}}{q_V} \cdot \frac{q_V}{\Delta q_V}\right)$, yielding:

$$\frac{\Delta q_V}{q_V} + \frac{2\Delta\bar{q}}{q_V} = \frac{\Delta q_V + 2\Delta\bar{q}}{q_V + 2\bar{q}} \left(1 + \frac{2\bar{q}}{q_V}\right). \tag{2.49}$$

Substituting $q_V = q - \bar{q}$ into the first term on the right-hand side, we arrive at:

$$\frac{\Delta q_V}{q_V} = \frac{\Delta q + \Delta\bar{q}}{q + \bar{q}} \left(1 + \frac{2\bar{q}}{q_V}\right) - \frac{2\Delta\bar{q}}{q_V}. \tag{2.50}$$

To extract the PDF ratio for valence quarks only, we take our experimentally-extracted result of $(\Delta q + \Delta\bar{q})/(q + \bar{q})$, via g_1/F_1 measurements, and make corrections for the sea quark distributions as seen above, where the ratios $2\bar{q}/q_V$ and $2\Delta\bar{q}/q_V$ are obtained from fits to world data (i.e., parameterizations of $\bar{q}$ and q_V). We can estimate the error on the valence PDF ratio by propagation of errors:

$$\delta\left(\frac{\Delta q_V}{q_V}\right)^2 = \left(\frac{\delta q_V}{q_V}\right)^2 \left[2\bar{q}\frac{\Delta q + \Delta\bar{q}}{q + \bar{q}} - 2\Delta\bar{q}\right]^2 + \left(\frac{\delta(2\bar{q})}{q_V}\right)^2 \left(\frac{\Delta q + \Delta\bar{q}}{q + \bar{q}}\right)^2 + \left(\frac{\delta(2\Delta\bar{q})}{q_V}\right)^2. \tag{2.51}$$

We can also estimate the error for leaving out the strange contribution by following a similar procedure for the valence quark ratios (cf. Equation 2.43 and 2.44):

$$\frac{\Delta u + \Delta\bar{u}}{u + \bar{u}} = \left(\frac{\Delta u + \Delta\bar{u}}{u + \bar{u}}\right)_{s,\bar{s}=0} + \frac{s + \bar{s}}{u}\left[\frac{4}{15}\frac{g_1^p}{F_1^p} - \frac{1}{15}\frac{g_1^n}{F_1^n} - \frac{1}{5}\frac{\Delta s + \Delta\bar{s}}{s + \bar{s}}\right] \tag{2.52}$$

$$\frac{\Delta d + \Delta\bar{d}}{d + \bar{d}} = \left(\frac{\Delta d + \Delta\bar{d}}{d + \bar{d}}\right)_{s,\bar{s}=0} + \frac{s + \bar{s}}{d}\left[\frac{4}{15}\frac{g_1^n}{F_1^n} - \frac{1}{15}\frac{g_1^p}{F_1^p} - \frac{1}{5}\frac{\Delta s + \Delta\bar{s}}{s + \bar{s}}\right] \tag{2.53}$$

The error could be bounded by considering the positivity constraints of $|\Delta s/s| \leq 1$ and $|\Delta\bar{s}/\bar{s}| \leq 1$.

The current experimental data for $(\Delta u + \Delta\bar{u})/(u + \bar{u})$ and $(\Delta d + \Delta\bar{d})/(d + \bar{d})$ are shown in Figure 2.14, where the red (blue) data represents the up (down) quark ratio. The data shown are from HERMES [66], a semi-inclusive DIS measurement, and JLab experiments

E99-117 [71] and CLAS EG1b [73], both of which are inclusive DIS measurements. The dashed curve is a pQCD calculation from Leader *et al.* [86], which requires hadron helicity conservation (Sect. 2.4.3); the dashed-dotted curve is another pQCD calculation from Avakian *et al.* [88], which explicitly includes orbital angular momentum in their calculations. The solid curve is a statistical quark model from Bourrely *et al.* [89, 90], and the dash triple-dotted curve is a modified NJL model from Cloët *et al.* [114]. We can see that both pQCD models predict that $\Delta q/q \to 1$ at large x, which implies that q^+ must dominate as $x \to 1$. The data for $\Delta u/u$ is consistent with this prediction; however, we note that the current $\Delta d/d$ data shows no sign of turning positive as we approach the large x region. The Avakian *et al.* calculation fits the down quark data better, but still has a zero-crossing at $x \sim 0.75$. The data in Figure 2.14 imply that in general, the up quark spins tend to be parallel to that of the nucleon spin, whereas the down quark spins are antiparallel to the nucleon spin. It is evident from the data and the model from Avakian *et al.* that quark orbital angular momentum is playing an important role in the spin of the nucleon.

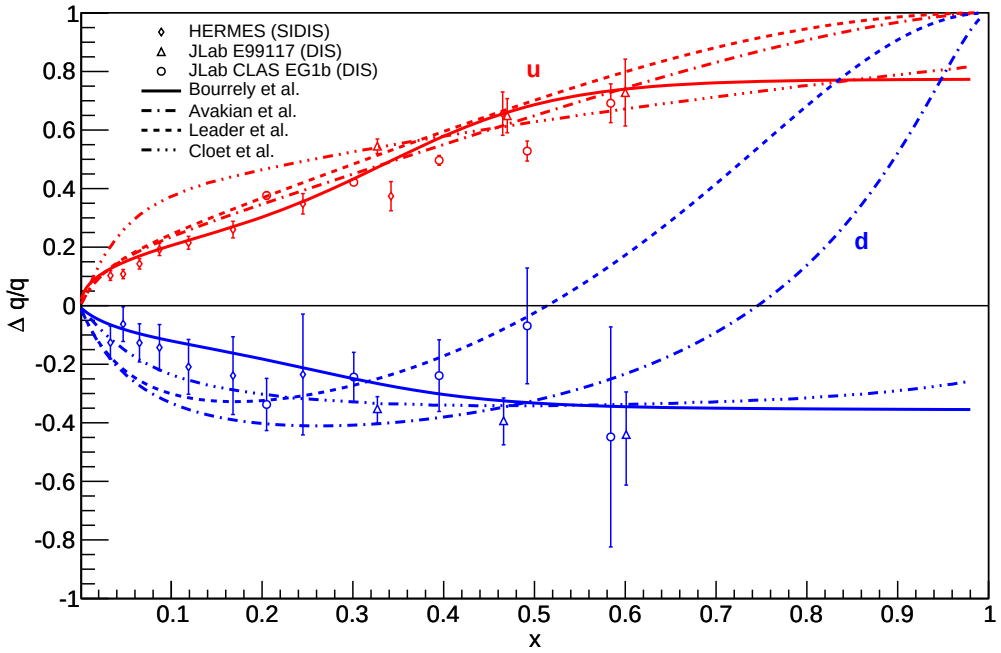

Figure 2.14: The world data for the up and down quark polarized-to-unpolarized PDF ratios. The data shown is from HERMES [66], a semi-inclusive DIS measurement, and JLab E99-117 [71], and CLAS EG1b [73], both of which are DIS measurements. The models are pQCD calculations from Leader *et al.* [86] (dashed) and Avakian *et al.* [88] (dash-dotted). The solid curve shows a statistical quark model from Bourrely *et al.* [89, 90] and the dash triple-dotted curve shows a modified NJL model calculation from Cloët *et al.* [114].

CHAPTER 3

THE EXPERIMENT

In this chapter we will discuss the E06-014 experiment. In particular, in Section 3.1 we give an overview of the physics and goals of E06-014. Section 3.2 introduces the Jefferson Lab (JLab) Continuous Electron Beam Accelerator Facility. The electron beam line is discussed in Section 3.4 and the target is discussed in Section 3.5. The Left High-Resolution spectrometer is presented in Section 3.6 and the BigBite spectrometer is shown in Section 3.7. The trigger set up for each spectrometer is examined in Section 3.8, while Section 3.9 describes the data acquisition system utilized. Finally, Section 3.10 shows the software used to process the data.

3.1 Overview of the Experiment

The E06-014 experiment, also known as d_2^n, ran in Hall A from February 7$^{\text{th}}$ to March 17$^{\text{th}}$ of 2009. It consisted of scattering a longitudinally polarized electron beam from a longitudinally and transversely polarized ^{3}He target. The goal of the experiment was to perform a measurement of the quantity d_2 on the neutron. d_2 is the x^2 moment of a linear combination of the spin structure functions g_1 and g_2:

$$d_2\left(Q^2\right) = \int_0^1 x^2 \left[2g_1\left(x,Q^2\right) + 3g_2\left(x,Q^2\right)\right] dx. \tag{3.1}$$

The spin structure function g_2 is known to contain quark-gluon correlations. It follows from a spin-flip Compton amplitude and may be written as:

$$g_2\left(x,Q^2\right) = g_2^{\text{WW}}\left(x,Q^2\right) + \bar{g}_2\left(x,Q^2\right), \tag{3.2}$$

where g_2^{WW} is the Wandzura-Wilczek term, which may be expressed entirely in terms of g_1 [49]:

$$g_2^{\mathrm{WW}}\left(x,Q^2\right) = -g_1\left(x,Q^2\right) + \int_x^1 \frac{g_1\left(y,Q^2\right)}{y} dy. \tag{3.3}$$

The second term is given as:

$$\bar{g}_2\left(x,Q^2\right) = -\int_x^1 \frac{1}{y}\frac{\partial}{\partial y}\left[\frac{m_q}{M} h_T\left(y,Q^2\right) + \xi\left(y,Q^2\right)\right] dy, \tag{3.4}$$

where h_T is the transverse polarization density, and ξ is a term arising from quark-gluon correlations. Here, h_T is suppressed by the ratio of the quark mass m_q to the target mass M. Therefore, $\bar{g}_2$ provides access to quark-gluon interactions inside the nucleon [130]. Utilizing this form of g_2, we see that d_2 is given by:

$$d_2\left(Q^2\right) = \int_0^1 \bar{g}_2\left(x,Q^2\right) dx. \tag{3.5}$$

Here, we see that a measurement of d_2 gives a direct measurement of quark-gluon correlations. The quantity d_2 also appears as a matrix element of the twist-3 gluon field-strength operator $\tilde{G}^{\mu\nu} = (1/2)\varepsilon^{\mu\nu\alpha\beta} G_{\alpha\beta}$ in the operator product expansion [131]:

$$\langle P,S \mid \frac{1}{4} g \tilde{G}^{\sigma(\mu}\gamma^{\nu)}\psi \mid P,S\rangle = 2d_2 S^{[\sigma}P^{(\mu]}P^{\nu)}, \tag{3.6}$$

where the brackets $(\ldots)$ and $[\ldots]$ indicate the symmetrization and anti-symmetrization of indices, respectively; P and S are the momentum and spin of the nucleon, respectively, and g is the QCD coupling constant. The structure of $G^{\mu\nu}$ suggests that it measures a quark *and* a gluon amplitude in the initial nucleon wave function.

There are two interpretations of d_2 based on the energy scale $\left(Q^2\right)$ at which the system is probed. The first of which being where Q^2 is low enough so that the virtual photon wavelength is larger than the nucleon size and the virtual photon's electromagnetic field appears to be uniform over the nucleon volume. This leads to g_2 (and subsequently d_2) being able to be described in terms of *spin polarizabilities* [132]. Due to the fact that the strong force and the electromagnetic force conserve parity, an analogy between the strong force's color fields and the electromagnetic force's electromagnetic fields may be drawn: the color magnetic field $\vec{B}$ can be induced along the direction of the nucleon polarization and the color electric field $\vec{E}$ is in the plane perpendicular to the polarization. Defining the color singlet operators $\hat{O}_B = \psi^\dagger g\vec{B}\psi$ and $\hat{O}_E = \psi^\dagger \vec{\alpha} \times g\vec{E}\psi$ in terms of the quark fields ψ, we determine the gluon field polarizabilities χ_B and χ_E in the rest frame of the nucleon:

$$\langle PS \mid \hat{O}_{B,E} \mid PS\rangle = \chi_{B,E} 2M^2 \vec{S}. \tag{3.7}$$

Utilizing these formulae, it can be shown that:

$$d_2 = \frac{1}{4}\left(2\chi_B + \chi_E\right). \tag{3.8}$$

From Equation 3.8 it can be seen that d_2 gives the color electric and magnetic fields' response to the polarization of the nucleon [131].

Recent work has shown [133] that at high Q^2, d_2 is more appropriately seen as a color Lorentz force averaged over the volume of the nucleon. To illustrate this, a parallel may be drawn to electromagnetism, where the $\hat{y}$ component of the Lorentz force F^y acting on an electron moving with $v \sim c$ along the $\hat{z}$-axis gives:

$$F^y = e\left[\vec{E} + \vec{v} \times \vec{B}\right]^y = -e\sqrt{2}F^{+y}, \tag{3.9}$$

where F^{+y} is in light-cone coordinates and contains the same Lorentz components that appear in the field tensor G in Equation 3.6. This suggests how d_2 is connected to a *color* Lorentz force on the active quark immediately following its interaction with a virtual photon, given by:

$$F^y(0) \equiv -\frac{\sqrt{2}}{2P^+}\langle P,S \mid \bar{\psi}_q(0)\, gG^{+y}(0)\, \gamma^+ \psi_q(0) \mid P,S\rangle = -\frac{1}{2}M^2 d_2. \tag{3.10}$$

The quantity d_2 may be measured on either the proton $\left(d_2^p\right)$ or the neutron $\left(d_2^n\right)$. While bag and soliton model calculations of d_2 for the neutron yield numerical values consistent with those of lattice QCD, current experimental data differs by roughly two standard deviations (see the highest Q^2 data in Figure 3.1). One of the goals of our experiment is to improve the experimental error on the value of d_2^n by a factor of four. It subsequently provides a benchmark test of lattice QCD calculations, shown in Figure 3.1.

3.1.1 The Measurement of d_2^n

The experiment ran in Hall A for six weeks with 15 μA of polarized electron beam on a longitudinally and transversely polarized ^{3}He target. Since the lifetime of the neutron is < 15 minutes [35], a free-neutron target is not practical. Therefore, ^{3}He is used as an effective polarized neutron target since roughly 86% of the polarization is carried by the neutron. This is due to the two protons in the nucleus being primarily bound in a spin singlet state [143, 144].

There were two main data sets, with beam energies of $E = 4.74$ and 5.89 GeV, covering the resonance and deep inelastic valence quark regions, characterized by $0.2 \leq x \leq 0.7$ and $2 \leq Q^2 \leq 6$ GeV^2. The coverage in the x and Q^2 plane is shown in Figure 3.2.

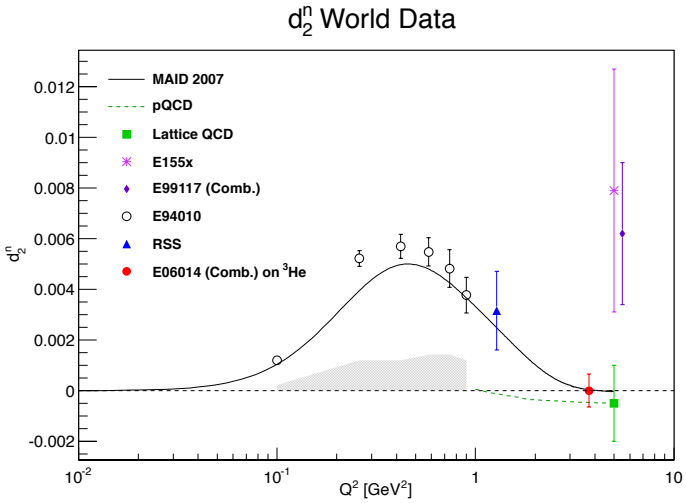

Figure 3.1: d_2^n as a function of Q^2. All the data shown with the exception of the SLAC E155x and JLab E99-117 data are dominated by resonance contributions. E06-014 data observed mostly the DIS contribution. The projected error on from E06-014 [134] is shown, along with the lattice QCD result [135]. The dashed green curve shows the pQCD evolution from the lattice point [136] based on the calculations of [137, 138]. Data from JLab experiments E94-010 [139] and RSS [140] are included in the plot. For comparison to the resonance contribution, a MAID model [141] is plotted. Also plotted is the total d_2 from SLAC experiment E155x [142] and JLab E99-117 [71].

We measured the unpolarized total cross section σ_0 and the asymmetries $A_\parallel$ and $A_\perp$. The cross section was measured by the Left High-Resolution Spectrometer (LHRS) (Sect. 3.6), while the asymmetries were measured by the BigBite spectrometer (Sect. 3.7). The LHRS and BigBite were oriented at scattering angles of $\theta = 45^\circ$ to the left and right of the beamline, respectively.

Expressing the structure functions entirely in terms of these experimental quantities, we have the expression for d_2^n:

$$d_2^n = \int_0^1 \frac{MQ^2}{4\alpha^2} \frac{x^2y^2}{(1-y)(2-y)} \sigma_0 \left[\left(3\frac{1+(1-y)\cos\theta}{(1-y)\sin\theta} + \frac{4}{y}\tan(\theta/2) \right) A_\perp + \left(\frac{4}{y} - 3 \right) A_\parallel \right] dx, \tag{3.11}$$

where $x = Q^2/2M\nu$, $\nu = E - E'$ is the energy transfer to the target, E' is the scattered electron energy, and $y = \nu/E$ is the fractional energy transfer to the target. The asymmetries are given by:

$$A_\parallel = \frac{N^{\downarrow\Uparrow} - N^{\uparrow\Uparrow}}{N^{\downarrow\Uparrow} + N^{\uparrow\Uparrow}} \quad \text{and} \quad A_\perp = \frac{N^{\downarrow\Rightarrow} - N^{\uparrow\Rightarrow}}{N^{\downarrow\Rightarrow} + N^{\uparrow\Rightarrow}},$$

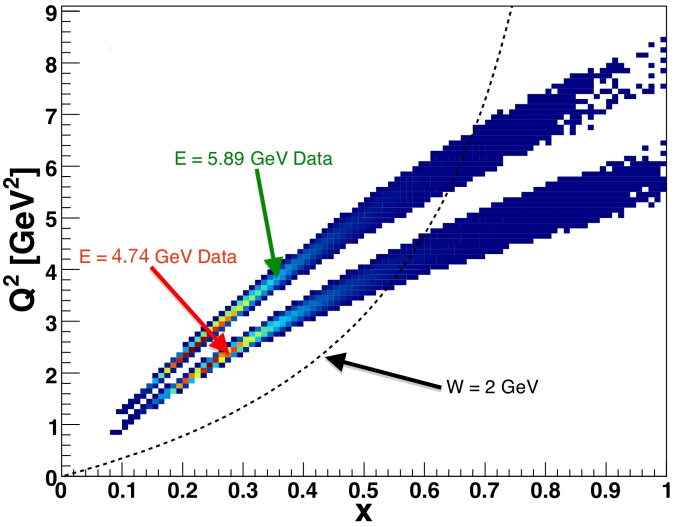

Figure 3.2: The E06-014 kinematic coverage in Q^2 and x. The lower band is the 4.74 GeV data set and the upper band is the 5.89 GeV data set. The black dashed line shows W = 2 GeV. The data to the left and right of this line corresponds to DIS and resonance data, respectively.

where N is the number of electron counts measured for a given configuration of beam helicity (single-arrows) and target spin direction (double-arrows).

The experiment was designed to minimize the error on the quantity d_2^n, rather than the structure function g_2. Expressing d_2^n in terms of the experimental observables (cross sections and asymmetries) simplifies the issue of optimizing the statistical error on d_2^n, as $A_\perp$ contributes the most to the error. Due to this, the majority of the data taking was for the transversely polarized target configuration.

3.1.2 Kinematics

In order to obtain results at constant Q^2, the original proposal called for two Q^2 measurements for each x bin and an interpolation between the two measurements would be made. This results in the need for two beam energies of 4.74 and 5.89 GeV. Another important reason for the two beam energies was to have more input data for radiative corrections. A single magnet setting in the BigBite Spectrometer covers the entire kinematic phase space, while the LHRS, with its smaller acceptance, required twenty magnet settings (ten at each beam energy) to accomplish the equivalent coverage.

Unfortunately due to time constraints, not all the data needed was collected*. The kinematics describing the data that was collected is shown in Tables 3.1 and 3.2.

*The originally proposed kinematics can be found in [134].

Table 3.1: Kinematic bins for the LHRS for a beam energy of 4.74 GeV. The LHRS momentum setting is labeled as p_0.

p_0 (GeV)	x	Q^2 (GeV^2)
0.60	0.215	1.66
0.80	0.301	2.22
1.12	0.458	3.10
1.19	0.496	3.30
1.26	0.536	3.49
1.34	0.584	3.71
1.42	0.634	3.93
1.51	0.693	4.18
1.60	0.755	4.43

Table 3.2: Kinematic bins for the LHRS for a beam energy of 5.89 GeV. The LHRS momentum setting is labeled as p_0.

p_0 (GeV)	x	Q^2 (GeV^2)
0.60	0.209	2.07
0.70	0.248	2.42
0.90	0.332	3.11
1.13	0.437	3.90
1.20	0.471	4.14
1.27	0.506	4.38
1.34	0.542	4.62
1.42	0.584	4.90
1.51	0.634	5.21
1.60	0.686	5.52
1.70	0.746	5.87

3.2 CEBAF at Jefferson Lab

The high-energy polarized electron beam is provided by the Continuous Electron Beam Accelerator Facility (CEBAF) at JLab. It delivers a continuous-wave electron beam of high polarization, reaching up to $\sim$ 85% which is sent to each of the three experimental Halls: A, B and C. The beam currents range up to 100 μA for Halls A and C, while Hall B typically receives $\lesssim$ 100 nA. The energy of the beam can go up to $\sim$ 6 GeV, achieved by two superconducting radio-frequency (RF) linear accelerators (linacs), connected by two magnetic recirculating arcs (Fig. 3.3).

3.2.1 The Polarized Electron Source

Since the experimental goals of each hall are necessarily different from one another, their beam requirements tend to differ as well. To accommodate this situation, three different

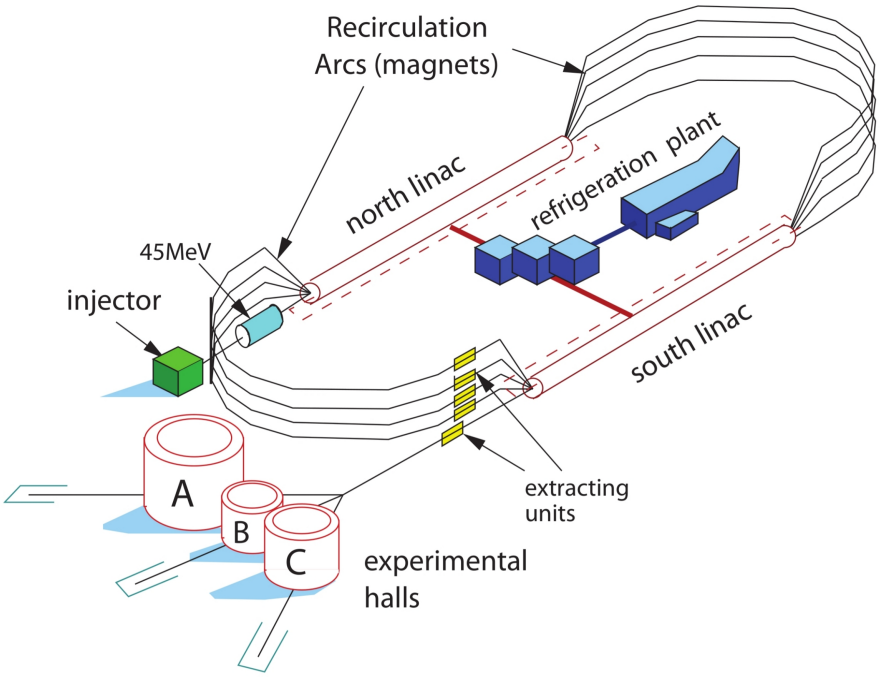

Figure 3.3: CEBAF recirculation arcs for ramping up the electron beam energy. Figure reproduced from [40].

lasers (one for each hall) are used. The laser system used by each hall consists of a 1560 nm seed laser, an ErYb-doped fiber amplifier and a periodically poled lithium niobiate (PPLN) crystal*. Each laser is gain-switched so that the pulse rate, and consequently the repetition rate of the electron bunches, is 499 MHz†, and 120° out of phase with each hall. By way of beam splitters, polarizers and dichoric mirrors, all three lasers are directed along a common axis to illuminate the same photo-cathode used to obtain polarized electrons [147].

The laser light starts out linearly polarized and goes through a Pockels cell, which converts it to circular polarization. The cell is voltage-controlled, where flipping the voltage polarity of the Pockels cell changes the polarization of the laser light from left-circular to right-circular and vice-versa. This effectively changes the helicity of the electrons. To impose restrictions on the helicity-correlated charge asymmetry of the beam, the linearly polarized light passes through a Pockels cell placed before a cell that converts it to circularly-polarized light. The voltage of this first Pockels cell varies according to the helicity flipping sequence is set to vary the intensity of the laser light, which in turn minimizes the helicity

*This is used to double the photon frequency [145, 146].
†The third harmonic of the 1497 MHz fundamental frequency of the accelerator.

correlated asymmetry. This Pockels cell is a part of a feedback loop that also includes the Hall A beam current monitor and a special data acquisition system, developed by the Hall A Proton Parity Experiment [148]. In addition to this feedback loop, an insertable half-wave plate (IHWP) can be placed in the photon beam line. This flips the helicity sign produced by the Pockels cells for a given voltage [47, 149].

Once the laser light is circularly polarized, it then illuminates the photocathode, made of strained superlattice gallium arsenide (GaAs). The laser light excites the valence electrons in the sample, moving them into the conduction band. From here, the conduction band electrons are extracted by applying a voltage of -100 kV to the photo-cathode, and are extracted to the injector. Inside the 100 keV beamline, a Wien filter [150] is utilized to rotate the electron spin direction without changing the central beam orbit. The Wien filter, combined with the known spin precession of the electron in the accelerator and beamline, allows for the optimization of the polarization direction of the electrons for each experimental hall.

3.2.2 Accelerator

The accelerator consists of the injector, two superconducting linacs, and two acceleration arcs. The polarized electrons are accelerated through the linacs and are recirculated through the arcs. After a specified number of recirculations, the beam is extracted to each of the experimental halls.

The injector is the starting point for the polarized electron beam in the acceleration procedure. It consists of 18 accelerating cavities, where each provides the initially 100 keV electrons from the electron source with 2.5 MeV of energy. The electrons emerge from the injector and are inserted in the North Linac with an energy of ~ 45 MeV.

Each linac is composed of twenty superconducting cryomodules, where each cryomodule has eight cavities. This amounts to each linac having a total of 160 cavities. These cavities are made of niobium, a superconducting material at a temperature of 2.08 K. To cool the cavities, they are immersed in liquid He, produced at the Central Helium Liquefier (CHL). The CHL acts as a large refrigerator that keeps the He cooled to ~ 2.2 K; the cooled He is sent to the cryomodules at a pressure of ~ 2.8 atm. The cavities are driven by 1497 MHz electromagnetic waves in order for the wave crests to align with the electron bunches, causing them to accelerate. Passing through a single linac, electrons gain $\sim$ 500–600 MeV.

To bend the electrons from one linac into the other, there are two recirculation arcs (east and west). They are composed of hundreds of magnets, responsible for bending and focusing the electron beam. The electrons with lower energies are bent the most into the upper

pipe (Fig. 3.3), while those with larger energies have their trajectories the least affected, and travel along the beam pipes closest to the floor. This energy-dependent bending results in electrons traversing the designated pipes based upon how many times it has circled the accelerator.

At the end of the South Linac, the beam is bent into the North Linac in the same fashion as described for bending the electrons from the North Linac into the South Linac. Recirculation of the beam can be done up to five times*, with the electron beam reaching a maximum energy of $\sim 6\,\text{GeV}$.

3.2.3 Delivery of Beam to the Experimental Halls

Following each beam pass, the beam may be extracted to a given experimental hall. This is realized by an RF separator which is located in the beamline. It extracts every *third* bunch, sending a single pulse of beam to each hall.

To control the systematic errors on the electron beam polarization in the experiment, the helicity of the electrons are flipped at a rate of 30 Hz, done at the Pockels cell. This 30 Hz time frame is considered a helicity *window*, and multiple windows are separated by Master Pulse Signals (MPSes). For each window, there is a definite helicity state, either parallel $(+)$ or anti-parallel $(-)$, where the electron spin is parallel or anti-parallel to its momentum, respectively. The helicity windows are organized into quartets, in the form $+--+$ or $-++-$. Each quartet is composed of two helicity *pairs*, with complimentary helicity states. The helicity state of the first window of a quartet is decided by a pseudo-random number generator, therefore determining the helicity state for the last three windows. At this point, a signal indicating the helicity direction is sent to the data acquisition systems, along with a signal indicating the beginning of the quartet.

3.3 Coordinate Systems

There are various coordinate systems employed in the data analysis, and it is useful to give a brief overview here. The coordinate systems that describe electrons before scattering from the target is the accelerator coordinate system and the Hall A coordinate system; to describe the scattered electrons, the target coordinate system and the detector coordinate systems, one for the LHRS and one for BigBite, are used.

In the accelerator coordinate system, the positive x direction is taken to be on the right side of the beamline. The z-axis is taken along the beamline, with increasing z pointing in

*One full circulation is considered to be one *pass*.

the downstream direction (that is, pointing towards the target). The positive y direction is taken as $\hat{y} = -\hat{z} \times \hat{x}$; hence, we see that this is a *left-handed coordinate system*. This system is used in the EPICS data management system (Sect. 3.9).

The Hall A coordinate system has the positive x direction defined as pointing towards the left of the beamline. The z-axis is again along the beamline, with increasing z in the downstream direction. The y-axis is given as $\hat{y} = \hat{z} \times \hat{x}$. The origin of the coordinate system is at the target center.

The target coordinate system (TCS) is defined such that positive x is vertically down (with gravity), and the z-axis points down the central ray of the spectrometer (either the LHRS or BigBite), away from the target, parallel to the floor. The y-axis is defined as $\hat{y} = \hat{z} \times \hat{x}$. The origin of the TCS is at the target center. The TCS is typically used in the data analysis when projecting events from the detector planes back to the target to determine scattering vertices and momenta.

The final coordinate systems to consider are the detector coordinate systems for the LHRS and BigBite, respectively. In the LHRS, the positive x direction is defined as pointing vertically downward (with gravity) and z is along the central ray of the spectrometer, away from the target. The y-axis is defined as $\hat{y} = \hat{z} \times \hat{x}$. The origin of the coordinate system is placed at the center of the first vertical drift chamber plane, also known as the focal plane. In BigBite, the positive x-direction points vertically downward, and the z-axis is along the central ray of BigBite, away from the target. The y-axis is given by $\hat{y} = \hat{z} \times \hat{x}$. The origin of the coordinate system is placed at the center of the first multi-wire drift chamber plane.

A diagram of the various coordinate systems is given in Figure 3.4.

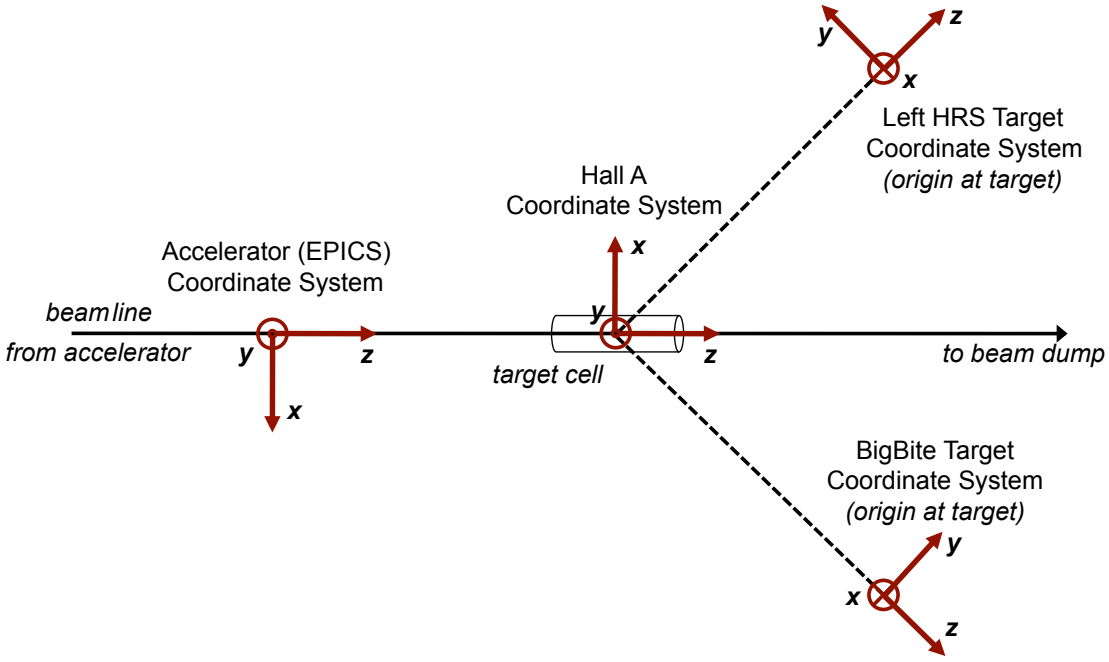

Figure 3.4: A top-view diagram of the four coordinate systems utilized in Hall A during the E06-014 experiment. The beamline moves from left to right in the figure. Figure reproduced from [47].

3.4 Hall A Beamline

The Hall A beamline is upstream of the target and consists of a number of devices to monitor the beam's characteristics. These include the beam position monitors (Sect. 3.4.1); the beam charge monitors (Sect. 3.4.2); the Møller and Compton polarimeters, used to measure the beam polarization (Sect. 3.4.3); and finally, the energy of the beam is measured via the Tiefenback method (Sect. 3.4.4).

3.4.1 Beam Position

3.4.1.1 Beam Position Monitors

For accurate vertex reconstruction and proper momentum calculation for a given track, the position of the beam in the plane transverse to the nominal beam direction at the target is needed. The beam position is affected by the beam's orbit in the accelerator, the Møller and Compton magnets and the fast raster.

The measurement of the beam position is accomplished by utilizing beam position monitors (BPMs). They are "slow," in the sense that they operate on a time scale of tenths of seconds. The BPMs consists of four antenna arrays placed 7.524 m and 1.286 m upstream

of the target. The wires are positioned at $\pm 45^{\circ}$ relative to the horizontal and vertical directions in the hall. The signal induced in the wires by the beam is recorded by ADCs, and is inversely proportional to the distance from the beam to the wire. The differences of the signals in pairs of wires in a given plane gives a positional resolution of $100\,\mu$m [151]. Combining the measurements from both monitors gives the trajectory of the beam. Extrapolating this data gives the position at the target.

The calibration of the ADC signals is accomplished by using wire scanners, or harps. They are situated next to the BPMs. This is a destructive procedure, where the wires are scanned *across* the electron beam, resulting in scattered particles which are measured. These harps are surveyed, so their positions are known. As a result, the BPMs can be calibrated to the harps.

3.4.1.2 Raster

In order to avoid damage to the target glass cell, the beam is rastered (scanned) across a large rectangular cross section at the target. If the beam were not rastered, it could lead to damaging the cell due to the heat transfer from the beam.

The size of the raster is a few millimeters ($\approx 4 \times 6\,\text{mm}^2$) in the horizontal and transverse directions. This rectangular distribution of the beam is achieved by two dipole magnets (one for the horizontal, one for vertical) located 23 m upstream of the target. The small transverse magnetic field produced by the dipoles deflects the beam as it traverses the magnet, resulting in a small deviation of the beam position at the target, filling out a rectangular area.

The calibration of the raster requires the determination of transformation coefficients to convert the raster currents into beam positions. This is accomplished by utilizing the average beam position from the BPMs and the raster currents recorded in their ADCs.

3.4.2 Beam Current and Charge

To measure the beam current and subsequently the charge accumulated on target from the beam, beam current monitors (BCMs) are utilized. These (two) monitors are resonant RF cavities, made of stainless-steel cylinders with a high Q factor of ≈ 3000, tuned to the fundamental beam frequency of 1.497 GHz [152]. One is positioned upstream and one downstream (relative to one another). The voltage signal measured in these monitors is proportional to the beam current.

There are three copies of this signal for each BCM: x1, x3 and x10. The "x" corresponds to the upstream (u) or downstream (d) BCM. The numbers correspond to the gain applied.

Each copy of the signal is amplified by its assigned gain and then sent to a voltage-to-frequency (VtoF) converter. Copies of these signals are read out by scalers in both the LHRS and the BigBite data streams, so that there is a continuous measurement of the beam current during data taking.

To calibrate the BCMs, data is taken at predetermined beam current set-points. There are two distinct steps in the process. First, at the injector, the OL02 resonant cavity is calibrated to the Faraday cup*, which blocks the beam current flow downstream of it. Second, the OL02 readout is compared to the BCM readout, as the injector cavity does not interfere with the beam.

Plotting the Faraday cup reading against the OL02 reading determines the beam current. From here, the scaler rate of one of the signals may be plotted as a function of the beam current (Fig. 3.5) and fit to a line. The form of the fit is: $\omega_n = \text{offset}_n + \text{slope}_n \cdot I$. The fit does not extend to zero because the BCMs are nonlinear at low currents and the fit is not valid. The offset term in the fit is obtained from a Gaussian fit to the scaler rates recorded over the course of five minutes with the beam turned off. Rearranging the fit, the beam current can be expressed as:

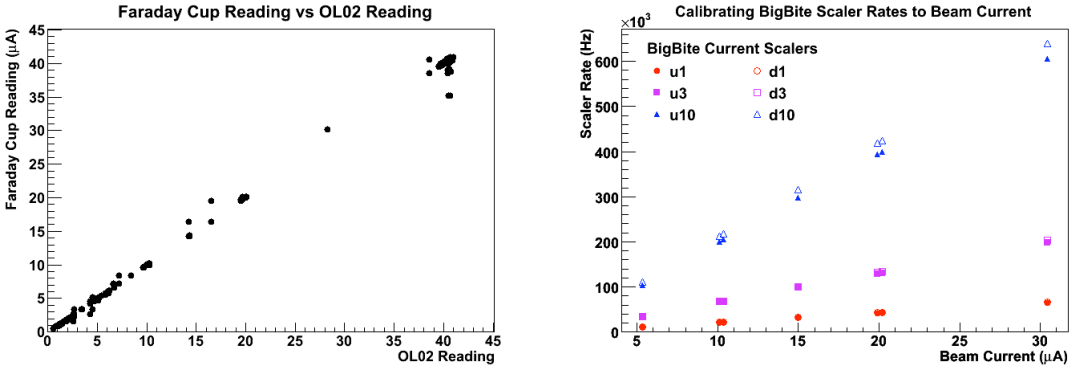

Figure 3.5: On the left, the Faraday cup reading is plotted as a function of OL02 reading, which determines the beam current. On the right, the scaler rate is plotted against the beam current. Fitting to a linear function allows for the extraction of the fit parameters used to calculate the beam charge. Analysis by D. Parno. Reproduced from [47].

$$I = \frac{\omega_n - \text{offset}_n}{\text{slope}_n}. \tag{3.12}$$

The charge may be calculated as:

*A water-cooled copper beam dump, inserted into the injector beamline to collect all of the current [153].

$$Q = I \cdot t = \frac{(\omega_n - \text{offset}_n)\, t}{\text{slope}_n}. \tag{3.13}$$

Measurements on the LHRS and BigBite give consistent results as they have copies of the same signals. The results for the fit parameters may be seen in Table 3.3. Neglecting errors on the clock rate, the error on the fit to the data shown in Figure 3.5 gives a systematic error of $\approx 0.03\%$ when considering the beam current calculated from the u3 scaler rate [47].

Table 3.3: Calibration results for the fit parameters used in the determination of the beam current for all three upstream (u) and all three downstream (d) BCMs. Errors on the offsets are on the order of 10^{-2} Hz. Analysis by D. Parno. Table reproduced from [47].

Scaler	Slope (Hz/μA)	Offset (Hz)	Scaler	Slope (Hz/μA)	Offset (Hz)
u1	2101 ± 1	396	d1	2152 ± 1	154
u3	6480 ± 2	453	d3	6658 ± 3	133
u10	19731 ± 11	771	d10	21008 ± 10	293

3.4.3 Beam Polarization

3.4.3.1 Mott Polarimetry

Before the electron beam leaves the injector, a measurement of the beam polarization may be done via Mott scattering of 5 MeV electrons from a gold, copper or silver target. Due to the spin-orbit coupling of the scattered electron with respect to the target nucleus's Coulomb potential, an asymmetry can be measured. From this measurement, the electron's polarization may be determined. The polarization result from this method tend to be systematically *lower* than those obtained by polarimeter measurements in Hall A or C. The high photon backgrounds in the injector could point to the reason as to why this occurs [154].

In order to carry out this measurement, data taking must be stopped while the measurement is performed, and takes up to a few hours to complete. Due to the stoppage of data taking, this method is considered a *destructive* method.

There were no Mott measurements taken for E06-014 due to the time constraints of the experiment.

3.4.3.2 Møller Polarimetry

Møller polarimetry consists of exploiting Møller ($e^- e^- \rightarrow e^- e^-$) scattering. In particular, the cross section of the reaction is dependent upon the polarizations of the incident electrons (P^{beam}) and the atomic electrons of the target (P^{targ}):

$$\sigma \propto 1 + \sum_{i=X,Y,Z} \left(A_{ii} P_i^{\text{beam}} P_i^{\text{targ}} \right), \tag{3.14}$$

where the sum runs over all polarization directions. A_{ii} is the analyzing power of the measurement. It is dependent upon the scattering angle in the center-of-mass frame. The maximum analyzing power is 7/9, corresponding to the longitudinal component of the beam polarization [152].

The measurement is performed as follows: electrons are scattered from a 10.9 μm thick iron foil with a polarization of 7.1% due to a 28 mT magnetic field produced by Helmholtz coils. The scattered electrons pass through three quadrupole magnets and one dipole magnet en route to a two-arm lead-glass calorimeter, which measures coincident particles. The longitudinal asymmetry of electrons is computed from the average measurement of two opposing target angles*. From Equation 3.14, the beam polarization is computed.

Like the Mott measurement, the Møller measurement is also destructive. Since it utilizes a solid target, data taking must be halted for a measurement. The thin foil target is susceptible to depolarization effects due to heating from the beam. Because of this, the beam current is limited to 1.5 μA, a factor of 10 less than E06-014's production current. However, the low statistical and systematic errors make this measurement an important component of beam polarimetry in Hall A.

There were seven measurements completed during E06-014, and are shown in Table 3.4.

Table 3.4: Beam polarization measurements via Møller scattering. These measurements are corrected for beam energy fluctuations. The errors listed are statistical and systematic, respectively. The sign is based on an arbitrary convention and flips when the half-wave plate is inserted or removed at the injector.

Date	Beam Energy (GeV)	Beam Polarization
7 February	5.90	-0.7943 $\pm$ 0.0013 $\pm$ 0.0159
9 February	1.23	-0.7164 $\pm$ 0.0014 $\pm$ 0.0143
11 February	5.90	+0.7450 $\pm$ 0.0015 $\pm$ 0.0149
19 February	5.90	-0.7448 $\pm$ 0.0011 $\pm$ 0.0149
3 March	5.90	-0.7970 $\pm$ 0.0012 $\pm$ 0.0159
6 March	4.74	+0.6394 $\pm$ 0.0010 $\pm$ 0.0128
12 March	4.74	-0.6079 $\pm$ 0.0013 $\pm$ 0.0122

*This results in the transverse contribution canceling out.

3.4.3.3 Compton Polarimetry

E06-014 was the commissioning experiment for the Compton polarimeter, which exploits Compton scattering ($e^-\gamma \to e^-\gamma$) to determine the electron's polarization, as the cross section of the interaction is sensitive to the relative polarizations of the electrons and photons [155, 156]:

$$\left(\frac{d^2\sigma}{dxd\phi}\right)_{\text{Compton}} = \frac{1}{2\pi}\left(\frac{d\sigma}{dx}\right)_{\text{unpol}} \left\{1 + P_\gamma \left[P_e^\ell A_\ell(\rho) + P_e^t \cos\phi A_t(\rho)\right]\right\}, \tag{3.15}$$

where P_γ is the photon polarization; $P_e^{\ell,t}$ is the electron polarization for the longitudinal and transverse components, respectively; $A_{\ell,t}$ is the longitudinal and transverse analyzing power, respectively. They correspond to asymmetries that would be measured if the circular polarization of the photons were perfect in addition to perfect polarization of the electrons.

Due to the large longitudinal momentum of the electrons in the lab frame, the Compton scattering angles are small enough so that the azimuthal distribution of the scattered particles is fully contained in the detectors. Therefore, integrating over the azimuthal angle ϕ leaves just the sensitivity to the longitudinal components (dropping the ℓ label on P_e):

$$\left(\frac{d\sigma}{dx}\right)_{\text{Compton}} = \left(\frac{d\sigma}{dx}\right)_{\text{unpol}} \left[1 + P_\gamma P_e A_\ell(\rho)\right]. \tag{3.16}$$

There are four possible spin configurations of the longitudinally polarized electrons and circularly polarized photons, as shown in Figure 3.6. Since Compton scattering is an electromagnetic process, it conserves parity. This allows for the reduction of the number of unique configurations to two: $\uparrow\downarrow$ and $\uparrow\uparrow$, corresponding to antiparallel and parallel spin configurations, respectively. Taking advantage of this, the measurement of the electron's polarization may be realized by an asymmetry:

$$A_{exp} = \frac{N^{\uparrow\uparrow} - N^{\uparrow\downarrow}}{N^{\uparrow\uparrow} + N^{\uparrow\downarrow}} = P_e P_\gamma \langle A_\ell \rangle. \tag{3.17}$$

The measurement is carried out when the electron beam is directed through a magnetic chicane. At the center of the chamber, Compton scattering occurs, as laser light is directed along the chicane at the incoming electrons. The scattered electrons and photons are detected at separate dedicated detectors, while the electrons that did not undergo scattering proceed towards the experimental hall. A diagram of the process is shown in Figure 3.7. The big advantage of this method is that it is *non*-destructive, allowing a measurement of the polarization on the same electrons that are being used in production running.

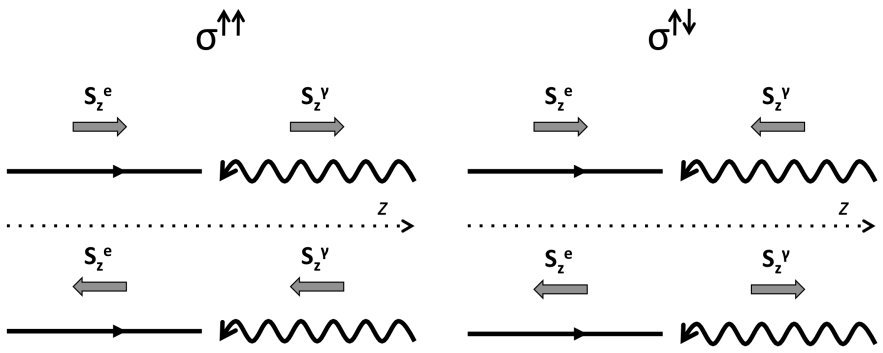

Figure 3.6: The various combinations of electron and photon spins. The two configurations in each column are equivalent. Figure reproduced from [47].

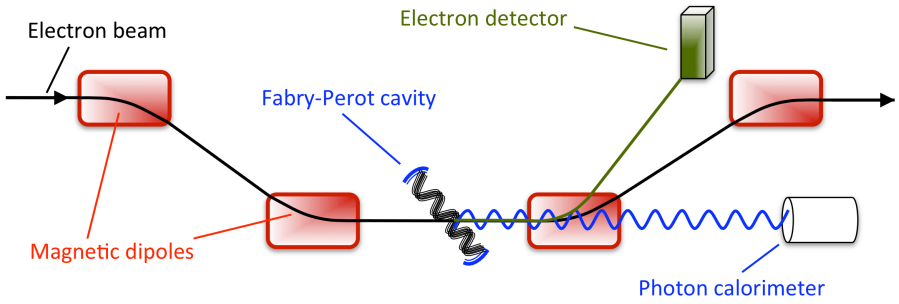

Figure 3.7: A representative drawing of the Compton polarimeter in Hall A. Not to scale. The electron beam (black line) enters the magnetic chicane from the left. Scattering occurs at the center of the chicane, and the scattered electrons and photons are detected in separate detectors. The unscattered electrons continue towards the experimental hall. Figure reproduced from [47].

The beam polarizations measured by the Compton polarimeter are shown in Table 3.5. They are in good agreement with the Møller measurements presented in Section 3.4.3.2. The results from both methods were combined and used in our double-spin asymmetry analysis (Sect. 5.5). For an in-depth discussion of the Compton polarimeter and the corresponding data analysis, see [47].

3.4.4 Beam Energy

In order to have accurate kinematic calculations, one needs to have an accurate measurement of the beam energy. During the running of E06-014, the beam energy was monitored via the Tiefenback method [157], which combines BPM measurements and the integral of the magnetic field produced by the Hall A arc magnets in order to compute the beam energy

Table 3.5: Beam polarization measurements from the Compton polarimeter compared to those from the Møller polarimeter. The error bars are the in quadrature sum of the statistical and systematic errors. The combined beam polarization is the weighted average of the two methods, with the errors being the weight. No Møller measurement was taken during the second run period. Table reproduced from [47].

Run Period	Beam Energy (GeV)	P_e from Compton	P_e from Møller	Combined P_e
1	5.90	0.726 ± 0.018	0.745 ± 0.015	0.737 ± 0.012
2	4.74	0.210 ± 0.011	—	0.210 ± 0.011
3	5.90	0.787 ± 0.020	0.797 ± 0.016	0.793 ± 0.012
4	4.74	0.623 ± 0.016	0.628 ± 0.012	0.626 ± 0.010

upon its entry into the hall.

The method is calibrated by the use of comparisons to an arc-measurement (Fig. 3.8), where eight dipoles deflect the beam through a nominal angle of 34.3°. Deviations from this angle is measured by the so-called SuperHarps, which are pairs of wires located before and after the magnet. The bend angle through the arc of magnets is related to the beam momentum (and therefore its energy) by:

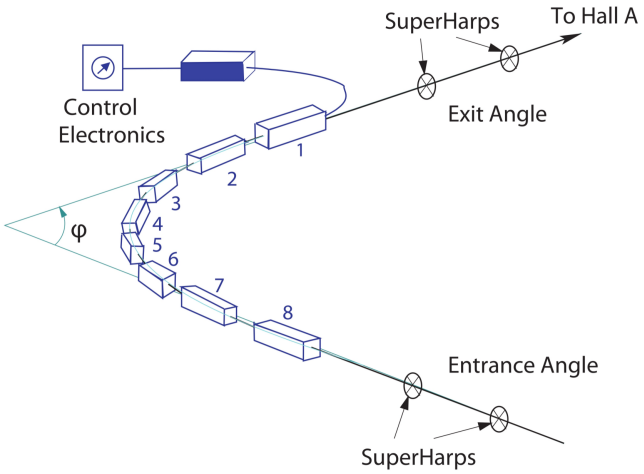

Figure 3.8: A diagram of how the arc-measurement is done for the electron beam energy. Figure reproduced from [40].

$$p = k\frac{\int \vec{B}\cdot d\vec{l}}{\theta},$$

where $k = 0.29972/c$ GeV·rad·T^{-1}·m^{-1} [152]. The integral of the magnetic field is measured by a ninth dipole, which is a reference magnet located outside of the vacuum and

is measured directly using a Hall probe. The error on this measurement is $\delta E/E \approx 2 \times 10^{-4}$ [158].

There were no arc measurements during E06-014, but we utilized the measurements from the previous experiment, E06-010, see Table 3.6.

Table 3.6: Comparison of the arc measurement to the Tiefenback measurement during the running of E06-010. The measurement shown is from November 17, 2008. Reproduced from [47].

Arc Result (MeV)	Tiefenback Result (MeV)
$5889.4 \pm 0.5_{\text{stat}} \pm 1_{\text{syst}}$	$5891.3 \pm 2.5_{\text{syst}}$

3.5 ^{3}He Target

In this section, we discuss the motivation for using a ^{3}He target to study the neutron (Sect. 3.5.1); how the target is polarized (Sect. 3.5.2) and the methods used to measure the polarization (Sect. 3.5.4). In Section 3.5.3.1, we show the various targets used in E06-014. Finally, the analysis required to obtain the target polarization is presented in Section 3.5.5.

3.5.1 Motivation: Why ^{3}He?

As with any electron scattering experiment to study nucleon structure, an appropriate target must be chosen. Unfortunately, in studying the neutron, there are no free neutron targets. They are unstable particles, where they decay in a short time (885.7 $\pm$ 0.8s [35]) via β decay into a proton, electron and an electronic anti-neutrino. Because of this, a viable alternative is needed.

^{3}He, a spin-1/2 nucleus consisting of two protons and a neutron, is one candidate for a neutron target*. When ^{3}He is polarized, there are three principle states that characterize the polarization: $\approx 90\%$ of the polarization is carried by the neutron in the symmetric S state; $\approx 1.5\%$ of the polarization is carried by the S' state, and $\approx 8\%$ is carried by the D state (Fig. 3.9). In the S state, the spins of the protons are anti-parallel to one another, resulting in the neutron carrying the majority of the ^{3}He polarization. As a result, a polarized ^{3}He target acts as an effective polarized neutron target.

Polarized ^{3}He targets have been used in experiments around the world, including experiments at JLab, SLAC, HERMES at DESY, and at the Mainz Microtron MAMI.

*Deuterium, a spin-1 nucleus consisting of a proton and a neutron, is another option. Both nucleons have their spin aligned with the nuclear spin. However, large corrections due to the proton result in large uncertainties.

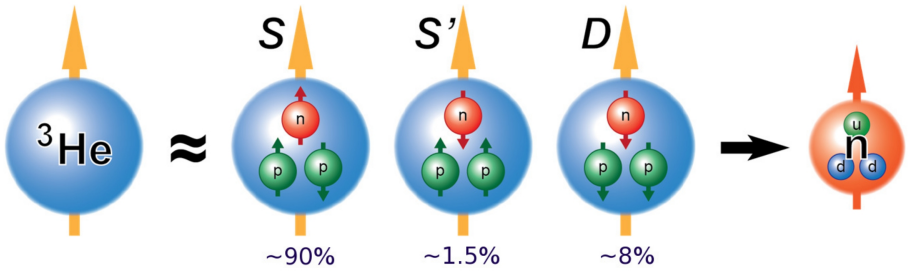

Figure 3.9: The nucleon polarization states in ^{3}He. The large arrow indicates the spin direction of the nucleus, while the smaller arrows indicate the spin direction of the nucleons. Figure reproduced from [159].

3.5.2 Method of Polarization

In order to polarize the ^{3}He nuclei, a three-step process is utilized, known as *hybrid spin-exchange optical pumping*. First, the rubidium $\left(^{85}\text{Rb}\right)$ atoms in a gaseous mixture is optically pumped using 795 nm circularly-polarized laser light, inducing the D1 transition: $5S_{1/2} \rightarrow 5P_{1/2}$. Second, the polarization of the ^{85}Rb atoms is transferred to potassium $\left(^{39}\text{K}\right)$ atoms via spin-exchange binary collisions. In the third and final step, the polarization of the ^{85}Rb and ^{39}K atomic electrons is transferred to the ^{3}He nuclei via the hyperfine interaction.

3.5.2.1 Optical Pumping of ^{85}Rb

Neglecting nuclear effects, the energy levels of ^{85}Rb atomic electrons in an external magnetic field are governed by angular momentum selection rules with the notation $N^{2S+1}L_J$, where N indicates the electron shell; S indicates the electron spin; L is the orbital angular momentum, and $J = L + S$ is the total orbital angular momentum. Right-circularly polarized laser light induces the transitions from the $5^2S_{1/2}$ ($m = -1/2$) ground state to the $5^2P_{1/2}$ ($m = +1/2$) excited state, in accordance with the selection rule of $\Delta L = +1$, see Figure 3.10. The excited electrons transition from the P orbital to the S orbital with equal probabilities for the $m = \pm 1/2$ sub-states, but the excitation only occurs for the $m = -1/2$ state, therefore *populating* the $m = +1/2$ state.

As the electrons de-excite to the ground state, they emit photons. These photons typically have different polarization states, and therefore will impose limitations on the pumping process. To minimize this effect, a small amount of N_2 is added to the chamber to

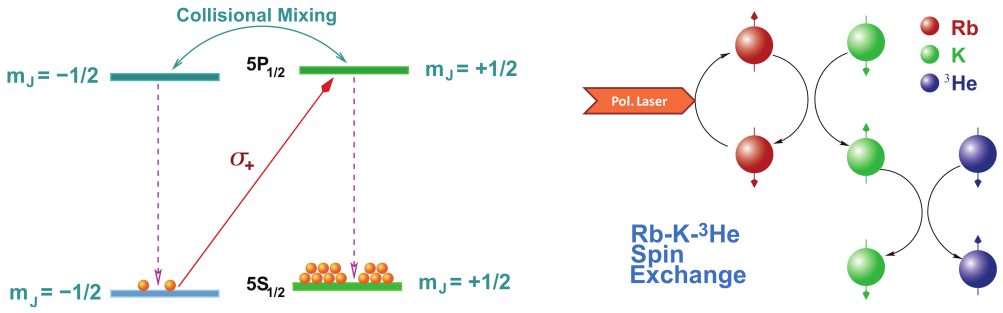

(a) Optical pumping of ^{85}Rb (b) ^{85}Rb-^{39}K-^{3}He spin-exchange

Figure 3.10: (a) Optical pumping on ^{85}Rb with right-circularly polarized photons. (b) The two-step process of spin-exchange from ^{85}Rb to ^{39}K, and then from ^{39}K to ^{3}He. Figures reproduced from [161].

absorb these photons into their rotational and vibrational degrees of freedom [160]. This allows for a non-radiative decay of the excited ^{85}Rb electrons to their ground state.

3.5.2.2 Spin Exchange

The potential of the interaction between two spin-1/2 atoms like ^{85}Rb and ^{39}K is composed of a spin-dependent part and a spin-independent part, which characterizes the hyperfine interaction. This allows the spin of the atoms to be *interchanged* some percentage of the time. This percentage is determined by the relative sizes of the two potentials. The collisional cross section for the ^{85}Rb–^{39}K mixture is $\sim 2 \times 10^{-14}\,\mathrm{cm}^2$, resulting in a spin-exchange rate of $\sim 100\,\mathrm{kHz}$, and a spin-relaxation rate of $\sim 500\,\mathrm{Hz}$ for a particle density of $10^{14}\,\mathrm{cm}^3$. Due to the large cross section, the time needed to transfer the spin of one set of atoms to the other is typically quite short, on the order of hours [162]. This is true even if the spin-dependent component is dominated by the spin-independent component, since the ^{85}Rb atoms are continuously re-polarized via optical pumping.

^{3}He may also undergo spin-exchange interactions; however, its valence electrons are in a spin singlet state, so its nuclear spin takes part in the process, via a Fermi-contact interaction [163, 164]. The inefficiencies of these interactions arise largely due to spin-relaxation where the spin of the alkali metal couples to the rotational angular momentum of the pair of colliding atoms, instead of the nuclear spin of ^{3}He. It turns out that the spin-relaxation cross-section (for collisions involving ^{3}He) is dominated by the alkali metal's spin-orbit interaction. Therefore, the use of a lighter alkali metal (like ^{39}K instead of ^{85}Rb) can greatly decrease the spin-relaxation cross-section and thus increase the spin-exchange

efficiency [165]. A diagram of the two-step process of transferring the ^{85}Rb electron spin to the ^{3}He nuclei is shown in Figure 3.10.

As an example, we consider the spin-exchange transfer rate to ^{3}He from alkali-metal atoms, η_{SE}*. Measurements at typical spin-exchange optical pumping temperatures give $\eta_{SE} \sim 2\%$ for ^{85}Rb–^{3}He, while $\eta_{SE} \sim 25\%$ for ^{39}K–^{3}He [166]. As a result, the time it takes to polarize a ^{3}He hybrid cell† is only $\sim$ 3–5 hours, compared to $\sim$ 15 hours for a cell that contains only ^{85}Rb for the polarizing process [151]. This faster so-called "spin-up" time reduces the overhead for spin-rotations and improves the ability of continuous optical pumping to reduce depolarization effects.

3.5.3 Target Apparatus

The target apparatus is composed of a number of different elements, including the target cells, target oven, target ladder system, Helmholtz coils for the holding magnetic field, RF coils and polarizing lasers.

3.5.3.1 Targets

The *production* target cell is shown in Figure 3.11. It consists of an upper chamber, called the *pumping chamber*, containing ^{3}He, ^{85}Rb, ^{39}K and N_2. It is in this chamber where the polarization takes place. There is then a thin transfer tube‡ leading down to the *target chamber*. This is the chamber where the electron beam passes through for the experiment. The production cells were made out of aluminoscilicate glass (GE-180) and were hand-blown by Mike Souza of Princeton University [151]. They were filled with ^{3}He and characterized at the University of Virgina and the College of William and Mary. Characterization consists of measuring the polarization, gas density, thickness of the cell and spin-up time. The ratio of ^{85}Rb to ^{39}K is also optimized.

An empty target cell was also used, which can be filled with various other gases like H_2, N_2 and ^{3}He. This allowed for the determination of dilution factors that contribute to the cross sections and asymmetries. Such dilutions appear due to the presence of materials other than ^{3}He in the target cell. Other targets utilized include a multi-carbon foil ("optics") target, used for the calibration of the optics for the two spectrometers. In addition to these targets, an "empty" target was used, corresponding to a hole in the target ladder. It was used for Møller measurements, so that the other targets do not get damaged in the process.

*The quantity $1/\eta_{SE}$ is the minimum number of photons needed to provide $\hbar/2$ units of spin to fully polarize an initially unpolarized ^{3}He nucleus [159].

†Cells containing the mixture of ^{85}Rb and ^{39}K for the polarizing process are referred to as hybrid cells.

‡A temperature gradient along the transfer tube confines the alkali-metals to the pumping chamber [167].

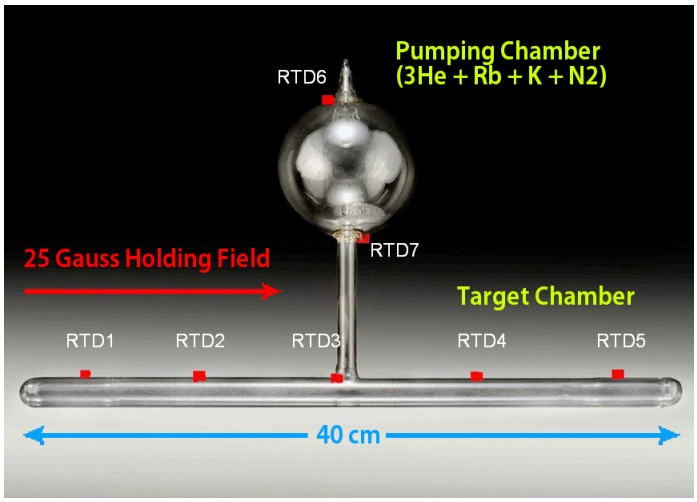

Figure 3.11: A production target cell, consisting of three regions: pumping chamber, transfer tube and target chamber. The optical pumping process is carried out on the pumping chamber, while the electron scattering of the experiment is carried out on the target chamber. Also shown are the resistive temperature devices (RTDs).

3.5.3.2 Target Oven and Ladder System

The pumping chamber needed to be placed in a high temperature environment (230°C) in order to achieve a high ^{39}K vapor pressure. To this end, the pumping chamber was mounted inside an oven system that had a constant flow of compressed hot air. The air flow was controlled by a PID feedback system so as to keep the temperature constant. A number of resistive temperature devices (RTDs) were placed on the target to monitor its temperature. One RTD was placed at the top of the pumping chamber, and another at the base of it, close to the transfer tube. Five more were placed equidistant from one another along the length of the target chamber, see Figure 3.11.

The target ladder system consists of a stacked arrangement of the various targets, and could be controlled remotely from the counting house. This allows for the shift workers to switch targets appropriate for the physics goals of a given shift. The target that was in use is aligned properly with respect to the electron beam, with the other targets effectively out of the way, either above or below the electron beam. The targets in the ladder system consist of the targets listed in Section 3.5.3.1.

3.5.3.3 Target Enclosure

The target enclosure is a spherical, fiberglass material that surrounds the target cell and ladder system. Its purpose is to confine the laser light that is incident on the target pumping chamber, and also serves to protect workers in the other parts of the hall (when there is no

beam) from the target materials. The enclosure is filled with ^{4}He gas to reduce energy loss effects for the incident and scattered electrons*. The upstream and downstream sides of the beamline interface with the enclosure via beryllium windows, which are 0.254 mm and 0.508 mm thick for upstream and downstream sides, respectively. The windows prevent glass shards from the target cell contaminating the beamline if the target were to explode. The window at the target enclosure exit for scattered electrons is covered by 0.076 mm of aluminum foil (on the enclosure side) to keep air out of the target.

3.5.3.4 Target Magnetic Field Coils

Figure 3.12 shows the orientation of the various coils. The red lines indicate Helmholtz coils, while blue lines indicate the radiofrequency (RF) coils. The pickup coils are mounted very close to the target cell are indicated by the orange and light blue colors.

There were three pairs of Helmholtz coils utilized, capable of producing magnetic fields in three orthogonal directions: longitudinal (along the direction of the beam), transverse in-plane (perpendicular to the beam) and vertical (perpendicular to the beam, up and down). The field can reach a magnitude of 25 G, requiring ~ 7 A of current in each coil. The RF coils and pickup coils are important for the measurement of the target polarization (Sect. 3.5.5).

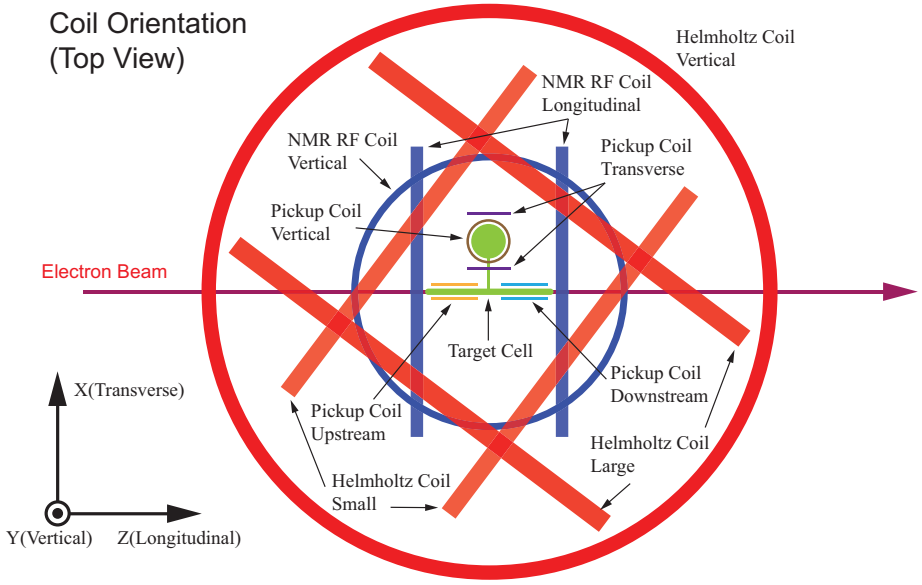

Figure 3.12: Target coils layout in the experimental hall. Figure reproduced from [152].

*^{4}He has a larger radiation length than air, thus reducing energy loss effects.

3.5.3.5 Polarizing Lasers

There were three COMET lasers, each with a linewidth of 0.2 nm, power of 25 W and a wavelength of 795 nm. They were used to optically pump the ^{85}Rb in the pumping chamber. The three lasers are combined into one via a 5-to-1 combiner, so that all three could simultaneously deliver light to the target chamber. The output of the combiner was sent to a beamsplitter, yielding two linearly polarized components. One component passed twice through a quarter-wave plate, after which both had the same linear polarization. Sending each component through another quarter wave plate converts the linear polarization into circular polarization. The resulting beams are then combined into one, with a spot size of 7.5 cm in diameter, corresponding to the size of the chamber [168]. There were three optics lines, corresponding to longitudinal, transverse and vertical polarization directions.

3.5.4 Measurement of Target Polarization

To measure the polarization of the ^{3}He in the target cell, there are two methods utilized: nuclear magnetic resonance (NMR) and electron paramagnetic resonance (EPR). The NMR measurement is a *relative* measurement, in that it needs to be calibrated to a theoretically calculable quantity (like the polarization of a water sample in a magnetic field). The EPR measurement is an absolute one. The results from the two methods are compared (and combined) in the data analysis upon computing the polarization of ^{3}He. Note that the direct measurements of the polarization were done on the pumping chamber, and the results were translated to the target chamber in both the EPR and NMR cases* (Sect. 3.5.5).

3.5.4.1 Nuclear Magnetic Resonance

The magnetic moments of nuclei will align themselves along the direction of a constant magnetic field (called the holding field). The magnetic moments will precess about the direction of the holding field when a radiofrequency (RF) field is applied in the perpendicular direction. If the RF field frequency is swept through the resonance of the ^{3}He nucleus, the spins of ^{3}He will reverse their direction. This is known as *nuclear magnetic resonance*. The motion of the spins changes the field flux through the pick-up coils (Fig. 3.12), inducing an electromotive force. The signals from the coils are pre-amplified and combined†, and sent to a lock-in amplifier, where the lock-in identifies the NMR signal which has the same frequency as the reference RF signal. The magnitude of the lock-in output is proportional to the ^{3}He polarization.

*The NMR measurement on the water cell was performed on the target chamber [169].

†The signals from the pickup coils are sent to pre-amplifier inputs A and B. Due to the way the coils are set up, in the output signal (A-B), the noise cancels, while the real signal is enhanced [159, 168].

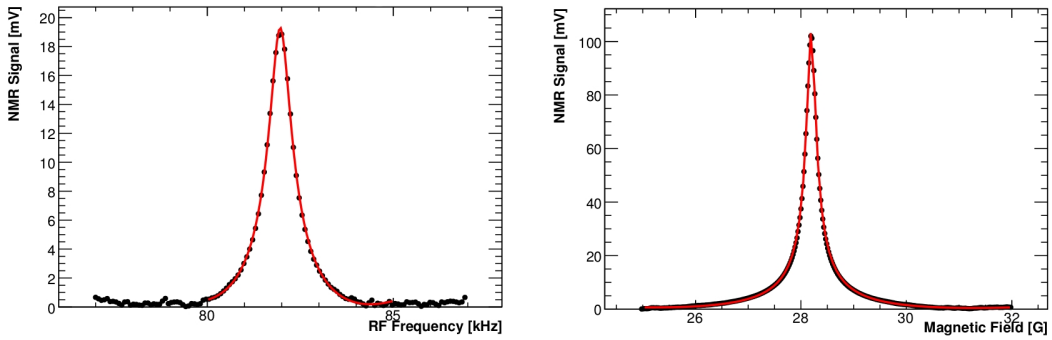

(a) RF field sweep (b) Holding field sweep

Figure 3.13: Typical NMR signals. (a): NMR signal obtained when sweeping the RF field through the resonance; (b): NMR signal obtained when sweeping the holding field through the resonance. This was done for NMR measurements needed in the water calibration. The RF field was held at a frequency of 91 kHz and the holding field was swept from 25 G to 32 G at a rate of 2.1 G/s, where the resonance was at 28 G [169]. Figures reproduced from [169].

When conducting a measurement, it is important to do it in such a way that the effect on the polarization is as small as possible. To accomplish this, sweeps of the RF frequency are done according to the adiabatic fast passage (AFP) technique, where the speed the at which the sweep through the resonant frequency is done is faster than the spin relaxation time, but also it is slow enough so that the nuclear spins can follow the sweep of the RF field.

In principle, the spins may be rotated by either sweeping the *holding* field through a range of values or sweeping the *RF* field through a range of frequencies. As long as the requirements given by AFP are met, then the ^{3}He spins will flip their direction as one of the fields is swept through the resonance. The AFP conditions were met during the experiment by performing the NMR measurement in the following way: the frequency of the RF field was swept from 77 kHz to 87 kHz at a rate of 5 kHz/sec and back, where the resonant frequency is $\omega_0 = 81$ kHz.

An NMR measurement is a *relative* measurement, so it needs to be compared against a known measurement that is calculable in theory. A measurement of NMR done on water is typically used, and can be calculated exactly from statistical mechanics [170]. This experiment used a water calibration, and electron paramagnetic resonance measurements (Sect. 3.5.4.2). The NMR measurement was done every four hours. Typical signals of NMR measurements are displayed in Figure 3.13.

3.5.4.2 Electron Paramagnetic Resonance

Electron paramagnetic resonance (EPR) is an absolute polarization measurement. It utilizes Zeeman splitting of energy levels for electrons when placed in an external magnetic field. This phenomenon occurs for the ^{85}Rb and ^{39}K atoms, which are present in the pumping chamber. In particular for ^{85}Rb, the $F = 3$ ground state splits into seven sublevels corresponding to $m_F = -3, -2, \ldots, 2, 3$, where F is the total angular momentum quantum number. The splitting corresponds to a frequency that is proportional to the holding field: $\nu_0 = \gamma B_0$, with $\gamma = 0.466$ MHz/G for a ^{85}Rb atom. The shift in this frequency is due to the small effective magnetic field created by the spin-exchange mechanism of ^{85}Rb–^{39}K and ^{39}K–^{3}He, in addition to the polarization of the ^{3}He nuclei. This shift in frequency is known as the EPR frequency shift, $\Delta\nu_{EPR}$.

For the measurement of the ^{3}He polarization, the component due to the spins of the ^{3}He nuclei must be isolated. This can be accomplished by sweeping the RF field at AFP conditions with a constant holding field. The frequency shift due to ^{3}He is a few tens of kHz in this experiment. The frequency shift may be broken down into its components as:

$$\Delta\nu_{+} = \Delta\nu_{\mathrm{He}} + \Delta\nu_{SE} + \Delta\nu_{B} \tag{3.18}$$

$$\Delta\nu_{-} = -\Delta\nu_{\mathrm{He}} + \Delta\nu_{SE} + \Delta\nu_{B} \tag{3.19}$$

$$\Rightarrow \Delta\nu_{+} - \Delta\nu_{-} = 2\Delta\nu_{\mathrm{He}}. \tag{3.20}$$

The terms in Equations 3.18 and 3.19 corresponding to $\Delta\nu_{SE}$ and $\Delta\nu_{B}$ are the spin-exchange and holding field contributions, respectively. Equation 3.20 shows how the contribution due to ^{3}He, $\Delta\nu_{\mathrm{He}}$, may be isolated from the two opposite frequency-shifted states. The change in frequency is related to the polarization of ^{3}He by:

$$\Delta\nu_{EPR} = \frac{8\pi}{3}\frac{d\nu_{EPR}}{dB}\kappa_0\mu_{^3\mathrm{He}}\eta_{^3\mathrm{He}}P, \tag{3.21}$$

where $\kappa_0 = \kappa_{oo}T_{\mathrm{ref}} + \kappa_{oT}\,(T - T_{\mathrm{ref}})$, a dimensionless quantity that depends on the geometry and temperature of the cell [151]; $d\nu_{EPR}/dB$ is the change in the frequency with respect to the magnetic field, and can be calculated from the Breit-Rabi equation; $\eta_{^3\mathrm{He}}$ is the density of ^{3}He; $\mu_{^3\mathrm{He}}$ is the magnetic moment of ^{3}He, equal to 6.706984×10^{-14} MeV/T; P is the polarization of ^{3}He in the target cell. The value of κ_{oT} is known at $T \sim 170^{\circ}$ C and is extrapolated to the operating temperature of 255°C. This results in a large uncertainty in κ_{oT}.

In order to measure the frequency shift $\Delta\nu_{EPR}$, the RF field that corresponds to the energy difference between the $m_F = -3$ and $m_F = -2$ ground state sub-levels is first applied

to the target. This increases the number of electrons in the $m_F = -2$ sub-level. These electrons absorb laser light and are excited to the $P_{1/2}$ state. Upon decaying back to the $S_{1/2}$ state, the number of emitted photons increases, corresponding to the D1 transition at a wavelength of 795 nm. This is detected by a photodiode*. The ^{3}He spins are flipped by sweeping the RF field through the resonance and measuring the change in the frequency. Figure 3.14 shows a typical EPR AFP sweep spectrum, which is a result of three frequency sweeps under AFP conditions†. EPR measurements were done every few days at the same time that NMR measurements were conducted.

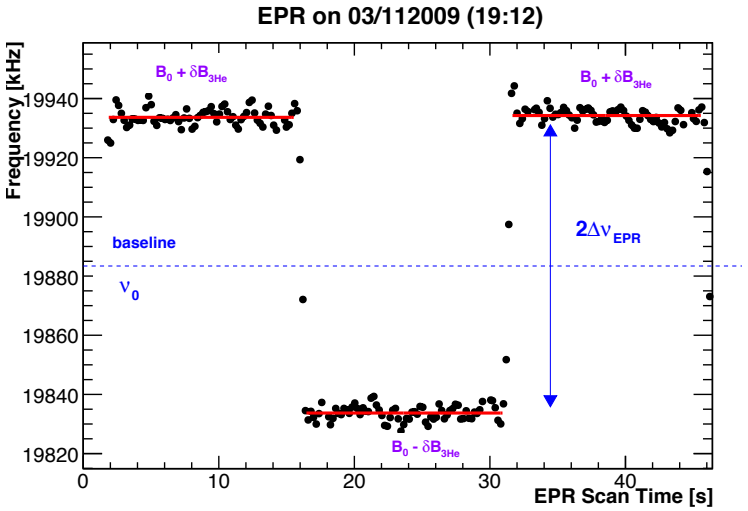

Figure 3.14: A typical EPR AFP sweep for three of the four sweeps. The frequency shift for when the spins of ^{3}He are parallel ($B_0 + \delta B_{^3\mathrm{He}}$) and anti-parallel ($B_0 - \delta B_{^3\mathrm{He}}$) are shown. Figure reproduced from [169].

3.5.5 Calculation of Target Polarization

To compute the target polarization, the signals from the NMR and EPR measurements must be fit to an appropriate function and then utilized in the proper equation to extract the polarization. The NMR measurement is a relative measurement, and needs to be calibrated by an absolute measurement. For E06-014, the NMR ended up being calibrated to the EPR measurement, and also to a water NMR measurement. This leads to the relations:

*Further details of the detection of the signal are discussed in [159, 168, 169].
†AFP sweeps were usually done four times per EPR measurement.

$$P_{^3\mathrm{He}}^{EPR} = C_{EPR} \cdot C_{diff} \cdot S_{EPR}^{prod} \tag{3.22}$$

$$P_{^3\mathrm{He}}^{NMR} = C_{EPR,\mathrm{H_2O}} \cdot C_{NMR} \cdot S_{NMR}^{prod}, \tag{3.23}$$

where the coefficients are particular to which method is used. Note that there are two different approaches for the NMR polarization, which is due to it being a relative measurement. The coefficient $C_{EPR} = P_{EPR}/S_{EPR}$, where P_{EPR} is the polarization measured via EPR (Eqn. 3.22) and S_{EPR} is the height of the ^{3}He NMR signal measured. C_{diff} is a diffusion constant needed to propagate the EPR polarization from the pumping chamber to the target chamber, and C_{NMR} serves a similar role for the NMR measurements. The constant $C_{\mathrm{H_2O}}$ is a coefficient to account for the differences between the ^{3}He and water targets.

All of the target analysis—except for the magnetic flux calculations—was conducted by M. Posik, and a more detailed discussion may be found in [169]. In the following, we will discuss the details of the magnetic flux calculations and how it contributes to the coefficient $C_{\mathrm{H_2O}}$.

3.5.5.1 Magnetic Flux: Connection to the Coefficient $C_{\mathrm{H_2O}}$

The ^{3}He and water target cells have similar geometries, but the differences need to be taken into consideration. This is accomplished by the constant $C_{\mathrm{H_2O}}$ which takes the form:

$$C_{\mathrm{H_2O}} = \left(\frac{P_{\mathrm{H_2O}}}{S_{\mathrm{H_2O}}}\right)\left(\frac{G_{\mathrm{H_2O}}}{G_{^3\mathrm{He}}}\right)\left(\frac{\mu_p}{\mu_{^3\mathrm{He}}}\right)\left(\frac{n_p \Phi_{\mathrm{H_2O}}}{n_{^3\mathrm{He}}^{pc}\Phi_{^3\mathrm{He}}^{pc} + n_{^3\mathrm{He}}^{tc}\Phi_{^3\mathrm{He}}^{tc}}\right), \tag{3.24}$$

where $P_{\mathrm{H_2O}}$ and $S_{\mathrm{H_2O}}$ correspond to the polarization and NMR signal height for water; $\mu_{p,^3\mathrm{He}}$ is the magnetic moment for a proton or ^{3}He; $G_{\mathrm{H_2O},^3\mathrm{He}}$ is the pre-amplifier gain for the water and ^{3}He signals; $\Phi_{\mathrm{H_2O},^3\mathrm{He}}$ are the magnetic fluxes measured in the pick-up coils for the water and ^{3}He cells; *pc* and *tc* refer to pumping chamber and target chamber, respectively. C_{NMR} is a coefficient to account for the NMR measurement for water and ^{3}He being performed at different physical locations.

The magnetic flux through the pickup coils depends upon the geometry of the coils, and is calculated according to:

$$\oint \vec{A} \cdot d\vec{\ell} = \int_V d^3\vec{r} \frac{\hat{z} \times \vec{r}}{|\vec{r}|^3} \tag{3.25}$$

for the pumping chamber, transfer tube and target chamber, yielding values for each flux term seen in Equation 3.24. The basic geometry of the pickup coils is shown in Figure 3.15. The geometry of the pickup coils, including their distances relative to the cell were obtained

from pictures of the target cells*. The pictures included a ruler in the frame, so that a conversion from pixels to centimeters could be made. This was accomplished by importing the photograph into the GNU Image Manipulation Program [172], and determining the lengths of the various components in terms of pixels. With the ruler included in the photograph, a simple conversion factor was used to obtain the quantities in centimeters. These geometrical inputs went into Equation 3.25. The results of the flux calculations are tabulated in Table 3.7. The systematic uncertainty assigned was 4%, estimated from the uncertainty in the extraction of the various geometrical parameters.

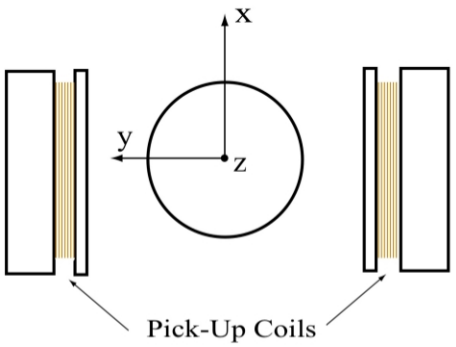

Figure 3.15: Diagram of the geometry of the pickup coils and the target cell. Figure reproduced from [173].

Table 3.7: The computed flux through the water cell, ^{3}He pumping chamber and target chambers. The error listed is the systematic error of 4%. All errors are absolute.

Flux Parameter	Upstream (cm^2)	Downstream (cm^2)
Φ_{H_2O}	4.983E+1 $\pm$ 1.990E+0	5.279E+1 $\pm$ 2.110E+0
$\Phi^{pc}_{^3He}$	5.000E-2 $\pm$ 2.000E-3	5.000E-3 $\pm$ 2.000E-4
$\Phi^{tc}_{^3He}$	5.076E+1 $\pm$ 2.030E+0	4.989E+1 $\pm$ 1.990E+0

3.5.5.2 Target Polarization Results

The final target polarization measurements as a function of BigBite run number are shown in Figure 3.17 for the pumping chamber (upper panel) and the target chamber (lower panel). As expected from the polarization diffusion analysis, it is seen that the polarization in the target chamber is lower than that seen in the pumping chamber [169].

*The pictures were obtained from Y. Zheng [171].

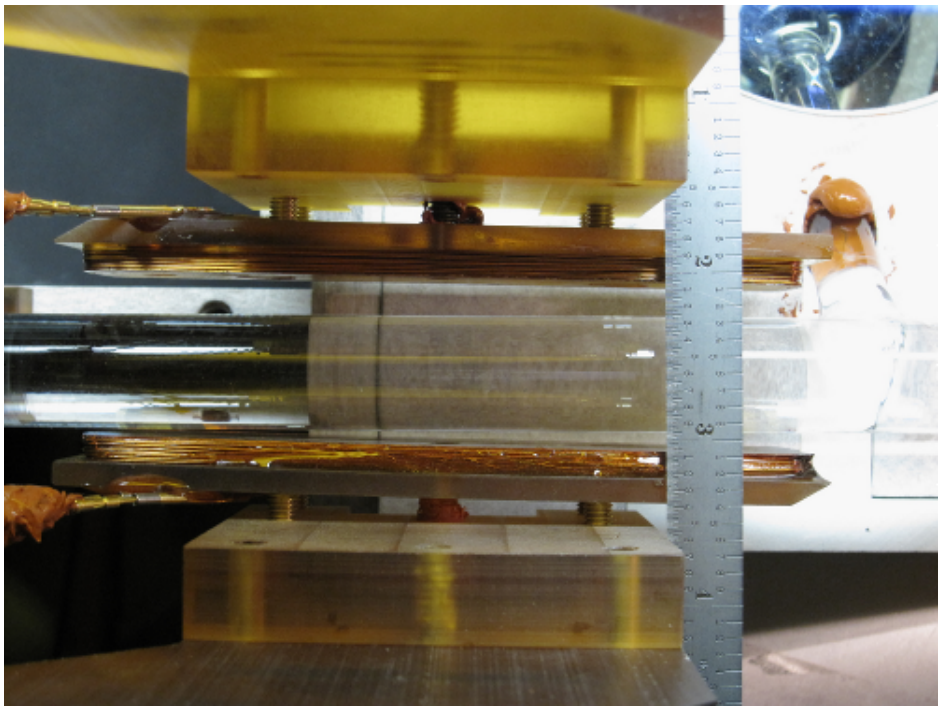

Figure 3.16: A photo of our water cell. A ruler is included so that a conversion of pixels to centimeters may be done. Photo obtained from [171].

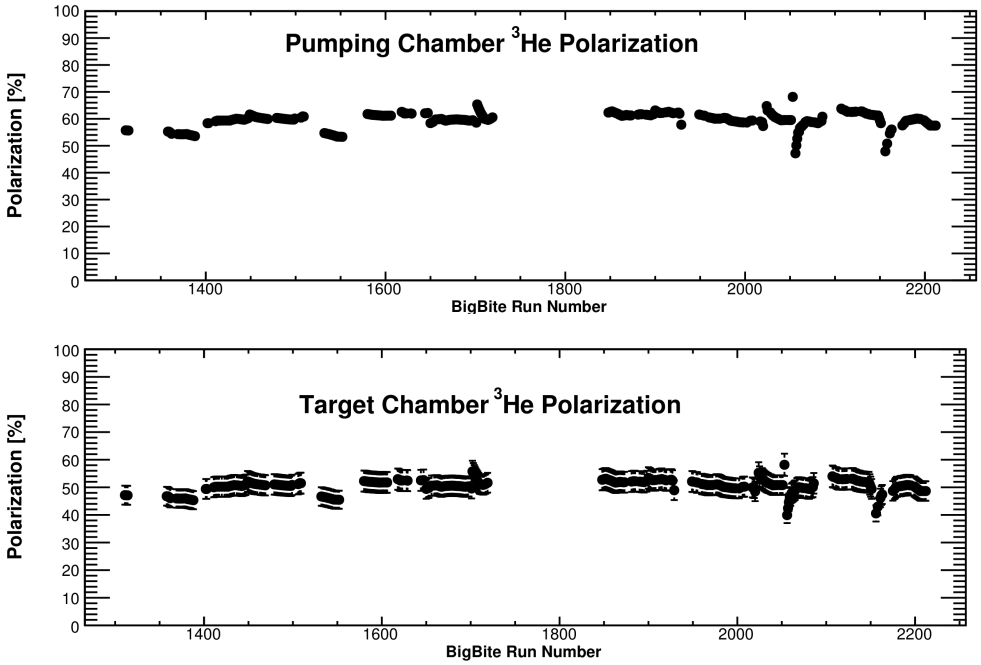

Figure 3.17: The computed ^{3}He target polarization for the pumping chamber (upper panel) and target chamber (lower panel). Figure reproduced from [169].

3.6 Left High-Resolution Spectrometer

3.6.1 Design and Characteristics

The LHRS is a small-acceptance spectrometer, detecting particles in a small momentum range of $\delta p/p \approx \pm 4.5\%$ with a solid angle of ≈ 6 msr. In this experiment, it was used to detect electrons.

Upon entering the LHRS, there are two superconducting quadrupoles for focusing the charged particles. Then there is a dipole magnet that bends the charged particles upwards through a nominal 45° bending angle. After this, the particles are again focused through another quadrupole before the first VDC plane. This sequence of magnets is referred to as a QQDQ configuration. The layout of the spectrometer is shown in Figure 3.18 and Table 3.8 shows important design characteristics.

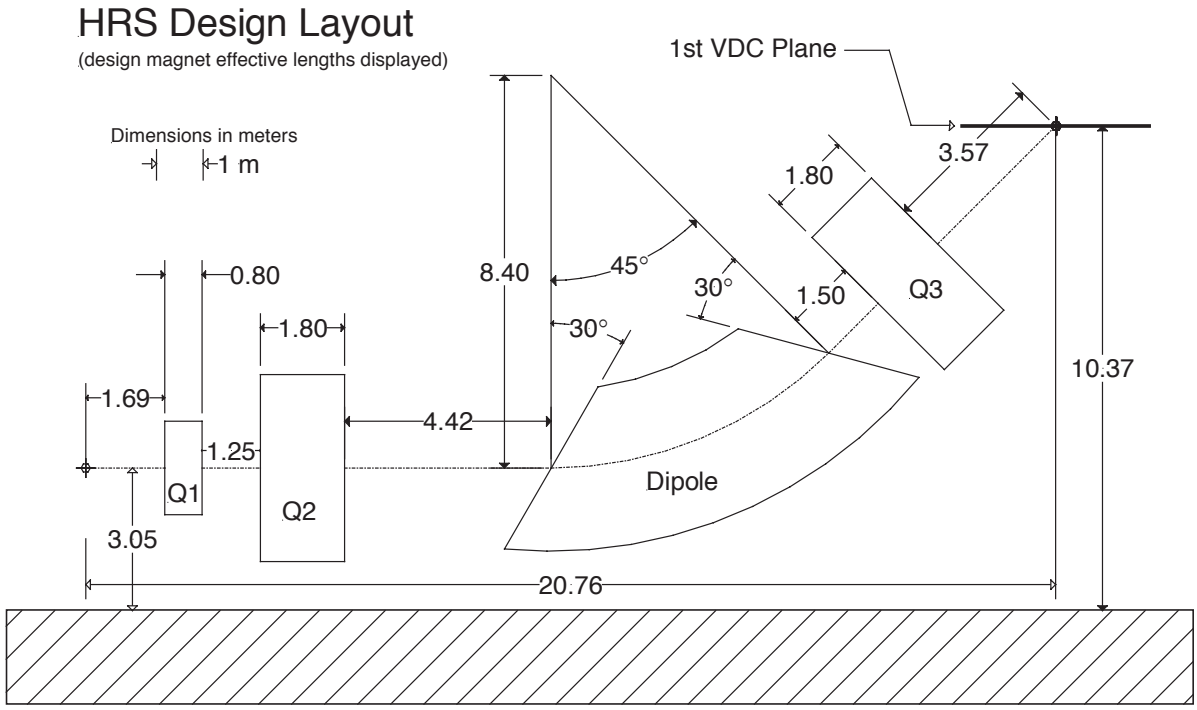

Figure 3.18: The design layout of the LHRS. Figure reproduced from [152].

3.6.2 Detector Packages

The LHRS is composed a number of sub-packages, located in the shield hut at the end of the magnet configuration. The detector sub-packages include the Vertical Drift Cham-

Table 3.8: LHRS characteristics. For more details, see [152].

Configuration	QQDQ
Optical Length	23.4 m
Bending Angle	45°
Momentum Range	0.3–4 GeV/c
Momentum Acceptance	$\pm$ 4.5%
Momentum Resolution ($\delta p/p$)	1×10^{-4}
Angular Range	12.5°–150°
Horizontal Angular Acceptance	$\pm$ 30 mrad
Vertical Angular Acceptance	$\pm$ 60 mrad
Horizontal Angular Resolution	0.5 mrad
Vertical Angular Resolution	1.0 mrad
(Solid Angle)$_{\frac{\delta p}{p}=0, y_0=0}$	6 msr

bers, which provide tracking information for scattered particles (Sect. 3.6.3); the S1 and S2m scintillating planes, which serve as the main trigger (Sect. 3.6.4); and finally, the gas Čerenkov (Sect. 3.6.5) and the pion rejector (Sect. 3.6.6) provide particle identification (PID) capabilities. There are also two other PID detectors, an aerogel gas Čerenkov and a Ring-Imaging Čerenkov detector, but they were not utilized in our experiment. For more information on these detectors, see [168]. The layout of these packages is shown in Figure 3.19.

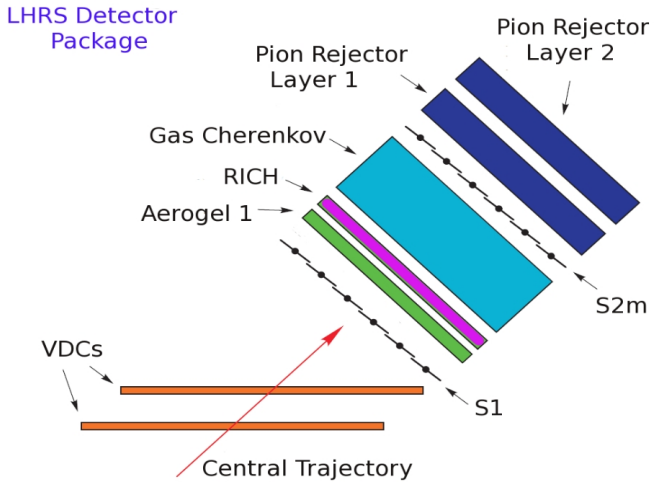

Figure 3.19: The LHRS detector package. Figure reproduced from [174].

3.6.3 Vertical Drift Chambers

The LHRS utilizes vertical drift chambers (VDCs) in order to achieve precise reconstruction of particle trajectories. The chambers have a standard U-V configuration, where the

U and V planes each contain 368 sense wires and each plane is oriented orthogonally with respect to one another; the two planes lie in the horizontal plane of the laboratory. They are oriented at 45° with respect to the (scattered) particle trajectory. See Figure 3.20.

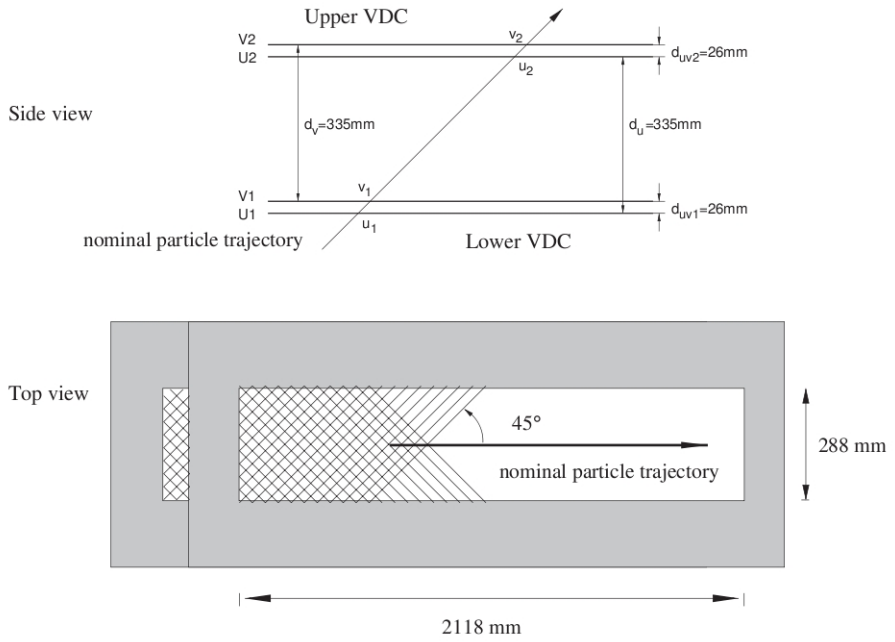

Figure 3.20: Geometrical configuration of the U and V planes of the VDC. Figure reproduced from [152].

Gold-plated Mylar high voltage planes are placed above and below each wire plane at an operating voltage of $-4\,\mathrm{kV}$, thus imposing and electric field between the HV planes. This in turn sets up a "sense region" for each wire plane. The chambers are filled with 62% Argon and 38% ethane by weight [175].

Primary ionization occurs when incoming particles (typically electrons and pions) collide with the molecules of the gas, ionizing them. The ionization electrons then drift along the field lines to the sense wires. The electric field is constant in regions relatively far from the wires, whereas in regions close to the wires, the electric field becomes quasi-radial [175], see Figure 3.21. This accelerates the ionization electrons, producing an avalanche. The resulting positive ions induce a *negative* signal on the wire, while neighboring wires acquire a *positive* charge. This results in no ambiguity as to which wire got a hit for a particular (ionizing) event [176].

A nominal track has a laboratory angle of $\sim 45°$, which corresponds to an angle of $\sim 55°$ in the coordinate system of the VDC. This results in five sense wires firing on average in a particular plane. On the other hand, an extreme track has an angle of $\sim 52°$ in the lab frame, corresponding to an angle of $\sim 62°$ in the VDC coordinate system; therefore, only

three wires will fire. For the average track, the positional resolution is $\sim 100\,\mu$m, with an angular resolution of ~ 0.5 mrad.

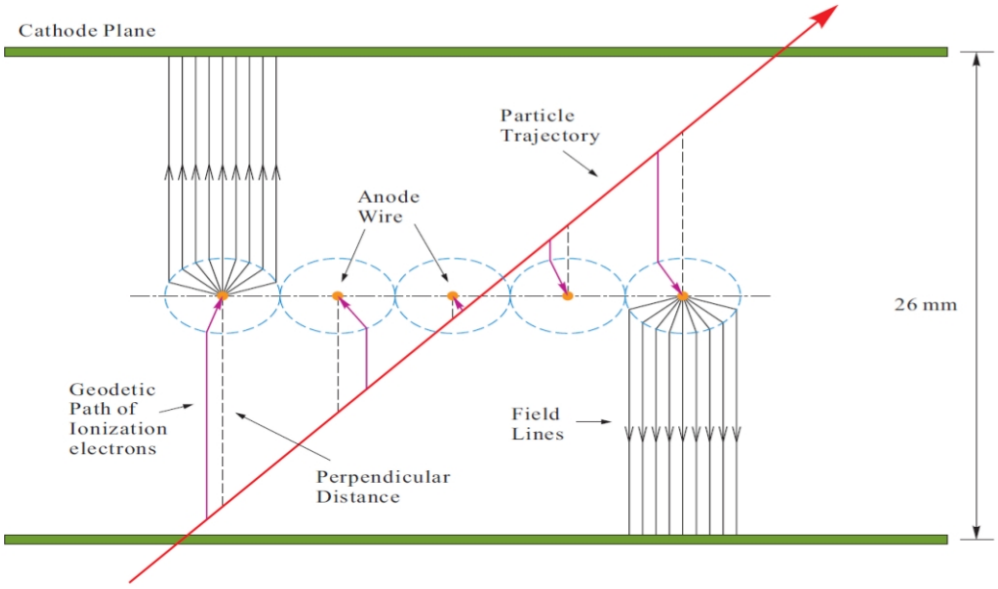

Figure 3.21: Electric field lines between the high-voltage cathode planes in the LHRS VDCs. Figure reproduced from [174].

3.6.4 Scintillators

There are two planes of plastic scintillating material, labeled S1 and S2m. S1 is composed of six scintillating paddles with $29.5 \times 35.5\,\text{cm}^2$ active area. Each paddle is viewed by a 2" diameter Burle 8575 photomultiplier tube (PMT) on each end. The paddles have a small angle with respect to the S1 plane, so that the paddles overlap by 10 mm. A diagram of the S1 plane is shown in Figure 3.22. The S2m plane has a similar configuration, but here there are sixteen paddles with the dimensions: 17" $\times$ 5.5" $\times$ 2". These paddles do not overlap. The timing resolution of each plane is ≈ 0.30 ns.

When a paddle absorbs ionizing radiation, it emits light which travels down the length of the paddle and is collected by the PMTs attached at each end. The timing information encoded in the PMTs' Time-to-Digital Converters (TDCs)* is utilized in the formation of the LHRS main trigger, to be discussed in Section 3.8.

* TDCs record timing information of particles or "hits." In particular, the scattered electrons leave a well-defined peak in the TDC, which corresponds to the events of interest. "Accidental" events, such as pions, are typically uncorrelated in time and thus their distribution is scattered randomly throughout the spectrum. The TDCs in the LHRS are single-hit. This will be elaborated on further in Section 5.3.2.4.1.

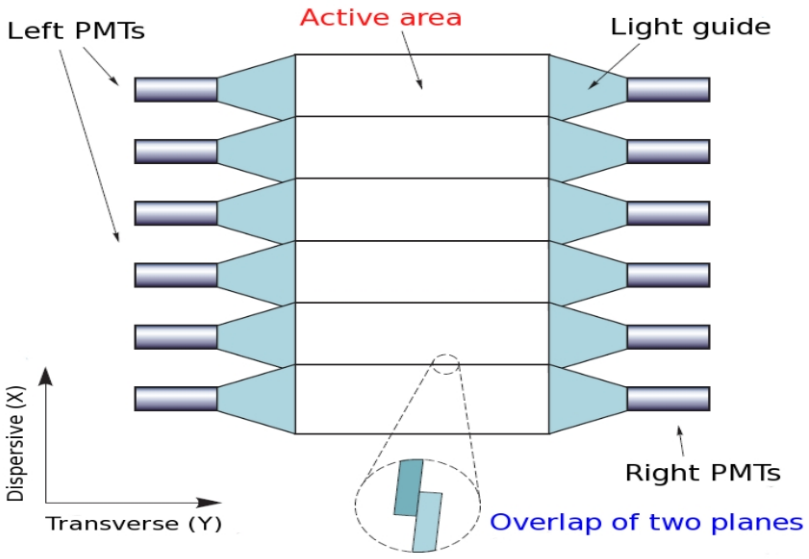

Figure 3.22: A depiction of the S1 scintillating plane. S2m has a similar configuration, but without the overlapping paddles. Figure reproduced from [174].

3.6.5 Gas Čerenkov

The gas Čerenkov detector is used as a particle identifier (PID) to distinguish electrons from pions via Čerenkov radiation, which occurs when a particle travels faster than the speed of light in a given medium, with $v = c/n$. Therefore, the requirement for Čerenkov radiation is for the speed of the particle to be:

$$\beta \geq \frac{1}{n} \tag{3.26}$$

Here, β is the speed of the particle in units of c and n is the index of refraction of the medium. Hence, Čerenkov radiation is seen to be a threshold effect. When this occurs, the particle emits electromagnetic radiation in a conical shape. This is similar to that of an aircraft moving faster than the speed of sound, emitting sonic shock-waves [176]. This is shown in Figure 3.23.

Čerenkov radiation occurs because the traversing particle polarizes the atoms along its path for a small amount of time, yielding electric dipoles. As the particle leaves the immediate vicinity of the polarized atoms, these atoms release Čerenkov radiation as the polarized state disappears. Now, if the velocity v of the charged particle is smaller than that of light in the medium, then this polarization is symmetric about the path of the particle. Therefore, there is zero net dipole moment and no Čerenkov radiation. However, when $v > c/n$, then the polarization is asymmetric, leading to a non-zero dipole moment. As a result, Čerenkov light is emitted.

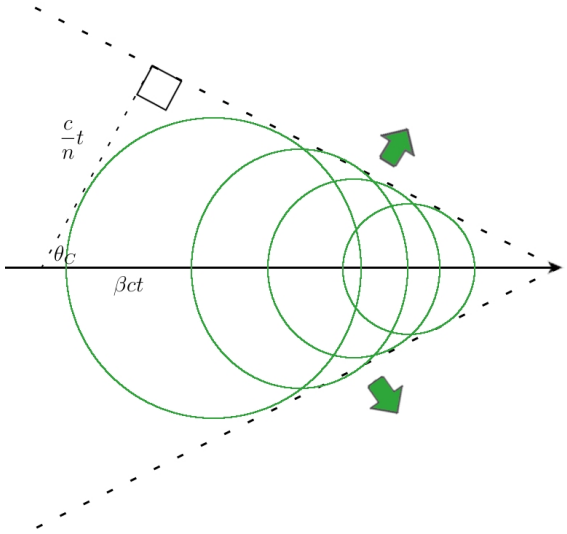

Figure 3.23: Čerenkov radiation.

From Figure 3.23, we can determine the angular distribution of the radiation. Considering that the particle travels a distance of $x_p = \beta ct$ in a time t, while the radiation is restricted to travel the distance of $x_{\text{rad}} = ct/n$, we obtain:

$$\begin{aligned} \cos\theta_C &= \frac{ct/n}{\beta ct} \\ &= \frac{1}{n\beta} \end{aligned}$$

Since this is a threshold effect, it is important to know what momentum an electron or a pion would need in order to trigger the Čerenkov counter. To see this, we consider the expression for the energy. Utilizing Equation 3.26, we write the expression for the momentum of the particle in terms of its mass m and the index of refraction n:

$$\begin{aligned} E = \gamma mc^2 &= \sqrt{m^2c^4 + p^2c^2} \\ \gamma &= \frac{1}{\sqrt{1-\beta^2c^2}} \end{aligned}$$

$$p = \frac{mc}{\sqrt{n^2-1}}. \tag{3.27}$$

From this expression, we can obtain the threshold momentum for an electron or pion to trigger the Čerenkov detector, which is filled with CO_2 gas at STP and $n = 1.00043$ [177]:

$$p^{\pi^-}_{\text{min}} = 4.77\ \text{GeV}$$
$$p^{e^-}_{\text{min}} = 17.4\ \text{MeV}.$$

The designed momentum acceptance of the LHRS is 0.3–4.0 GeV, so pions should not fire the gas Čerenkov. The kinematic range of our experiment is $0.60 \leq p \leq 1.70$ GeV. Therefore, it is seen that the Čerenkov detector is an excellent tool for PID.

The gas Čerenkov chamber in the LHRS is configured as shown in Figure 3.24. It houses ten spherical mirrors of focal length $f = 80$ cm. Each mirror is viewed by a photo-multiplier tube (PMT), placed 45 cm from the mirror.

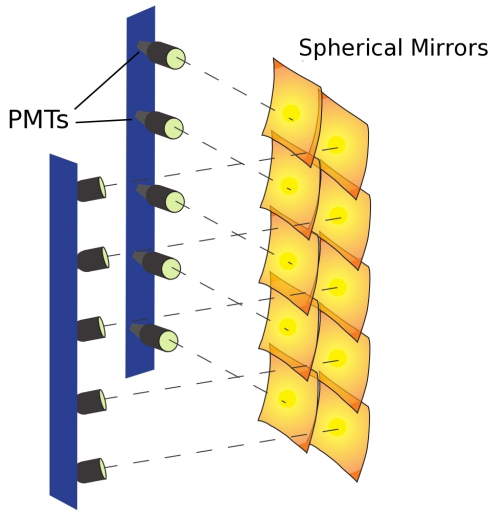

Figure 3.24: The gas Čerenkov in the LHRS. Figure adapted from [178].

The Čerenkov radiation is collected by the PMT and sent to its attached Analog-to-Digital Converter (ADC). The summation of all ten ADC signals gives the total amount of light produced by the particle.

Despite the fact that pions cannot fire the gas Čerenkov, they may still have an influence on the ADC spectrum of the gas Čerenkov. This occurs because pions can ionize the atoms of the gaseous medium, producing electrons with enough energy to trigger the detector. Such electrons are called δ-rays, or *knock-on electrons*. The distribution of these electrons has a peak at the one p.e. peak with a long tail that falls underneath the multiple (main) p.e. peak; however, the knock-on events that have a signal corresponding to the main peak tend to leave less energy on average in the pion rejector and are effectively removed from the analysis with a cut on the energy deposited in the calorimeter divided by the reconstructed

momentum (Sect. 5.2.2.2). Scattered electrons produce an ADC signal corresponding to the main p.e. peak. The number of photo-electrons produced in each PMT describes the PID quality of the detector. The calibration of this ADC signal is discussed in Section 4.1.4. The PID quality of the gas Čerenkov is discussed in Section 5.2.2.4.

3.6.6 Pion Rejector

The electromagnetic calorimeter installed in the LHRS is composed of two layers of lead-glass blocks, collectively called the pion rejector. It provides PID capabilities, in addition to the gas Čerenkov. Combining these two PID detectors results in a very clean electron sample (i.e., very little pion contamination) for the data analysis.

The pion rejector in the LHRS is configured as shown in Figure 3.25. It is composed of two layers of thirty-four $14.5 \times 14.5 \times 30$ cm^3 and $14.5 \times 14.5 \times 35$ cm^3 lead glass blocks, stacked in the orientation shown in Figure 3.25, where the long dimension of the blocks are transverse with respect to the direction of the scattered particle from the target. The gaps between the blocks in the first layer are compensated for by the second layer blocks being slightly offset so as to cover them. This is done to minimize the loss of a signal from particles traversing this region, see Figure 3.26.

The blocks are composed of the material SF-5, of which the main components are PbO_2 and SiO_2. The radiation length of SF-5 is $X_0 = 2.55$ cm [179], so scattered particles normal to the surface of the pion rejector will traverse $5.7X_0$ for each layer.

Each block is viewed by a PMT, which gathers the signal generated by the particles traversing the lead glass and sends it to its corresponding ADC. This ADC signal is linearly proportional to the particle's energy deposit. Therefore, the ADC spectrum of each PMT is a measure of the energy deposited in each block. The calibration of the pion rejector is discussed in Section 4.1.5 and the PID study is shown in Section 5.2.2.5.

Particles incident upon the lead-glass blocks interact with the material via bremsstrahlung and pair-production. The electrons, positrons and photons produced here then undergo these same processes, generating an electromagnetic cascade. The result is that the majority of the initial particle's energy is deposited in the calorimeter.

Electrons and heavier particles like hadrons have different energy deposition distributions in electromagnetic calorimeters. Electrons tend to leave most (if not all) of their energy in the calorimeter, while hadrons only deposit a small amount of their energy. This is primarily due to pions acting like minimum ionizing particles (MIPs), where they lose a small amount of energy with each ionizing reaction with the material. The energy loss of a MIP can be approximated by 1.5 MeV per g/cm^2 traversed [180]. Considering the density of SF-5 to be ≈ 4 g/cm^3 [177], then pions would deposit ≈ 175 MeV in the calorimeter

(both layers taken together), whereas electrons will deposit nearly all of their energy. The result of this is that there are two distinct peaks in the energy distribution with good separation in the calorimeter: one due to pions and the other due to electrons. Taking advantage of this, one can choose electrons while rejecting pions in the analysis.

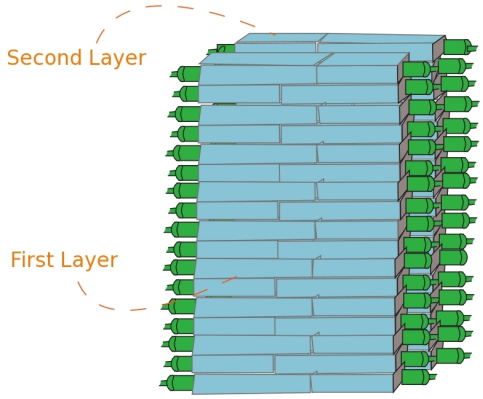

Figure 3.25: The pion rejector in the LHRS. Figure adapted from [178].

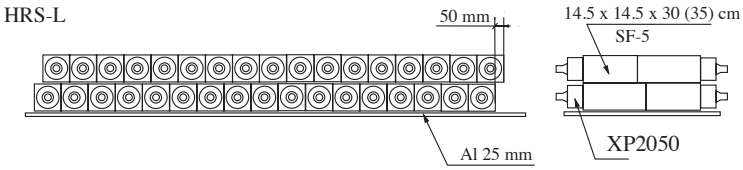

Figure 3.26: Side view of the pion rejector in the LHRS, showing the slight offset of the second layer (top) of the pion rejector relative to first (bottom). The circles in each square (block) indicates the PMT attached to that block (also shown in the right figure). Figure reproduced from [152].

3.7 BigBite Spectrometer

3.7.1 Design and Characteristics

The BigBite spectrometer is a large acceptance spectrometer, able to detect particles with a wide range in scattering angle and momentum. It was used to detect electrons.

BigBite consists of one large bending magnet, producing a maximum magnetic field of $\approx$ 1.2 T. The magnet face was located 1.5 m from the target center, resulting in an angular acceptance of 64 msr. The momentum range covered by the spectrometer was

0.6–2.5 GeV. There are a number of sub-detectors, including multi-wire drift chambers (MWDC) (Sect. 3.7.3), a gas Čerenkov (Sect. 3.7.4), a scintillating plane (Sect. 3.7.5) and a electromagnetic calorimeter (Sect. 3.7.6). The schematic layout of the detector is shown in Figure 3.27.

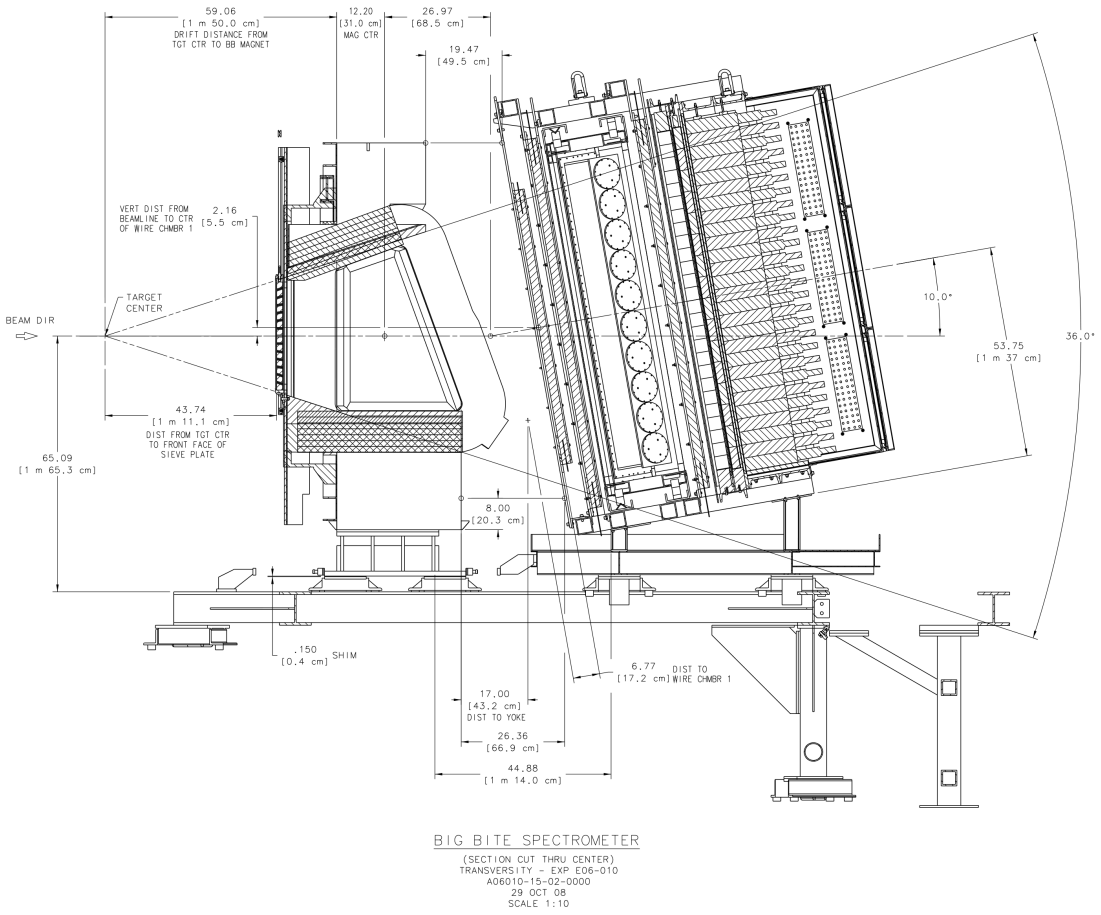

Figure 3.27: The design layout of BigBite. Scattered particles from the target enter from the left of the diagram. Figure reproduced from [181].

3.7.2 BigBite Magnet

The magnet was supplied with a current of 710 A, yielding a magnetic field of 1.2 T inside the magnet. The field is parallel (horizontal) to the floor and perpendicular to the scattered particle path from the target. The dispersion of the field is in the vertical direction. The magnetic field mapping measurements were performed before the E06-010

experiment [181]. The largest component of the magnetic field, B_y, is plotted for two different current settings of 600 A and 710 A as a function of the $\hat{z}$-direction in the detector coordinate system in Figure 3.28.

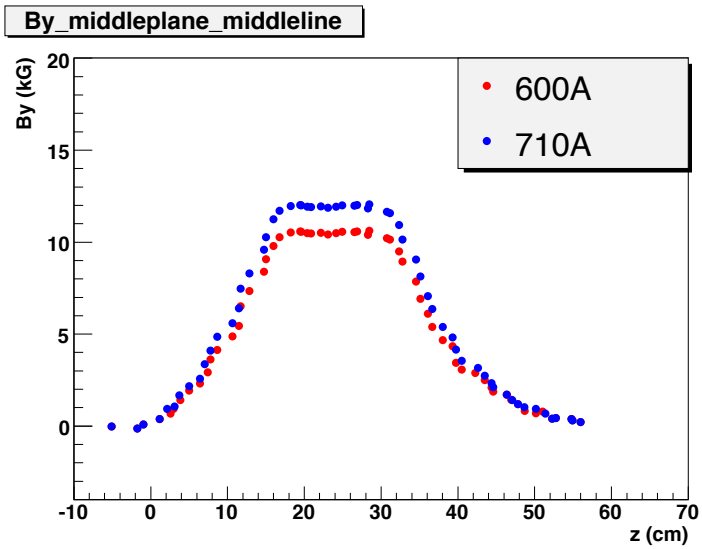

Figure 3.28: The y-component of the BigBite magnetic field as a function of the scattered particle's nominal velocity direction. Figure reproduced from [181].

3.7.3 Multi-Wire Drift Chambers

The Multi-Wire Drift Chambers (MWDC) are utilized for particle tracking, and work in much the same way as described for the VDC planes in the LHRS (Sect. 3.6.3). There are three chambers, each filled with a 50–50 mixture of argon and ethane gas. Each chamber has three pairs of wire planes, giving a total of eighteen planes in all.

Each of the eighteen planes is perpendicular to the detector's central ray, and is bounded by cathode planes 6 mm apart from one another (Fig. 3.29). At a distance of 3 mm from the cathodes is a plane of wires, composed of alternating field and sense wires. The sense wires have a spacing of 1 cm. The field wires and the cathode planes are held at the same constant high-voltage, producing a nearly symmetric potential in the region close to the sense wires.

There are three pairs of wire planes, each pair having a slightly different orientation. This is done to optimize track reconstruction in three dimensions. The two so-called X-planes (X,X') run horizontally (in detector coordinates), while the U and V planes are oriented at +30° and -30° with respect to the X-planes, respectively, see Figure 3.30. The wires in each plane are separated by 1 cm, and the primed planes (X', U', V') are offset

from their unprimed counterpart by 0.5 cm. This allows the tracking algorithm to determine if the track passed to the left or right of a given wire in the X plane based upon which wire got a hit in the X' plane, for example. This alignment results in a positional resolution of less than 0.3 mm.

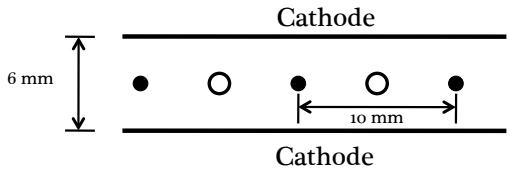

Figure 3.29: Cathode planes in the BigBite MWDC. Figure reproduced from [47].

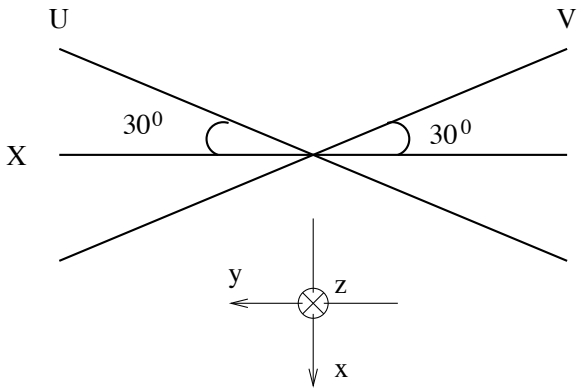

Figure 3.30: Orientation of the X, U and V planes in the BigBite MWDCs. Figure reproduced from [151].

3.7.4 Gas Čerenkov

The gas Čerenkov in the BigBite spectrometer works based on the same principles as already discussed for the LHRS gas Čerenkov (Sect. 3.6.5) in detecting electrons. This experiment served as the commissioning experiment for the Čerenkov detector, built to remove pions and protons from the main trigger.

The gas utilized is C_4F_8O, which has an index of refraction of $n = 1.00135$ at a pressure of 1 atm [169]. This results in the thresholds for generating a signal due to various particles in the Čerenkov to be:

$$
\begin{aligned}
p_{\text{min}}^{e^{\pm}} &= 9.83\ \text{MeV} \\
p_{\text{min}}^{\pi^{\pm}} &= 2.69\ \text{GeV} \\
p_{\text{min}}^{p} &= 18.05\ \text{GeV}.
\end{aligned}
\tag{3.28}
$$

The tank is has dimensions of $60 \times 80 \times 200\,\text{cm}^3$ and houses twenty spherical focusing mirrors in two columns of ten. The mirrors are 31 cm wide and 21 cm tall, with a radius of 116 cm and a focal length of 58 cm. Čerenkov light incident upon these mirrors is reflected onto a corresponding secondary mirror, 24 cm wide and 21 cm tall. These mirrors then direct the Čerenkov light onto the face of a corresponding PMT. To boost the amount of light collected, each PMT was fitted with a Winston cone [182]. This extends the effective diameter of each PMT from five inches to eight inches. A diagram of the Čerenkov tank is shown in Figure 3.31.

The gas Čerenkov also played a role in the main trigger for BigBite (Sect. 3.8) in conjunction with the shower calorimeter (Sect. 3.7.6).

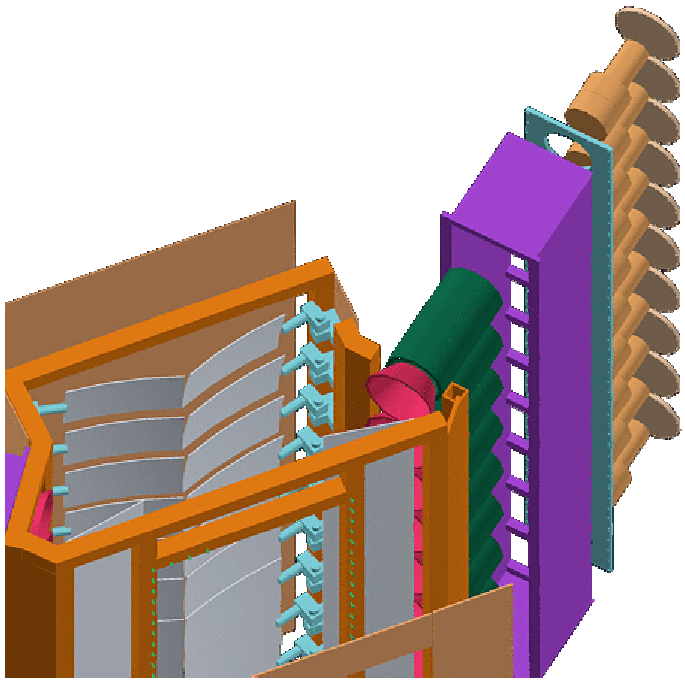

Figure 3.31: Exploded CAD diagram of the BigBite gas Čerenkov detector. The Winson cones are shown in red, and the PMTs are housed inside the green μ-metal shielding. Figure reproduced from [183].

3.7.5 Scintillating Plane

The scintillating plane in the detector package consists of 13 paddles of plastic scintillator, each of which has a PMT at each end with a timing resolution of 300 ps. Each paddle has the dimensions: $17 \times 64 \times 4\,\text{cm}^3$. The long dimension is transverse with respect to the scattered particles, while the short dimension is along the scattered particle path. This results in an active area of $221 \times 64\,\text{cm}^2$. The layout of the scintillating paddles is shown in Figure 3.32.

This plane provided an additional source of pion rejection to compliment the gas Čerenkov and the shower calorimeter, as the charged pions would leave a large signal in the low-end of the ADC spectrum (Sect. 5.3.4).

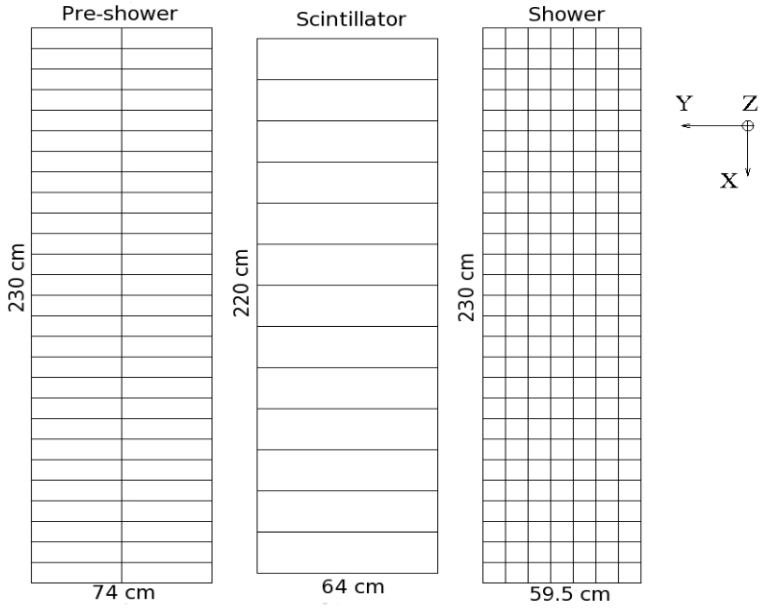

Figure 3.32: The orientation of the scintillating paddles along with the preshower and shower calorimeter blocks on the left and right, respectively. The detector coordinate system is also shown at the top-right of the diagram. Scattered particles from the target are incident normal to the page. Figure reproduced from [168].

3.7.6 Electromagnetic Calorimeter

The electromagnetic calorimeter works based on the same principles discussed in Section 3.6.6. It is used for rejecting pions and selecting electrons in the data analysis.

The calorimeter is composed of two layers of lead-glass blocks*. The first layer is the preshower, located 85 cm from the first drift chamber plane. It contains 54 blocks of

*The preshower blocks are made of TF-5 and the shower blocks are made of TF-2.

dimensions $8.5 \times 8.5 \times 35\,\text{cm}^3$. They are organized in two columns of 27 rows. The long dimension is oriented transverse with respect to scattered particles coming from the target. The shower layer, located 1 m from the first drift chamber, has 189 blocks of the same dimensions, but organized in seven columns and 27 rows. The long dimension of the block is oriented along the scattered particle path, giving more material for the particle to traverse, to ensure the capture of the full electromagnetic shower of the particle. The orientation of the two layers is shown in Figure 3.32.

Similar to the situation seen in the LHRS (Sect. 3.6.6), MIPs tend to deposit a small amount of their energy in the preshower and shower calorimeters; in particular, considering the density of TF-5 to be $\approx 4.77\,\text{g/cm}^3$ [169], a pion would deposit $\approx 60\,\text{MeV}$ in the preshower, and $\approx 300\,\text{MeV}$ in the shower calorimeter (made of TF-2, with a density of $\approx 4.09\,\text{g/cm}^3$). However, due to the various materials in between the MWDCs, gas Čerenkov, preshower and shower calorimeters, MIPs deposited $\approx 81\,\text{MeV}$ in the preshower and $< 350\,\text{MeV}$ in the shower [169].

The shower calorimeter also plays a role in the main trigger for BigBite, in addition to having its own trigger (Sect. 3.8).

3.8 Trigger Logic

With the large amount of data generating signals in the detectors, it is impossible to record all of it in a continuous fashion. To make the task of taking data more feasible, short *windows of time* are chosen during which the detectors are receptive to generated signals.

Triggers and their logic systems provide a way of determining "good events." In our case, this consists of the scattered electrons. There are eight triggers utilized by the Hall A data acquisition, some of which are used for troubleshooting purposes only. For instance, there is the trigger labeled T8 which is a pulser based on a 1024 Hz clock which has no physics attached to it. It is injected into the data stream to ensure that the electronics are working correctly. All of the triggers are listed in Table 3.9.

3.8.1 LHRS Triggers

The way in which the main LHRS trigger (T3) is generated is as follows: first, the PMTs of each paddle of S1 (S2m) are ANDed together, generating a signal for each paddle that has a hit. Then, the signals across the six (sixteen) paddles are ORed together to generate *one* signal for S1 (S2m). Finally, the signals for S1 and S2m are ANDed together to give the T3 trigger, whose timing is defined by the leading edge of the TDC* signal in the PMT

*LeCroy 1875 TDCs with a time resolution of 50 ps.

Trigger	Spectrometer(s)	Description
T1	BigBite	Low shower threshold
T2	BigBite	Overlap between T6 and T7
T3	LHRS	Overlap between S1 and S2m
T4	LHRS	Overlap between either S1 or S2m and Čerenkov
T5	LHRS, BigBite	Overlap of T1 and T3
T6	BigBite	High shower threshold
T7	BigBite	Gas Čerenkov
T8	LHRS, BigBite	1024 Hz Clock

Table 3.9: Triggers used during E06-014.

attached to the right side of the scintillator paddle [151]. From here, the T3 trigger is sent to the trigger supervisor (TS).

The way in which a T4 is generated follows closely to that which is seen for the generation of a T3 trigger. The only difference is that a T4 is generated when there is a logical AND between either S1 or S2m with the gas Čerenkov detector, but were vetoed by the T3 trigger. This trigger is used for studying the efficiency of the T3 trigger, as these events are potentially good events since they have a signal in the gas Čerenkov. It was found that the efficiency of the T3 trigger was 99.95% over the course of the experiment (Sect. 5.2.3).

A diagram of the trigger logic for a given spectrometer in Hall A is shown in Figure 3.33.

3.8.2 BigBite Triggers

There are four triggers associated with the BigBite spectrometer. The T1 trigger corresponds to the shower calorimeter; the T2 corresponds to an overlap of the shower and the gas Čerenkov, which serves as the main trigger in production running; T6 is another shower trigger; T7 is a gas Čerenkov trigger.

The T1 and T6 triggers work in a similar fashion. They are formed by taking the hardware (voltage) sum of the *cluster*[*] with the largest signal. This was done separately for the preshower and shower calorimeters. Their sum was then formed and sent to a discriminator. If this signal was greater than the threshold then the trigger is formed. The difference between T1 and T6 is that their thresholds may be set to different values[†]. The circuit logic of T1 and T6 is shown in Figure 3.34.

[*] A cluster is two rows of calorimeter blocks. There are 26 clusters for the preshower and shower calorimeters, respectively.

[†] The T6 threshold was set to $\approx$ 500–600 MeV. The threshold for the T1 trigger was set to $\approx$ 300–400 MeV [169].

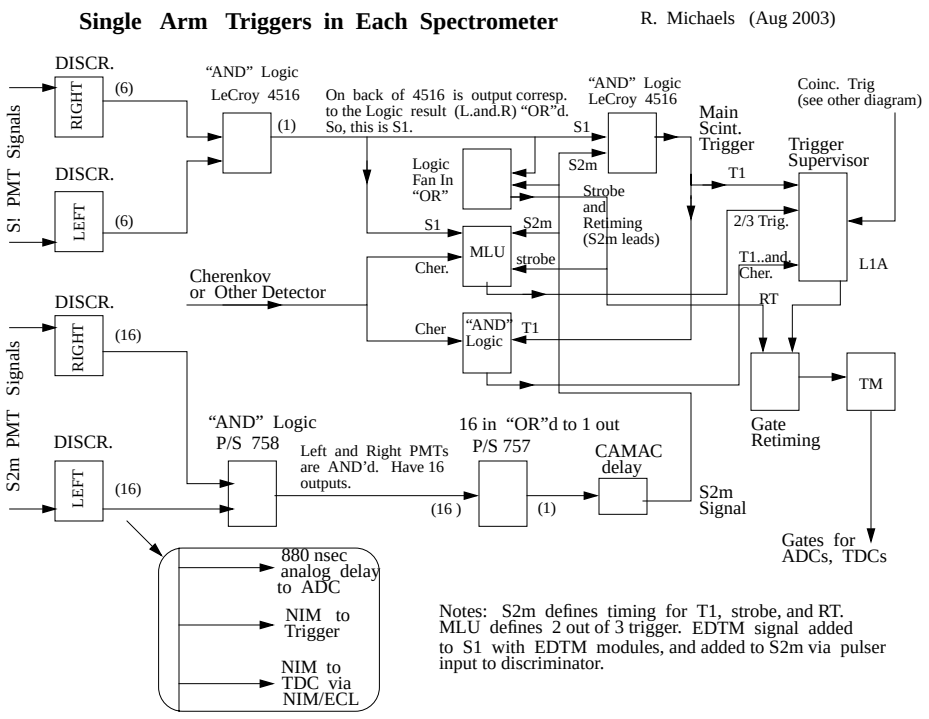

Figure 3.33: The logic diagram for single-trigger operation mode in an HRS in Hall A. In the diagram, T1 corresponds to E06-014's T3, and "2/3 trigger" corresponds to T4. Figure reproduced from [184].

The Čerenkov trigger works in a similar fashion to T1 and T6, but instead of clusters of lead-glass blocks, it considers clusters of mirrors*, see Figure 3.35. If any one of the mirror cluster signals is greater than the set threshold, then the T7 trigger is formed. The T7 trigger had a threshold of $\approx$ 1–1.5 p.e., but had a large prescale† factor assigned to it, resulting in no T7 events being written to disk.

The main trigger (T2) requires a *geometric overlap* of the shower and Čerenkov triggers. This geometric overlap is shown in Figure 3.36. We label the Čerenkov mirror clusters C1–C9 and the twenty-seven rows of preshower and shower blocks A–Z. Figure 3.36 shows which Čerenkov clusters overlap with which shower cluster. For instance, those events that fire the Čerenkov C1 cluster *and* fire any one of the A–E clusters in the calorimeter which overlaps with C1, then a T2 trigger is generated.

The triggers start the gates for the ADCs and provide the common stop for TDCs.

*There are 9 clusters of mirrors.

†A prescale factor restricts the number of events accepted for a given trigger. For example, a prescale of 100 means that one event per every 100 will be accepted. It is used to either remove certain types of events entirely, or to restrict events due to high rates.

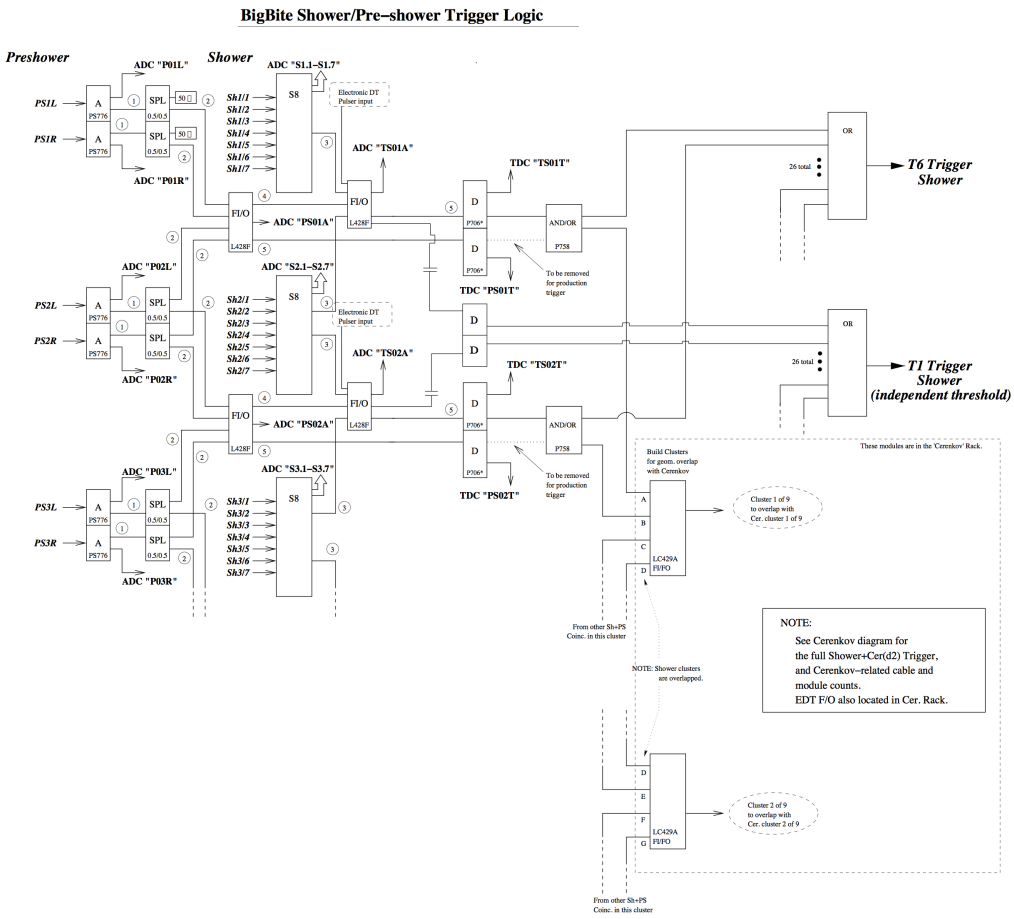

Figure 3.34: The T1 and T6 triggers corresponding to the BigBite shower. Figure adapted from [185].

Because of this, the timing of the various triggers needs to be consistent. To this end, the timing was chosen to be defined by the T6 trigger. This is shown in Figure 3.37.

3.8.3 Coincidence Trigger

The coincidence trigger (T5) is formed by an overlap *in time* of the T1 trigger from BigBite and the T3 trigger from the LHRS. T5 is characterized by the time-of-flight (TOF) and trigger formation times of the spectrometers. The TOF is determined by considering the detector's geometry and the kinematics of the particle to be detected. The trigger formation time depends upon the electronics schematics, in that one has to consider the time to propagate a pulser signal though the circuitry. Since these two things are generally not the same for each detector, such differences must be considered when determining the cabling and other electronics.

The LHRS T3 signal had a width of 140 ns which defined the coincidence window. The

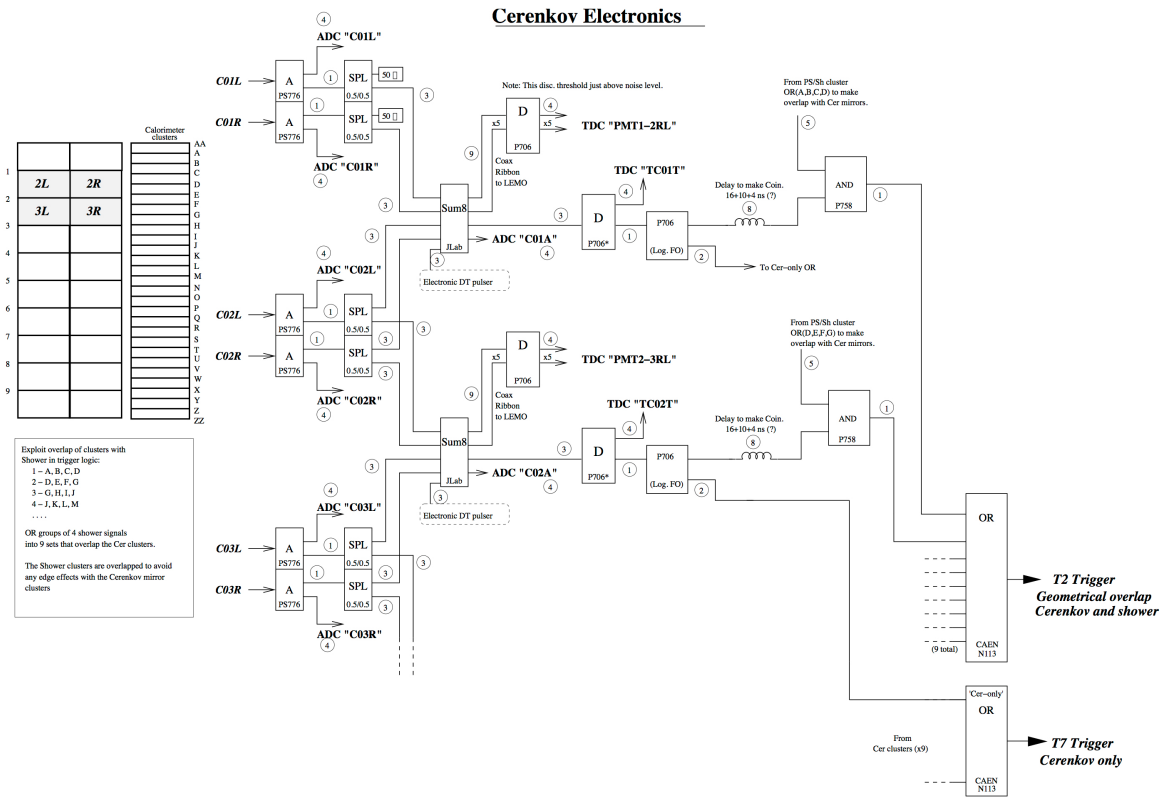

Figure 3.35: The T7 trigger corresponding to the BigBite gas Čerenkov. Figure adapted from [185].

BigBite T1 signal had a width of 40 ns, set to arrive 60 ns after T3. Therefore, T1 defined the timing of T5, see Figure 3.38.

The coincidence trigger is used for detecting events that occur simultaneously (or very nearly so) in the LHRS and BigBite. This is the case typically in semi-inclusive pion electro-production experiments where an electron is detected in one spectrometer in coincidence with a pion on another detector, for instance. Another case where this occurs is elastic scattering, where the electron is detected in coincidence with the recoiling target particle.

For E06-014, elastic scattering data on hydrogen and ^{3}He was taken for an electron beam of $E = 1.23$ GeV. These data were used as a check of the calibrations of our detectors. For the majority of these runs, the LHRS was set to positive polarity mode to detect protons, while BigBite was set to negative polarity mode to detect electrons. The ability to successfully produce the invariant mass spectrum for elastic scattering from a hydrogen target shows that our hardware and software are operating as expected (Sect. 4.2.2).

In production running, both the LHRS and BigBite were set to single-arm mode in negative polarity to detect electrons. The T5 trigger was disconnected from both detectors.

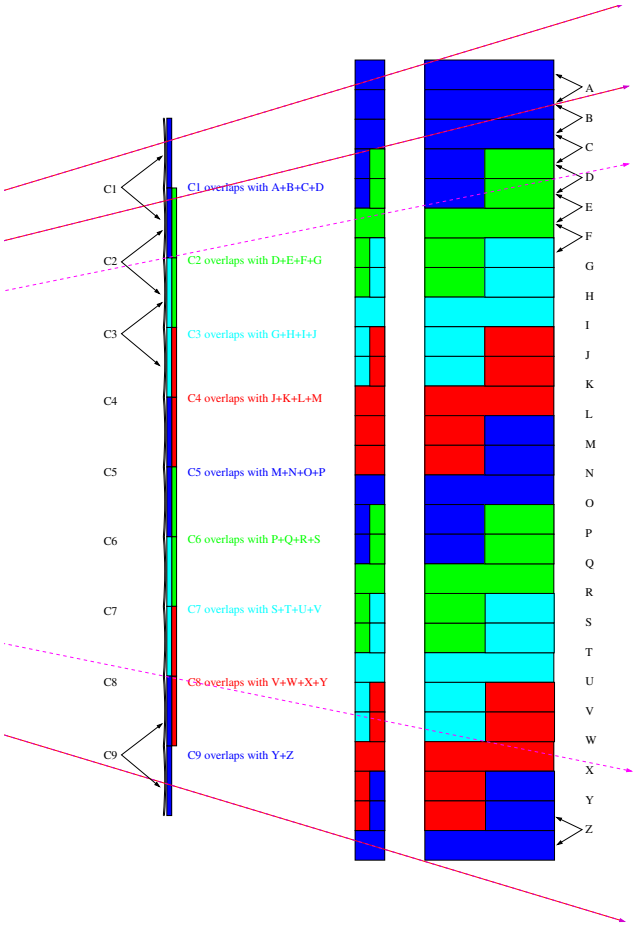

Figure 3.36: The main (T2) trigger in BigBite. The dashed lines show typical particle tracks through the detector. The matching colors show the which cluster of Čerenkov mirrors correspond to which shower blocks that would yield a T2 trigger. Figure reproduced from [185].

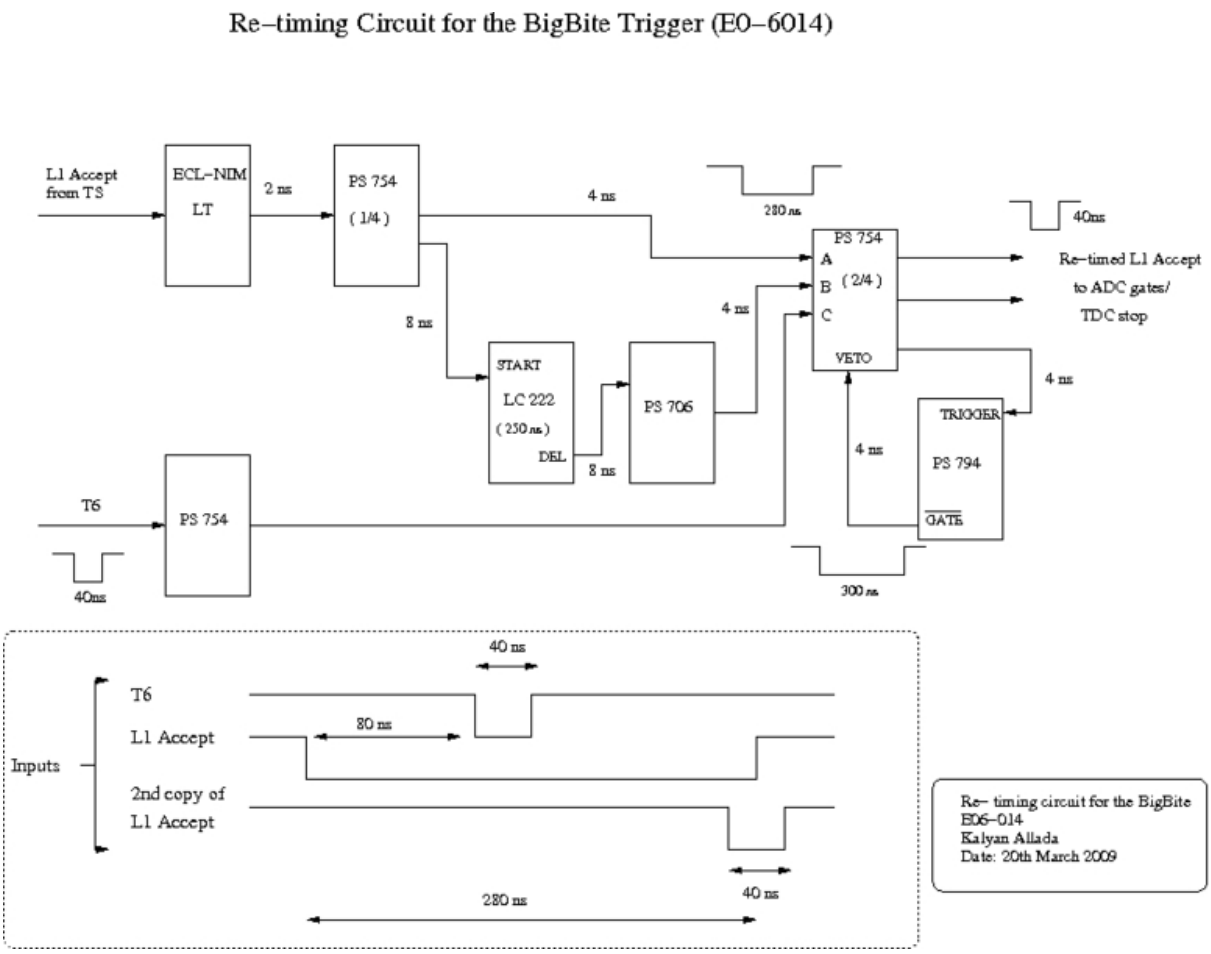

Figure 3.37: The retiming of the BigBite trigger. Figure reproduced from [186].

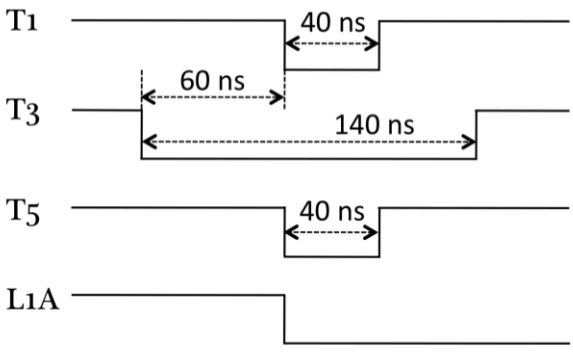

Figure 3.38: Coincidence trigger timing. Fiugre reproduced from [169].

3.9 Data Acquisition

A typical particle physics experiment generates a very large amount of data that needs to be managed in an organized and efficient way. This process is carried out and overseen by the data acquisition (DAQ) system. The voltages and signals of hundreds of PMTs corresponding to scattered electron detection and monitoring, along with spectrometer settings corresponding to the current through its magnet(s), momentum setting and more are monitored and recorded by the DAQ.

3.9.1 CODA

The CEBAF Online Data Acquisition system (CODA) interfaces with the Readout Controllers (ROCs), passing directions concerning how to process and handle the signals from modules such as Time-to-Digital Converters (TDCs) and Analog-to-Digital Converters (ADCs). These directions are C-based, encoded in control (.crl) files that are uploaded to the ROCs at the start of a *run*, which is a data-taking period for some given amount of time. Instead of taking data as one huge set, the experiment breaks the data into runs for distinguishability between different types of data sets and to minimize the probability of recording poor data if a problem should arise. Run sets also make the offline analysis procedure more streamlined and easier to identify potential issues.

Upon the receipt of the level-one accept (L1A, see Section 3.9.4), the front-end electronics are gated and timed, and the data is passed to the CODA event builder and written to disk.

The run control system effectively oversees CODA, providing control over runs. Shift workers may manipulate it via a graphical user interface (GUI) to start and stop runs. The various DAQ configurations may also be set from a specific GUI. Control files to be uploaded to the ROCs are stored here as well.

3.9.2 Scalers

So-called "scaler" events are responsible for counting raw signals generated from PMTs *without* dead time. From scaler events, raw counts and rates are obtained, and used for normalization purposes along with real-time monitoring of a number of parameters, including beam current, target temperatures, voltages, and so on. The LHRS and BigBite have separate scalers, as they may not necessarily have the same hardware, requiring unique setups. This configuration was inherited from the previous experiment, E06-010 [151].

The scalers are designed to be gated using the target spin and beam helicity states, yielding spin-spin dependent scalers. In this sense, there are four scaler combinations of the form ordered by the target spin (targ.) and beam helicity (hel.) given by (targ.,hel.): (+,+) or (pp), (+,-) or (pm), (-,+) or (mp) and finally (-,-) or (mm). A fifth configuration was spin independent.

Using the run gate obtained from the trigger supervisor (Sect. 3.9.4), the scalers are gated. The scaler gating scheme is shown in Figure 3.39; where the scaler event is formed from the logical AND between the run gate, target spin and beam helicity signals. These signals are sent to the control bit on S1S3800 for counting purposes [151].

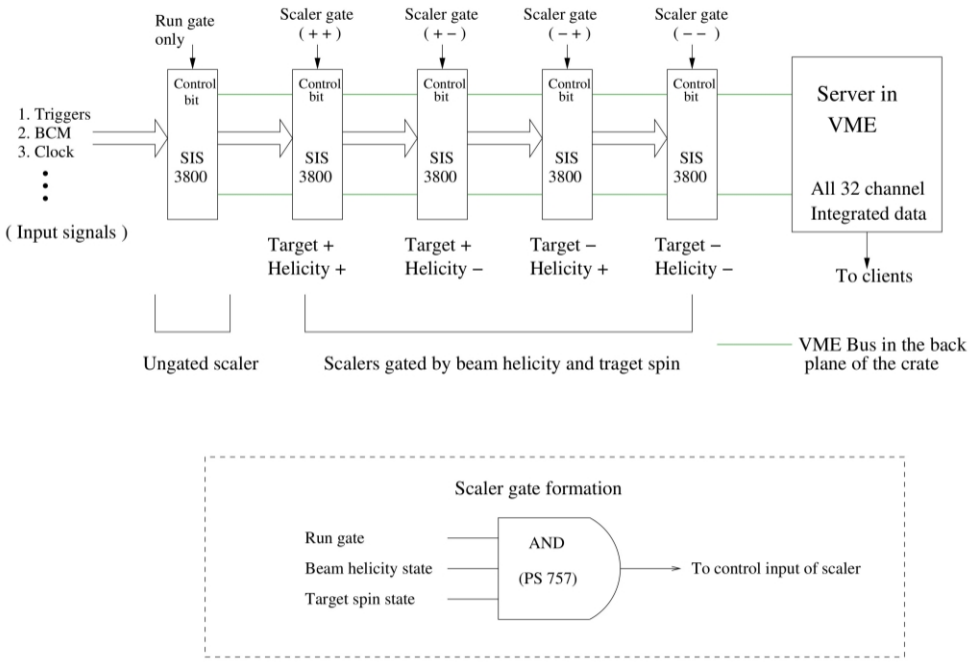

Figure 3.39: Scaler gating scheme for E06-010. In our experiment, the target spin state logic was always set to +1, see text. Figure reproduced from [151].

The main difference between the E06-010 setup and ours is that their target spin was flipped every 20 minutes, whereas we flipped the target spin every few days. Because of this, we did not need to gate the scalers by the target spin. As a result, the target spin-gated scaler was always set to +1. This resulted in two redundant scalers in the pp and mp settings.

3.9.3 EPICS

The Experimental Physics and Industrial Control System (EPICS), developed by a number of collaborations at universities and laboratories [187], is used for device control and slow

readout of parameters. It is designed to interface remotely with detectors and devices. In particular, the operating commands and instructions are altered via a GUI.

The parameters that are stored consist of scalers like high voltages, a spectrometer's central angle, mispointing, magnet currents and momentum settings, to name a few. A logger script prompts the various detectors for a given set of parameters and writes an "EPICS event" to data, which occurs every thirty seconds. Additionally, start-of-run and end-of-run summaries are posted to the electronic logbook (HALOG).

System monitoring is accomplished by processing alarms based on the parameter values from the detectors. These alarms manifest themselves as GUI-based notifications, accompanied by sounds.

3.9.4 Trigger Supervisor

The trigger supervisor (TS) effectively connects the ROCs to the triggering system, via a 9U multi-functional VME board and several ECL inputs [168]. There are eight input channels used for the eight triggers, labeled T1–T8.

The gating and timing of the front-end electronics is governed by the level-one accept (L1A). The process is as follows: the TS accepts multiple triggers from the various detectors and applies the prescale condition. If a trigger passes the prescale condition, the trigger bit pattern is set* and generates the L1A and the DAQ starts [188].

The trigger supervisor also monitors the ROCs such that there are no triggers accepted during the processing of the current trigger, allowing for the synchronization of the trigger system and the DAQ. This *non-extendable dead time* [176] prevents a "pile-up effect" that would occur if the trigger supervisor was allowed to accept triggers during the processing of events, known as extendable dead time.

3.10 Analysis Software

In order to analyze the data, it needs to be converted from a collection of TDC and ADC signals into meaningful data that describes the physics in terms of the kinematics and characteristics of the particles involved.

This conversion of raw data is realized by the C++-based software package ROOT [189], which is free under the GNU General Public License. ROOT is developed by CERN to simplify the processing of large data sets at the event level. There are also libraries available that allow for the visualization of data by plotting one-, two- and three-dimensional histograms of data.

*A multi-hit 1877 TDC with twelve channels, one for each trigger type.

The Hall A Analyzer [190], based on ROOT, handles the processing of our raw data. There are specific C++ classes written to interpret the data recorded by the various detectors and their sub-detectors. For instance, there are classes that convert the ADC signals registered in a calorimeter block into the corresponding amount of energy deposited. There are also classes that handle the rather complex computation of a particle's path (or track) through the LHRS up to its focal plane and its reconstructed position back at the target. This process occurs in a set of ROOT macros called "replay scripts," which parses the data and outputs so-called "ROOT files." These files store a variety of variables like ADC and TDC signals of detectors and kinematic variables like Bjorken-x and Q^2. Looking at histograms of these variables shows their event distributions. These ROOT files are useful for on-the-fly online analysis during the experiment to monitor the quality of the data and the performance of the detectors. Also, the framework of the Hall A Analyzer allows for a more in-depth offline analysis once the experiment is complete.

Offline analysis for the computation of physics observables like cross sections and asymmetries is accomplished by the user writing a number of ROOT macros that interface with these ROOT files and extracting the relevant quantities needed and then computing the observable of interest.

3.11 Run Summary

Our experiment started running after the E06-010 (Transversity) experiment. For their experiment, the LHRS was at 15° to the left of the beamline and BigBite was placed at 30° to the right of the beamline. Due to the very similar hardware setup to our experiment, it allowed for the sharing of knowledge and expertise on detectors and software, and an overlap of calibration data sets. In particular, the optics calibration data for Transversity was utilized in our data set for the LHRS.

The commissioning of E06-014 saw a move of the LHRS and BigBite to 45° to the left and right of the beamline, respectively. The target saw an installation of new target cells, while the DAQ was reconfigured for our setup; in particular, single-arm mode, where the LHRS and BigBite can run independently of one another. Coincidence running was still an option for calibration purposes. There was also the use of new detectors: a gas Čerenkov in BigBite and a Compton photon polarimeter was installed along the beamline. There was also the installation of a Compton electron polarimeter, but its commissioning proved to be unsuccessful.

A number of runs were done in coincidence mode taking elastic data on ^{3}He and H_2 targets. The LHRS was set to positive polarity to detect positively charged particles like

protons, while BigBite was set to negative polarity to detect negatively charged particles like electrons.

E06-014 saw high event rates, setting a Hall A record at 12 MB/s. The design limit of Hall A is 10 MB/s. These high event rates typically lead to high dead times in our detectors. To circumvent this issue, the beam current was lowered to 14 and sometimes 13 μA in coordination with setting the prescales of various triggers to appropriate values to achieve a reasonable rate.

The experimental program saw the collection of data for beam energies of 4.74 and 5.89 GeV. Due to the fact that there are two other experimental halls running simultaneously with our experiment, coordination with their runs is needed, since a beam energy change in one hall will affect the beam quality in another hall. To this end, our production data taking was staggered in the following way: one and a half weeks of highly polarized beam at 5.89 GeV; three days of minimally polarized beam at 4.74 GeV; one week of highly polarized beam at 5.89 GeV and finally one and a half weeks of moderately polarized beam at 4.74 GeV.

There were a number of issues encountered during the experiment. Early on in the running, it was noticed in histograms of the energy deposited in the BigBite shower calorimeter that there was a sizable gap in the acceptance. This turned out to be due to issues in the trigger electronics. A NIM bin was providing an insufficient amount of power to a particular set of summing modules for the shower signal. This lead to an absence of data in the event distribution at the face of the calorimeter. This was soon fixed, and the so-called "trigger-hole" is not present in the 4.74 GeV data set.

There were power fluctuations during a storm, which lead to damage to the central helium liquefier (which cools equipment cryogenically), LHRS high voltage systems and beamline equipment.

One of the biggest problems encountered was that there was an air leak into a cryomodule in the north linear accelerator (linac). This lead to moisture contamination which then spread to its neighboring cryomodules. The JLab Machine Control Center (MCC) decided to bring the affected modules to room temperature and remove them from the accelerator circuit. This resulted in the need for the beam to go through five passes in the accelerator ring to deliver a beam energy of 4.7 GeV, ultimately improving the quality of the beam relative to what was seen when the problem occurred.

As a result of the complications which delayed the experimental program, a week-long extension of the experimental run was requested and approved, allowing us to collect $\sim 80\%$ of the desired statistics.

CHAPTER 4

DETECTOR CALIBRATIONS

In this chapter, we discuss the detector calibration procedures employed for the various sub-detectors of the LHRS and the BigBite spectrometer.

4.1 LHRS

In this section we discuss the way in which the calibrations of the various sub-detectors of the LHRS were carried out. In particular, we discuss the VDC in Section 4.1.1; the optics in Section 4.1.2; the gas Čerenkov in Section 4.1.4; in Section 4.1.5 we discuss the pion rejector, and in Section 4.1.6 we discuss the scintillator calibration.

4.1.1 Vertical Drift Chambers

The principle of how the VDC operates is discussed in Section 3.6.3. A typical drift time spectrum of a given wire plane is shown in Figure 4.1, where the drift times of all wires in a plane are plotted in terms of a Time-to-Digital Converter* (TDC) spectrum. The TDCs in the VDC were operated in a common-stop mode, such that large TDC values correspond to short drift times. The various regions of this spectrum may be understood as follows (Fig. 4.1): for low TDC channels, and long TDC times (region A), particles have large-angle trajectories, and are therefore further away from the drift cell around the sense wires; in the middle range of the spectrum (region B), the electric field lines are parallel, and the drift velocity of the electrons are constant which corresponds to a relatively flat TDC response; towards large TDC channels and shorter times (region C), the electric field lines become quasi-radial near the sense wires; as a result, the probability of detecting a particle increases. In the region of the largest TDC channels and the shortest drift times (region D),

*A Time-to-Digital Converter is a device that converts a signal of pulses over a time interval into a digitized representation.

which corresponds to a region very close to the sense wires, drift velocities of electrons increases drastically. Here, the probability of detecting a particle is at the maximum.

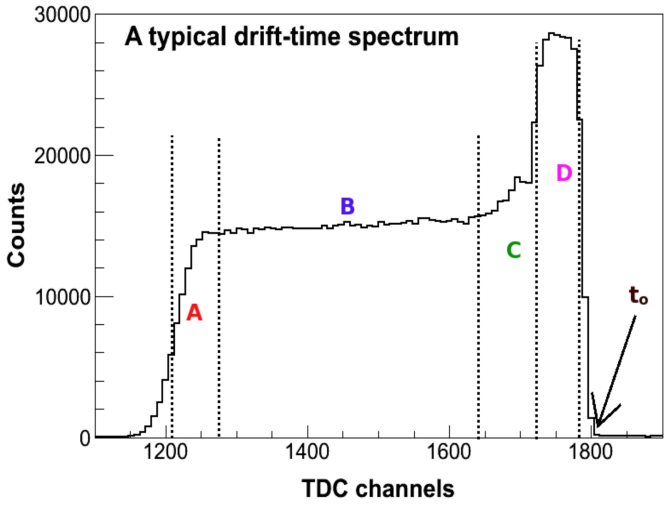

Figure 4.1: A typical drift time spectrum for a VDC plane. Reproduced from [168].

To utilize all the drift time spectra for each wire in a given plane, a reference time t_0 must be defined for each wire. This *time offset* t_0 accounts for and eliminates various timing offsets like differing cable lengths and signal processing times for a given wire. The calibration procedure, as performed by Chiranjib Dutta for the preceding E06-010 experiment [168], involves the determination of t_0 for each wire in each VDC plane and matching them to a common reference point. To determine the time offset for each wire, the derivative of the region of short drift times (large TDC channels, ~ 1800) was computed via a numerical procedure. The maximum slope was identified and extrapolated to the x-axis (channel axis) of the TDC spectrum (see the region labeled with t_0 in Figure 4.1). This procedure was done for each of the four planes in the two VDCs. A calibrated TDC spectrum is shown in Figure 4.2, where the time offset t_0 sits at 0 ns.

4.1.2 Optics

The main purpose of the optics matrix is to determine the coordinates of particles in the target coordinate system (TCS) from their corresponding coordinates in the focal plane coordinate system (FCS). In order to check how well our optics matrix performs this task, we need to check and understand certain characteristic plots and variables. Since we did not take data using the sieve collimator during the experiment due to time constraints, we can only examine the reconstructed z-vertex and will have to rely on another experiment's optics matrix, JLab E06-010 [159, 191].

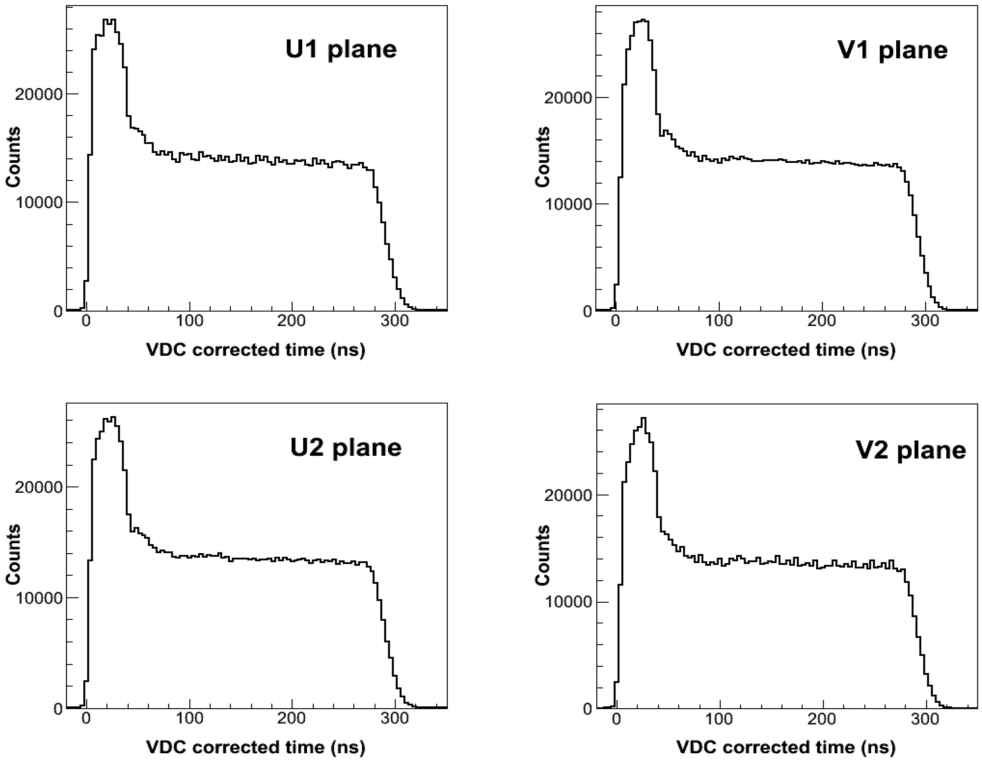

Figure 4.2: Calibrated time spectra for the VDC planes. Reproduced from [168].

4.1.2.1 The Optics Matrix

The mathematical relation between the TCS and the FCS is given by the matrix equation to first order, utilizing mid-plane symmetry of the LHRS:

$$\begin{pmatrix} \delta \\ \theta \\ y \\ \phi \end{pmatrix}_{tg} = \begin{pmatrix} \langle\delta|x\rangle & \langle\delta|\theta\rangle & 0 & 0 \\ \langle\theta|x\rangle & \langle\theta|\theta\rangle & 0 & 0 \\ 0 & 0 & \langle y|y\rangle & \langle y|\phi\rangle \\ 0 & 0 & \langle\phi|y\rangle & \langle\phi|\phi\rangle \end{pmatrix} \cdot \begin{pmatrix} x \\ \theta \\ y \\ \phi \end{pmatrix}_{fp} .$$

The optimization is typically done to 4^{th} order, where the matrix is given by:

$$\begin{pmatrix} \delta \\ \theta \\ y \\ \phi \end{pmatrix}_{tg} = \begin{pmatrix} \langle\delta|x\rangle & \langle\delta|\theta\rangle & \langle\delta|y\rangle & \langle\delta|\phi\rangle \\ \langle\theta|x\rangle & \langle\theta|\theta\rangle & \langle\theta|y\rangle & \langle\theta|\phi\rangle \\ \langle y|x\rangle & \langle y|\theta\rangle & \langle y|y\rangle & \langle y|\phi\rangle \\ \langle\phi|x\rangle & \langle\phi|\theta\rangle & \langle\phi|y\rangle & \langle\phi|\phi\rangle \end{pmatrix} \cdot \begin{pmatrix} x \\ \theta \\ y \\ \phi \end{pmatrix}_{fp} ,$$

where the target (tg) variables are: δ is the fractional momentum reconstructed at the target, given as $(p-p_0)/p_0$, and p_0 is the momentum setting of the spectrometer; θ_{tg} is the scattering angle in the dispersive direction, in radians; ϕ_{tg} is the horizontal scattering angle,

in radians; y is the horizontal position, in meters. The variables corresponding to the focal plane (fp) coordinate system are: x_{fp}, the vertical position in meters, and corresponds to δ in the TCS; θ_{fp} is the scattering angle in the dispersive direction in radians, and corresponds to θ_{tg} in the TCS; ϕ_{fp} is the horizontal scattering angle, and corresponds to ϕ_{tg} in the TCS; y_{fp} is the horizontal position in the focal plane in meters, and corresponds to y_{tg} in the TCS. Explicit calculations of each variable yield:

$$\delta = \sum_{j,k,l} D_{jkl}\theta_{fp}^{j} y_{fp}^{k} \phi_{fp}^{l} \tag{4.1}$$

$$\theta_{tg} = \sum_{j,k,l} T_{jkl}\theta_{fp}^{j} y_{fp}^{k} \phi_{fp}^{l} \tag{4.2}$$

$$y_{tg} = \sum_{j,k,l} Y_{jkl}\theta_{fp}^{j} y_{fp}^{k} \phi_{fp}^{l} \tag{4.3}$$

$$\phi_{tg} = \sum_{j,k,l} P_{jkl}\theta_{fp}^{j} y_{fp}^{k} \phi_{fp}^{l}, \tag{4.4}$$

where the tensors D_{jkl}, T_{jkl}, Y_{jkl} and P_{jkl} are polynomials in the focal plane track-x variable x_{fp}:

$$D_{jkl} = \sum_{i} C_{ijkl}^{D} x_{fp}^{i} \tag{4.5}$$

$$T_{jkl} = \sum_{i} C_{ijkl}^{T} x_{fp}^{i} \tag{4.6}$$

$$Y_{jkl} = \sum_{i} C_{ijkl}^{Y} x_{fp}^{i} \tag{4.7}$$

$$P_{jkl} = \sum_{i} C_{ijkl}^{P} x_{fp}^{i}. \tag{4.8}$$

4.1.2.2 Matrix Optimization

We have made use of the optics matrix that was optimized for the E06-010 analysis, which had a very similar detector setup compared to our experiment. Jin Huang has written extensive code and documentation to carry out the procedure of optimization [192], which follows the procedure outlined in [193]. The optimization consists of three main components: z-target vertex calibration, the angular calibration and momentum calibration. Here, we briefly describe the procedures associated with each.

The z-target vertex reconstruction is optimized by considering runs with a multi-foil carbon target. The known positions of the foils are used to align the reconstructed peaks

seen in the z-target event distribution. The average resolution achieved for z-target was ≈ 6 mm [181].

For the angular calibration, which corresponds to optimizing the out-of-plane angle θ_{tg} and in-plane angle ϕ_{tg}, carbon foil targets are used with a sieve-slit inserted in front of the spectrometer. Good events that are detected correspond to scattering from a specific carbon foil and passing through a certain hole in the sieve-slit. Comparing these detected events to the locations of the individual carbon foils and the holes in the sieve-slit via survey reports [194]*, which allows one to see how well the optics matrix does in reproducing the proper positions of the target and sieve-slit. Optimization in this case refers to the minimization of the deviation of the data from these surveyed positions of the target and sieve-slit.

The momentum calibration calls for using a similar run set. The full range of momentum is covered via a so-called "δ-scan" where the carbon elastic peak is moved across the focal plane in discrete momentum steps of a few percent. This is done for each momentum setting needed for the experiment, where a given ground state or excited state of carbon is examined. The final momentum resolution obtained was $< 5 \times 10^{-4}$ [181].

4.1.2.3 Reconstruction of the Reaction Vertex

In order to see if the optics matrix is properly transforming the focal plane variables into the target variables, we examine the plot of the reaction vertex variable z_{react} for a run for which a multi-carbon foil target was used. A plot of this quantity shows the position of each foil, which we may compare to their respective nominal positions as determined from the survey data.

Figure 4.3 shows z_{react} using the optics matrix that was used during the running of the experiment. The peaks seen here are the positions of the carbon foils, while the red vertical lines are the surveyed positions of the foils. We observe that the positions are not correctly reconstructed, which indicates that our optics matrix needs to be optimized.

Upon utilizing E06-010's optics matrix, we obtain the plot shown in Figure 4.4. We see that the positions of the Carbon foils are in much better agreement with their corresponding positions from survey data. The effect of the new matrix may be seen in Table 4.1.

4.1.3 Event Selection

Before we investigate the calibration of our detectors, we need to make sure that we are choosing good events for our study. Below is a list of the cuts used to define good events

*Survey reports document the physical locations of various components of the targets and detectors in the hall.

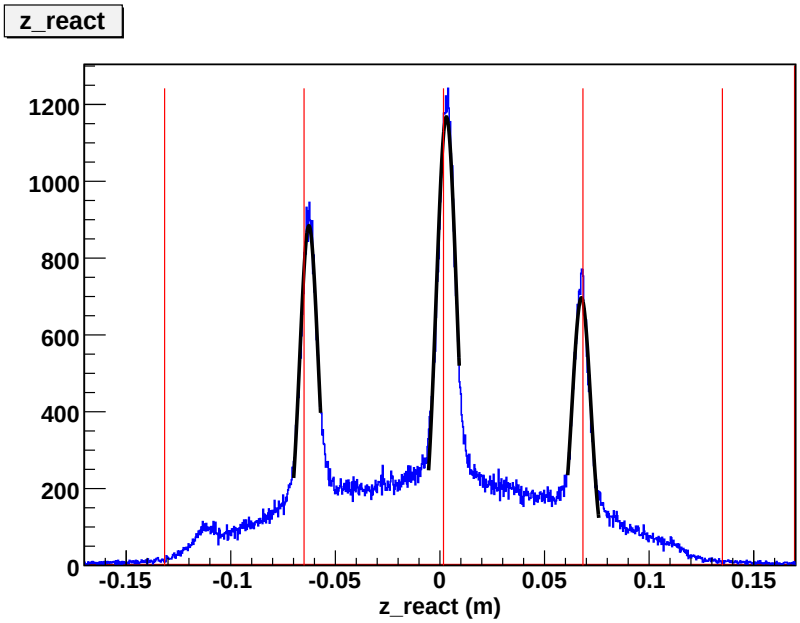

Figure 4.3: Reconstructed z-vertex using the optics matrix utilized during the running of the experiment. We see that the positions of the peaks are slightly off to the left for some peaks, while for others they are slightly off to the right. It is also seen that the leftmost peak's reconstruction is quite far from its surveyed position.

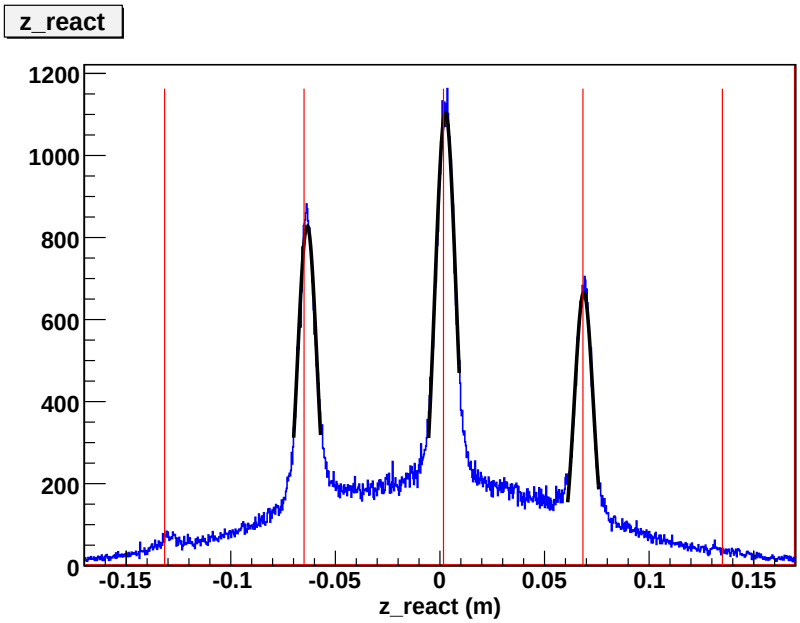

Figure 4.4: Reconstructed z-vertex using the optics matrix optimized and utilized for the Transversity data analysis. We see that the positions of the reconstructed peaks are in much better agreement with their corresponding surveyed positions.

Old Optics Matrix Results		
Peak Number	Position (mm)	Width (mm)
1	-62.65 ± 0.04	4.42 ± 0.05
2	3.08 ± 0.04	4.83 ± 0.05
3	67.64 ± 0.04	4.45 ± 0.05
New Optics Matrix Results		
1	-63.47 ± 0.04	4.63 ± 0.06
2	2.62 ± 0.04	5.05 ± 0.05
3	68.75 ± 0.04	4.49 ± 0.05

Table 4.1: Main peak positions and their respective widths before and after the utilization of the Transversity optics matrix. The peaks are labeled $1,2,3$ when going from left to right in Figs. 4.3 and 4.4. Errors shown are calculated as the uncertainties of the Gaussian fits used to extract the peak positions.

in our detectors:

- *trigger cuts*:
  (DL.edtpl==0)&&((DL.evtypebits&(1<<3))==(1<<3))

- *VDC cuts*:
  L.tr.n==1
  (L.vdc.u1.nclust==1)&&(L.vdc.v1.nclust==1)
  (L.vdc.u2.nclust==1)&&(L.vdc.v2.nclust==1)

- *cuts on acceptance*:
  (abs(L.tr.tg_y)<0.04)
  (abs(L.tr.tg_dp)<0.035)
  (abs(L.tr.tg_th)<0.05)&&(abs(L.tr.tg_ph)<0.03)

The first cut requires that the electronic deadtime pulse is excluded in the analysis. The second cut ensures that we have events that have produced a (main) trigger. This corresponds to a trigger word, a byte of information that encodes the value of each trigger (1 if fired, 0 if not fired) as a single bit; requiring the trigger bit corresponding to the T3 trigger being set to 1 selects T3 events; all other trigger types are rejected.

For the VDC cuts, in addition to requiring one-track reconstruction of one particle from the target, we also apply cuts to the VDC planes. This cut means that we make sure that only one cluster fired in each of the VDC planes as the particle passed through them [195]. This, together with requiring one-track reconstruction, assures that we are examining a good track corresponding to one particle.

The cuts on y-target, $\delta p/p$, θ, and ϕ are utilized to remove bad events that originate in the target's glass endcaps. These variables are defined in the target coordinate system.

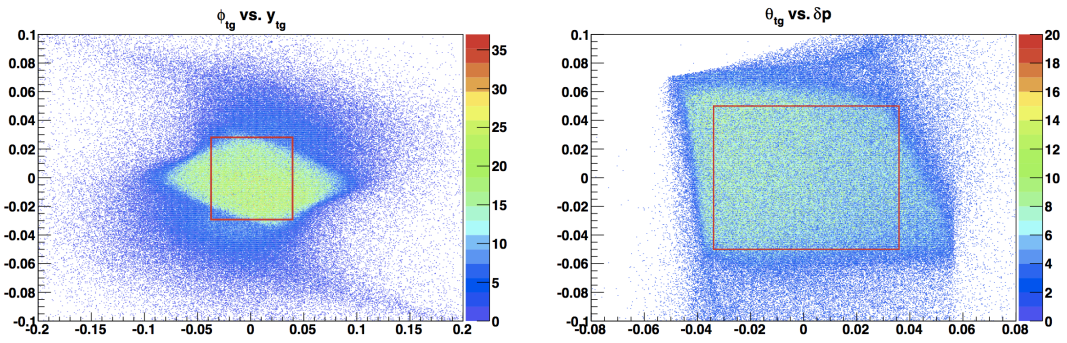

(a) ϕ_{tg} vs. y_{tg} (b) θ_{tg} vs. δp

Figure 4.5: (a) shows ϕ_{tg} vs. y_{tg}. The red box indicates the cut. Events inside the box pass the cut. Similarly, (b) shows θ_{tg} vs. δp with the chosen cut.

The variable y-target is the target's y-coordinate; the θ variable refers to the tangent of the θ angle, which is out of the scattering plane; the ϕ variable refers to the tangent of the ϕ angle, which is in the scattering plane. The quantity $\delta p/p$ ensures that the particle has a good momentum value, within $\pm 3.5\%$ of the momentum setting of the LHRS. Figure 4.5 shows how these cuts are determined for each variable. It should be noted here that these cuts are not the final cuts for the acceptance. Those will be determined in Section 5.2.5.

All of the cuts mentioned here will be applied to all analyses to follow in this section unless otherwise mentioned.

4.1.4 Gas Čerenkov

4.1.4.1 ADC Calibration

The calibrations needed for the gas Čerenkov detector correspond to making sure that each PMT has the same response for a given signal. This amounts to aligning the single photo-electron peak at an arbitrary channel in its ADC distribution. The single p.e. peak describes the response of the tube to a single photon, and was calibrated to 200 channels in the ADC for each PMT so that they each have the same response. This was done for each data set. A set of gain-matching coefficients were produced and added to the analysis database. They were calculated by: $a_{\text{new}} = a_{\text{old}}\,[c_{\text{new}}/c_{\text{old}}]$, where a_{old} is the old database gain-matching coefficient; a_{new} is the new coefficient; the quantities c_{new} and c_{old} are the peak locations in units of ADC channel numbers. The results are shown in Figure 4.6.

In our cross section and asymmetry analysis, we will utilize the gas Čerenkov ADC sum variable, which is a software sum of the ten ADC signals shown in Figure 4.6. A typical ADC sum is shown in Figure 4.7.

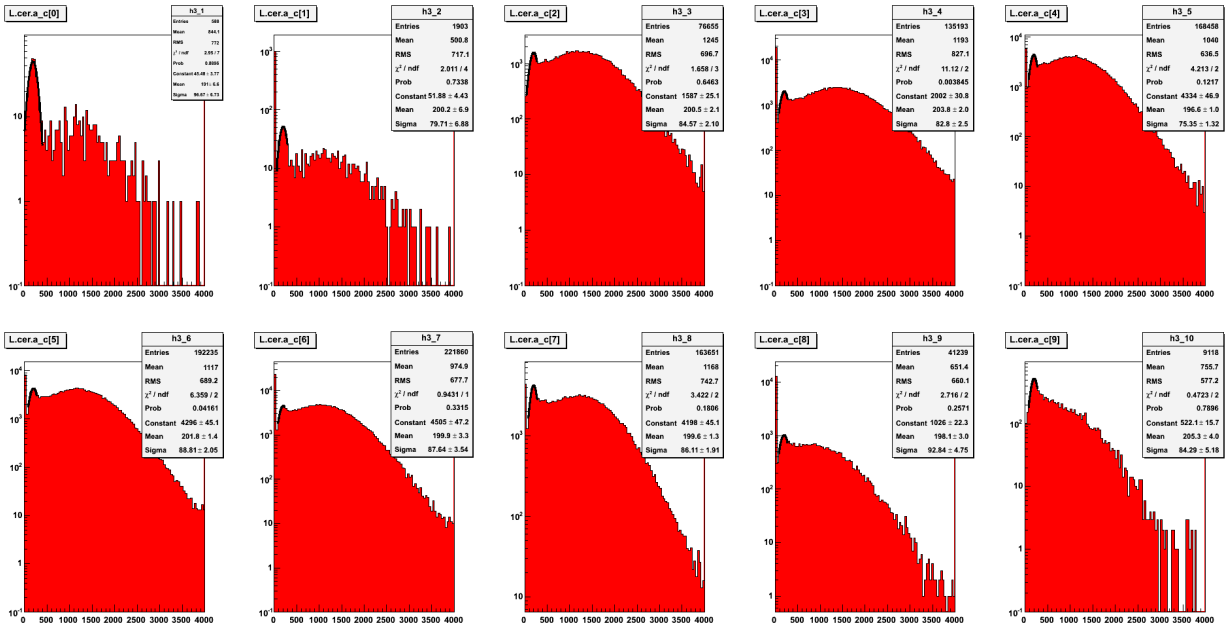

Figure 4.6: The ADC spectra for each PMT after calibration. A fit to the one photo-electron peak shows the peak position in the upper right window of each plot. This data is presented in more detail in Table 4.2.

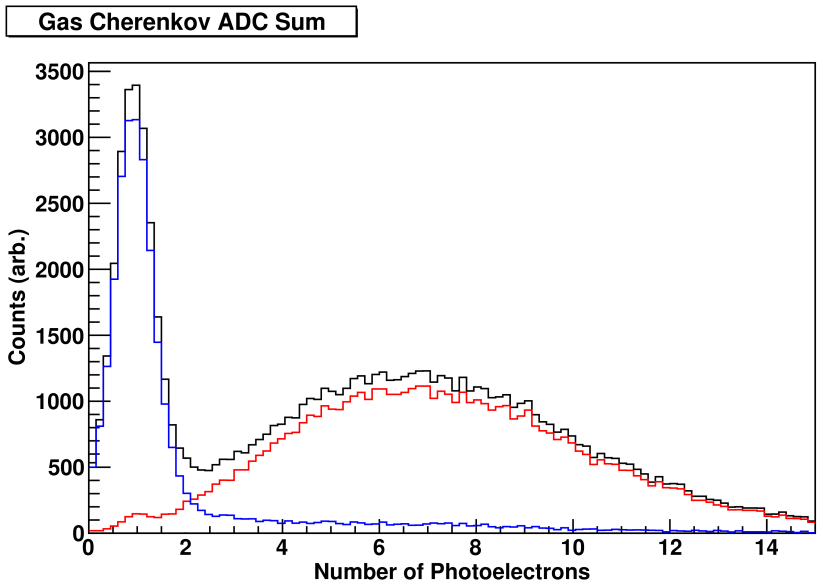

Figure 4.7: A typical gas Čerenkov ADC software sum after calibration. This is the histogram that is cut on to choose electrons in our analysis. Cuts on the pion rejector E/p distribution reveal the background (blue) and electrons (red). Section 4.1.5 discusses the E/p distribution.

4.1.4.2 PMT Performance

To investigate the performance of each PMT, we examine the position of the main peak in each ADC spectrum. This main peak is the average photo-electron yield for its corresponding PMT. To examine the main peak explicitly, we first look at the tracking variables in the plane of the Čerenkov detector. Figure 4.8 shows the tracking variables in the plane subject to cuts on the individual TDC spectra for each PMT, an example of which is shown in Figure 4.9. Such a TDC cut reveals the locations of each particular mirror which views the PMTs. In particular, a tight cut on one of the mirrors yields what is shown in Figure 4.10. Taking the peak value shown in the green histogram and dividing this by our (calibrated) one photo-electron peak yields the average number of photo-electrons for that particular PMT. This procedure was carried out for each of the ten PMTs. Table 4.2 shows the results.

The stability of the gas Čerenkov throughout the experiment is discussed in Section 5.2.1.1.

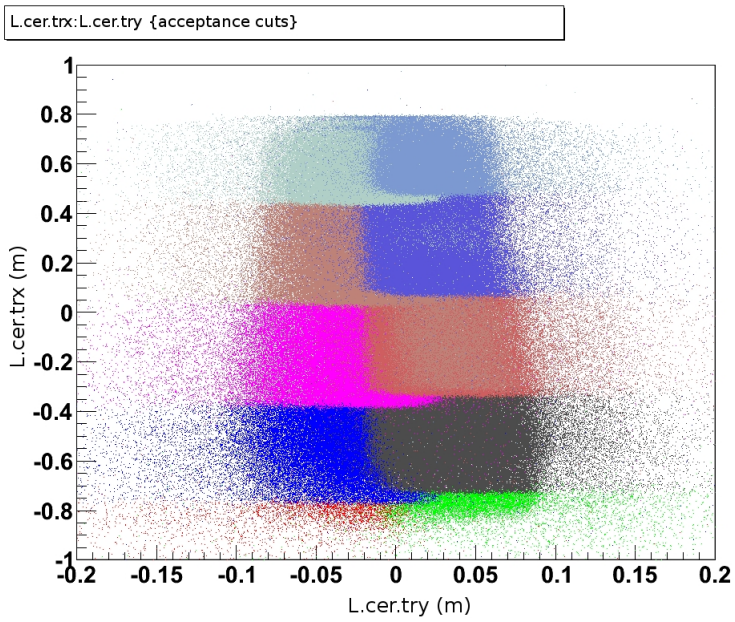

Figure 4.8: A plot of the tracking variable x against tracking variable y in the Čerenkov detector plane. The detector coordinates call for the x variable to be along the vertical axis. The colored regions show the locations of all ten Čerenkov mirrors in the detector plane. We can see that the bottom two mirrors have very low statistics, indicating that they are on the edge of the acceptance.

4.1.5 Pion Rejector

Electrons impinging upon the blocks of a calorimeter induce an electromagnetic shower that is typically spread across multiple blocks. Therefore, to accurately determine how

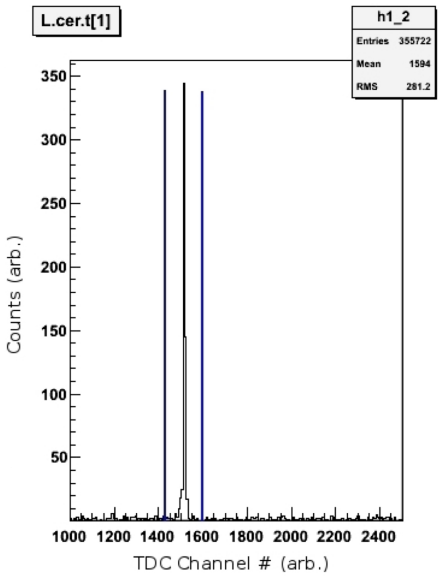

Figure 4.9: A typical gas Čerenkov TDC spectrum. The main peak corresponds to electron events, while the uncorrelated (in time) background events are scattered across the whole range. It is seen that the background in the TDC spectrum is quite small in the LHRS. The cut window used in the analysis is shown as the two blue vertical lines. Events that fall within the window are accepted.

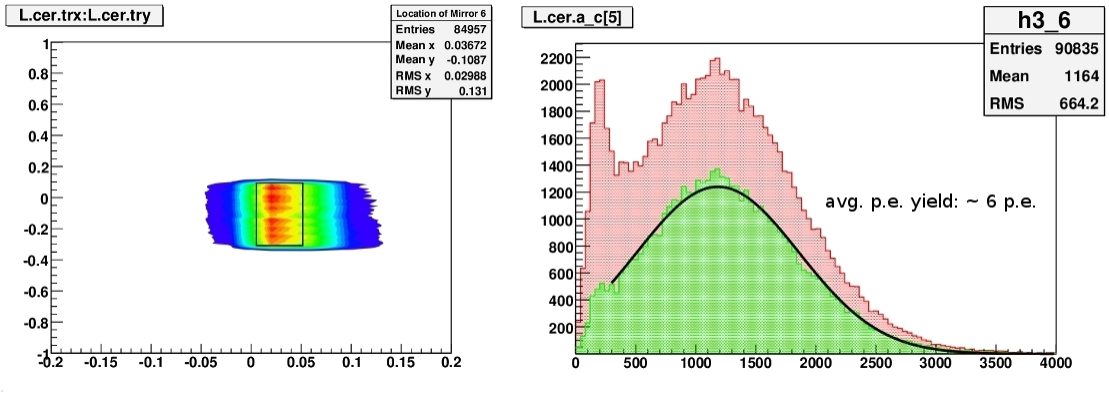

Figure 4.10: The plot on the left shows the tracking variables in the Čerenkov detector plane subject to a TDC cut for a particular PMT. Choosing the tight selection in this plot picks out the main peak in the corresponding ADC spectrum, shown on the right.

much energy is deposited by an electron, a sum over these groups of blocks, or *clusters*, must be done. In particular, a cluster is identified by a central block which sees the largest energy deposit. For the pion rejector, this sum is taken over the four blocks surrounding the block that had the largest energy deposit, for a total of five blocks. Only the largest cluster is considered in the algorithm used in the LHRS software. The energy E of the cluster is then given as the sum of all energies in the blocks of the cluster:

Table 4.2: The one photo-electron peak alignment and average photo-electron yield for each mirror (PMT) of the gas Čerenkov. The error bars are statistical.

Mirror	1 p.e.	$n_{\text{p.e.}}$	# p.e.
1	191.0 ± 6.6	1084.0 ± 27.9	5.7 ± 0.0
2	200.2 ± 6.9	925.3 ± 15.9	4.6 ± 0.1
3	200.5 ± 2.1	1292.0 ± 7.3	6.4 ± 0.0
4	203.8 ± 2.0	1430.0 ± 5.1	7.0 ± 0.0
5	196.6 ± 1.0	1125.0 ± 3.8	5.7 ± 0.0
6	201.8 ± 1.4	1189.0 ± 4.8	5.9 ± 0.0
7	199.9 ± 3.3	1086.0 ± 4.8	5.4 ± 0.1
8	199.6 ± 1.3	1300.0 ± 4.0	6.5 ± 0.0
9	198.1 ± 3.0	1081.0 ± 6.7	5.5 ± 0.0
10	205.3 ± 4.0	1012.0 ± 7.5	4.9 ± 0.0

$$E = \sum_{i=1}^{N} E_i, \tag{4.9}$$

and the *x*-*y* position of the particle in the plane of the pion rejector is determined from an energy-weighting method:

$$X = \sum_{i=1}^{N} \frac{E_i}{E} X_i \tag{4.10}$$

$$Y = \sum_{i=1}^{N} \frac{E_i}{E} Y_i. \tag{4.11}$$

The pion rejector is designed to separate electrons from pions based upon their differing energy depositions. Exploiting this difference, we can choose electrons and reject pions for our analysis.

To calibrate the pion rejector, we gain-matched the ADC spectra of each block to the same channel number for a particular peak. This is similar to what was done for the gas Čerenkov. Here, we align the *pion* peak to 100 ADC channels. Pions were isolated in the pion rejector by choosing a cut on the gas Čerenkov ADC sum spectrum to be less than 2.5 photoelectrons. Pions were utilized in this study as they deposit approximately the same amount of energy in each of the two layers of the pion rejector [35]. The result of the calibration of the block ADCs is shown in Figure 4.11.

As a consequence of the calibration, the ratio of the total energy deposited in the pion rejector layers E divided by the reconstructed momentum of the track p (the E/p distribution) for pions falls at values such that $E \sim 180\,\text{MeV}$. For electrons, the distribution peaks

at $E/p \sim 0.8$. This gives a good separation for removing the unwanted pion events from the data. The results are shown in Figure 4.12.

In order to understand the resolution of the pion rejector, the electron distribution in E/p is fit to a Gaussian. Its standard deviation (σ) is then obtained. Figure 4.13 shows σ/p as a function of p for all kinematics. This distribution is fit to: $f(x) = a_0 + a_1/\sqrt{x}$. The a_1 parameter gives the resolution of the pion rejector. From our fit, it is seen that it is $\sim 18\%$. Since this is not a full shower, the resolution is not expected to be as good as the expected value of 5% for a full shower [35].

The stability of the E/p distribution over the whole experiment is discussed in Section 5.2.1.2.

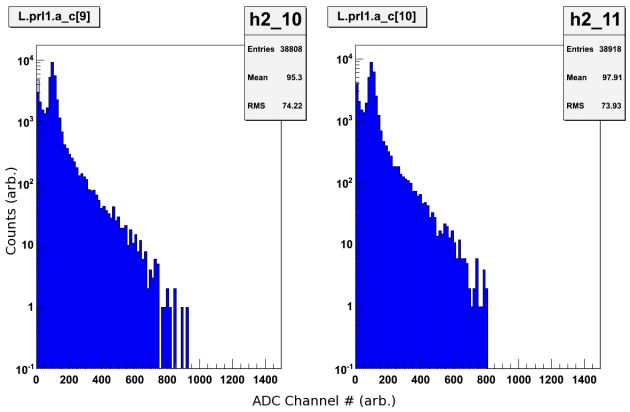

Figure 4.11: Examples of calibrated block ADC spectra in the pion rejector. Shown here are the calibrated pion peaks to 100 channels. Pions are chosen by a cut of less than 2.5 photoelectrons in the gas Čerenkov.

4.1.6 Scintillators

Since the scintillators provide the main trigger of the LHRS (Sect. 3.8), it is important that the timing information encoded in the TDCs is correct. To this end, each of the right-hand side TDCs of the S2m paddles were aligned to an arbitrary value, since it is these TDCs of this plane that define the timing*. Then, the left-hand side TDCs were aligned to the right ones. As long as the timing across the whole plane is consistent, then the value of the time chosen as the point of alignment does not matter. After this is done, the same procedure of aligning the peaks was done for the S1 TDC times. The results of this study are shown in Figure 4.14.

*The TDC times seen in the S1 plane are defined relative to the S2m plane.

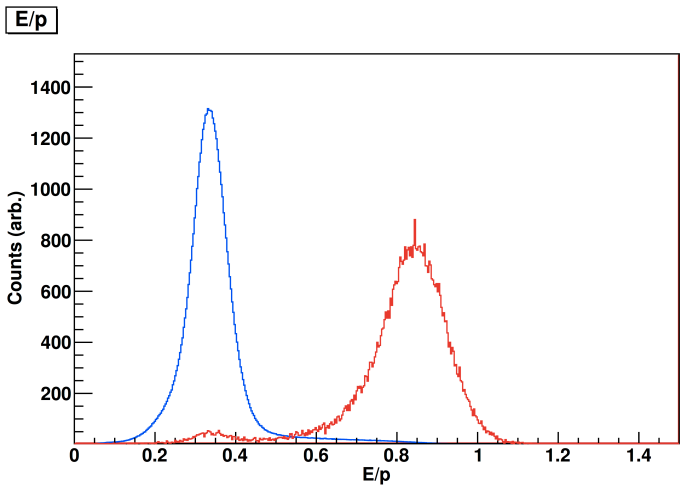

Figure 4.12: A calibrated E/p spectrum. Shown are the pion (blue) and electron (red) distributions. The pion curve is scaled down so it can be viewed on the same scale as the electron curve. Pions (electrons) are chosen by a gas Čerenkov cut less (greater) than 2.5 photoelectrons.

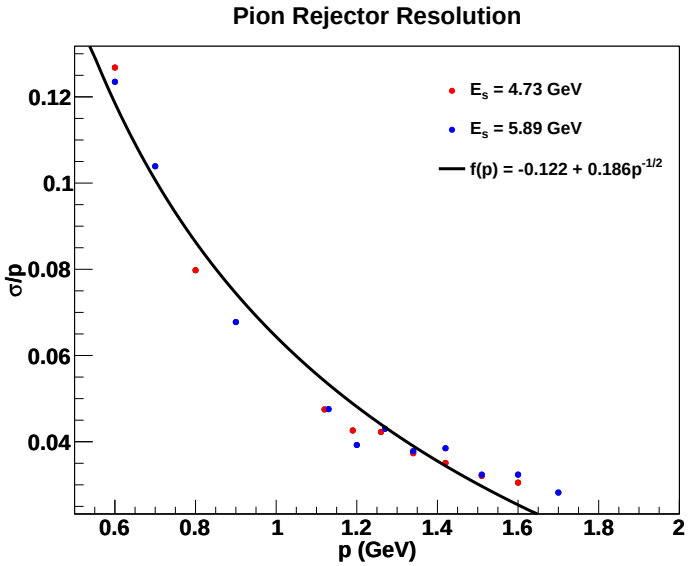

Figure 4.13: The resolution of the pion rejector as a function of p. The width of the electron peak divided by p is fit to the function shown. The parameter that multiplies $1/\sqrt{p}$ gives the resolution.

It can be seen in Figure 4.14 that the β distribution as a function of tracking variable x is not perfectly flat, with a small blip towards the positive values of track-x. This is due to "jitter" in the S1 TDC times as a function of track-x, despite the alignment of the S1 TDC peaks [196]. What occurs is that for events that have hits in S1 paddle i corresponding to hits in S2m paddles j or $j \pm 1$, the time differences $\Delta t_{i,j}$ and $\Delta t_{i,j\pm1}$ are *not* the same, despite

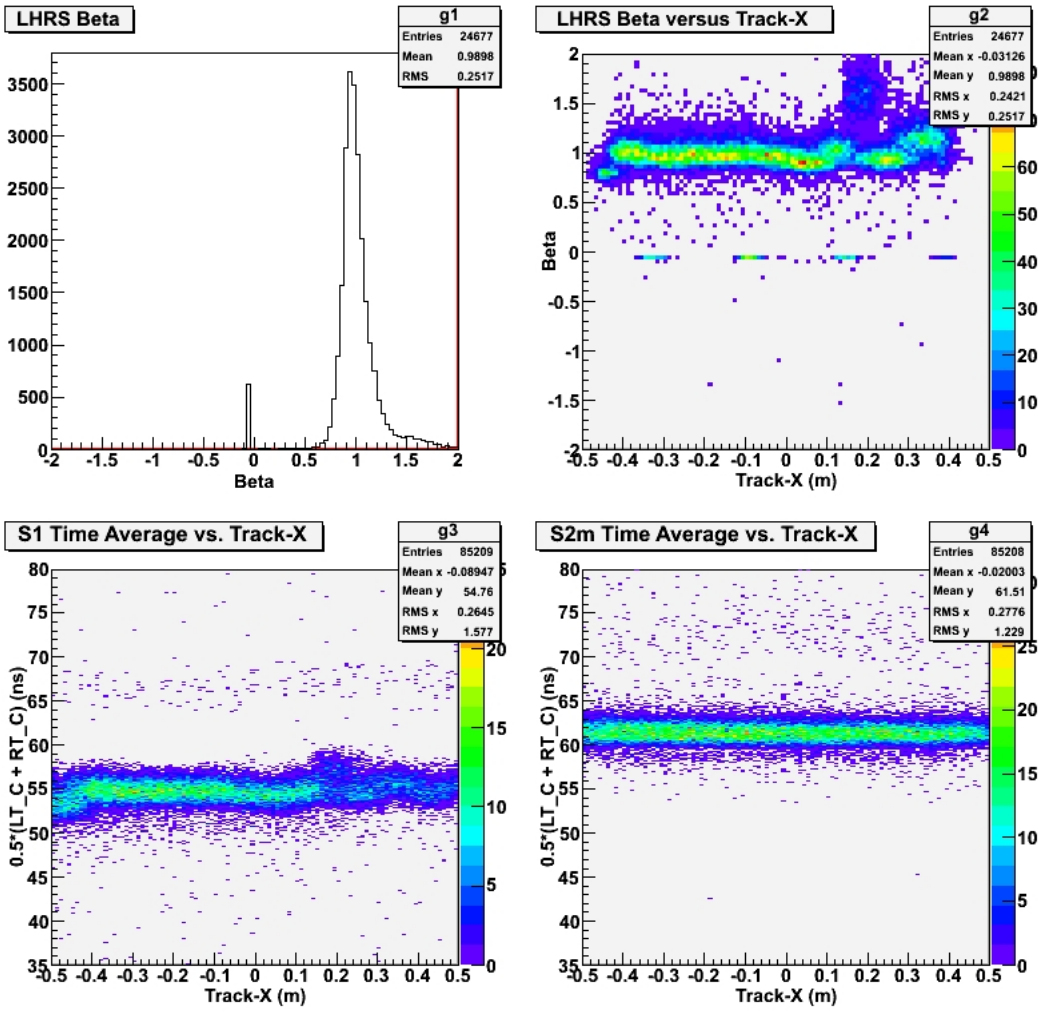

Figure 4.14: The results of the calibration of the S1 and S2m TDC times. The top left panel shows the β distribution. The top right shows β as a function of track-x; The bottom left and right panels show the S1 and S2m TDC time averages as a function of track-x.

the calibrations of both the S1 and S2m TDC times. This time difference contributes to the variable β. A cut on the β variable is used in the cross section analysis; however, the cut is a loose one (Sect. 5.2.2.7), so it was not needed to apply a correction to fix the jitter in the S1 timing.

The events corresponding to $\beta = 0$ in Figure 4.14 are in fact good electron events. The artifact of the pile-up at $\beta = 0$ is due to TDC times in paddles that did *not* set the timing of the event*. Since $\beta \propto 1/(t_2 - t_1)$, where $t_{1,2}$ are the TDC times in S1 and S2m respectively, β is effectively zero when certain paddles do not fire.

*At the beginning of each event, all times are set to an arbitrary large number.

4.2 BigBite

In this section, we give a brief overview of the calibrations needed for the BigBite spectrometer. In particular, we examine the multi-wire drift chambers in Section 4.2.1, the optics in Section 4.2.2, and the gas Čerenkov in Section 4.2.3. The scintillator calibrations are presented in Section 4.2.4, while the calibrations necessary for the shower calorimeter are explained in Section 4.2.5. These calibrations, with the exception of the optics, were done by M. Posik. A more detailed discussion can be found in [169].

4.2.1 Multi-Wire Drift Chambers

The calibration of the MWDCs follows a similar procedure done for the LHRS, outlined in Section 4.1.1. The calibration was performed by M. Posik [169], using code developed by X. Qian [181]. The software consists of an iterative procedure formulated into three loops: first, a global calibration of the time offset t_0 is done for each readout card; second, a global calibration of the vertical positioning of the wire chamber planes is done; and finally, a fine-tuning of the calibrations for each wire in each of the planes is conducted. Due to the similarities of the E06-010 experiment and our experiment, we utilized the E06-010 calibration as a starting point for our calibration. This eliminated the need for the first two stages of the iterative procedure outlined above, leading to a quick convergence of the final step.

Calibrations were done for each target polarization configuration and electron beam energy. Tables 4.3, 4.4 and 4.5 show the results, which lists the average track residual* σ for each plane in the three wire chambers; the first row gives results for the elastic e-p scattering from an unpolarized hydrogen target at $E = 1.23\,\text{GeV}$. The second and third rows show results for $15\,\mu$A production runs on a polarized ^{3}He target. A resolution of $< 300\,\mu$m was achieved for all wire chamber planes.

Table 4.3: Calibration results for each plane in the first MWDC. Each entry lists the average track residual for a given beam energy and target. Table reproduced from [169].

E (GeV)	Target	U (μm)	U' (μm)	V (μm)	V' (μm)	X (μm)	X' (μm)
1.23	^{2}H	215	216	209	209	206	208
4.74	^{3}He	270	271	263	261	247	250
5.89	^{3}He	286	287	273	272	258	261

*The track residual is defined as the distance between the track projections onto the hit-wire plane and the hit-wire position [181].

Table 4.4: Calibration results for each plane in the second MWDC. Each entry lists the average track residual for a given beam energy and target. Table reproduced from [169].

E (GeV)	Target	U (μm)	U' (μm)	V (μm)	V' (μm)	X (μm)	X' (μm)
1.23	^{2}H	213	211	216	216	203	198
4.74	^{3}He	267	265	262	262	245	240
5.89	^{3}He	283	279	275	273	255	250

Table 4.5: Calibration results for each plane in the third MWDC. Each entry lists the average track residual for a given beam energy and target. Table reproduced from [169].

E (GeV)	Target	U (μm)	U' (μm)	V (μm)	V' (μm)	X (μm)	X' (μm)
1.23	^{2}H	164	161	161	159	145	141
4.74	^{3}He	248	245	246	245	202	199
5.89	^{3}He	250	247	244	242	203	199

4.2.2 Optics

The BigBite spectrometer's optics are quite different from the LHRS, where in BigBite there is one dipole magnet compared to a QQDQ magnet configuration in the LHRS. In this section, we give a brief overview of the necessary steps for the optics calibration.

The trajectory of a charged particle passing through a known magnetic field can be determined from the particle's charge and momentum. With the momentum reconstructed from the MWDC and a good knowledge of the magnetic field, the particle's path can be computed with a high level of precision. The calibration procedure needed to accomplish this task was developed by X. Qian [181], which was an iterative algorithm. The inputs needed include specialized "calibration runs" with various targets so that the kinematics of the interactions may be calculated accurately; these included no-field runs ($\vec{B} = 0$), carbon runs, and elastic hydrogen runs. The carbon and hydrogen runs were conducted with and without a sieve plane inserted in front of the spectrometer*. The sieve plane is a large rectangular lead plate that has slits cut out of it, the geometry of which is well documented; it allows for accurate calibration of the particle's scattering angles.

4.2.2.1 No-Field Calibration

The no-field calibration is the first step of the calibration procedure, which was completed by X. Qian [181]. The locations of the target, magnet, and sieve plate are determined from survey reports [169]. The MWDC positions are determined by taking measurements with the magnetic field turned off, and the MWDCs reconstruct tracks that are subsequently not

*These so-called "optics runs" were also used for the LHRS (Sect. 4.1.2).

bent by the magnetic field; that is, the kinematics of the scattered particles are unchanged. The result of the no-field calibration are shown in Figure 4.15. The left panel shows the z-vertex, the middle panel shows what the sieve plane looks like, and the right panel is a plot of track-y vs. track-x showing where the sieve slits are (red) and where the data fall (black).

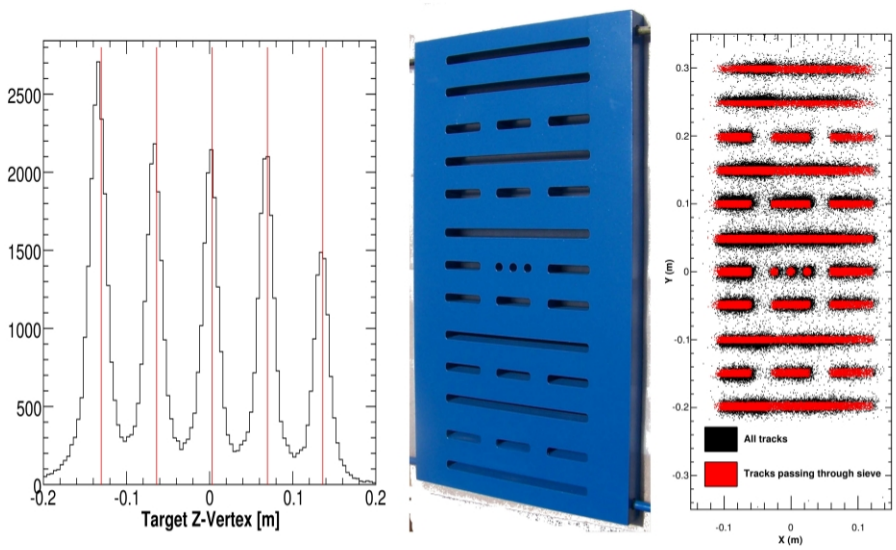

Figure 4.15: Results of the no-field calibration. The left panel shows the reconstructed z-vertex at the target; the middle panel shows the sieve plane, and the right panel shows where the data (black) fall on the sieve plane, compared to the sieve slit openings (red). Figure reproduced from [169].

4.2.2.2 First-Order Optics Model

To first order, the magnet is treated as a perfect dipole; that is, a uniform magnetic field is assumed to fill the volume. Charged particles are bent through a radius R, and the bend radius is measured relative to a *virtual* bend plane which passes through the center of the magnet, indicated by a heavy black-dashed line in Figure 4.16. A representation of the true path of the particle is given by the solid black curve. The approximated path of the particle is given by the red-dashed line segments $\overline{AC}$ and $\overline{CD}$, and the bend angle of the trajectory is given by $\theta_{\text{bend}} = \angle ABD$. Using the path length l and the bend angle, the bend radius R is given as [47]:

$$R = \frac{l}{2\tan\left(\theta_{\text{bend}}/2\right)}. \tag{4.12}$$

Using the equation for R along with the charge of the particle q and the magnetic field magnitude B, the total momentum may be computed as:

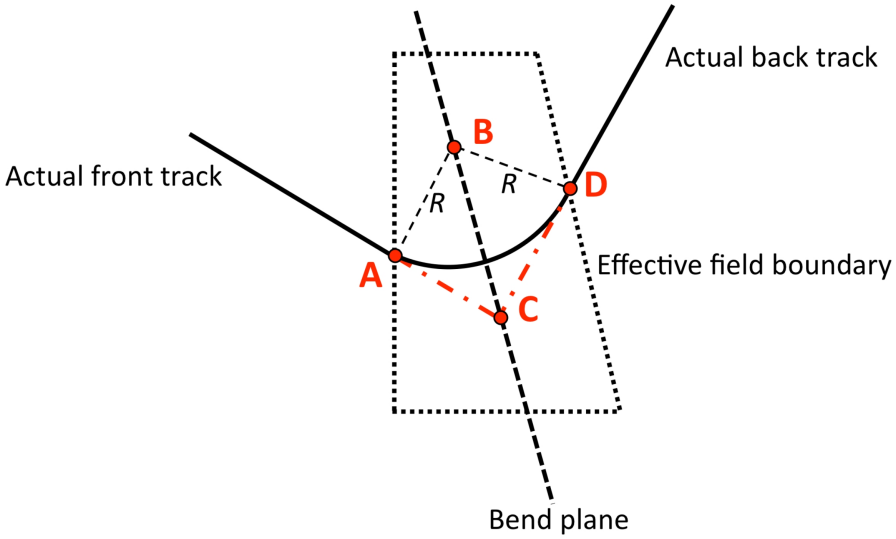

Figure 4.16: Diagram of the first-order optics model for the BigBite magnet, used in E06-010 and E06-014. Figure reproduced from [47].

$$p = \frac{|q|lB}{2\sin\phi\tan\left(\theta_{\text{bend}}/2\right)}, \tag{4.13}$$

where ϕ is the angle between the momentum and the magnetic field, given by $\cos\phi = \vec{B}\cdot\vec{p}/\left(|\vec{B}||\vec{p}|\right)$.

The first-order optics calculations are used to reconstruct the target vertex and scattering angles. The back-track, reconstructed by the MWDCs, is extrapolated to find the point C, where the track intersects the virtual bend plane; because BigBite is modeled as a perfect dipole, the front-track should also intersect the bend-plane at the same point, with the same angle ϕ with the magnetic field as the back-track does. Such requirements restrict the potential trajectories for the front-track to a cone with an apex at point C and an opening angle of ϕ. The front-track that is reconstructed is the one that intersects with the beamline; this is the first-order vertex position. The first-order scattering angles are then defined by the vector connecting the first order vertex point and midpoint of the bend-plane (point C) [47, 181].

4.2.2.3 Fine-Tuning of First-Order Corrections

The BigBite magnet is not a perfect dipole, so higher-order corrections are needed. These were done during the E06-010 experiment, for $E = 1.23$ and $2.39\,\text{GeV}$. Unfortunately, there was not enough optics data during our experiment to determine such corrections;

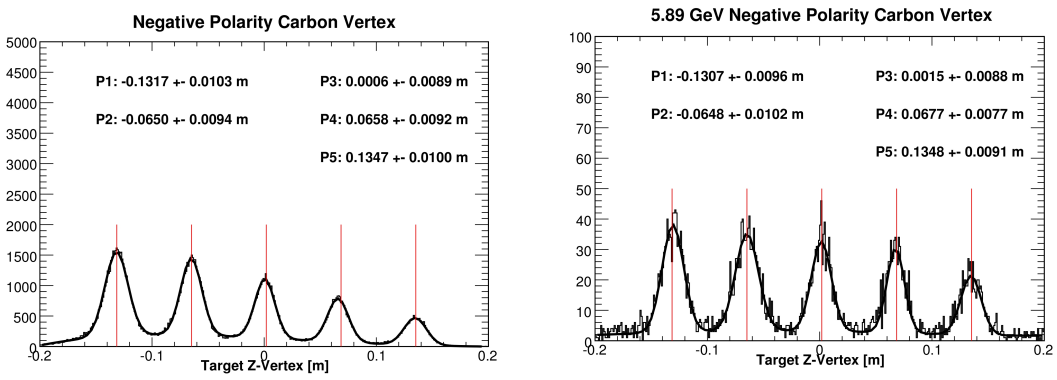

(a) Elastic, $E = 1.23\,\text{GeV}$ (b) $E = 5.89\,\text{GeV}$

Figure 4.17: The results of the z-vertex calibration on a carbon target. The red lines indicate the surveyed foil positions. (a): elastic data at $E = 1.23\,\text{GeV}$; (b): inelastic data at $E = 5.89\,\text{GeV}$. Figures reproduced from [169].

therefore, we utilized the corrections obtained for E06-010 or neglected them where appropriate [169].

Due to the inhomogeneous magnetic field, the particle trajectory depends on what region of the field the particle is traversing; this dependence can be seen in the data when looking at correlations between the target vertex, reconstructed momentum and several other tracking variables*. Utilizing these correlations, correction factors are applied so that the reconstructed target vertex from data agrees well with the surveyed positions of Carbon foils. The corrections were performed by X. Qian for the E06-010 experiment and implemented into our experiment by M. Posik and D. Parno. A more detailed discussion may be found in [169, 181]. The results of the scattering vertex calibration are presented in Figure 4.17, which shows the vertex reconstruction for elastic carbon runs at $E = 1.23\,\text{GeV}$. The resolution obtained was 1 cm. A check was performed during our production runs using $E = 5.89\,\text{GeV}$, where the resolution was found to be at the centimeter level [169].

For the calibration of the scattering angles θ and ϕ, we used carbon and hydrogen targets, taking runs with and without the sieve slit. The initial angles were determined by projecting the final interaction vertex position to the middle point of the bend plane (point C in Figure 4.16). Similar to the vertex reconstruction corrections, offset and higher-order corrections were done by X. Qian [181]. The results of the calibration are shown in Figure 4.18, which shows a multi-foil carbon target run at $E = 1.23\,\text{GeV}$. The red points indicate the location of the sieve slits, and the data is given by the black points. The angular resolution was found to be 10 mrad [169].

*There are six tracking variables used to describe how and where a charged particle passes through the magnetic field [169].

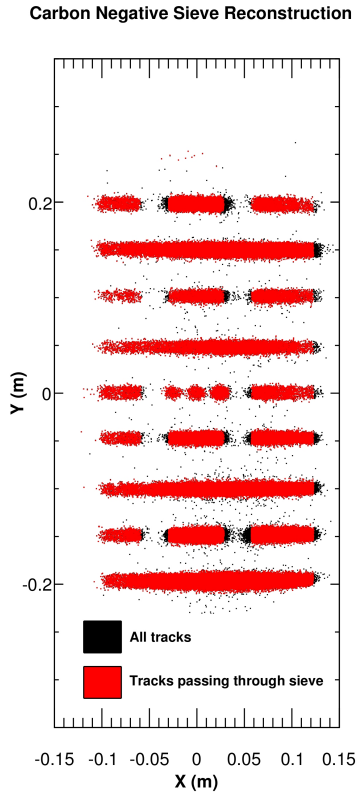

Figure 4.18: Results of the angular calibration. The data (black) are plotted in the sieve plane, compared to the positions of the sieve slits (red). Figure reproduced from [169].

With an accurate positional and angular reconstruction in hand, the momentum was then calibrated. In the elastic scattering of electrons from a hydrogen (proton) target, the scattered momentum is known exactly:

$$p_{el} = \frac{p_i}{1 + \frac{2p_i}{M}\sin^2(\theta/2)}, \tag{4.14}$$

where p_i is the initial momentum, M is the target mass (proton mass); ignoring the small electron mass, the initial electron momentum is given by the beam energy; the scattering angle is known from the previous calibrations, so the calculated momentum p_{el} can be compared to the measured scattered momentum and the discrepancy is then corrected.

In the E06-010 experiment, correction factors were applied to the reconstructed momentum so that the Δ resonance fell at $W = 1.232\,\text{GeV}$. In our experiment, we followed a similar prescription, with some slight modifications. By simulating the BigBite spectrometer, it was found that the Δ resonance is affected by variations in Q^2 and the acceptance of the spectrometer, and sits at $W = 1.215 \pm 0.005\,\text{GeV}$. Due to this, the correction factors were adjusted so that this was achieved in the data [47]. The effects of the calibrated mo-

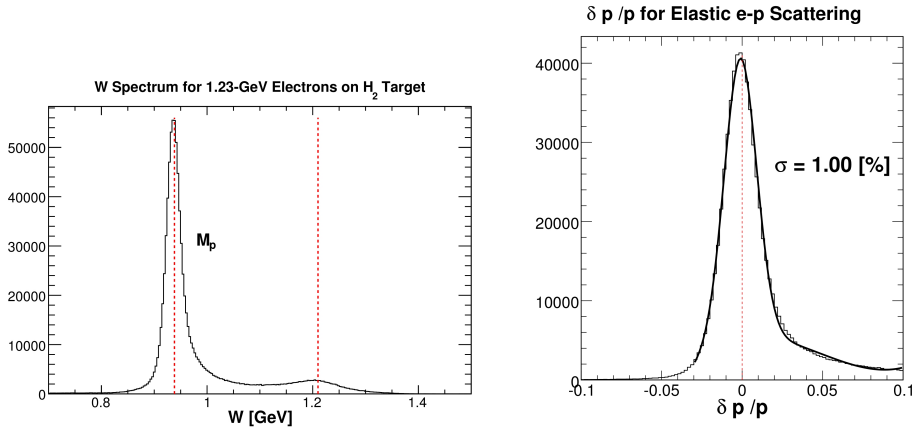

(a) W spectrum for bend-up particles.

(b) Momentum resolution for bend-up particles.

Figure 4.19: The results of the momentum calibration for bend-up particles. (a): W spectrum for bend-up particles. The red lines indicate the proton mass and the Δ mass; (b): momentum resolution for bend-up particles. Figures reproduced from [169].

mentum are displayed in Figure 4.19, which shows a representative W spectrum for elastic e-p scattering in the left panel. We see here that the elastic peak is aligned at the proton mass, while the Δ resonance is aligned at 1.212 GeV. The achieved momentum resolution was $\delta p/p = (p - p_{el})/p \approx 1\%$, as is shown in the right panel of Figure 4.19.

4.2.2.4 Positive Optics

The optics calibrations only used particles that bend upwards into the detector. However, we also need a calibration for those particles that bend *downwards*, as the large acceptance of BigBite allows for the detection of such particles. To accomplish this, the polarity of the magnet was reversed so that those (positively charged) particles now bend up; electrons bending *down* are now selected and the procedure outlined in this section is repeated. The calibrations for the positive polarity optics were done by X. Qian [181]; however, the low momentum and higher-order corrections were removed, and other adjustments were made [169]. The results of the vertex, angular and momentum reconstruction are similar to what is seen for the negative polarity data.

4.2.3 Gas Čerenkov

4.2.3.1 ADC Calibration

To calibrate the ADC signals for each of the PMTs in the gas Čerenkov detector, a two-step calibration was used. This consisted of doing a rough calibration during the running of the experiment, where the high voltage (HV) was adjusted so that the one p.e. peak would fall at roughly the same ADC channel for each PMT. This was done using LED flashers, which were installed in the Čerenkov tank as the source to produce the one p.e. peak. This was accomplished via specialized "LED runs" *. In the second step of the calibration, each PMT was gain-matched via software, in a similar fashion as was done for the LHRS gas Čerenkov PMTs (Sect. 4.1.4). The fit function used in the fitting of the ADC spectra was a Gaussian-Poisson convolution, used to obtain the one p.e. peak position. An example ADC spectrum fitted by the Gaussian-Poisson convolution is shown in Figure 4.20. The one p.e. peaks were aligned to ADC channel 30.

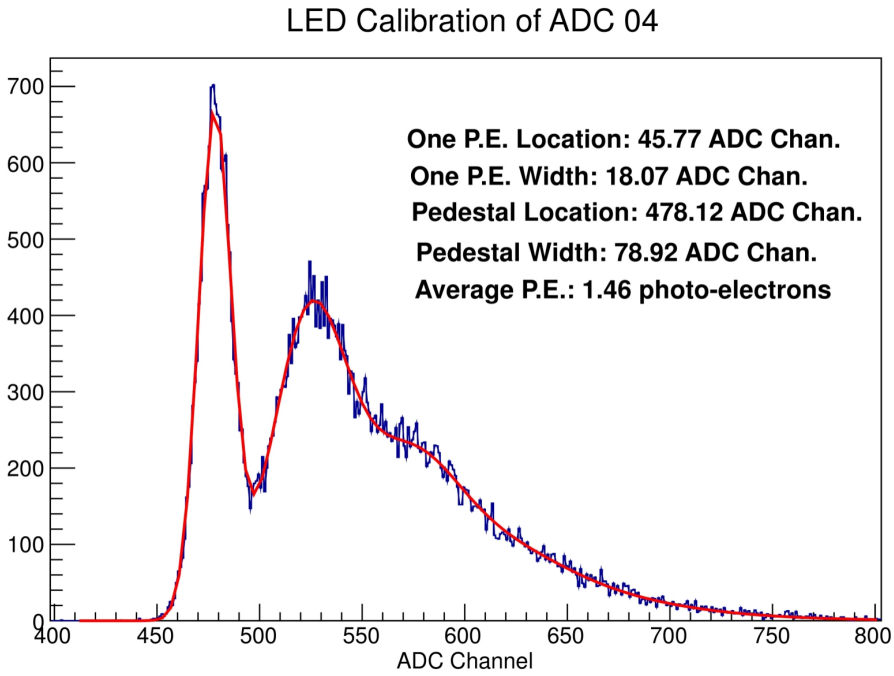

Figure 4.20: The ADC response of a PMT in the BigBite gas Čerenkov. The red curve indicates the fit result for the spectrum. This spectrum is *not* pedestal subtracted, where the first peak is the pedestal. The second peak is the one photoelectron peak. Figure reproduced from [169].

Unfortunately, not all LED runs were saved for the calibration process. To account for this, the LED-calibrated runs were used as a basis for calibrating PMTs for runs early in the

*Such runs were not taken during production mode.

production data taking, where LED runs were not available. In the calibration process, the pedestal of the ADC signal is subtracted off first; it was found that the pedestals for PMTs closest to the beam (small-angle side) when the beam was off were in large disagreement with the pedestal for LED runs when the electron beam was on. Pedestals with the beam on were selected using the T8 trigger (1024 Hz pulser), which selects uncorrelated background events. The beam-on pedestals were found to be shifted lower in the ADC spectrum relative to the beam-off pedestals. To fix this, a correction offset was applied in software by a time-stamped database which applied the pedestal correction for a given beam current. After this, gain-matching coefficients were applied to align the one p.e. peak at 30 channels in the ADC spectrum.

4.2.3.2 TDC Calibration

In order to make applying cuts to the TDC spectra of each PMT easier in the analysis, the main peak of each TDC spectrum was aligned to TDC channel 0, where a Gaussian fit was used to find the peak position and a correction via software was applied to the data. The cut used on each TDC spectrum was then 0 ± 50 channels (0 ± 25 ns).

4.2.4 Scintillating Plane

The calibration of the PMTs that view the scintillating paddles were calibrated by Jin Huang [159] during the E06-010 experiment [191], which consisted of gain-matching the ADC responses of the PMTs. The TDCs were also aligned to a common channel. These were checked by M. Posik and found to be valid for our experiment [169]. Unfortunately, the timing resolution of TDCs (300 ps) was not good enough to discriminate between electrons and pions; consequently, the timing information obtained from the scintillating plane was not used in the analysis.

4.2.5 Shower Calorimeter

4.2.5.1 Energy Calibration

The BigBite shower calibration was conducted in a two-step process. First, cosmic rays were used to gain-match detector responses. Second, the reconstructed momentum obtained from the tracking algorithms employed by the MWDCs were used to refine the calorimeter energy obtained in the first step.

Ideally, all the calorimeter blocks should have the same response for a given deposited energy. To calibrate the calorimeter to have such a property, high-energy cosmic rays

(mainly muons) were used. These particles pass vertically through the preshower and shower calorimeters and act as minimum ionizing particles (MIPs), which leave a well-defined energy loss peak in each block's ADC spectrum. The ADC peaks were gain-matched via software using a method similar to what was done for the pion rejector layer calibrations in the LHRS (Sect. 4.1.5). Cosmic events were identified by using plastic scintillators, mounted at the top and bottom of the detector. Each scintillator had a PMT attached on either end of it, with a logical AND between the four PMTs yielding a trigger to identify cosmic muons. The ADC peaks of the blocks of the preshower calorimeter were aligned to ADC channel 240, while the shower blocks had their ADC peaks aligned to channel 120. This analysis was done by K. Allada [151].

In *cluster reconstruction*, the energy *and* position of the particle that generated the electromagnetic shower is determined. A complication of this is that if more than one cluster is found for a given event, it leads to issues in trying to determine which cluster is associated with a given reconstructed track. The algorithm that was employed follows a similar method that was used in the LHRS (Sect. 4.1.5); however, in this case, eight blocks surrounding the main block of the cluster were summed, as opposed to five. To improve upon the cosmic ray calibration, 243 gain-matching coefficients (54 for the preshower and 189 for the shower) were generated by minimizing the χ^2 value corresponding to the squared-difference between a known energy (the momentum) and the reconstructed energy. A linear minimization was used to determine the block coefficients, which transform the ADC amplitudes into an energy, similar to what was seen for the LHRS (Sect. 4.1.5). The full details of the calibration, which was carried out by M. Posik, may be found in [169].

Ideally, the energy calibration would use elastic electrons in e-p scattering, since the electron energy is known exactly for a given beam energy E_b and scattering angle θ. However, we only had time in the experiment to take elastic data for $E_b = 1.23\,\text{GeV}$, which covered only a small part of the acceptance of the BigBite spectrometer. Because of this, the calibration was done on the production data at $E_b = 4.74$ and $5.89\,\text{GeV}$ on a ^{3}He target where electron events were selected using PID cuts. Figure 4.21 shows the calibration results, where a resolution of 8–9% was obtained across the whole data set*. The bottom right panel shows a plot of E vs. p reveals a one-to-one ratio for electron events, as would be expected, given that the mass of electrons is much smaller than their momentum in these kinematics; pion events fall at lower E/p values. Because the calorimeter was in the trigger, each time the trigger hardware changed, the calibration needed to be repeated. In total, there were five hardware changes, and thus five calibrations [169].

*This was obtained by examining a plot of $(E-p)/p$.

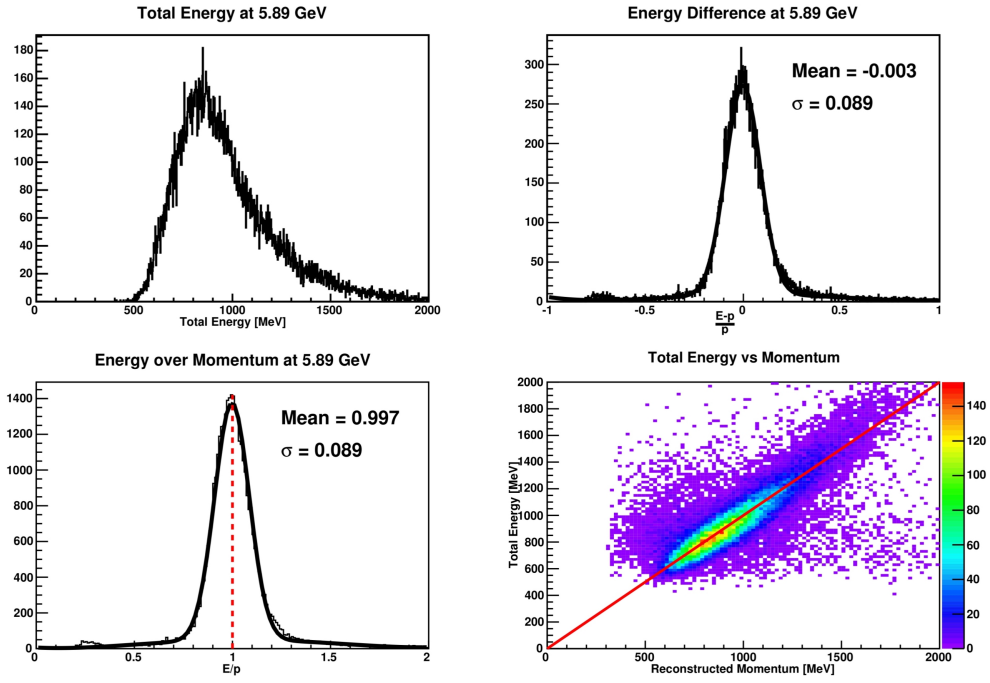

Figure 4.21: Results of the shower calibration for $E_b = 5.89\,\text{GeV}$. The calibration for $E_b = 4.74\,\text{GeV}$ gives similar results. The diagonal red line in the lower right panel gives a guide for the eye in the E vs p plot. Figure reproduced from [169].

4.2.5.2 Track Reconstruction

In addition to the energy calibration, a valid track from the MWDC must be associated with the reconstructed energy. To ensure this, the difference between the reconstructed track projected onto the calorimeter planes and calorimeter cluster position needs to be minimized for the detector x and y coordinates:

$$\Delta x = x_{\text{cal}} - \left(x_{trk} + dx'_{trk}\right) \tag{4.15}$$

$$\Delta y = y_{\text{cal}} - \left(y_{trk} + dy'_{trk}\right), \tag{4.16}$$

where x_{cal} is the (vertical) calorimeter cluster position, x_{trk} and x'_{trk} are the position and slope of the reconstructed track at the first MWDC plane, and d is the distance along the z-axis in the detector coordinate system; the same idea applies for the horizontal position y. The poor energy resolution of the calorimeter prevents the precise determination of the location of the track in the calorimeter plane; however, with good tracking resolution, one can vary the distance d so as to obtain the best minimization of Δx and Δy. On the other hand, an incorrect value of d can lead to a large misalignment of the tracks, as shown

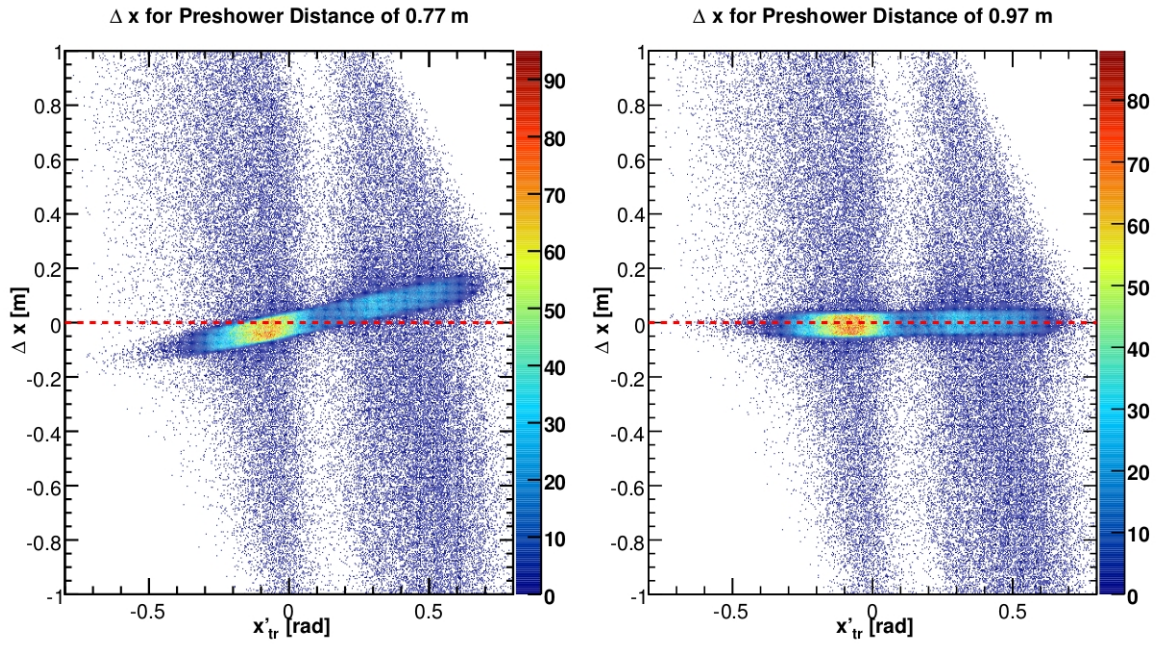

Figure 4.22: The difference between reconstructed tracks projected onto the shower plane and the preshower cluster position plotted against the slope of the track at the first MWDC plane. On the left, the inaccurate value of $d = 77$ cm is used; on the right, the better value of $d = 97$ cm is used. Figure reproduced from [169].

in Figure 4.22, where the left panel shows the use of an inaccurate $d = 77$ cm, while an accurate $d = 97$ cm is shown on the right.

4.2.5.3 Preshower Sum TDCs

In a similar fashion as seen for the gas Čerenkov, the preshower sum TDC peaks* were aligned to a common TDC channel of 0. This makes applying TDC cuts easier in the data analysis [169].

*The BigBite triggers used the shower calorimeter as a common stop, resulting in the shower timing being self-timed [169].

CHAPTER 5

DATA ANALYSIS

In this chapter, we examine the various components of the data analysis. In particular, analysis of the LHRS data is presented in detail in Section 5.2. The analysis particular to the BigBite detector is examined in Section 5.3. The unpolarized cross section analysis is given in Section 5.4, and the double-spin asymmetry analysis is presented in Section 5.5. The analysis to extract A_1 and g_1/F_1 on both ^{3}He and the neutron is discussed in Section 5.6, and the analysis for the flavor-separated ratios $(\Delta u + \Delta\bar{u})/(u + \bar{u})$ and $(\Delta d + \Delta\bar{d})/(d + \bar{d})$ is given in Section 5.7. The extraction of the twist-2 matrix element a_2 on ^{3}He and the neutron starts in Section 5.8 with the analysis to obtain $g_1^{^3\mathrm{He}}$, leading to Section 5.9.

5.1 Analysis Procedure

The analysis procedure is outlined in Figure 5.1, where we start with replaying the raw data followed by the calibration and data quality checks. Data calibrations corresponds to gain-matching ADCs of PMTs of the gas Čerenkov and shower calorimeters to have the same responses, respectively. Calibrations also consisted of optimizing the software packages that describes the optics of the two spectrometers. Multi-foil Carbon targets, a sieve slit collimator and elastic $^1\mathrm{H}(e,e')p$ data at an incident energy of E = 1.23 GeV was used to calibrate the optics software package for the BigBite spectrometer. The same setup was also used for the LHRS [191]. All of the calibration analysis was discussed in Chapter 4. Data quality checks correspond to removing beam trips from the data and faulty runs from the analysis.

Following calibrations and data quality checks, the electron sample is determined by carefully choosing various cuts that choose events that have generated a good trigger and have a proper track reconstruction. Cuts are also chosen that efficiently remove background signals due to charged pions, as well as remove the target windows from the data. In

the BigBite data set, events rescattering from the BigBite magnet pole pieces were found to contaminate the data; geometrical cuts to remove such events were applied. The raw physics observables, consisting of cross sections and asymmetries, are then extracted. Corrections are applied to remove the background signals due to the presence of nitrogen in the target and pair-produced electrons, both of which cannot be removed by cuts placed on the raw data. After these corrections are applied, we obtain the physics asymmetries and the experimental cross sections. Applying radiative corrections yields the Born quantities. From here, the spin structure function g_1 on ^{3}He is constructed*. The twist-2 matrix element a_2 on ^{3}He is obtained from the $g_1^{^3\mathrm{He}}$ data. The asymmetries $g_1^{^3\mathrm{He}}/F_1^{^3\mathrm{He}}$ and $A_1^{^3\mathrm{He}}$ are extracted using the measured asymmetries according to Equations 2.16 and 2.21, respectively. Nuclear corrections are then applied to the ^{3}He results to obtain the neutron quantities for A_1, g_1/F_1 and a_2. Using our extracted g_1^n/F_1^n data, we can then obtain $(\Delta u + \Delta\bar{u})/(u+\bar{u})$ $(\Delta d + \Delta\bar{d})/(d+\bar{d})$.

*One can also obtain $g_2^{^3\mathrm{He}}$ from combining the cross sections and asymmetries; the structure function analysis was done by M. Posik [169], and will be only briefly summarized for $g_1^{^3\mathrm{He}}$ in this chapter.

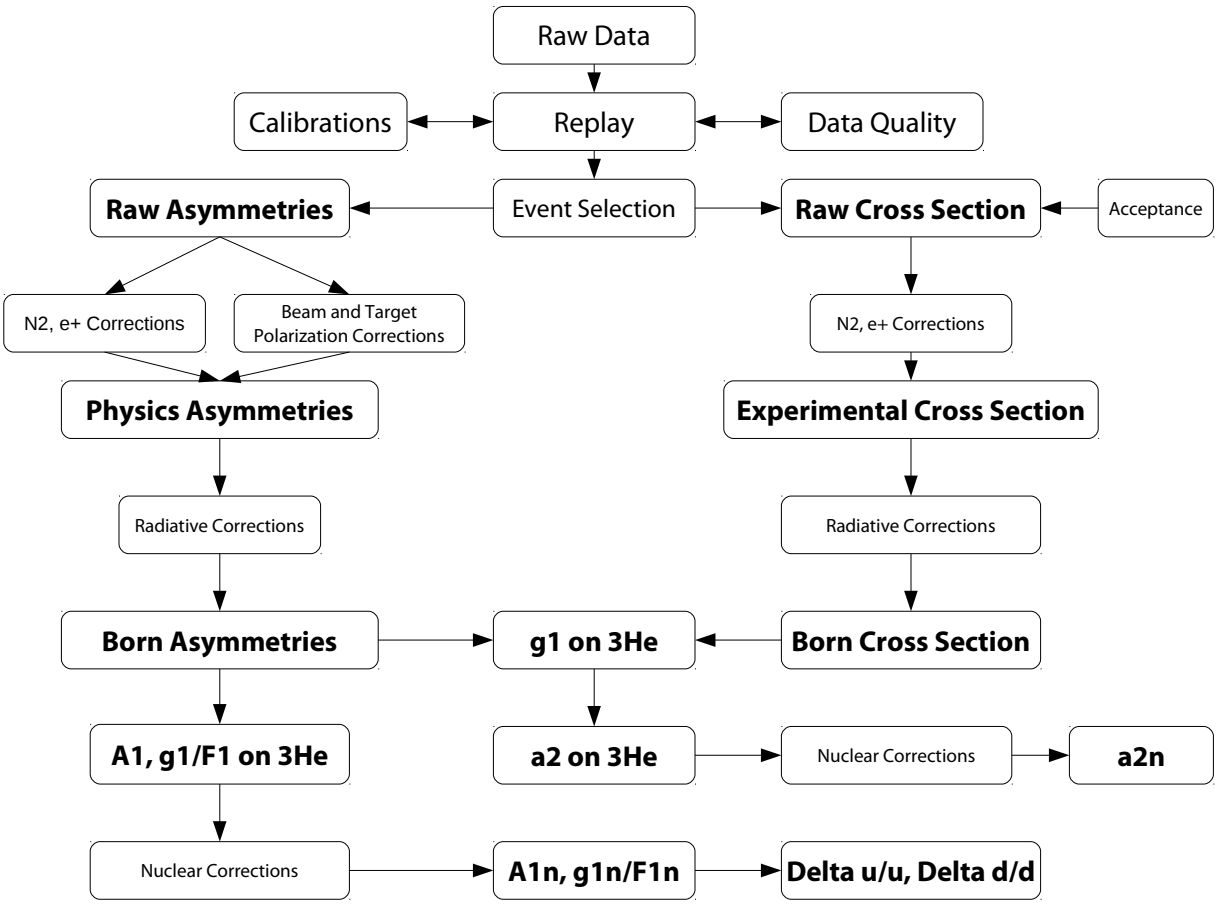

Figure 5.1: Analysis flow chart. After the acquisition of raw data, it is replayed and calibrated. Data quality checks are performed as well. At the event selection stage, electron analysis cuts are chosen and studied. The left and right portions show the steps taken to calculate Born-level asymmetries and cross sections, respectively. The steps required to obtain A_1^n, g_1^n/F_1^n, a_2^n, $(\Delta u + \Delta\bar{u})/(u+\bar{u})$ and $(\Delta d + \Delta\bar{d})/(d+\bar{d})$ are also shown.

5.2 LHRS

5.2.1 Data Quality

So that we may trust our cuts when we do the full-scale analysis on all of the data, we need to carry out a number of data quality checks to make sure that our calibrations are reliable (i.e., stable) for the entire dataset. In particular, such studies were carried out for the gas Čerenkov, pion rejector and the VDC detectors. A study was also conducted to remove events associated with beam trips.

5.2.1.1 Gas Čerenkov

The cut applied to the gas Čerenkov data is on the ADC sum. We examined the ADC sum as a function of run number. We found that these data were stable across the whole dataset, in that the cut that will eventually be applied will be for events to have a Čerenkov signal greater than 400 channels in the ADC (Sect. 5.2.2.4). Since the one photo-electron peak is consistently near 200 ADC channels, no further corrections were needed for the Čerenkov ADC spectra. Figure 5.2 shows the results of the stability check.

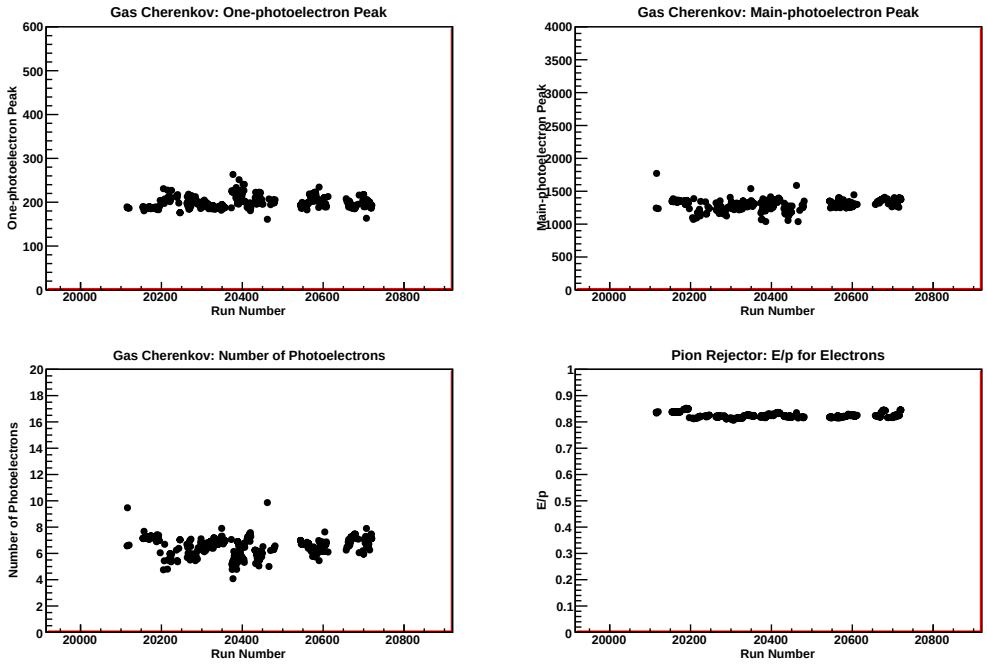

Figure 5.2: Data quality study for the gas Čerenkov and pion rejector. Plotted on the x-axis is the production run number. The one- and main-photoelectron peak are in units of ADC channels. The number of photoelectrons is the ratio of the main- to one-photoelectron peak.

5.2.1.2 Pion Rejector

To ensure the stability of the pion rejector, we examined the electron E/p spectrum as a function of run number. In this study, the deposited energy for a given momentum *bin* was desired to be stable, and it was not necessarily expected that $E/p = 1$ since this is not a full shower. Additionally, the PID analysis yielded that the cut to select electrons using this spectrum was $E/p > 0.54$, and since the main electron peak is consistently near $E/p \sim 0.8$, there was no concern with losing good electron events, nor accepting pion events (Sect. 5.2.2.5). As a result, it was found that the data for the pion rejector was reliable for all kinematic bins as shown in Figure 5.2.

5.2.1.3 VDC

For the VDC, we examined the VDC drift time spectrum (for electrons) as a function of run number in the same fashion as explained in Section 5.2.1.1. This drift time spectrum is a combination of two TDC propagation times: the time for the signal to travel from the hit wire to its corresponding TDC and the time for the trigger signal to propagate from the trigger detector to the TDC (common stop) (Sect. 4.1.1).

We examine this spectrum since any inconsistencies in this data will surely manifest itself in the tracking cut used to select one-track events. The VDC data was found to be reliable for the entire run set, where we plot the *main peak* of the VDC spectrum. Any shift observed in this peak would indicate a shift of the calibrated t_0. In Figure 5.3, it is seen that such spectra are stable for all runs.

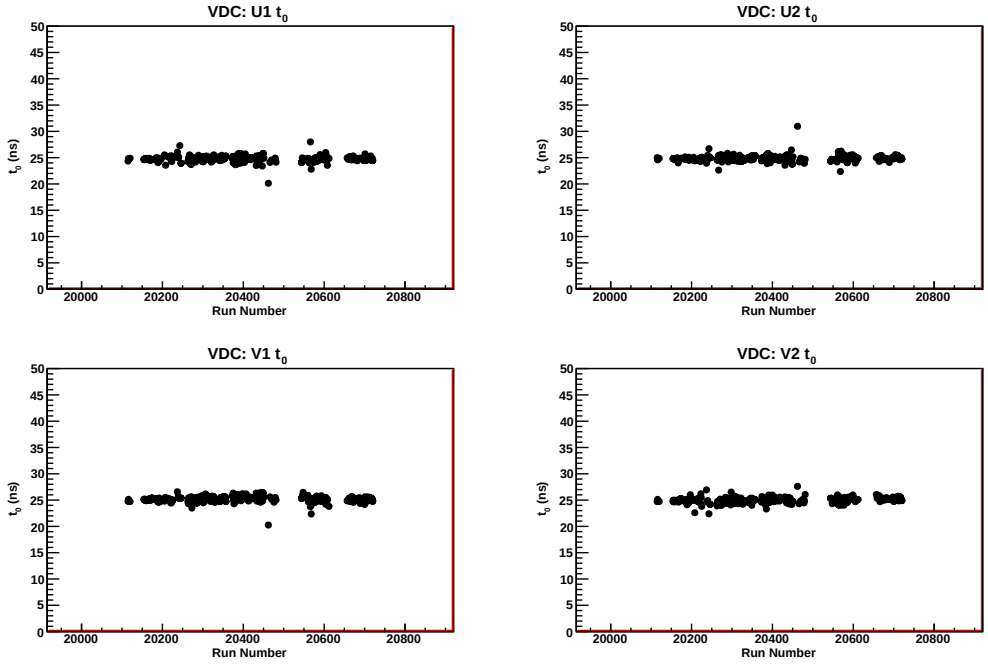

Figure 5.3: Data quality study for the VDC. Plotted on the x-axis is the production run number. Plotted on the y-axis is the *main peak* of the VDC drift time spectrum.

5.2.1.4 Beam Trip Removal

During a run, there are time periods where beam delivery was interrupted. This results in a sudden drop of the beam current. The beam recovers in a slow ramping up back to the set-point value; these periods of time are called *beam trips*, and are undesirable for data analysis. This is because the beam position and charge asymmetry are unstable, resulting in a non-linear BCM [47].

Beam trips are identified by using the u3 BCM readouts, which are scaler events written into the data stream approximately once every 100 triggered events. Using the scaler rate, the beam current can be measured in considering the difference between two consecutive scaler readings. In particular, the beam current sample is fit to a Gaussian distribution, and beam currents within $\pm 1.5\sigma$ of the mean were labeled as good beam regions; otherwise they are rejected. Upon finding a sample that transitions from good beam to poor beam or vice-versa, a timestamp is recorded based on the 103.7 kHz clock time* and stored to a database. We then insert these timestamps into the ROOT files via a "beam trip flag." This has the effect such that when it is turned off, the beam trips are removed from the run, as shown in Figure 5.4.

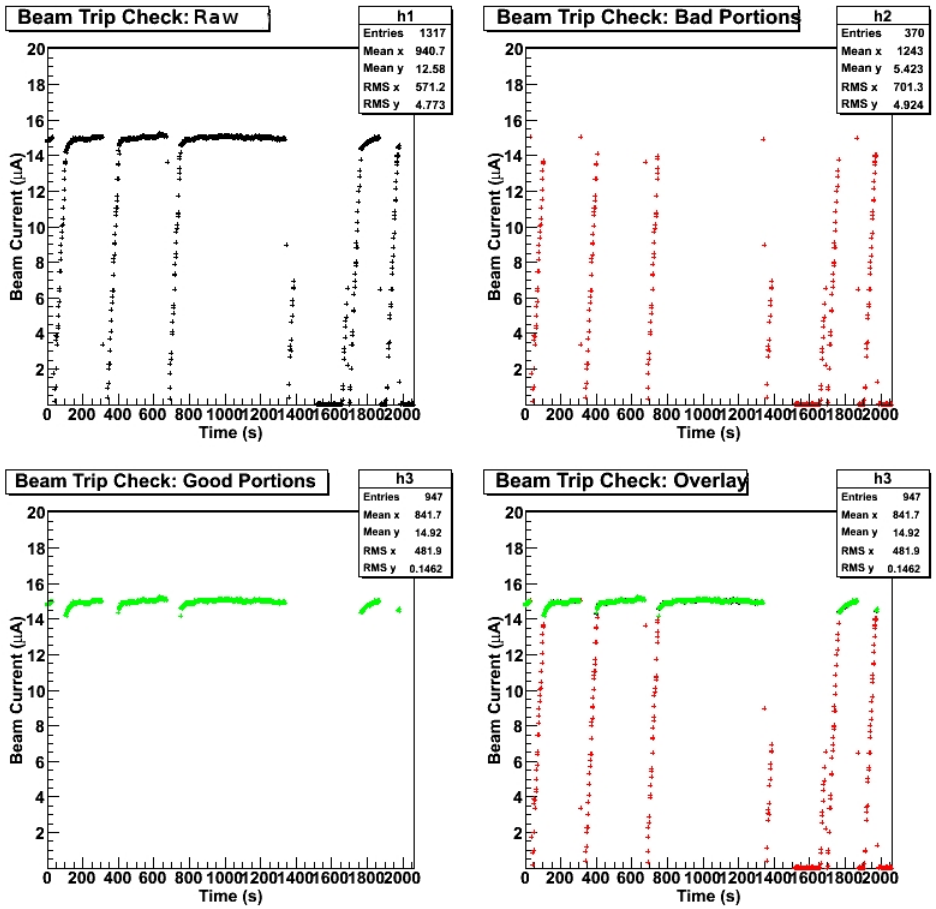

Figure 5.4: Data quality study for the beam current. Plotted on the x-axis is the time of the run. Plotted on the y-axis is the beam current. Each subsequent panel shows the effect of removing either the good or bad portions of the beam using the flag built into the ROOT file.

*This acts as a proxy for the run time.

5.2.2 Cut Efficiencies

To understand how well the detectors perform in discerning electrons from pions, we evaluate their respective abilities to detect electrons and reject pions. For a particular detector, the study is carried out with the help of the other. For instance, if we are investigating the gas Čerenkov, we would use the pion rejector as a reference point, and vice-versa.

5.2.2.1 Electron Detection Efficiency

The *electron detection efficiency*, ε, is the ability to separate electrons from pions. It is defined as:

$$\varepsilon = \frac{N_d}{N_s}, \tag{5.1}$$

where N_s is the number of sample electrons selected using a detector other than the one under investigation. N_d is the number of electrons detected in the detector of interest. For example, if we want to study the electron detection efficiency of the gas Čerenkov, we would chose an electron sample in the pion rejector (N_s) and see how many of those events fire the gas Čerenkov (N_d). Detection efficiencies for both the gas Čerenkov and pion rejector were at the level of $\sim 99\%$ for all data sets.

5.2.2.2 Electron Cut Efficiency

The *cut efficiency* was also studied. Both electrons and pions (via knock-on electrons) can be selected by the gas Čerenkov and the pion rejector. A clean sample is needed for calculating a cross section. Thus, cuts are more stringent than those used to obtain N_d above. Calculating the cut efficiency requires that in addition to firing the detector, the sample events must satisfy a given threshold cut, where N_s is the same as in Equation 5.1 and now N_d is the number of events that pass a certain cut value.

5.2.2.3 Pion Rejection Factor

Another important study that may be carried out for our PID detectors is determining the *pion rejection factor*, f_{rej}, as a function of cut position. The method is the same as discussed in Section 5.2.2.2, but this time we select *pions*, and calculate:

$$f_{\text{rej}} \equiv \frac{\text{Particles identified as pions}}{\text{Particles mis-identified as electrons}} = \frac{N_s}{N_d}, \tag{5.2}$$

For the pion rejector, particles are chosen in the gas Čerenkov by selecting events that *do not* fire the Čerenkov (N_s) and see how many pass a certain E/p value in the pion rejector (N_d).

For each data set, it was determined that the rejection factor was ≈ 660 for the gas Čerenkov and the pion rejector, yielding a *combined* rejection factor of $> 10^5$.

5.2.2.4 Gas Čerenkov

To understand how well the gas Čerenkov performs, we evaluate its ability to detect electrons and reject pions. This is accomplished with the use of the Pion Rejector.

5.2.2.4.1 Electron Cut Efficiency Study

Figure 5.5 shows a typical set of plots used for selecting good electrons for the cut efficiency study. On the left is a plot of the energy deposited in the first layer of the pion rejector versus the energy deposited in the second layer of the pion rejector. The events shown in blue correspond to pions, while the events shown in red correspond to electrons. The black line indicates the cut region used to choose electrons for the study. On the right is their corresponding gas Čerenkov ADC (sum) spectrum. The ratio of the events seen in the gas Čerenkov above some cut value to those counted in inside the cut shown on the left is the electron cut efficiency.

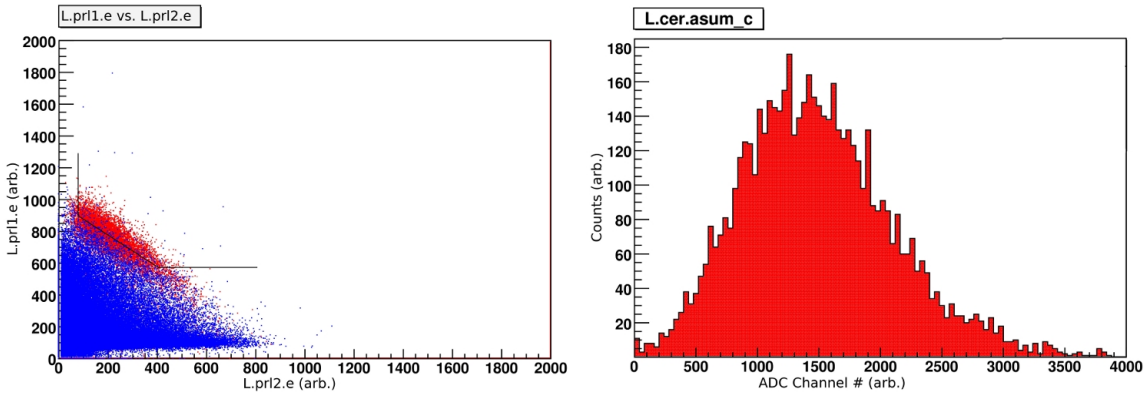

Figure 5.5: The figure on the left shows the cut used (semi-trapezoidal black line) to select the electron sample in the two-dimensional energy plot in the Pion Rejector. On the right is its resulting gas Čerenkov ADC (sum) spectrum.

One should take note that the electron cut is chosen judiciously such that the chosen electron sample is as clean as possible. Any impurity introduced to the sample will invariably lead to an incorrect result. On the other hand, the impurity of the chosen electron

sample reveals a *contamination* present in the detector, and must be analyzed and corrected for.

5.2.2.4.2 Background Correction

Due to the large amount of background across the whole kinematic range of the experiment ($E_{\text{beam}} = 4.74$, 5.89 GeV; $0.60 \leq p \leq 1.70$ GeV), it was found that the initial electron sample chosen in the pion rejector was not as clean as initially thought. Ideally speaking, the chosen electron sample in the pion rejector would consist *only* of electrons; subsequently, examining how many of those events fire the gas Čerenkov gives a true measure of the electron detection efficiency.

In order to correct the background, we need to examine our electron sample in the pion rejector and determine which events are electrons and which events are pions. To this end, we choose a particle sample in the two-dimensional energy plot in the pion rejector. Then, we plot this sample's E/p distribution, subject to an anti-Čerenkov cut and a cut that shows how many events fired the gas Čerenkov. This is shown in Fig. 5.6. We then fit the pion curve (shown in blue), and *subtract* it from the original sample:

$$N_{\text{cor}} = N_i - N_\pi. \tag{5.3}$$

Therefore, it is seen that the *corrected electron detection efficiency* is determined as:

$$\varepsilon_{\text{cer}}^{\text{cor}} = \frac{N_{\text{cer}}}{N_{\text{cor}}}. \tag{5.4}$$

Before these corrections were applied, the detection efficiency as determined for data taken at $p = 0.60$ GeV was on the order of 80%. After the correction is applied, we obtain $\varepsilon_{\text{cer}} \gtrsim 96\%$.

5.2.2.4.3 Pion Rejection Factor

The plot on the left in Figure 5.7 shows the selected a pion sample in the pion rejector, while the plot on the right shows the resulting gas Čerenkov distribution. The ratio of the events selected in the pion rejector to those that pass a given cut in the gas Čerenkov is the pion rejection factor.

5.2.2.4.4 Results

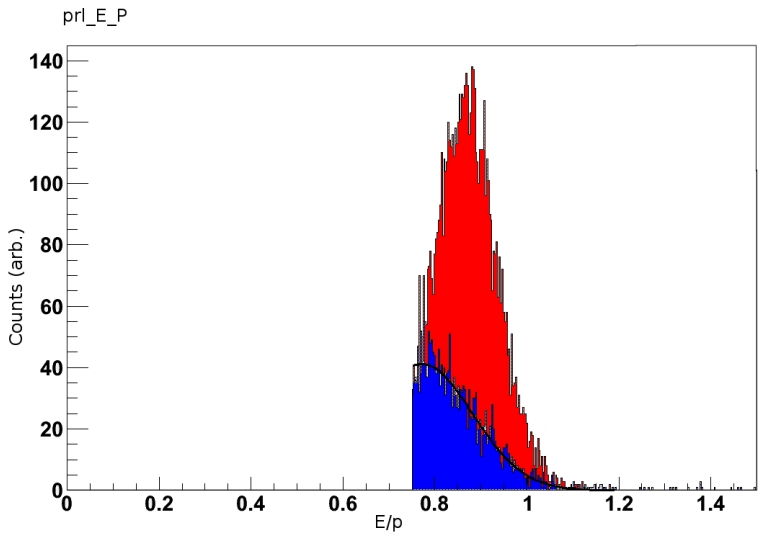

Figure 5.6: This plot shows an example of how the background subtraction is carried out. We plot the E/p distribution corresponding to the selected electron sample as seen in Figure 5.5, and now differentiate between electrons and pions via a cut on the gas Čerenkov either firing or not firing. The fit used is a simple Gaussian.

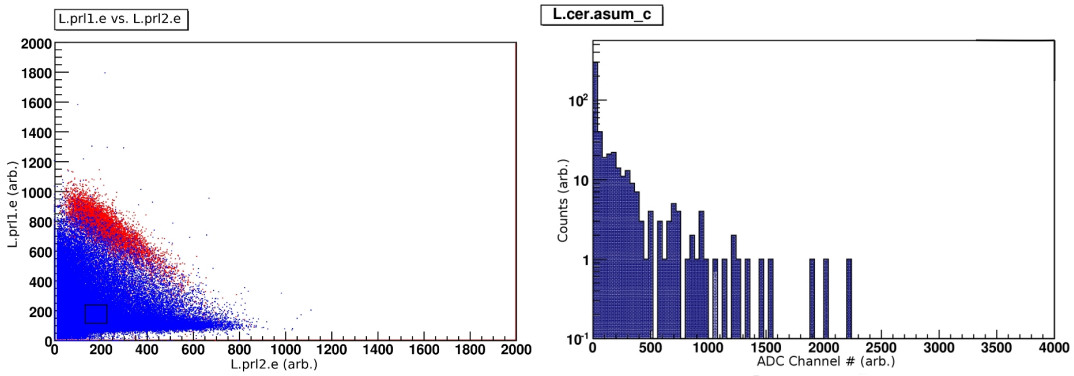

Figure 5.7: The plot on the left shows the how pions are chosen in the pion rejector (black box) for the study of the gas Čerenkov's ability to reject pions. On the right is its resulting gas Čerenkov ADC (sum) spectrum.

The results of the gas Čerenkov cut efficiency study are shown in Figure 5.8 for the $p = 0.60$ GeV, $E = 4.74$ GeV data set. From this plot, we decide that the best position for the gas Čerenkov cut is at 400 ADC channels (2 photoelectrons). This allows us to maintain a high electron cut efficiency of $\sim 96\%$ while keeping a high pion rejection factor of ≈ 660. These results are typical across the all data sets, see Appendix A.

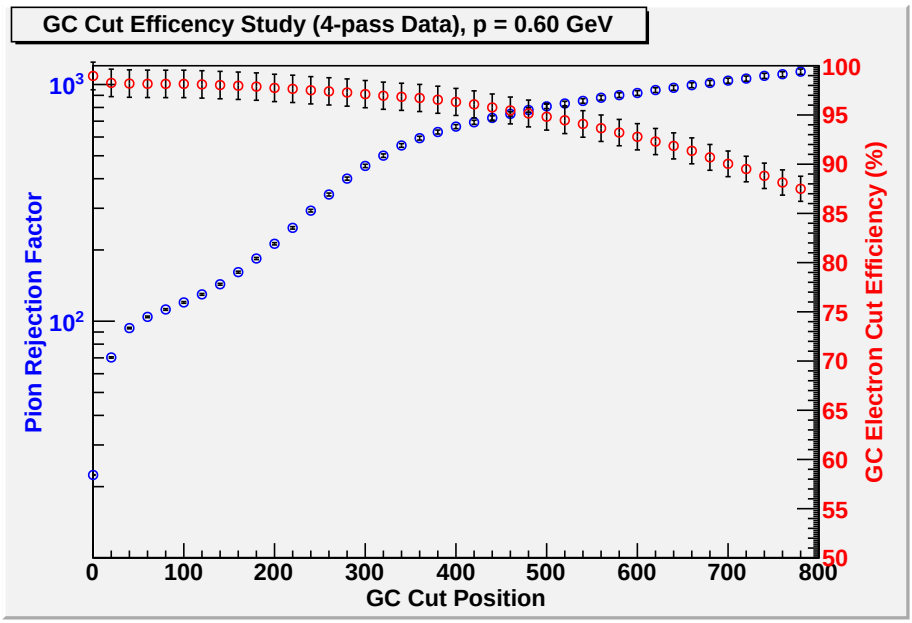

Figure 5.8: Gas Čerenkov cut efficiency study results. From this plot, we deduce that it will be best to place our cut in the gas Čerenkov at 400 channels (2 photoelectrons) in our final analysis. The error bars shown are purely statistical.

5.2.2.5 Pion Rejector

To understand how well the pion rejector performs, we evaluate its ability to detect electrons and reject pions. This is accomplished in a similar manner with respect to Section 5.2.2.4 with the use of the gas Čerenkov. Due to the fact that the pion rejector is *not* a full shower, its performance will not be as good as that seen from a full shower, because of its poorer energy resolution [35].

5.2.2.5.1 Electron Cut Efficiency Study

To select an electron sample defined by the gas Čerenkov, we examine the ADC (sum) spectrum of the gas Čerenkov, subject to the cuts mentioned in Section 4.1.3. We then apply a cut to the main peak of the gas Čerenkov ADC (sum) spectrum. From here, we see how many of these events fire *both* layers of the pion rejector. See Figure 5.9. We choose this requirement as electrons in general will fire both layers of the pion rejector, while pions may fire only one of the layers as the particle traverses the detector. It is better to remove some good electrons that fire one layer *in addition* to removing particles that are not electrons, as opposed to counting any event that fires at least one layer, which allows for counting these pions as good events.

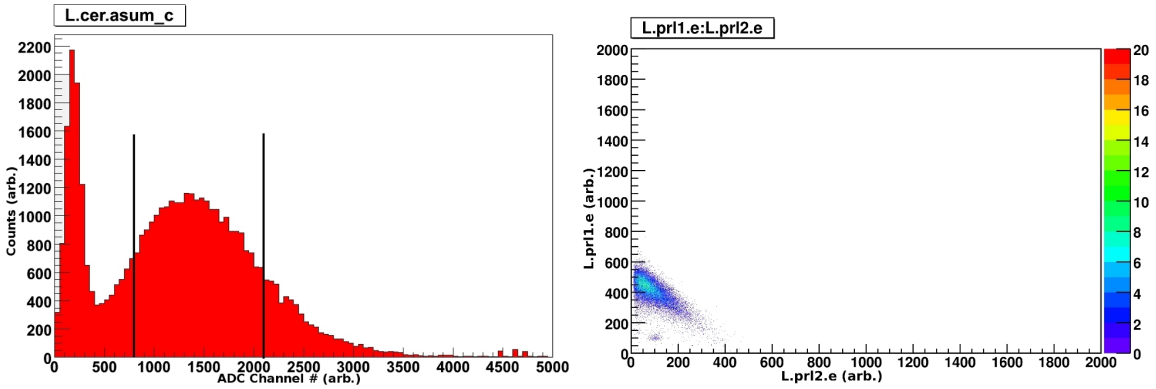

Figure 5.9: This figure demonstrates how to determine a clean electron sample (left) and what the resulting pion rejector energy distribution is (right). The ratio of the number of events determined by the cut shown in the gas Čerenkov to those found in the pion rejector gives the electron cut efficiency for a given E/p cut value.

When conducting the study of the electron cut efficiency, N_d refers to the number of events that fire both layers of the pion rejector and pass the *combined* cut of '(prl_E_P $>$ X_i)&&(L.prl1.e $> X_j$)', where $X_{i,j}$ are some threshold values. This is shown in Figure 5.10. The first cut investigates explicitly the E/p distribution in the pion rejector. This is the main cut that is varied for this study, as the E/p distribution shows a distinct separation between the pion and electron curves. This subsequently provides a powerful and crucial cut to be used in the final analysis. The cut on the first layer of the pion rejector is implemented so as to reject events that are most likely pions and δ-rays, whose properties were mentioned in Section 5.2.2.4.2.

The equation for this study is the same as Equation 5.1, with the appropriate interpretation for N_{pr} as mentioned above.

5.2.2.5.2 Background Correction

Similar to the investigation of the gas Čerenkov electron cut efficiency, it was determined that the initially selected electron sample in the gas Čerenkov was not as clean as possible. This background was determined to be due to δ-rays events mentioned previously. This is shown in Figure 5.11

The procedure for correcting this background follows closely to what was mentioned in Section 5.2.2.4.2. First, we plot the gas Čerenkov ADC (sum) spectrum subject to the cuts mentioned in Section 4.1.3. Then, we plot the same ADC spectrum now subject to the cut shown in Figure 5.12, choosing the *pion* region. Here, we examine explicitly how the δ-rays contaminate the cut window chosen in the gas Čerenkov (sum) ADC spectrum

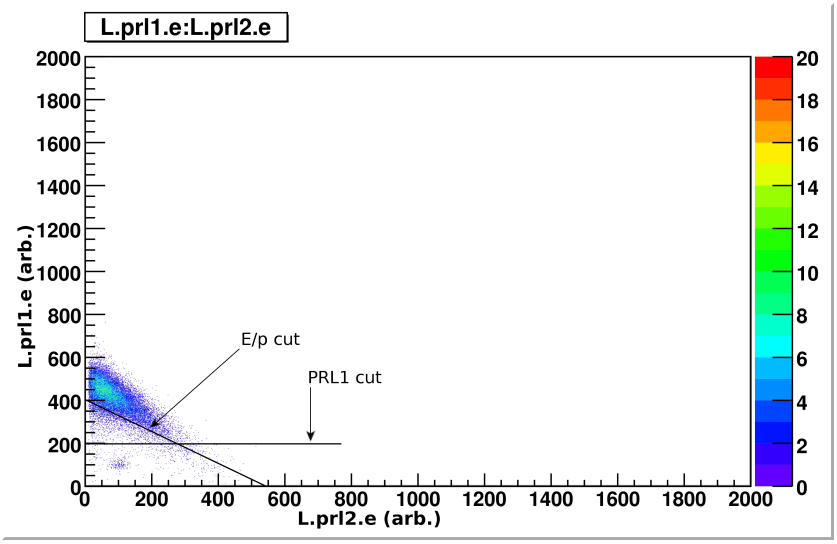

Figure 5.10: This figure shows how the electron cut efficiency in the pion rejector is determined. We place a cut on both E/p and the first layer of the pion rejector (PRL1). The PRL1 cut serves to remove any δ-rays that may have fired the gas Čerenkov. The number of events that pass this combined cut are then compared to our electron sample chosen in the gas Čerenkov (Fig. 5.9). Only the E/p cut is varied for this study.

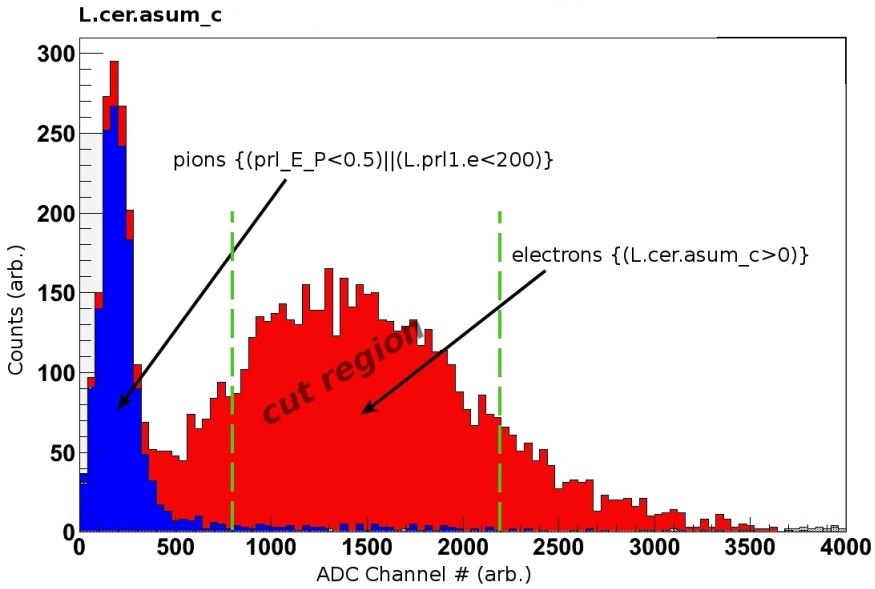

Figure 5.11: This figure gives an example plot showing the background contamination of the electron sample chosen (between the vertical dashed lines) in the gas Čerenkov. The blue curve is due to pion collisions with low-energy electrons. Due to the high pion rates, this effect is seen across the whole kinematic range of the experiment. The blue curve is fit to an exponential, and subtracted from the original electron sample.

(Fig. 5.11). This background is fit to an appropriate function and its contribution to the electron sample is subtracted:

$$N_{\rm cor} = N_i - N_\delta, \tag{5.5}$$

where N_i is the inital sample and N_δ is the contamination seen in the blue curve in the figure. The electron cut efficiency is now corrected to be:

$$\varepsilon_{\rm pr}^{\rm cor} = \frac{N_{\rm pr}}{N_{\rm cor}}. \tag{5.6}$$

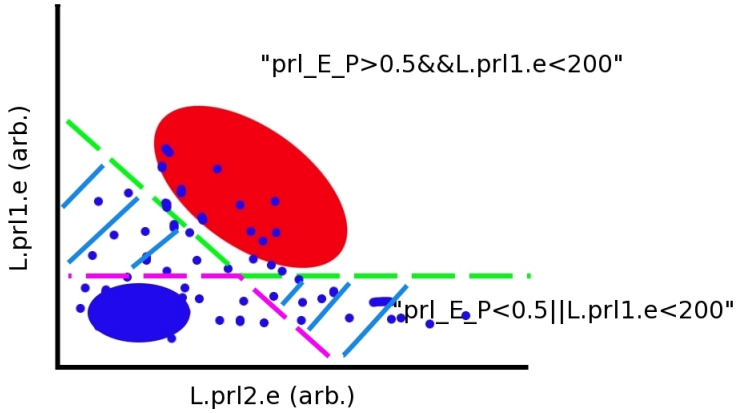

Figure 5.12: This figure gives an example drawing of how the background was determined in the gas Čerenkov. Good electrons (in red) populate the region *above* the green dashed line. If we choose the näive 'inverse,' (i.e., having the E/p and PRL1 values *less than* some value(s)) we will not sample the full contamination (the magenta region). The full contamination seen in the gas Čerenkov is obtained when we plot the events shown in the magenta dashed line *plus* the region shown with the light blue slashes. This corresponds to the cut written in quotes in the lower right of the drawing.

The correction is on the order of $\sim 5\%$ at the low momenta, while decreasing to $\sim 2\%$ as one increases the spectrometer momentum. Due to the large pion rates across the kinematic range, the background correction is not negligible even at the highest momentum setting in the LHRS.

5.2.2.5.3 Pion Rejection Factor

The determination of the pion rejection factor $f_{\rm pr}$ is slightly more difficult than it is for the gas Čerenkov. This is due to the fact that the determination of the pion sample is not straight forward in the gas Čerenkov, as pions do not fire the gas Čerenkov. They may, however, be inferred by examining the δ-ray distribution.

The process is as follows: we first plot the E/p distribution subject to the cuts outlined in Section 4.1.3. Second, we plot the same E/p distribution subject to the aforementioned "good event" cuts and also a tight cut in the gas Čerenkov. We choose a tight cut in the gas Čerenkov as it chooses good electrons, with a *minimal* amount of δ-rays. Then, the *pion rejection factor* is formed as (Fig. 5.13):

$$f_{\text{pr}} \equiv \frac{N_i}{N_f}, \tag{5.7}$$

To get a better understanding of what these terms mean, let us consider their explicit meanings and how they are calculated [197]:

- $N_i = \pi_i + e_i$
  $\pi_i =$ initial π^- excluded by E/p
  $e_i = \varepsilon \cdot \pi_i$ initial e^- excluded by E/p

- $N_f = \pi_f + e_f$
  $\pi_f =$ remaining π^- excluded by E/p
  $e_f = \delta \cdot \pi_f =$ final e^- excluded by E/p

Now, $e_i = e_f$, since the gas Čerenkov cut does not affect the electrons. This implies:

$$\begin{aligned} \varepsilon \cdot \pi_i &= \delta \cdot \pi_f \\ \frac{\varepsilon}{\delta} &= \frac{\pi_f}{\pi_i} \leq 1. \end{aligned}$$

Therefore, we may define the *pion rejection factor* as:

$$f_{\text{pr}} \equiv \frac{N_i}{N_f} = \frac{\pi_i}{\pi_f} \cdot \frac{1+\varepsilon}{1+\delta}. \tag{5.8}$$

Now, the true pion rejection factor is given as $f_{\text{true}} = \pi_i/\pi_f$. Therefore, our calculated value in Equation 5.8 is clearly less than the true value. Considering the fact that ε and δ are small corrections, our equation as shown above is a reasonable approximation, adequate for high pion rates. As shown by our study of the background contamination, encouraged by our kinematic range, this approximation is a very good one.

5.2.2.5.4 Results

Figure 5.14 shows the results of the E/p cut efficiency study for the $p = 0.60$ GeV, $E =$ 4.74 GeV data set. From this plot, we decide that the best position for the E/p cut is at

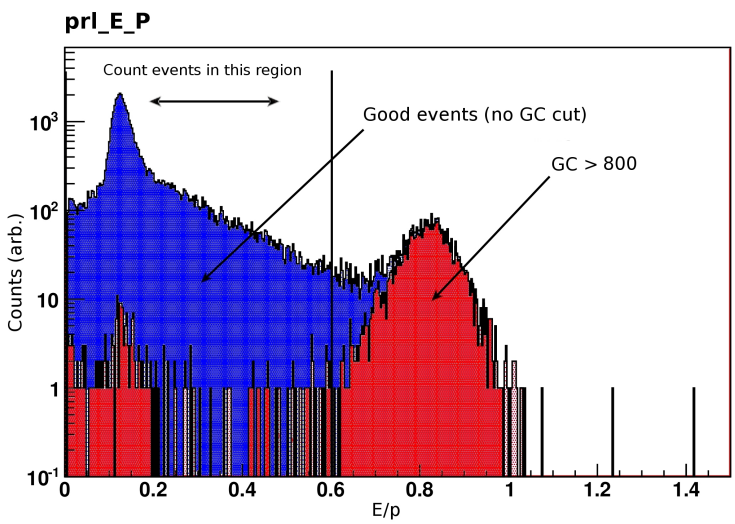

Figure 5.13: This figure shows how pions are rejected in the pion rejector. We place a cut on E/p and the gas Čerenkov (cut result shown in red). The ratio of the blue curve to the red curve *below* the E/p value in question gives the pion rejection factor. Only the E/p cut is varied for this study.

$E/p = 0.54$. Here, we maintain an electron cut efficiency better than 99% while keeping a high pion rejection, at ≈ 660. These results are typical across all data sets, see Appendix A.

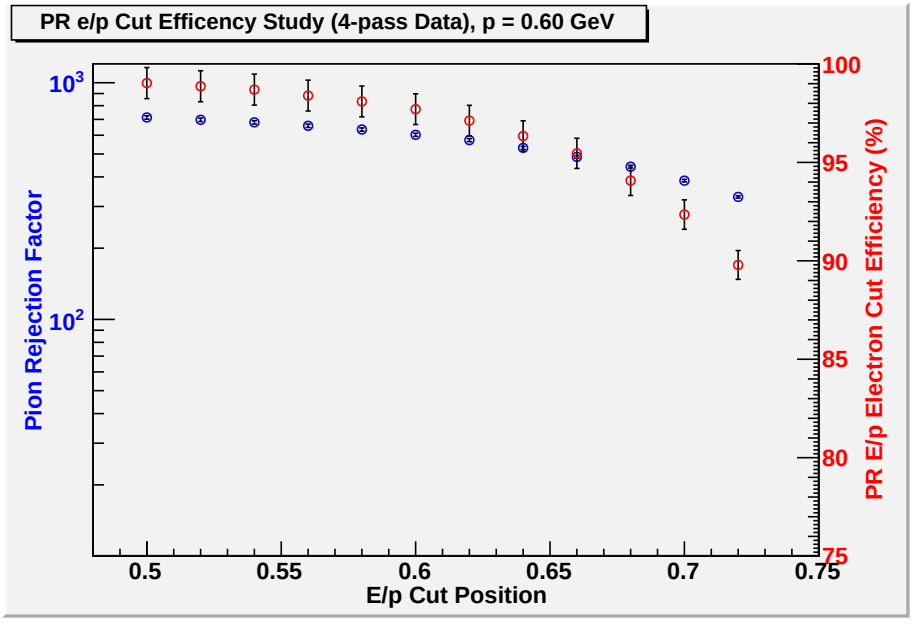

Figure 5.14: Pion rejector E/p cut efficiency study results. From this plot, we deduce that it will be best to place our cut at $E/p = 0.54$ in our final analysis. The error bars shown are purely statistical.

5.2.2.6 One-Track Efficiency for Good Electrons

5.2.2.6.1 Determination of Good Events

In order to choose good events for our study, we consider only those events which induced the main trigger, and pass our 'good electron' cuts:

- *Trigger Cuts*:
  (DL.edtpl==0)&&((DL.evtypebits&(1<<3))==(1<<3))

- *PID Cuts*:
  (L.cer.asum_c> 300)&&(Graphical Cut on 2D Pion Rejector Energy Plot)
  &&(TDC Cuts on the Gas Čerenkov)

The PID cuts listed refer to choosing good electrons in both the gas Čerenkov and the pion rejector. It is important to note that we *cannot* use the E/p variable in our PID cuts since it relies on tracking to reconstruct the momentum p, which is then used in the determination of the quantity E/p. Therefore, as a substitute, we determine graphical cuts on a 2D plot of the energy deposited in layer 1 of the Pion Rejector versus the energy deposited in layer 2 of the pion rejector shown in Figure 5.15.

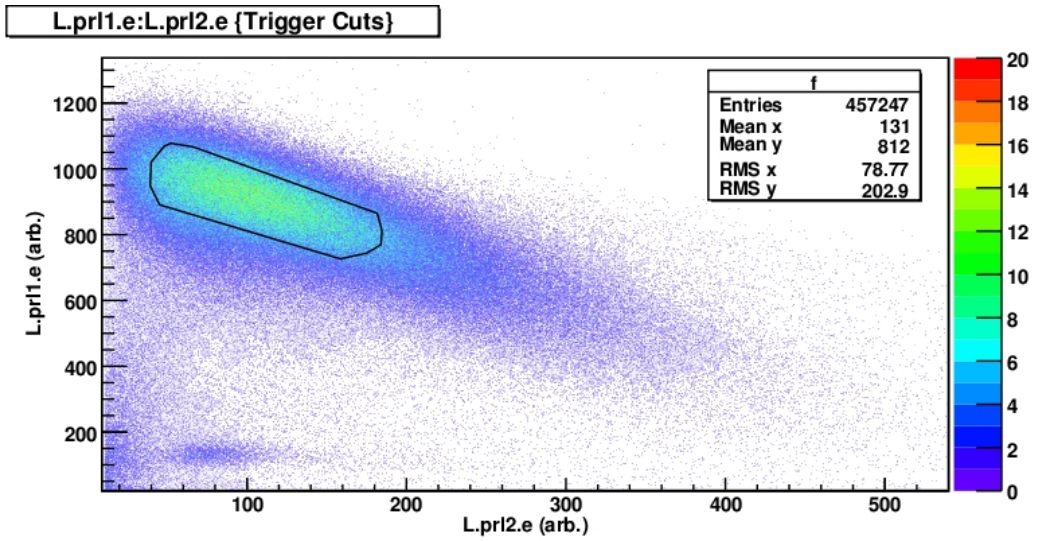

Figure 5.15: Graphical cut on the 2D energy plot of the Pion Rejector. We utilize this cut as it is independent of the tracking variables.

5.2.2.6.2 VDC Tracking Efficiency

While the hardware efficiency of the VDCs is known to be on the order of 100% [152], it is nonetheless important to investigate the efficiency and subsequently the inefficiency of the detector. To understand such quantities, we examine the track multiplicity measurements in addition to the zero- and one-track efficiencies.

5.2.2.6.3 Results

The inefficiency of the VDCs arises due to the VDC software algorithm incorrectly reconstructing tracks as a result of multi-track events or no-track events. The former is due largely to many particles crossing the VDC planes simultaneously. In such a case, there are a large number of possible trajectories that may be determined by the software. Therefore, we retain only one-track events in our analysis of the various physics quantities of interest; however, we need to be aware that such a requirement may discard good events that may show up as multi-track events. To understand the effect of the one-track event requirement, we examine the zero-,multi-, and one-track efficiencies, taking zero- and multi-track efficiencies as the *inefficiency* of the VDC tracking algorithm [178].

We define the *one-track efficiency* as follows: we count the number of one-track events and compare this sum to the sum of all zero-, one-, and multi-track events. Mathematically, we have:

$$\varepsilon_1 = \frac{N_1}{\sum_{i=0}^{4} N_i}, \tag{5.9}$$

where N_1 is the number of one-track events, and N_i is the number of i-track events $(i = 0,\ldots,4)$. It is important to note that the software reconstructs a maximum of up to four tracks per event [152, 175]. Similarly, we may determine the other j-track efficiencies $(j \neq 1)$ as:

$$\varepsilon_j = \frac{N_j}{\sum_{i=0}^{4} N_i}. \tag{5.10}$$

Table 5.1 shows the results of the study for the $p = 0.60$ GeV, $E = 4.74$ GeV kinematic. We see that the one-track efficiency is on the order of $\sim 99\%$. We see that the largest contribution to the inefficiency is due to two-track events, at $\sim 0.67\%$.

Table 5.1: The VDC Tracking Efficiency for the $p = 0.60$ GeV, $E = 4.74$ GeV data. The one-track efficiency is $\sim 99\%$, while the two-track events dominate the inefficiency at $\sim 0.67\%$. The errors shown are purely statistical.

VDC Tracking Efficiency		
# of Tracks	# of Events	ε (%)
0	20	0.036 ± 0.008
1	56004	99.282 ± 0.592
2	377	0.668 ± 0.035
3	8	0.014 ± 0.005
4	0	0.000 ± 0.000

The results for the one-track efficiency turns out to be $\sim 99\%$ across all data sets, with the leading inefficiency being due to the two-track events at $\lesssim 1\%$. See Appendix A for the results for each momentum bin.

5.2.2.7 Beta Cut Efficiency

In choosing good events in the LHRS, we apply PID cuts from the gas Čerenkov and the pion rejector to isolate electrons. We also apply a cut on the particle's β distribution to explicitly exclude cosmic events ($\beta < 0$). The cut applied is $\beta > -0.15$, as shown in Figure 5.16. The cut is not placed at zero because it was determined [198] that the events at $\beta = 0$ are in fact good electron events (Sect. 4.1.6).

Considering that this is another cut that determines good events for our cross section analysis, it has an efficiency tied to it. We evaluate the efficiency as the ratio of the number of good events that pass the β cut to the number of events selected by using *all* PID and target cuts mentioned in the previous sections. The efficiency of this cut comes out to be $\sim 99\%$ for all data sets, as shown in Appendix A.

5.2.3 Trigger Efficiency

5.2.3.1 Determination of Good Events

In order to choose good events for our study, we consider only those events that induce either a T3 or a T4 trigger, and pass our "good electron" cuts (Sect. 4.1.3). We also include PID cuts on the gas Čerenkov and pion rejector.

- (L.cer.asum_c> 300)&&(prl_E_P> 0.54)
  &&(TDC Cuts on the Gas Čerenkov)

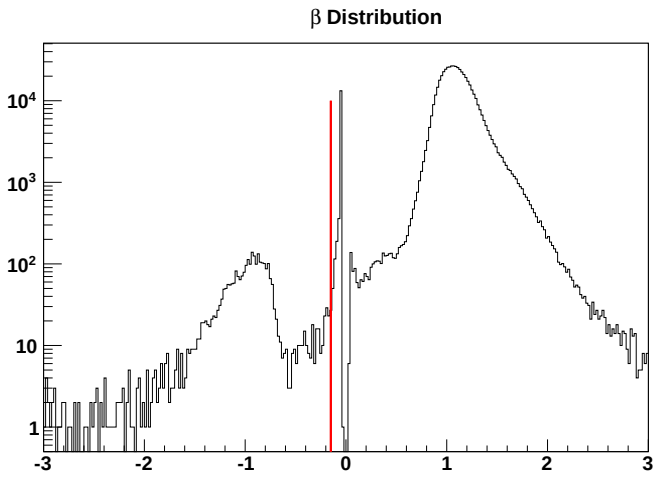

Figure 5.16: This plot shows a typical β distribution. The events that have a β value greater than the red line are kept in the cross section analysis.

5.2.3.2 Method

In order to determine the T3 trigger efficiency, we consider the equation:

$$\varepsilon_{T3} = \frac{N_{T3}}{N_{T3} + N_{T4}}, \tag{5.11}$$

where N_{T3} is the number of T3-type events *adjusted* for prescaling. The same definition follows for T4-type events. Therefore, to prevent an inaccurate determination of the T3 trigger efficiency, we have the following definition for N_i ($i = T3, T4$):

$$N_i = t_i^{ps} \times \text{bit}_i, \tag{5.12}$$

where t_i^{ps} is the prescale value for the i^{th} trigger and bit_i is the number of times the bit pattern was set—that is, the number of events that passed the prescale condition. The reason for using this definition for N_i is to avoid a possible situation where, for instance, some T4 triggers do *not* pass the prescale condition. This would automatically imply (based on Equation 5.11) that the T3 trigger efficiency is a lot better than it really is, where it may in fact not be as good.

5.2.3.3 Results

The plot in Figure 5.17 shows the T3 trigger efficiency as a function of run number. Averaging over all runs used in the analysis, the average T3 trigger efficiency turns out to be

99.95%. Appendix A shows the T3 trigger efficiency binned by the momentum setting in the LHRS.

The runs for which the efficiency is exactly 100% is due to a statistical issue. Performing a check of all the cuts used, it has been noted that with each successive PID cut applied, the number of events drops significantly (especially for the T4-type events). The fact that the PID cuts remove most, if not all, of the T4-type events indicates that such events were not in fact good electrons – as these events (knock-on electrons from collisions with pions) must have shown up under the one photoelectron peak in the gas Čerenkov ADC sum spectrum (the cut was placed so that only events for which *more than* 1.5 photoelectrons are generated are kept). Furthermore, due to the cut in E/p in the pion rejector, the pion peak is explicitly excluded from the analysis – another point at which knock-on electrons would show up, and are therefore excluded. Keeping this in mind, the results for the T3 trigger efficiency are satisfactory.

The results of the T3 trigger study reveal that such a cut on the T3 trigger will not affect the analysis as the losses in the data are less than 0.05%.

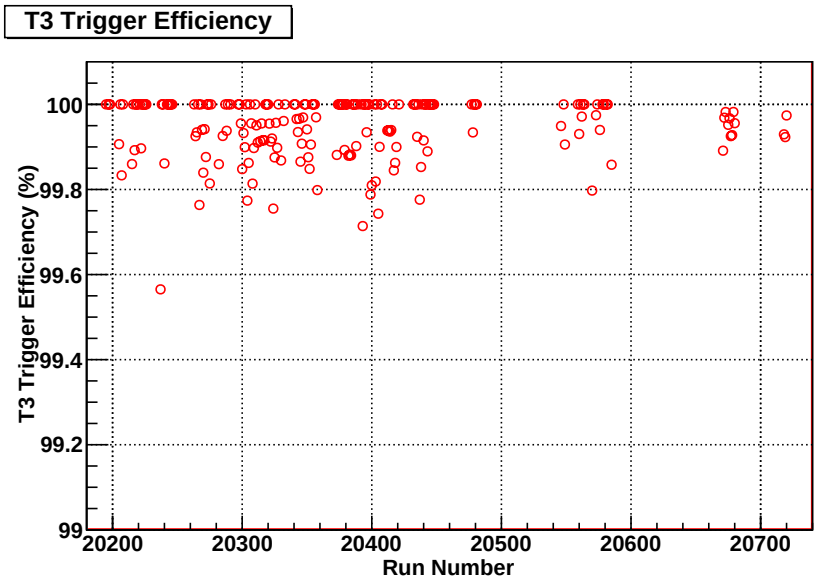

Figure 5.17: The T3 trigger efficiency as a function of (production) run number. Due to a lack of statistics, there are runs for which the efficiency is exactly 100%, which has been confirmed by observing ε_{T3} as each PID cut was applied and varied. See text.

5.2.4 Live Time

Once the main triggers of the LHRS (Sect. 5.2.3) have reached the trigger supervisor (TS), they are synchronized and sent to the DAQ system. Ideally, all of the events that generated

a trigger and subsequently reached the DAQ would be recorded. However, it is possible that the trigger rate is too high and some events are not recorded. Such a situation is known as *dead time* (t_{DT}) for the detector. This phenomenon has to be accounted for in the final cross sections, and is done so by implementing a correction called the *live time correction factor*, $t_{LT} = 1 - t_{DT}$.

5.2.4.1 Method

We determine the live time for a given run according to:

$$t_{LT} = \frac{\text{evtypebits3}}{t3c}, \tag{5.13}$$

where evtypebits3 is the number of T3 triggers accepted by the TS and $t3c$ is the total number of triggers generated for a given run. Ideally this number would be 100%; however, due to the limitations of the hardware combined with the rates of the experiment, this quantity typically turns out to be somewhat lower.

To calculate the live time, we count the number of good triggers recorded for a given run and compare it to the total number of triggers generated for the run, which is read out in the scaler data. We then form the ratio of these two numbers to obtain the live time. Before that, we first correct the data for the possibility of beam trips (Sect. 5.2.1.4).

In order to carry out this procedure, we examine the data event-by-event for a given run and check whether or not it occurred during a beam trip. If it is a good event (i.e., not during a beam trip), we check to see if it passes the requirement that it generated a T3 trigger that was accepted by the TS. This is carried out for each good section of beam during the run. This determines our numerator in Equation 5.13. To determine the denominator, we record the scaler count $t3c$ at the start and end of each good beam segment for the run. The difference of these counts for the segment tells us how many triggers were generated for that segment. The sum of all these scaler counts for all good beam segments for the run gives the denominator above.

5.2.4.2 Results

The results of the study are shown in Figure 5.18. The live times are $\geq 90\%$ for most runs.

5.2.5 Acceptance

The *acceptance* describes the solid angle that can be seen by the opening of the spectrometer. Mathematically, it is the product of $r\Delta E'\Delta\Omega\Delta Z$, where r is a weight factor determined

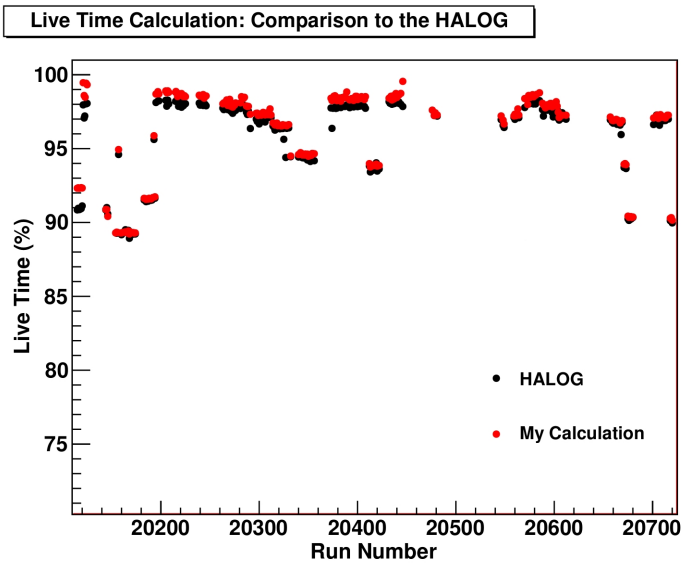

Figure 5.18: Live time study. Plotted on the x-axis is the production run number. Plotted on the y-axis is the live time. The black points are the estimated values during the experiment, while the red points represent the offline calculation taking into account the removal of beam trips.

from a Monte Carlo simulation (Sect. 5.2.5.1); the energy width viewed by the spectrometer is $\Delta E'$; the angular distribution $\Delta\Omega$ is defined by $\Delta\theta$ in the vertical (dispersive) direction and $\Delta\phi$ in the horizontal (transverse) direction; ΔZ is the length of the target.

5.2.5.1 Single-Arm Monte Carlo

Determining the effective angular acceptance utilized the Single-Arm Monte Carlo (SAMC) simulation. To determine how the geometrical acceptance of the LHRS deviates from the ideal rectangular acceptance, SAMC begins by generating events uniformly distributed in the kinematical phase space. Particles are transported to the focal plane using [199], an optical model of the HRS. As the particle encounters each magnet aperture in the HRS, a check is performed to see if it successfully passed through the aperture. If the event successfully makes it to the focal plane, it is then reconstructed at the target using the optics matrix utilized during the experiment.

The ratio of the number of reconstructed events to the number of thrown events gives the acceptance weight r that is used to determine the effective acceptance, written as:

$$\Delta E'\Delta\Omega\Delta Z = r\Delta E'_{\rm MC}\Delta\Omega_{\rm MC}\Delta Z_{\rm MC}, \tag{5.14}$$

where the subscript MC refers to the illuminated widths in SAMC, which are larger than the acceptance of the LHRS, so as to avoid edge effects. The computed acceptance using

SAMC is shown in Figure 5.19.

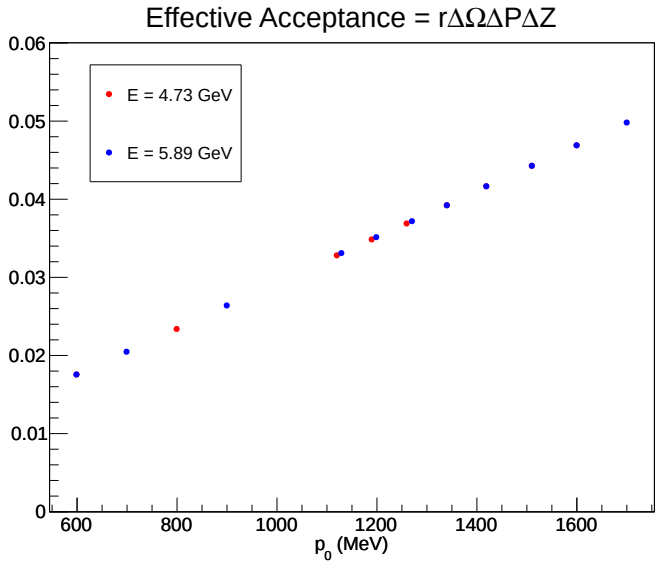

Figure 5.19: The effective acceptance for each momentum bin measured in the LHRS. The red data points indicate the $E = 4.74\,\text{GeV}$ data, while the blue data points represent the $E = 5.89\,\text{GeV}$ data.

Figure 5.20 shows a comparison of SAMC to data (black). The green curve shows the simulated distributions without cross section weighting; the red curve shows the simulated data weighted by the Mott cross section; and finally, the blue curve shows the simulation weighted by a cross section model by P. Bosted [200]. Multiple scattering and energy loss processes are applied to all simulated distributions.

To compute the numerical value of the angular acceptance, the angular variables, θ and ϕ, are thrown *larger* than the nominal values of the LHRS ($\pm$ 60 mrad and $\pm$ 28 mrad respectively, for a solid angle of ≈ 6.7 msr [152]). The number of generated events which reach the focal plane satisfying the analysis cuts is determined. The ratio of the number of these events to the number thrown gives the weight r. The effective angular acceptance is then determined from Equation 5.14 by solving it for $\Delta\Omega$, and inserting the *cuts* used in the data analysis to define $\Delta E'$ and ΔZ. This yields an effective angular acceptance $(\Delta\Omega_{\text{eff}})$ that is roughly constant at ≈ 3.2 msr as a function of momentum bin. The effective angular acceptance is smaller than the nominal value because the full acceptance is not used in our analysis. Events that scatter from the target windows and edge effects from scattering from the magnets are removed. In the calculations of the acceptance, energy loss effects are turned *off*. These effects are taken care of in the radiative corrections (Sect. 5.4.3).

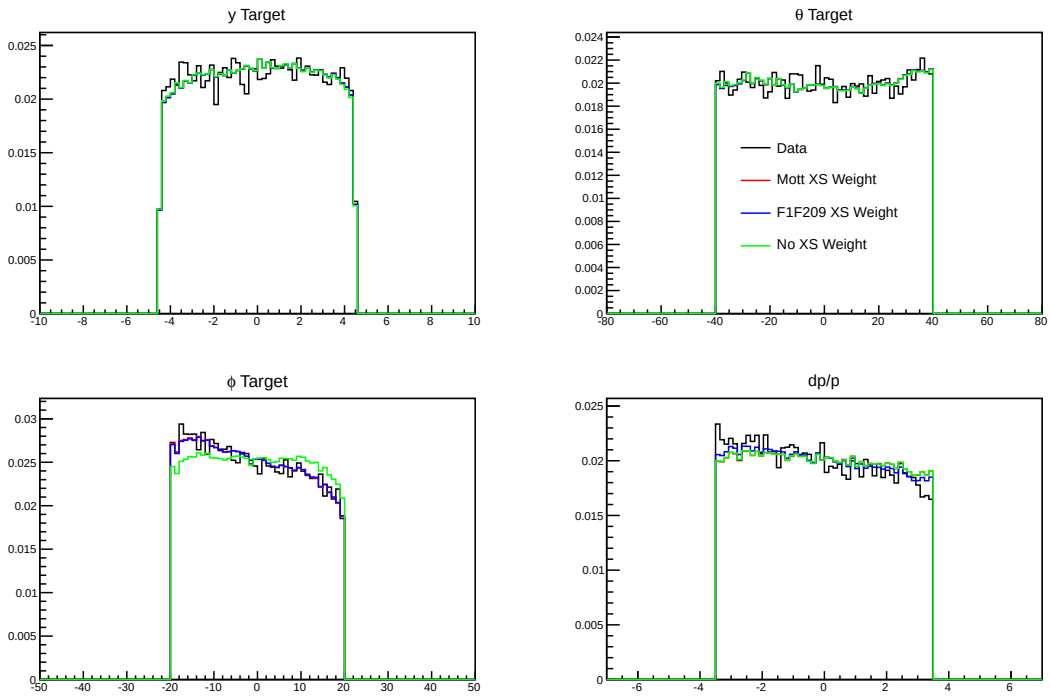

Figure 5.20: SAMC compared to data for the target variables. The black curves show the data, while the various colors show the simulation.

5.2.6 Analysis Cuts

We list below the final cuts that were determined as a result of the preceding studies. These cuts are used in the cross section analysis (Sect. 5.4):

- *Trigger cuts*:
  (DL.edtpl==0)&&((DL.evtypebits&(1<<3))==(1<<3))

- *PID cuts*:
  (L.cer.asum_c> 400)&&(TDC cuts on the gas Čerenkov)
  (prl_E_P> 0.54)&&(L.prl1.e> 200)
  (L.tr.beta> -0.15)

- *VDC cuts*:
  L.tr.n==1
  (L.vdc.u1.nclust==1)&&(L.vdc.v1.nclust==1)
  (L.vdc.u2.nclust==1)&&(L.vdc.v2.nclust==1)

- *Acceptance cuts*:
  (abs(L.tr.tg_y)<0.045)

(abs(L.tr.tg_dp)<0.035)
(abs(L.tr.tg_th)<0.04)&&(abs(L.tr.tg_ph)<0.02)

- *Data quality cuts*:
  skim.beam_trip==0
  (abs(ExTgtCor_L.p)>0)&&(abs(ExTgtCor_L.p)<10)

The TDC cuts for the gas Čerenkov are determined on a run-by-run basis, where a Gaussian fit is performed on each TDC spectrum and the mean is extracted. A cut window of $\pm$25 TDC channels (50 ns) is applied to each TDC spectrum. These TDC cuts are ORed together, so that if an event generates a signal that passes any one of the TDC cuts, the event is counted. The cut on the variable "ExTgtCor_L.p" is on the extended target-corrected reconstructed momentum, and is used to restrict reconstructed momenta to have reasonable values*. It was found that this cut had little effect on the results, and the difference between this variable and the regular momentum reconstructed from tracking, "L.tr.tg_p", was negligible for good electrons. The beam trip cut indicated removes beam trips from the data set.

5.3 BigBite

In this section, we outline the data analysis required for the BigBite data set. This includes data quality studies (Sect. 5.3.1), particle identification (Sect. 5.3.2), acceptance studies (Sect. 5.3.3) and detector performance studies (Sect. 5.3.4). The majority of these analyses were conducted by M. Posik, and a more detailed account may be found in [169].

5.3.1 Data Quality

Similar to what is seen in the LHRS, data quality cuts are needed to remove unwanted events for the data recorded on BigBite. These cuts include beam trip cuts (Sect. 5.3.1.1), events scattering from outside the target region (Sect. 5.3.1.2), events passing through poorly understood regions of the magnet (Sect. 5.3.1.3), and checks concerning the position of reconstructed tracks in the wire chambers compared to the calorimeter (Sect. 5.3.1.4), and finally, the quality of the reconstructed tracks (Sect. 5.3.1.5).

*At the beginning of an event in the Analyzer, all values are set to an arbitrarily large number; if tracking fails, the momentum retains such an unphysical number.

5.3.1.1 Beam Stability

The definition of beam trip cuts should be identical to that seen for the LHRS (Sect. 5.2.1.4); however, the LHRS had a lower scaler readout rate. As a result, the LHRS beam current reading as a function of time appears to be more stable, due to the effective averaging over the noise that would occur with faster readout rates. This leads to an average beam current within $\pm 1\ \mu$A of the current set-point value. Because of the faster readout rates, a slightly modified approach compared to the LHRS had to be utilized in removing beam trips from the BigBite data.

The analysis was conducted by D. Parno [47], and follows closely to what was explained in Section 5.2.1.4. The difference between the two approaches is that 50 consecutive scaler readings were averaged together to form a beam current sample, as opposed to the LHRS where no averaging was done. Despite scaler readouts needing to be averaged together for the analysis, the resulting beam current still had a timing resolution of ≈ 1.25 s per readout group [47].

5.3.1.2 Vertex Cut

In the data analysis, we want our sample of events to contain electrons scattering from ^{3}He in the 40 cm cell. A number of things were done to ensure that such electrons were detected: first, 10 cm-thick tungsten-powder collimators were inserted between each of the target windows and the BigBite spectrometer [169]. This lowers the background produced from electrons scattering from the target windows. Second, cuts on the reconstructed scattering vertex are applied via tracking and optics software. The cut used was 0 ± 17 cm, where $z = 0$ is the nominal target center. This cut was applied for the $E = 4.74$ and 5.89 GeV data sets.

5.3.1.3 Magnet Cuts

As discussed in Section 4.2.2, the BigBite optics package assumes a uniform magnetic field throughout the magnet volume. However, there are non-uniformities which directly affect a particle's path and momentum. There are two approaches to fix this problem. The first is to correct the particle's path-dependent momentum as it passes through the magnet. The second option is to remove regions of the magnet where the field variations are seen to be large. Due to the limited elastic calibration data taken during the experiment and the limited production statistics, the latter method was employed.

To restrict events to regions of the magnet that are well understood, geometric cuts were applied according to where the front and back tracks of an event intersected with the magnet

bend-plane (Sect. 4.2.2). A second cut employed was determined from looking at elastic scattering data, removing events where a sharp change in the reconstructed momentum occurred [169].

Another effect that had to be considered were events that would rescatter from an iron pole or coil housing of the magnet; such rescattering could result in an electromagnetic shower or the event could have a reconstructed track in the MWDC, and thus affect the reconstructed momentum. Events of this type were removed from the electron sample by looking at events with $E < 1\,\text{GeV}$ and $p > 1.5\,\text{GeV}$, which were found to be disproportionately likely to intersect the magnet bend-plane at its horizontal edges. The correlation between the tracks' horizontal positions on the bend-plane and their horizontal slopes at the wire chamber was examined, and it was determined that rescattering occurred at $\approx 23\,\text{cm}$ upstream of the bend-plane. Such events were removed from the analysis. This analysis was done by D. Parno [47].

An additional cut on the reconstructed momentum was used. This was needed because tracking and optics reconstruction algorithms sometimes fail, resulting in unrealistic values being assigned to the reconstructed momentum. Such failed tracks are removed from the data analysis by requiring that the reconstructed momentum p falls within $0 < p < 10\,\text{GeV}$ [169].

5.3.1.4 Track-Matching With the Calorimeter

In constructing the ratio of E/p for an open-geometry detector like BigBite, we need to be certain that both E and p are obtained from the same event. To this end, the central cluster position in each calorimeter was compared to the reconstructed track from the MWDC projected onto the calorimeter layer in question. In considering a histogram of the difference of these two quantities, events showing a difference that was within 3σ were retained and all others were rejected.

5.3.1.5 Track Quality Cut

The track quality was determined by comparing how well a computed track position in each wire plane agrees with the reconstructed track hit position in the planes. This can be expressed as the χ^2 for each track, summing over the difference between the reconstructed track and the computed track position; the weight of the sum was the inverse of the resolution of the wire planes. However, the calculated quantity peaks well below 1, which was due to an overestimate of the wire plane resolutions; despite this, it is still useful in determining the tracking quality. It was redefined as k^2/N_{dof} to avoid the confusion of χ^2/N_{dof}; we keep events for $k^2/N_{\text{dof}} < 5$ [169].

5.3.2 Particle Identification

For all valid tracks, electrons are selected using particle identification cuts in the analysis. Pions or positrons can be selected when studying background contaminations of the asymmetries (Sect. 5.5).

5.3.2.1 Charge Cut

Negatively charged particles bend upwards into the BigBite detector stack when the magnet is set to negative polarity mode, while positively charged particles bend downwards. When the magnet polarity is reversed, this trend is reversed.

Due to the large acceptance of BigBite, both negatively- and positively charged particles can be detected for a given run. Each type of charged particle is tagged with a "charge flag," -1 for upward-bending particles, and +1 for downward-bending particles. This is demonstrated in Figure 5.21, which plots the vertical track position x vs. the vertical slope of the track x'; both positions are located at the first MWDC. A negative vertical slope means that the particles bent upwards, based on the BigBite detector coordinate system. At the center of the plot are tracks that did not get assigned a charge flag; these events have large momentum and their bend trajectory cannot be determined. As a result, they are removed from the analysis [169].

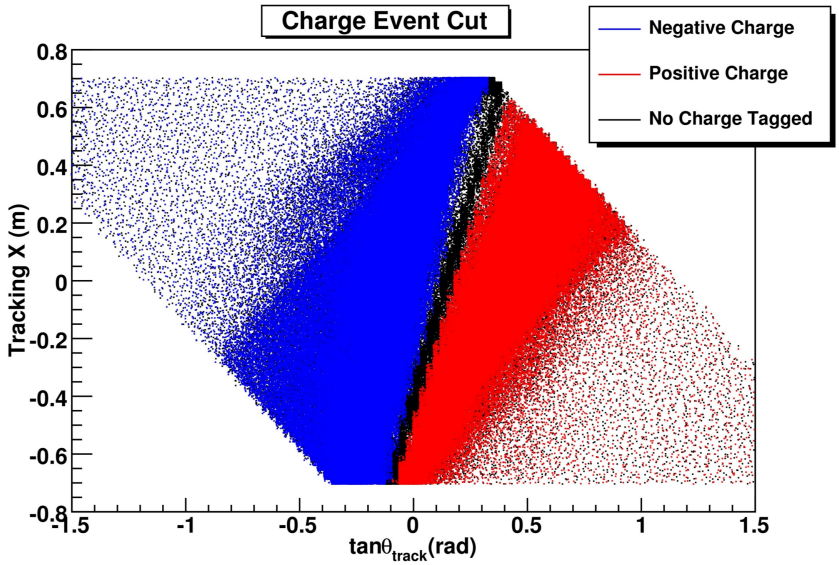

Figure 5.21: The plot of the event distribution in the vertical track position x vs. the vertical slope of the track x'. Negatively charged events are highlighted in blue, while positively charged particles are highlighted in red. Figure reproduced from [169].

5.3.2.2 Trigger Cut

The main trigger used for production mode was the T2 trigger, corresponding to the geometrical overlap of the gas Čerenkov and shower signals. Pions were removed from the online trigger by imposing a hardware threshold on the shower signal, where the particle needs to deposit a given amount of energy* to generate a signal.

In the offline analysis after the experiment run was completed, the electron sample was improved by requiring events that generate a T2 trigger, the so-called "T2 trigger cut" (Sect. 4.1.3).

5.3.2.3 Scintillator Cuts

Due to the nature of our experiment being effectively two single-arm experiments with one on the LHRS, the other on BigBite, the timing information provided by the scintillating plane was not important. However, the PMTs of the scintillating paddles do record ADC signals corresponding to the energy deposited by impinging particles. This turned out to be a useful PID tool to reject charged hadrons like $\pi^{\pm}$, as these particles tend to deposit less energy than electrons in the scintillating paddles. Therefore, cuts applied to the ADC signals can assist in rejecting pions while selecting electrons. In particular, the cut used in the analysis was such that particles depositing less than 500 MeV in the scintillators were rejected in the analysis, as these represented pion-like events [169].

5.3.2.4 Gas Čerenkov Cuts

The gas Čerenkov was included in the T2 trigger, which resulted in the removal of pions already, as mentioned in Section 5.3.2.2. Additional cuts were applied in the data analysis to further clean up the electron sample through TDC cuts and PMT acceptance (mirror) cuts.

5.3.2.4.1 TDC cuts

The timing information recorded by each PMT was stored in multi-hit TDCs†, where each TDC can record and store information for up to 16 hits (signals); however, it was found that only the first hit carried any relevant timing information. All other hits had times that were far from the electron timing peak [169].

To distinguish between the hits that form the trigger and accidentals, the Čerenkov TDC spectrum can be analyzed as shown in Figure 5.22. The black spectrum shows events that

*This threshold corresponded to ≈ 500 MeV [169].

† This differed from the LHRS, where the TDCs were single-hit.

have at least one track associated with them, and the blue histogram corresponds to events that satisfy the requirements of data quality cuts. We note the sharp peak at TDC channel 0, which is the electron timing peak, along with a rectangle-shaped shoulder. It is seen that applying data quality cuts reveals that the shoulder in the black histogram corresponds to accidental events*.

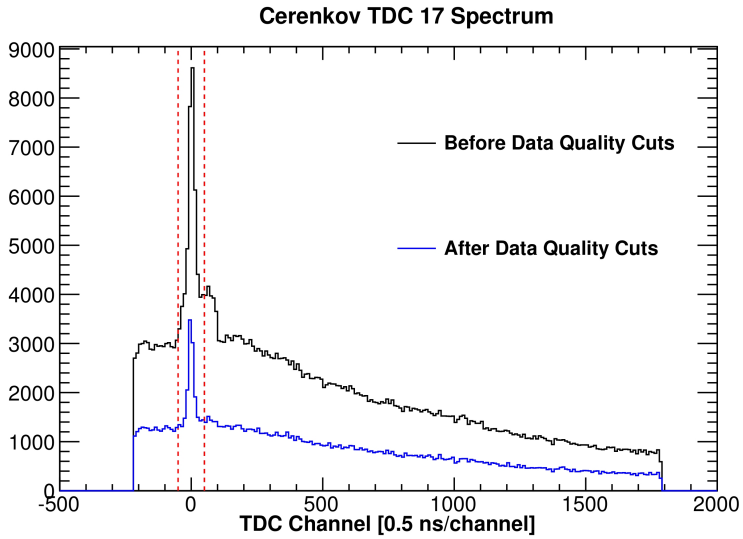

Figure 5.22: A representative TDC for a PMT in the gas Čerenkov. The black histogram has no cuts. The blue histogram shows the TDC distribution after data quality cuts have been applied. The vertical red lines indicate the cut window. Figure reproduced from [169].

The cut utilized in the analysis is displayed in Figure 5.22, where the red-dashed lines indicate the cut, at 100 TDC channels (50 ns) wide. Because the timing peak varies for each PMT, an offset was applied to each spectrum to align them at TDC channel 0. Even with these Čerenkov timing cuts, there is still a significant amount of hits that are accidentals.

5.3.2.4.2 PMT Acceptance Cuts

In order to remove more accidental events, one can exploit the acceptance of the PMTs. This is accomplished by associating the particle track in the MWDCs with a given hit in the Čerenkov, thus determining upon which PMT the given track should impinge upon. Additionally, the location of a particular PMT's acceptance can be determined by requiring a PMT's TDC to have a hit within its timing cut, along with having an ADC signal greater

*The shoulder seen in the black histogram correspond to events that generate a T6 trigger; due to the way the electronics was set up, it is seen then that accidental events that fall in the T6 gate can falsely generate a T2-type event [169].

than three photoelectrons. After identifying the PMT acceptance in the vertical and horizontal direction in the Čerenkov plane, geometrical cuts are determined. Combining both vertical and horizontal cuts yields significant improvement in cleaning up a given PMT's TDC spectrum, as shown in Figure 5.23. The black histogram shows the TDC distribution for a given PMT before the cuts, and the red histogram shows the spectrum after the cuts. The vertical red dashed lines mark the TDC timing window cut used (Sect. 5.3.2.4.1).

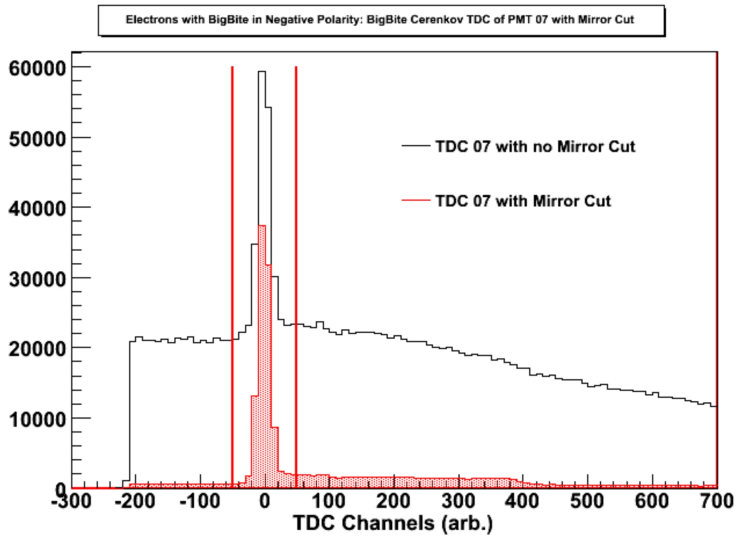

Figure 5.23: The effect of using the vertical and horizontal PMT acceptance cuts on an arbitrary TDC distribution. The black histogram shows the TDC distribution without PMT acceptance cuts; the red histogram has TDC cuts applied. Figure reproduced from [169].

5.3.2.4.3 Full Electron Cut

The electron sample, as defined by the gas Čerenkov, is determined by combining all the cuts just explained. To summarize, we require for a given PMT to record a hit in its TDC, and that hit has to fall within the timing window cut, and finally the projected track has to fall within the PMT acceptance. These cuts are applied individually for each PMT and are ORed together in the analysis. We also note here that no ADC cut was used in the analysis, as such a cut reduced the statistics uniformly across the acceptance, and did not improve the quality of the electron sample.

The full effect of the gas Čerenkov cut can be seen in Figure 5.24, which displays the ADC signal of an arbitrary PMT. The black histogram is the raw signal; the green histogram

has a TDC cut applied; the blue histogram utilizes a PMT acceptance cut*; and finally, the red histogram requires both a TDC cut and a PMT acceptance cut. We can see that most of the contamination of the signal has been removed. The vertical dashed line indicates the 5 photoelectron position.

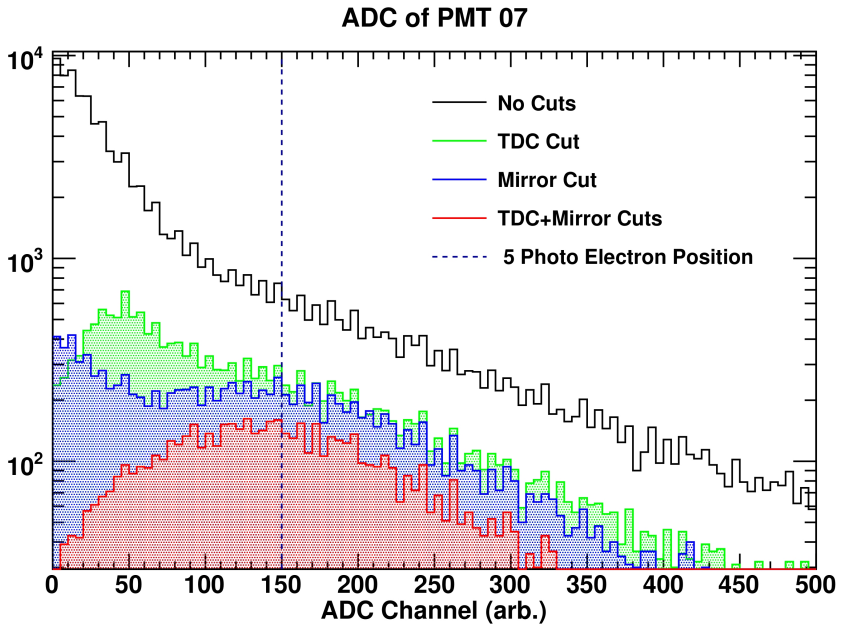

Figure 5.24: The effect of using all of the gas Čerenkov TDC and PMT acceptance cuts and how it affects that PMT's ADC spectrum. The various colors indicate the application of a different cut, see text. Figure reproduced from [169].

5.3.2.5 Calorimeter Cuts

5.3.2.5.1 Preshower Cuts

Due to the thickness of the preshower being only 8.5 cm, non-showering particles like pions deposit $\lesssim 100$ MeV in the calorimeter, whereas showering particles like electrons deposit $\gtrsim 200$ MeV. Therefore, to remove the unwanted pion events, a cut of $E_{ps} > 200$ MeV was used†. The same cut was used for both the $E = 4.74$ and 5.89 GeV data sets. In addition to an ADC signal for each PMT in the preshower, there were TDC signals that could be used for PID purposes. The cut used was similar to the ones used for the gas Čerenkov TDCs.

*Such a cut is also referred to as a "mirror cut," as it reflects the geometry of the mirror that the PMT views in the Čerkenov.

†This is comparable to the cut used in the LHRS analysis for the first layer of the pion rejector (Sect. 5.2.6).

5.3.2.5.2 Shower cuts

With electrons traversing more material in the shower blocks, they deposit nearly all of their energy in the shower. In the kinematics of our experiment, $E \sim p$ implies that $E/p \sim 1$. On the other hand, pions deposit much less energy, and so $E/p < 1$. This difference can be exploited to further reduce pion backgrounds. The cut used for the shower calorimeter was:

$$|E/p - \langle E/p \rangle| < 2\sigma, \tag{5.15}$$

where E/p is the measured value and $\langle E/p \rangle$ is the mean of a Gaussian fit to the data, with σ being the width. Due to changing triggers, hardware issues and detector threshold changes, a cut was needed for each run period corresponding to the $E = 5.89\,\text{GeV}$ data set. More details may be found in [169].

5.3.3 Acceptance

Physical gaps in the acceptance of the shower calorimeter were discovered during the experiment. This was due to the overloading of the summing module associated with the calorimeter towards the beginning of E06-014. As a result, events did not pass energy thresholds set on the shower energy, leading to an absence of generated T1, T2 and T6 triggers. The effect of this can be seen in by examining the reconstructed tracks from the MWDCs projected onto the shower plane.

After the summing module was fixed, there were still observed gaps in the acceptance, see Figure 5.25. This was traced back to faulty calorimeter blocks. If a block has a problem, then its ADC signal will be lower than other ADC signals.

Fortunately, the acceptance gaps did not affect the (offline) asymmetry analysis. To compensate the blocks with low ADC signals, larger calibration gain-matching constants were applied (Sect. 4.2.5). Additionally, gaps in the acceptance should not have too much of an effect, since the acceptance cancels in the calculation of the asymmetry (Sect. 5.5).

5.3.4 Detector Performance

In this subsection, we summarize the performance of BigBite via PID cuts. In particular, we examine results for the gas Čerenkov, which includes photoelectron yields, electron detection and cut efficiencies and pion rejection factors. We also present similar studies for the preshower and shower calorimeters.

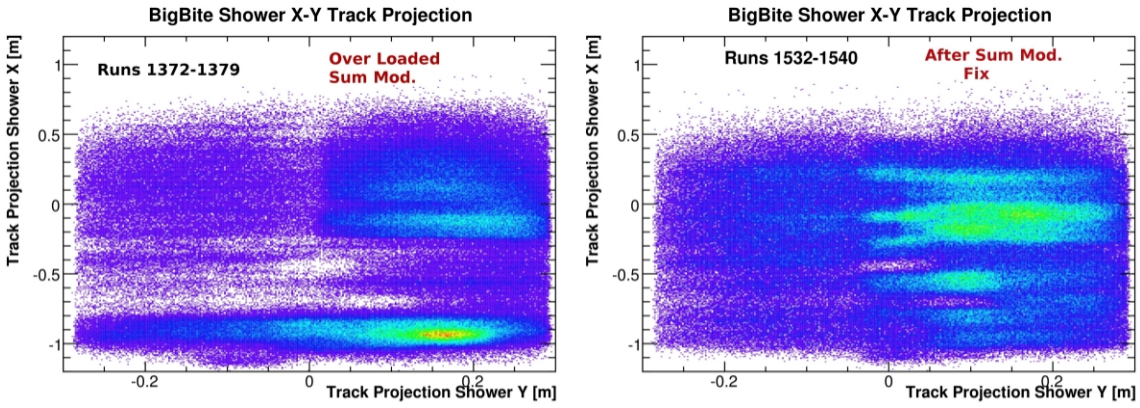

Figure 5.25: Event distribution in the BigBite shower plane, before and after the shower calorimeter summing module repair. Figure reproduced from [169].

5.3.4.1 Gas Čerenkov

The E06-014 experiment served as the commissioning experiment for the gas Čerenkov detector in BigBite. Thus a study of the performance of the detector is crucial for not only the current data analysis, but also future experiments that utilize the detector.

The small-angle side (beamline side) of the detector saw larger rates, at $\approx$ 400–500 MHz, while the large-angle side observed rates of < 100 kHz [169]. These higher rates on the beamline side resulted in a reduction of performance relative to the large-angle side.

Applying data quality and PID cuts to the ADC distributions and examining the photoelectron yield for each PMT, we can get a good understanding of how well the detector performed. On average, the photoelectron yield was 5–7 photoelectrons for each PMT [169].

The determination of the electron detection efficiency follows closely to what was done for the LHRS (Sect. 5.2.2.4). However, instead of using E/p and the first pion rejector layer, the cuts used for BigBite were as follows: PMT acceptance cuts were made tighter so as to better exclude edge effects; the target vertex cut was also tightened; a momentum cut of $0.8 < p < 1.5$ GeV was used; and finally, a cut on the preshower distribution of $E_{ps} > 400$ MeV was employed. Choosing the electron sample with these cuts, the number of events that fire the gas Čerenkov was then determined. The ratio of the number that fired the gas Čerenkov to the number in the sample chosen by the shower cuts gives the detection efficiency.

The electron cut efficiency was also evaluated for the gas Čerenkov, and follows the same principles outlined for the LHRS analysis (Sect. 5.2.2.4.1). This study was done for the T2- and T6-type events*. The results obtained for T6 events are shown in Figure 5.26,

*This study cannot be done for T1-type events as the statistics were too low, due to the large prescale

and results for the T2 trigger are shown in Figure 5.27. The efficiencies were found to be 90–95% at a Čerenkov cut of 0 p.e. for the T2 trigger; for the T6 trigger, it was found to be 95–100%[†]. The Čerenkov cut efficiency for a cut of 3 p.e. was found to be $\approx 80\%$ for both the T2 and T6 triggers [169].

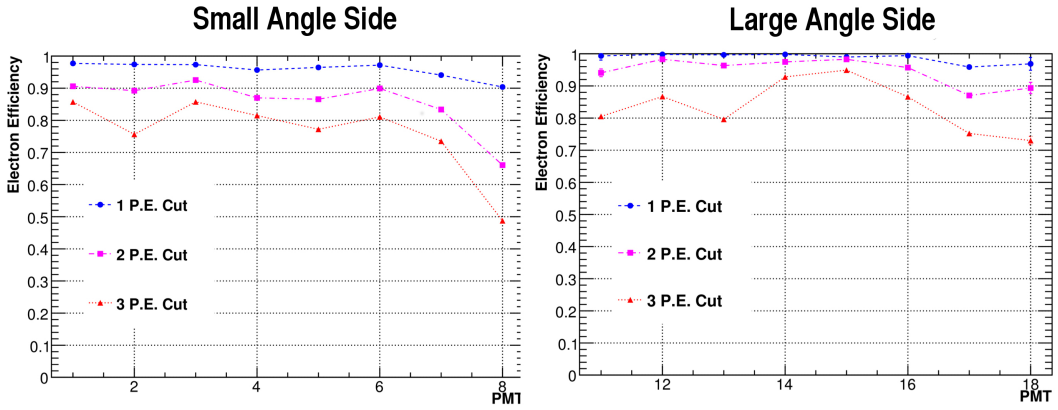

Figure 5.26: Gas Čerenkov electron cut efficiencies for T6 events. Figure reproduced from [169].

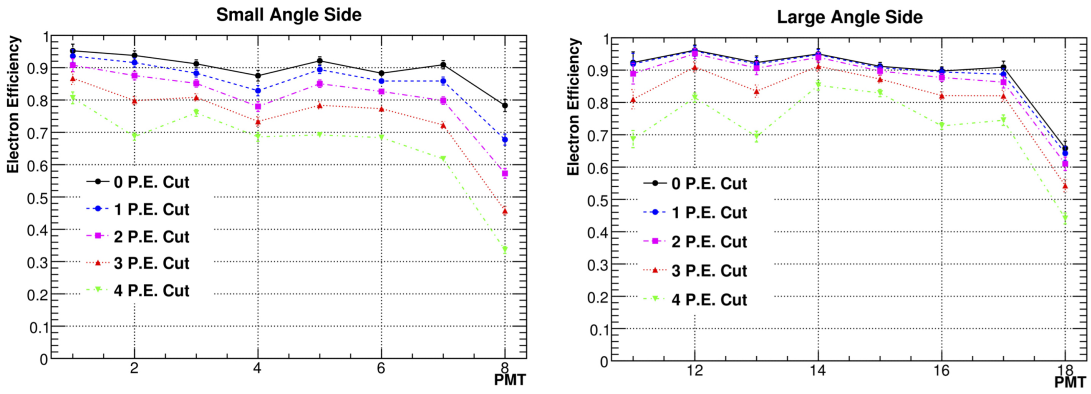

Figure 5.27: Gas Čerenkov electron cut efficiencies for T2 events. Figure reproduced from [169].

To evaluate the pion rejection factor, pions were selected by choosing events with preshower energies in the range $50 < E_{ps} < 80$ MeV, and a scintillator energy of $E_{scint} < 450$ MeV. Also, the E/p distribution was limited to $0.6 < E/p < 0.9$. In defining the denominator of the pion rejection factor (Sect. 5.2.2.3), requirements for the Čereknov included a hit in the TDC timing window, and various ADC cuts (to map out the rejection

setting used during the experiment.

[†]Due to the hardware threshold of 1.5 photoelectrons on the gas Čerenkov, the efficiencies for the T6 trigger had to be evaluated using a modified approach, where the baseline electron sample included a gas Čerenkov cut to effectively remove such a threshold effect [169].

factor as a function of ADC cut). The study was done for low-background runs of $I = 1\,\mu$A (using T1 events), and production currents of $15\,\mu$A using T6 events. The results are presented in Figure 5.28, where the study was broken down between the beamline side (blue), large-angle side (red), and the full acceptance (black). The left panel shows the $1\,\mu$A data, and the right panel shows the $15\,\mu$A data. The final rejection factor found for production data was 21.09 ± 0.02 [169].

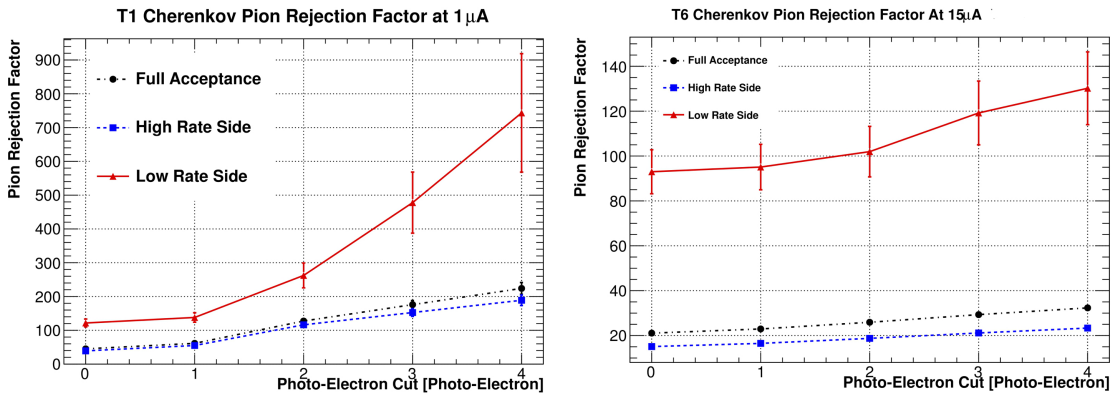

Figure 5.28: Gas Čerenkov pion rejection factors for T1 events for a beam current of $1\,\mu$A (left) and T6 events at a beam current of $15\,\mu$A (right). The blue (red) curve indicates results for the beamline (large-angle) side. The black curve is for results over the full acceptance. Figure reproduced from [169].

5.3.4.2 Calorimeter

In this subsection, we discuss the results of the pion rejection factor studies for the preshower and shower calorimeters. The electron cut efficiencies were not evaluated for these detectors [169].

5.3.4.2.1 Preshower

In evaluating the pion rejection factor for the preshower, pions are selected by placing cuts on the gas Čerenkov and scintillating plane. The cut for the Čerenkov requires the particle to pass through one of the PMT acceptances, and to *not* have a hit in the PMT's TDC timing window. The cut used for the scintillator was for $E_{scint} < 450$ MeV.

The pion rejection factor was determined as a function of preshower energy cut for an E/p distribution corresponding to $0.2 < E/p < 0.8$. The top left of Figure 5.29 shows the results for T1 events at $1\,\mu$A.

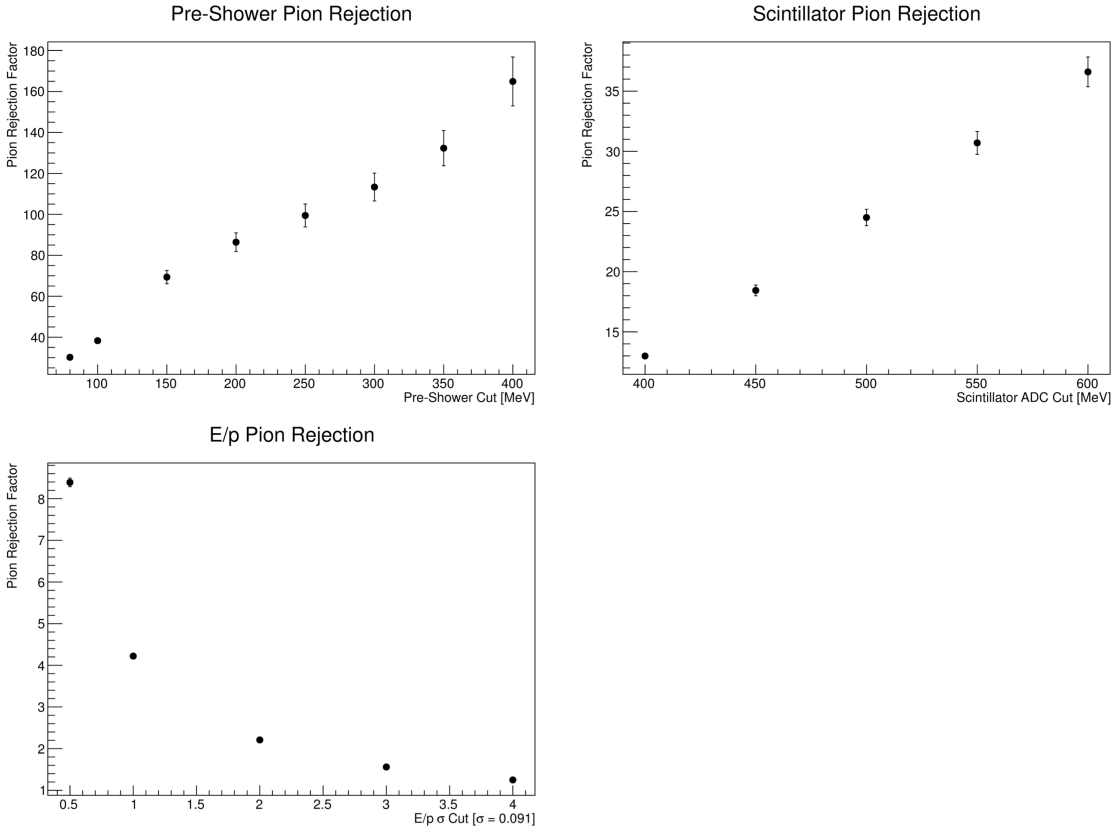

Figure 5.29: Pion rejection factors for the preshower (top left), scintillating plane (top right), and the shower E/p (bottom left). Each result is plotted as a function of their respective cuts. Figure reproduced from [169].

5.3.4.2.2 Shower E/p

In determining the pion rejection factor for the shower E/p distribution, the same pion sample was used as explained in the preshower analysis. The *width* of the E/p cut was varied for this study, which was done over the preshower energy range of $20 < E_{ps} < 160$ MeV. The results are shown in the bottom left of Figure 5.29 for T1 events at 1 μA.

5.3.4.3 Scintillator

The scintillator was found to be helpful in rejecting pions in our data analysis. Here, we discuss the pion rejection factor obtained for the scintillating plane.

Pions are selected using the gas Čerenkov and preshower. The Čerenkov cut used is the same as was seen for the calorimeter analysis. The cut used on the preshower corresponds to $E_{ps} < 120$ MeV, and the E/p cut employed was $0.2 < E/p < 0.8$. The pion rejection

factor was mapped out for various cuts in the scintillator energy, shown for T1-type events at a current of 1 μA in the top right of Figure 5.29.

5.3.4.4 Pion Rejection Results

The full results for the pion rejection factors for T6 events at various cut positions used during the electron analysis are summarized in Table 5.2. The total rejection obtained when combining the rejection power of each detector was on the order of 10^4. The resulting pion contamination in the double-spin asymmetries was found to be be negligible (Sect. 5.5.3.2.1).

Table 5.2: Pion rejection factor results for the gas Čerenkov, scintillator and the calorimeter for T6 events at a beam current of 15 μA. The product of all pion rejection factors from each detector yields the last row labeled "Total." Table reproduced from [169].

Detector	Cut	Pion Rejection
Preshower	Energy > 200 MeV	176.19 ± 0.41
Scintillator	Energy > 500 MeV	7.21 ± 0.00
E/p	2σ	2.59 ± 0.00
Čerenkov	TDC + PMT Acceptance	21.09 ± 0.02
Total	—	$(6.94 \pm 0.41) \times 10^4$

5.3.5 Analysis Cuts

In this subsection, we summarize all of the analysis cuts which are used in the double-spin asymmetry analysis (Sect. 5.5). For more information concerning these cuts and the corresponding analysis to determine them, see [169].

- *Data quality cuts*:
  - Beam trip removal: skim.beam_trip==0
  - At least one reconstructed track: BB.tr.n > 0
  - Momentum cut: skim.p[]>0 && skim.p[]<10
  - MWDC and shower track-matching (x): TMath::Abs(BB.ts.sh.x-1.01134e-2-BB.tr.x[]-1.28*BB.tr.th[])<0.1
  - MWDC and shower track-matching (y): TMath::Abs(BB.ts.sh.y+6.4908e-3-BB.tr.y[]-1.28*BB.tr.ph[])<0.1
  - MWDC and preshower track-matching (x): TMath::Abs(BB.tr.x[]+0.97*BB.tr.th[]-BB.ts.ps.x+7.8303e-3)<0.2

- MWDC and preshower track-matching (y): TMath::Abs(BB.tr.y[]+0.97*BB.tr.ph[]-BB.ts.ps.y-0.01)<0.19
- Tracking quality: BB.tr.chi2[]/BB.tr.ndof[]<5

- *Trigger cuts*:
  - (DBB.evtypebits&(1<<2))==(1<<2) (for the T2 trigger)

- *PID cuts*
  - Charge cut: BB.optics.charge[]==(1,-1)
  - Preshower cut: 0.5*BB.ts.ps.e $>$ 200
  - E/p cut: (0.5*BB.ts.ps.e + BB.ts.sh.e)/(1000*skim.p[]) $>$ 0.833 && (0.5*BB.ts.ps.e + BB.ts.sh.e)/(1000*skim.p[]) $<$ 1.158
  - GC TDC cuts: Ndata.DBB.BBcerT%02d>0 && (TMath::Abs(DBB.BBcerT%02d[Ndata.DBB.BBcerT%.2d - Ndata.DBB.BBcerT%.2d] - offset)<width)

- *Acceptance cuts*
  - z-vertex cut: TMath::Abs(BB.tr.vz[])<0.17
  - Geometrical optics cuts: (BB.optics.vzflag[]==1)&&(BB.tr.tg_th[]<0.2)
  - Rescattering cuts: (BB.optics.bendx + 0.23*BB.tr.ph)>-0.097 && (BB.optics.bendx + 0.23*BB.tr.ph)<0.13

5.4 Unpolarized Cross Sections

With our analysis cuts in hand (Sect. 5.2.6), we now turn to calculating the unpolarized cross section. In this section, we will discuss how the raw cross section, $\sigma_{\rm raw}$, was determined (Sect. 5.4.1). In Section 5.4.2, we will show how the experimental (or radiated) cross section, $\sigma_{\rm rad}$, was extracted from the raw result. Section 5.4.3 shows how the radiative corrections to $\sigma_{\rm rad}$ were performed to obtain the Born cross section, $\sigma_{\rm Born}$. The systematic errors due to various components like our analysis cuts and radiative corrections are given in Section 5.4.5.

5.4.1 Calculation From Raw Data

The cross section is calculated from the data for a given run as follows:

$$\frac{d^2\sigma_{\text{raw}}}{d\Omega dE'} = \frac{t_{ps}N_{\text{cut}}}{(Q/e)\rho t_{LT}\varepsilon}\frac{1}{\Delta E'\Delta\Omega\Delta Z}, \tag{5.16}$$

where each quantity is as follows: t_{ps} is the prescale value for the T3 trigger; N_{cut} is the number of electrons that pass all cuts (Sect. 5.2.6); Q/e is the number of beam electrons; ρ is the target density in amagats; t_{LT} is the live time which corrects for the high trigger rates during the experiment, resulting in the detectors not recording every event. ε is the product of all detector (cut) efficiencies; $\Delta E'$* is the energy width in MeV for the given momentum bin being studied; ΔZ† is the effective target length seen by the spectrometer in meters and $\Delta\Omega$ is the angular acceptance. The second fraction, characterized by $1/(\Delta E'\Delta\Omega\Delta Z)$, is determined from SAMC (Sect. 5.2.5).

Once we have the results for each run calculated, we then calculate a weighted-average to obtain the cross section for a given momentum bin. The weighted-average cross section $\langle\sigma\rangle$ over n runs is calculated as:

$$\langle\sigma\rangle = \frac{\sum_{i=0}^{n}\sigma_i\frac{1}{\delta\sigma_i^2}}{\sum_{i=0}^{n}\frac{1}{\delta\sigma_i^2}}, \tag{5.17}$$

where $\delta\sigma_i$ is the statistical error on the i^{th} cross section. The explicit form of the statistical error is:

$$\delta\sigma = \sigma\sqrt{\sum_{j=1}^{m}\left(\frac{\delta a_j}{a_j}\right)^2}, \tag{5.18}$$

where a_j is each component in Equation 5.16 that has a statistical error attached to it. These terms include N_{cut}, Q/e, t_{LT} and ε. Now, ε is a product sum of the cut efficiencies. Therefore, its derivative is written as:

$$d\varepsilon = \sum_{k=1}^{p} d\varepsilon_k\left[\prod_{\ell\neq k}^{p}\varepsilon_k\right]. \tag{5.19}$$

Adding each component in quadrature for the total error from cut efficiencies gives:

*$\Delta E' = 2\delta p/p\cdot p_0$, where $\delta p/p$ is the half-width of the $\delta p/p$ cut in percent and p_0 is the LHRS momentum setting.

†$\Delta Z = 2y_{\text{tg}}/\sin\theta$, where y_{tg} is the half-width of the cut on the target-y variable and θ is the scattering angle of the LHRS. See Appendix B for more details.

$$\frac{\delta\varepsilon}{\varepsilon} = \sqrt{\sum_{k=1}^{p}\left(\frac{\delta\varepsilon_k}{\varepsilon_k}\right)^2}. \tag{5.20}$$

5.4.2 From $\sigma_{\mathbf{raw}}$ to $\sigma_{\mathbf{rad}}$

5.4.2.1 Extracting the Experimental Cross Section

The raw ^{3}He cross section measured in the LHRS, $\sigma_{\rm raw}$, contains contributions from electrons that do not scatter from ^{3}He, but rather from electron-positron (pair) production processes and scattering from nitrogen nuclei. Pair-produced electrons arise from π^0 production in the target. Before escaping the target cell, a π^0 particle decays to two photons, which convert to e^+e^- pairs; to a much smaller degree, pions decay to γe^+e^-*. Contamination due to nitrogen scattering arise because nitrogen gas is present in the pumping chamber to optimize ^{3}He polarization (Sect. 3.5).

To remove the pair production contributions from $\sigma_{\rm raw}$, several runs were taken with the LHRS in positive polarity mode where positrons were detected. These runs were used to measure a positron cross section, σ_{e^+}. To obtain the nitrogen scattering contribution, a 'reference' target cell was used. The reference cell was similar in geometry to the ^{3}He cell, but was filled with nitrogen gas. Measuring electrons scattering from this target gives a nitrogen electron cross section, $\sigma^{e^-}_{\rm N_2}$. Pair production is also present when scattering from nitrogen nuclei, so a nitrogen positron cross section, $\sigma^{e^+}_{\rm N_2}$, was also measured with the LHRS in positive polarity mode. $\sigma^{e^+}_{\rm N_2}$ was subtracted from $\sigma^{e^-}_{\rm N_2}$ to avoid double counting the pair-produced events that were already accounted for in the measurement of σ_{e^+}. These measurements were then combined to obtain the *experimental* (or radiated) ^{3}He cross section, $\sigma_{\rm rad}$:

$$\sigma_{\rm rad} = \sigma_{\rm raw} - \sigma_{e^+} - \sigma^{dil}_{\rm N_2} \tag{5.21}$$

$$\sigma^{dil}_{\rm N_2} = \frac{n_{N_2}}{n_{N_2} + n_{^3{\rm He}}}\left(\sigma^{e^-}_{\rm N_2} - \sigma^{e^+}_{\rm N_2}\right), \tag{5.22}$$

where $n_{\rm N_2}$ is the number density of nitrogen in the production cell and $n_{^3{\rm He}}$ is the number density of ^{3}He in the production cell. The nitrogen cross sections are scaled down so as to account for the small density of nitrogen in the production target cell†. Figure 5.30 shows

*The branching ratio for $\pi^0 \to 2\gamma$ is 98.79%, and for $\pi^0 \to \gamma e^+e^-$ it is 1.19% [35].

†The amount of nitrogen present in the production cell is on the order of $\sim 1\%$ of the total gas mixture of ^{3}He and nitrogen in the cell.

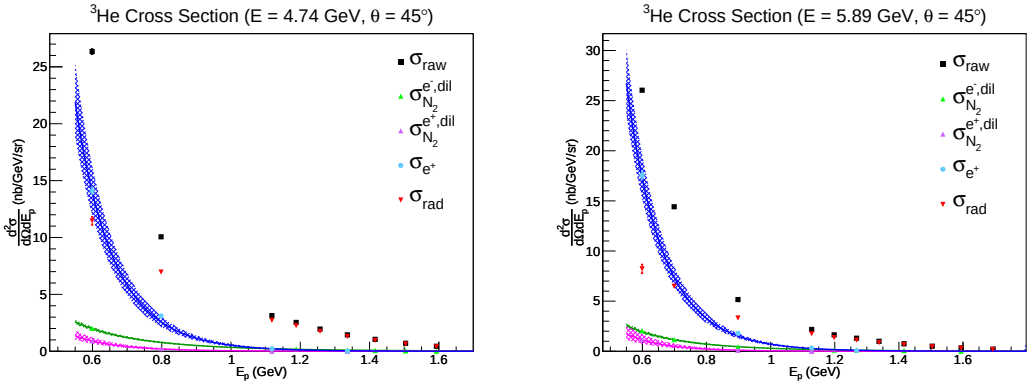

(a) E_s = 4.74 GeV (b) E_s = 5.89 GeV

Figure 5.30: Raw ^{3}He, positron, and diluted N_2 cross sections. The subtraction of all background signals from σ_{raw} yields σ_{rad}, shown in red. The fits to each background signal are shown with thier respective error bands. These fits were used to obtain σ_{rad}. (a): E_s = 4.74 GeV data; (b): E_s = 5.89 GeV data. Tables of σ_{rad} may be found in Appendix E.1.

each of these signals, where σ_{rad} is indicated by the red markers. These data are tabulated in Appendix E.1.

5.4.2.2 Fits to Background Signals

Due to time constraints and problems encountered during the experiment, we were not able to take as much data as desired to map out the background contributions to the raw cross section for all kinematic bins. To circumvent this issue, a fit was made to the nitrogen and positron data, which was then subtracted from the raw signal, as shown in Equation 5.21. The fit for the background contributions was:

$$f(E_p) = \frac{1}{E_p^2} e^{(a_0 + a_1 E_p)}, \tag{5.23}$$

where the variable E_p is the scattered electron energy. After fitting the data using ROOT [189], the error bands were determined by varying each parameter within the its errors and observing the change in the fit. How these errors contribute to the cross section errors will be discussed in Section 5.4.5. The parameters of the fits are summarized in Appendix D.1.

5.4.2.3 Positron to Electron Ratio

With the measurements of the raw electron cross section and the positron cross section in hand, we can extract the e^+/e^- ratio, and is given in Figure 5.38, compared to data from JLab Hall B (CLAS) data. The errors on our data are statistical only. These ratios will play

an important role in determining the positron contamination of the electron double-spin asymmetries (Sect. 5.5.3). Our data are tabulated in Appendix E.1.

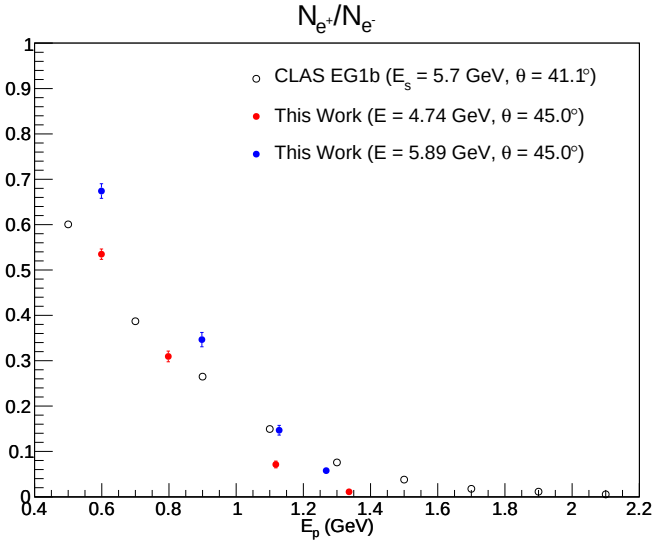

Figure 5.31: The measured e^+/e^- ratio at $E = 4.74$ GeV (red) and 5.89 GeV (blue) compared to JLab Hall B (CLAS) data. The errors on our data are statistical only.

5.4.3 Radiative Corrections

Electrons lose energy due to interactions with material. This includes the material before and after the target, and the target material itself. These interactions will alter the electron's *true* incident energy and also its *true* scattered energy. This ultimately results in a different cross section than the true value. These effects are characterized by ionization (or Landau straggling) and bremsstrahlung. There are also higher-order processes at the interaction vertex that must also be considered. Collectively, the removal of these effects is called *radiative corrections*.

A first correction that must be done *before* carrying out the radiative corrections is to subtract the elastic radiative tail, since it is long and affects all states of higher invariant mass W [201]. For these kinematics, the elastic tail is small and affects the lowest bins in scattered electron energy E_p at the $\lesssim 1\%$ level. The elastic tail was computed following the exact formalism given by Mo & Tsai [201]. We utilized elastic ^{3}He form factors from Amroun [202].

The ^{3}He quasi-elastic tail, however, is much larger, at $\sim$ 25–30% in the lowest E_p bin. The quasi-elastic radiative tail was computed by utilizing an appropriate model of the ^{3}He quasi-elastic cross section [203] and applying radiative effects [204]. The tail was then

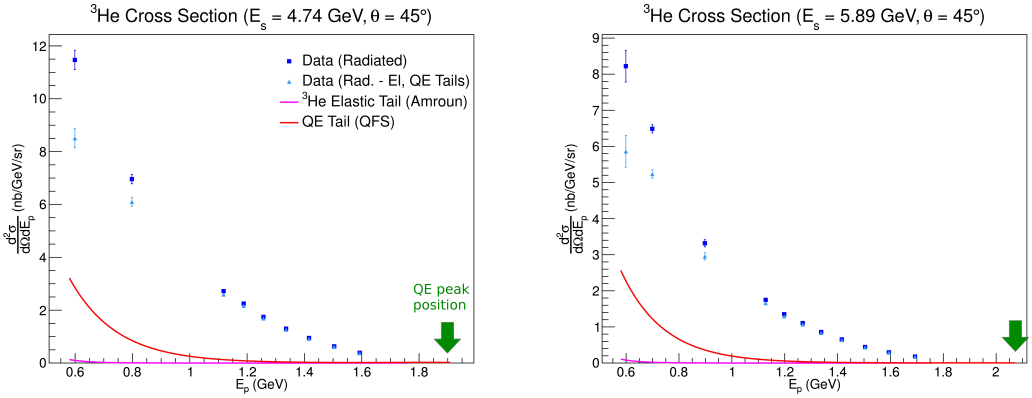

(a) E_s = 4.74 GeV (b) E_s = 5.89 GeV

Figure 5.32: Our data before (blue) and after (cyan) elastic and quasi-elastic tail subtraction. The magenta curve shows the elastic tail, while the red curve is the quasi-elastic tail. The green arrow indicates the position of the quasi-elastic peak. . (a): E_s = 4.74 GeV data; (b): E_s = 5.89 GeV data.

subtracted from the data. The model was checked against existing quasi-elastic ^{3}He data covering a broad range of kinematics.

Figure 5.32 shows our data before and after elastic and quasi-elastic tail subtraction as a function of E_p. The magenta curve shows the elastic tail, while the red curve shows the quasi-elastic tail. The blue (cyan) data show our data before (after) the tail subtractions. The error bars on the data points are statistical only. The green arrows indicate the position of the quasi-elastic peak for each respective data set.

In considering the effects due to ionization and bremsstrahlung mentioned above, the *measured* cross section is realized in terms of a triple-integral:

$$\sigma_{\text{rad}}(E_s, E_p) = \int_0^T \frac{dt}{T} \int_{E_s^{min}}^{E_s} dE_s' \int_{E_p}^{E_p^{max}} dE_p' I(E_s, E_s', t)\, \sigma_r(E_s', E_p')\, I(E_p, E_p', T-t), \quad (5.24)$$

where σ_{rad} is the measured (radiated) cross section, σ_r is the *internally*-radiated cross section. The incident electron energy is labeled as E_s and E_p is the scattered electron energy. The function $I(E_0, E, t)$ is the probability of finding an electron with incident energy E_0 that has undergone bremsstrahlung with energy E at a depth t inside a material [201, 204]. In order to *unfold* the Born cross section, an iterative procedure is carried out in RADCOR [205]. It amounts to an "energy peaking" approximation*, resulting in the lineariza-

*This approximation is valid as the integrands of the integrals in Equation 5.24 are peaked along the incident and scattered electron energies, where the neglected contributions are less than a few percent. Additionally, the equivalent radiator method is used for the internal radiation, where such contributions manifest as effective thicknesses in the electron path before and after scattering. For more details, see [201, 206].

tion of Equation 5.24 where the Born cross section is obtained via an iterative procedure. In particular, the Born cross section for the i^{th} iteration is written as:

$$\sigma_b^i = \frac{1}{\mathrm{C}}\left[\sigma_{\text{rad}} - \int(\ldots)\,dE_s' - \int(\ldots)\,dE_p'\right], \tag{5.25}$$

where C and the two integrals are defined in [204]. The term σ_b^i is the Born cross section obtained for the i^{th} iteration of the code and σ_{rad} is the radiated cross section to be corrected. The cross section σ_b^i is then re-inserted into equation for the next iteration. In E06-014, we took data for only two E_s values of 4.74 GeV and 5.89 GeV. However, we need enough data to properly calculate the integrals above. Therefore, we used the F1F209 [200] cross section parameterization* to fill in the rest of the phase space for each data set. It was found that the calculation converges within the first 3–4 iterations. The radiative corrections were as large as $\approx 50\%$ in the lowest measured E_p bin, and fell off to a few percent at the large E_p bins.

5.4.4 Born Cross Section

Figure 5.33 shows the Born cross sections as a function of E_p. The error bars indicate the statistical errors, while the gray band represents the systematic error, which includes contributions from the electron cuts, background subtraction, ^{3}He density, nitrogen dilution, beam charge calibration and radiative corrections. The systematic errors are discussed in detail in Section 5.4.5.

It was found that our cross section agrees with the F1F209 [200] model to roughly $\pm 8\%$ on average across our measured kinematic range.

5.4.5 Systematic Errors

There are a number of contributions to the systematic errors on the experimental and Born cross sections. There are errors coming from the analysis cuts we have chosen, which includes the gas Čerenkov, pion rejector, β, and acceptance cuts. There are also contributions from the determination of the beam charge [207], the target density [208], background subtraction and radiative corrections. The total systematic error on the Born cross section is computed as:

$$\delta\sigma_{\text{born}}^2 = \delta\sigma_{\text{rad}}^2 + \left(\frac{\sigma_{\text{Born}} - \sigma_{\text{rad}}}{\sigma_{\text{Born}}}\right)^2 \delta\sigma_{\text{RC}}^2, \tag{5.26}$$

*See Appendix C.2 for more details.

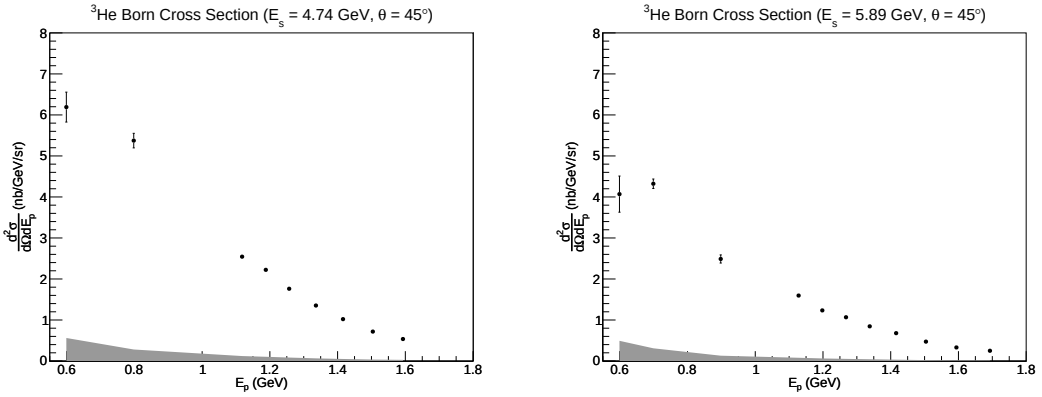

(a) E_s = 4.74 GeV (b) E_s = 5.89 GeV

Figure 5.33: Unfolded Born cross sections. The error bars shown on the Born cross section are statistical. The systematic errors are given by the gray band (Sect. 5.4.5). (a): E_s = 4.74 GeV data; (b): E_s = 5.89 GeV data. Tables of all data may be found in Appendix E.1.

where $\delta\sigma_{\rm rad}$ contains the systematic errors on the radiated (experimental) cross section. $\delta_{\rm RC}$ is the error due to the radiative corrections.

To determine the error that arises due to each of the cuts, we would compute the raw cross section after varying a single cut to a *reasonable* level, and compare that to the result obtained using our final cuts. The variation of the cut to a reasonable level means that we can still say with confidence that we are choosing good electrons for our studies. For instance, with the PID cuts on the gas Čerenkov and pion rejector, these cuts would be varied by $\sim \pm$ 20–30 ADC channels and ± 0.1 in E/p, respectively. These ranges were informed by our cut efficiency studies (see Sections 5.2.2.4 and 5.2.2.5). A similar approach was taken with the β cut. The ranges in which to vary the cuts on the target variables was determined by a comparison to how well our simulation (SAMC) could reproduce the data reliably, as well as being able to remove edge-effects due to scattering from the target endcap and cell walls [209].

The error bands on the background cross sections in Figure 5.30 were determined by varying each parameter of the fit to the data within the its errors and observing the change in the fit. This was done by varying the fit parameters at random for $\approx$ 50–60 trials for each background signal. The bands represent the maximum variation of the fit due to such a study. It was found that subtracting these background signals contributes at a level of $\approx 9\%$ at the lowest bin in E_p for E_s = 5.89 GeV. As E_p increases, this error drops quickly to sub-percent levels. A similar trend is seen for the E_s = 4.74 GeV data set.

The systematic errors corresponding to the radiative corrections include the elastic and quasi-elastic tail subtraction, material thicknesses in the electron's path, and dependence

on the input model used for the radiative correction calculations. The systematic error of subtracting the elastic tail from the data is $\ll 1\%$, determined by considering a different model [210] for the elastic ^{3}He form factors. In a similar fashion as the elastic tail, the systematic effect of the subtraction of the quasi-elastic tail was determined by considering different quasi-elastic cross section models to compute the tail [200]*. We found that the error is $\approx$ 5–6% for the lowest bin in E_p, and falling to $\approx 1\%$ for all other bins for which we have data. To determine the error related to the material thicknesses in the electron's path, we varied the thicknesses in our calculations by up to 10%, and saw a change in our resulting Born cross section of $\lesssim 1.5\%$. The error corresponding to the input model used in the radiative correction procedure was determined by using different models [89]. The resulting Born cross section changed by at most $\approx 5\%$ for the lowest bin in E_p and dropped to $\lesssim 1\%$ for all other bins.

All of the error contributions are plotted as a function of E_p for both the $E_s = 4.74$ and 5.89 GeV data sets in Figure 5.34. The black data corresponds to the statistical errors; the red data corresponds to errors due to the cuts that choose electrons; the blue data corresponds to the errors due to background subtraction discussed above; the magenta data labeled "misc." corresponds to errors from the density of N_2 and ^{3}He in the production cell and the error in the charge calibration†.

The individual contributions to the systematic uncertainties seen in Figure 5.34 are tabulated in Appendix E.1.

*Aside from using the F1F209 model in our systematic studies, we also computed the quasi-elastic tail using the approximation of ^{3}He being two protons plus a neutron with no smearing; this meant using the dipole model and the Galster [211] model for the proton and neutron form factors, respectively.

†This enters into the cross section when computing the incident number of electrons $N_{\text{inc}} = Q/e$.

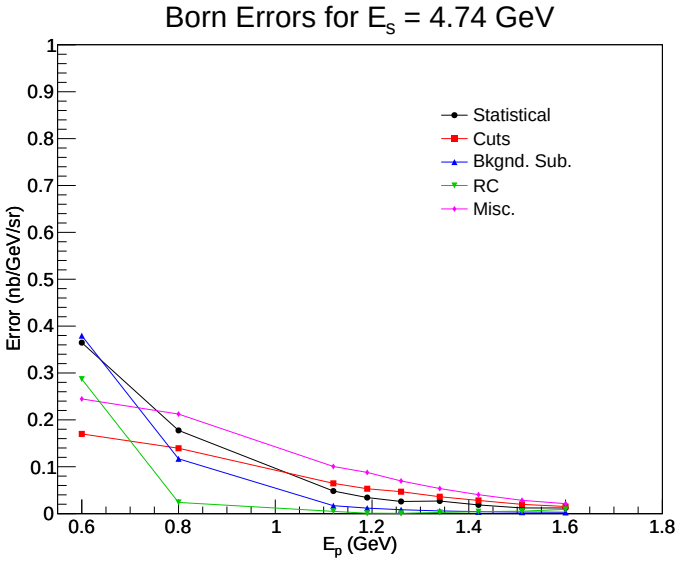

(a) $E_s = 4.74$ GeV

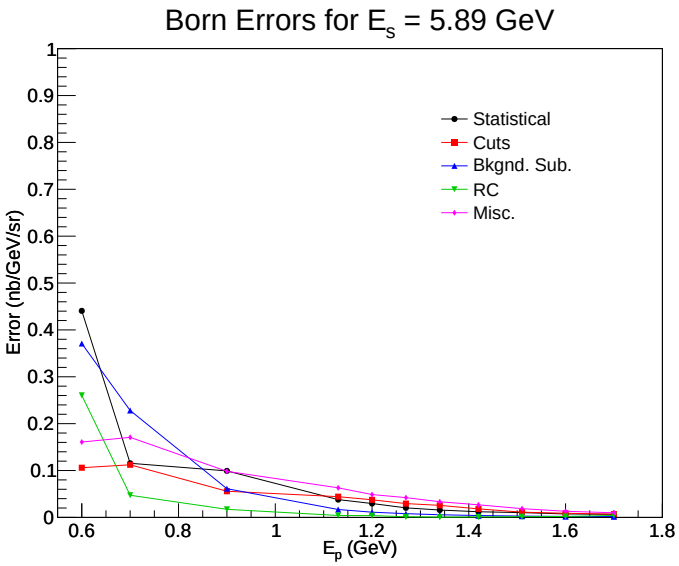

(b) $E_s = 5.89$ GeV

Figure 5.34: The various contributions to the errors on the cross section data. The black points are statistical errors; the blue points are background subtraction errors; the green points are errors due to radiative corrections, and the magenta points are due to the errors correlated to the N_2 density in the ^{3}He production target and the error in the charge calibration. See text for more details. (a): $E_s = 4.74$ GeV data; (b): $E_s = 5.89$ GeV data.

5.5 Double-Spin Asymmetries

In this section, we discuss the highlights of the double-spin asymmetry analysis. The majority of this work, with the exception of the pion asymmetries on the LHRS and the radiative corrections, was carried out by M. Posik, and more details may be found in [169].

5.5.1 Calculation From Raw Data

The extraction of the raw counting asymmetries from data follows the computation of:

$$A = \frac{N^{s,S} - N^{-s,S}}{N^{s,S} + N^{-s,S}}, \tag{5.27}$$

where s is the spin direction of the electron beam, either parallel ($\uparrow$) or antiparallel ($\downarrow$) to its momentum. There were three target spin configurations: parallel to the electron momentum ($S = 0^\circ$), and two transverse polarizations to the electron momentum; one pointing at the LHRS ($S = 90^\circ$), and the other pointing at BigBite ($S = 270^\circ$).

5.5.1.1 Sign Convention

To determine the sign convention for the asymmetry, one needs to know the physical direction of the electron beam helicity. To this end, measurements of the ^{3}He longitudinal quasi-elastic asymmetry were conducted for $E = 1.23\,\text{GeV}$ and $\theta = 45^\circ$, where the electrons with helicity -1 were assigned a positive sign, and those with helicity $+1$ were assigned a negative sign. We found $A_{\text{raw}}^{\text{QE}} = 0.012 \pm 0.003$ [169], compared to the theoretical estimate of 0.02 [212]. The measured result is within a factor of two of the calculated estimate, but is clearly positive. Given the agreement of the measurement with the calculation, a positive sign is applied to events with negative helicity electrons, and a negative sign is applied to events having positive helicity electrons.

In polarizing the target, the polarizing optics were set up in an antiparallel pumping configuration such that the target spin was always oriented opposite to the magnetic holding field; utilizing the magnetic field information recorded throughout the experiment, the target spin orientation is known [169].

With the sign convention understood, the extraction of the electron double-spin asymmetries from raw data for a longitudinally or transversely polarized target are accomplished according to:

$$A_{\parallel}^{\text{raw}} = \frac{N^{\downarrow\Uparrow} - N^{\uparrow\Uparrow}}{N^{\downarrow\Uparrow} + N^{\uparrow\Uparrow}} \tag{5.28}$$

$$A_{\perp}^{\text{raw}} = \frac{1}{\langle \cos\phi \rangle} \frac{N^{\downarrow\Rightarrow} - N^{\uparrow\Rightarrow}}{N^{\downarrow\Rightarrow} + N^{\uparrow\Rightarrow}}, \tag{5.29}$$

where $A_{\parallel}$ ($A_{\perp}$) is the longitudinal (transverse) asymmetry; the $\uparrow$ ($\downarrow$) indicates the incident electron spin parallel (antiparallel) to its momentum; the $\Uparrow$ ($\Downarrow$) indicates the target spin aligned parallel (antiparallel) to the electron beam momentum, and $\Rightarrow$ indicates the target polarized transversely with respect to the electron beam momentum, in the electron scattering plane. For the transverse asymmetry, we divide out by $\langle \cos\phi \rangle$* so as to remove any azimuthal angular dependence in the data.

5.5.1.2 Data Organization and Processing

Each run set corresponding to their target spin configuration is processed separately, where each run is averaged together, weighted by their statistical uncertainty and the insertable half-wave plate (IHWP) is accounted for. The IWHP status was recorded during the experiment in the electronic logbook and in the EPICS data stream. The IHWP change occurred only in between runs, so a definite status can be assigned to each run.

The asymmetries were binned into twenty equally spaced bins in x over the range $0 \leq x \leq 1$†, with a bin width of 0.05. For each x bin, the asymmetries for each run of a given target spin configuration S were averaged together according to:

$$\left\langle A_{\text{raw}}^{S} \right\rangle = \frac{\sum_i A_i^S \frac{1}{\left(\delta A_i^S\right)^2}}{\sum_i \frac{1}{\left(\delta A_i^S\right)^2}} \tag{5.30}$$

$$\delta A_{\text{raw}}^{S} = \sqrt{\frac{1}{\sum_i \frac{1}{\left(\delta A_i^S\right)^2}}}, \tag{5.31}$$

where the statistical error on the i^{th} asymmetry with target spin configuration S is:

$$\delta A_i^S = \sqrt{\frac{4 N_i^{\downarrow S} N_i^{\uparrow S}}{\left(N_i^{\downarrow S} + N_i^{\uparrow S}\right)^3}}. \tag{5.32}$$

*Plotting $\langle \cos\phi \rangle$ for each x bin revealed that it was > 0.99 for every bin [169].

†In the data analysis, we kept bins corresponding to $0.23 < x < 0.98$. Details on how we arrived at the final binning will be given in the following sections.

Since there were two transverse target spin configurations, there was a need for a consistent way to combine the results for both configurations, as the results for the 90° and 270° will have opposite signs relative to the other. To determine which target configuration should carry which sign, we follow the convention used in the JLab E99-117 experiment [71] where the positive sense of the target spin is taken as the direction that points towards the side of the beamline where the scattered electron is detected. In this experiment, the asymmetry measurement was done on BigBite; therefore, when the target spin is pointing towards BigBite (270°), it carries a positive sign; if the target spin is pointing towards the LHRS (90°), it carries a negative sign. Using this sign convention, the $S = 90°$ and $S = 270°$ asymmetries were combined via a statistically-weighted average after all contamination had been taken into account (Sect. 5.5.3).

The raw counting asymmetries are shown in Figure 5.35. The left panel shows the parallel asymmetries for $S = 0°$, while the middle and right panels show the perpendicular asymmetries for $S = 90°$ and $S = 270°$, respectively. The red (blue) markers indicate the $E = 4.74\,\text{GeV}$ (5.89 GeV) data.

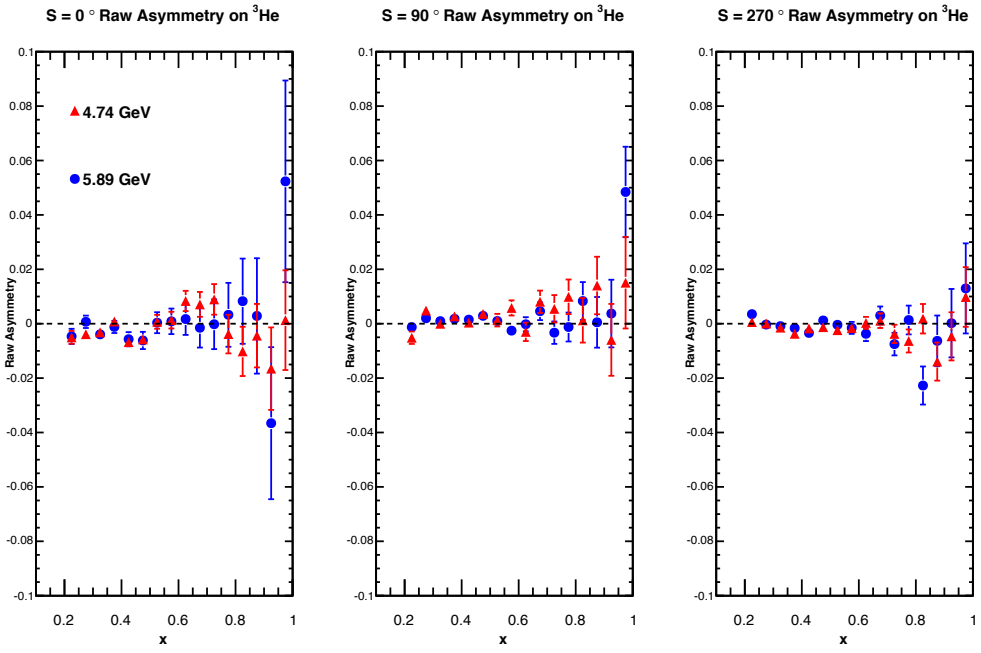

Figure 5.35: The raw electron asymmetries $A_{\parallel}$ and $A_{\perp}$ for each target spin configuration are shown. The red (blue) markers indicate the $E = 4.74\,\text{GeV}$ (5.89 GeV) data. Figure reproduced from [169].

5.5.2 False Asymmetries

When measuring an asymmetry, care must be taken to ensure that the asymmetry is due to electron spin-dependent scattering and not helicity correlated changes in the electron beam, known as *false asymmetries*. One such issue arises from a difference in the electron beam intensity for the parallel and antiparallel helicity states, which results in a charge asymmetry. During the experiment, the beam charge asymmetry was limited to $\approx$100 ppm; this was accomplished through the use of a feedback loop controlled by a specialized DAQ [213] and was verified by measuring the charge asymmetry using the Compton polarimeter [47]. Compared to the size of the electron asymmetry measurements, the charge asymmetry is negligible. Another source of concern is a the possibility of the detector's livetime having a helicity dependence. The helicity-dependent livetime asymmetry was extracted from the data and was found to be < 100 ppm for the entire data set, and was considered to be negligible [169].

In addition to charge- and DAQ-induced false asymmetries, software can also introduce a false asymmetry. For example, if the data rates are high enough, it may be more difficult to reconstruct good tracks related to the higher rate helicity state as compared to the lower one, resulting in an asymmetry [214]. However, E06-014 had a very low track multiplicity ($\sim 4\%$), and thus the rates were not high enough for such an asymmetry to have a significant impact on the measured electron asymmetries. Other potential false asymmetries can be limited through the 30 Hz helicity flipping rate of the electron beam; also, any false asymmetry that does not change sign with respect to the IHWP state, such as those due to electronic cross-talk [215], which would be canceled when combining the IHWP states.

5.5.3 From Raw to Physics Asymmetries

The raw asymmetry calculation shown in Equations 5.28 and 5.29 do not account for background effects due to the presence of nitrogen in the target or the beam and target polarizations. Therefore, the raw asymmetries are corrected for by these factors:

$$A_{\parallel,\perp}^{\text{phys}} = \frac{1}{D_{\text{N}_2} P_b P_t} A_{\parallel,\perp}^{\text{raw}}, \tag{5.33}$$

where P_b and P_t are the beam and target polarizations, respectively; D_{N_2} is the nitrogen dilution factor. This correction is applied to the longitudinal ($\parallel$) and transverse ($\perp$) raw asymmetries, yielding the *physics asymmetries*. Physics asymmetries for each run corresponding to a given target spin configuration were combined in the same fashion as shown for the raw asymmetries in Equation 5.30.

5.5.3.1 Nitrogen Dilution

The nitrogen dilution factor is extracted by comparing the N_2 target counting rates to the ^{3}He production cell counting rates. It is given as:

$$D_{N_2} = 1 - \frac{\Sigma_{N_2}(N_2)}{\Sigma_{\text{total}}(^3\text{He})} \frac{t_{ps}(N_2)}{t_{ps}(^3\text{He})} \frac{Q(^3\text{He})}{Q(N_2)} \frac{t_{LT}(^3\text{He})}{t_{LT}(N_2)} \frac{n_{N_2}(^3\text{He})}{n_{N_2}(N_2)}, \tag{5.34}$$

where Σ_{N_2} and Σ_{total} are the total number of counts that pass data quality and PID cuts detected during the N_2 and ^{3}He production target runs; $n_{N_2}(N_2)$ and $n_{N_2}(^3\text{He})$ are the nitrogen number densities present in the two targets. Due to the nitrogen and ^{3}He production runs having different characteristics (e.g., scattering rates, running time, etc.) the measured electrons must be normalized by taking into account the total charge, given by $Q(N_2)$ and $Q(^3\text{He})$ deposited on the two targets; the prescale factors for the nitrogen and ^{3}He runs are given as $t_{ps}(N_2)$ and $t_{ps}(^3\text{He})$; the live times for the nitrogen and ^{3}He runs are given as $t_{LT}(N_2)$ and $t_{LT}(^3\text{He})$.

When the nitrogen reference cell was in the beam, the number density for the cell was extracted using the measured temperature and pressure of the cell. A systematic uncertainty of 2.2% was estimated by computing the number densities while varying the temperature and pressure up to 2° C and 2 psig [169]. In the ^{3}He production cell, the number density of nitrogen was taken to be 0.113 amg. This value was recorded as the target was initially filled, and is accurate to 3% from pressure curve analysis [216].

The nitrogen dilution factor was extracted on a run-by-run basis and averaged together, weighted by its statistical error for a given target spin orientation. The resulting dilution factor was applied bin-by-bin in x, and was found to be roughly constant at $D_{N_2} \approx 0.920 \pm 0.003$ [169].

5.5.3.2 Contamination Studies

The main sources of background contamination come from charged pions and electrons via electron-positron pairs. Such electron-positron pairs arise from π^0 production in the target; due to their short lifetime, the π^0 particles decay before leaving the target, via $\pi^0 \to 2\gamma$; to a much smaller degree, $\pi^0 \to \gamma e^+ e^-$ also occurs. Despite applying PID cuts, electrons originating from these two processes were still misidentified in the electron sample as electrons.

5.5.3.2.1 Pion Contamination

To quantify the charged pion contamination in the electron sample, the shower calorimeter was used because pions leave a minimum ionization peak towards the lower end of the ADC spectrum; electrons have a peak at larger values, depending upon their momentum. The pion peak was fitted by a Gaussian function convoluted with a Landau function, and the electron peak was fitted by a Gaussian function. The ratio of the pion to electron curves was then evaluated for ADC values larger than 200 channels, as this was the threshold used in choosing electrons in the analysis [169]. This ratio was evaluated for π^- (π^-/e^-) and π^+ (π^+/e^+) particles. A similar study followed for the π^+ contamination, where the polarity of the BigBite magnet was reversed so that positively charged particles bent up into the detector stack*. The π^-/e^- ratio was largest in the lowest x bin of 0.277, at $\approx 2.7\%$, but dropped quickly below 1% by $x = 0.425$. The π^+/e^+ ratio was larger and more constant, at $\approx 5\%$ across the whole x range.

The asymmetry due to pions may dilute the measured electron asymmetries. Because of this, $\pi^\pm$ asymmetries were evaluated, where pions instead of electrons were chosen in the analysis. Corrections for the nitrogen dilution and the beam and target polarizations were applied to obtain $\pi^\pm$ physics asymmetries. The pion asymmetries were also measured on the LHRS†, providing a good cross-check of the asymmetries measured on the BigBite spectrometer. Figure 5.36 and 5.37 show the comparison of the π^- and π^+ raw asymmetries measured on the LHRS (red markers) and BigBite (blue markers). Due to time constraints, for the π^+ data there was only LHRS data for the target spin orientation corresponding to $S = 90^\circ$. It is seen that there is good agreement between the two spectrometers.

To determine how large of an effect these asymmetries have on the electron asymmetries, they are scaled by the extracted π/e ratios. It was found that the π^- (π^+) asymmetry contribution was less than 5% (3%) of the *statistical uncertainty* of the electron (positron) longitudinal and transverse asymmetries.

This pion contamination study was done for the $E = 5.89\,\text{GeV}$ data set only, because the $E = 4.74\,\text{GeV}$ data set was taken towards the end of the experiment when the main electron trigger on BigBite was optimized to remove a significant portion of the minimum ionization peak and trigger primarily on electrons. Because of this, the results found for $E = 5.89\,\text{GeV}$ were used for $E = 4.74\,\text{GeV}$ data. Due to the small contamination found in

*Our analysis revealed that particles bending downwards in BigBite had a different acceptance relative to those that bent upwards; therefore, particles with similar trajectories should be compared [169].

†To extract pion asymmetries using the LHRS, the same cuts as presented in Section 5.2.6 were used, but with the PID cuts on the gas Čerenkov and pion rejector "reversed" so as to choose pions; that is, the gas Čerenkov was required to *not* fire, and $E/p < 0.54$ and the energy deposited in the first pion rejection layer was required to be less than 200 MeV.

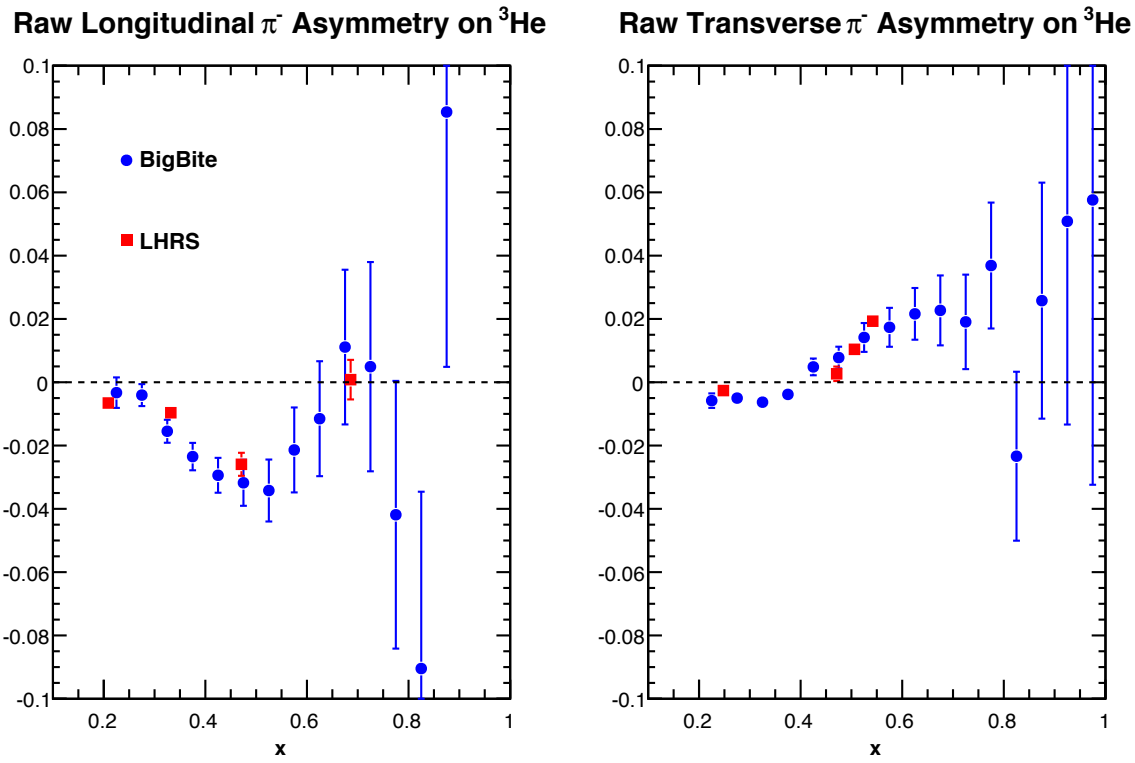

Figure 5.36: The raw π^- asymmetry as measured on the BigBite spectrometer compared to a measurement on the LHRS.

the 5.89 GeV data, the contamination at 4.74 GeV can be seen to be even smaller. Applying the 5.89 GeV results to the lower energy data is a conservative estimate.

5.5.3.2.2 Positron Contamination

To quantify the contamination due to pair-produced electrons, the ratio of positrons to electrons, e^+/e^- was evaluated. This was done for each bin in x, where positron counts were done with BigBite in positive polarity mode. Due to time constraints and hardware difficulties with the electron beam, this study was only able to be conducted for the $E =$ 4.74 GeV data set. To determine e^+/e^- for the $E = 5.89$ GeV data set, an indirect approach was used. This entailed considering our measurement on BigBite at $E = 4.74$ GeV and the LHRS at $E = 4.74$ and 5.89 GeV, along with data from JLab CLAS EG1b [217], which had $E = 5.7$ GeV and $\theta = 41.1^\circ$. The aforementioned data was plotted as $(1/E^2)(e^+/e^-)$ versus the transverse momentum $p_T = p\sin\theta$, where E is the electron beam energy, p is the electron momentum and θ is the electron scattering angle. The data was then fit to the function $f(p_T) = \exp(a + b \cdot p_T)$, with a and b as free parameters. Using this fit, the

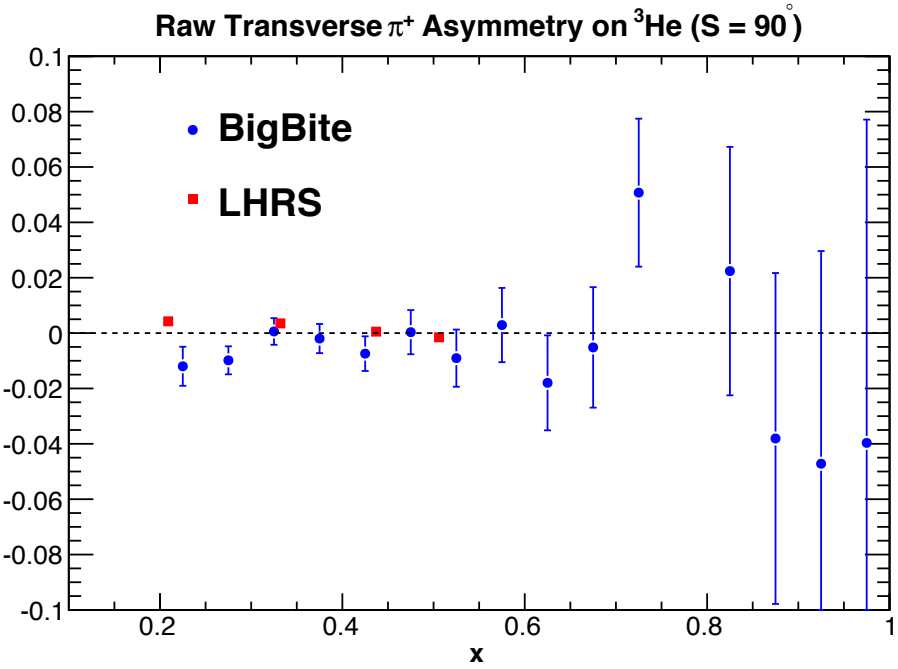

Figure 5.37: The raw π^+ asymmetry as measured on the BigBite spectrometer compared to a measurement on the LHRS.

e^+/e^- ratio for $E = 5.89\,\text{GeV}$ was found to be in excess of 1 at $x = 0.230$, as shown in Figure 5.38. This resulted in the decision to exclude this x bin, which was the lowest bin measured during the experiment. The e^+/e^- ratio was more reasonable towards larger values of x, where it was less than 50% at $x = 0.277$, our lowest x bin, and falling to less than 10% by $x = 0.473$. Beyond $x = 0.5$, the ratio dropped to below 3%.

Similar to the pion contamination study, the asymmetry due to electron-positron pairs could also contaminate the electron asymmetry. Ideally, the positron asymmetry would be measured by changing the BigBite magnet to positive polarity so that positrons bend up into the same acceptance as seen by electrons; however, due to the aforementioned time constraints, this was only done for one target spin configuration (270°) at one beam energy ($E = 4.74\,\text{GeV}$). Because of this, an alternative approach was used where positron asymmetries were measured on the particles that were bent *downwards* through the BigBite magnet*. However, the bend-down particles had lower rates, as it contained only $\approx 40\%$ of any given run's events *before* particle selection cuts were applied. Because of this, a constant (one-parameter) fit to the extracted asymmetries as a function of x was performed to remove any large fluctuations due to poor statistical precision. The fitted value of the

*It was found that the asymmetries measured on particles bending up or bending down through the BigBite magnet were in good agreement with one another [169], so using the bend-down positron asymmetries is a valid substitute.

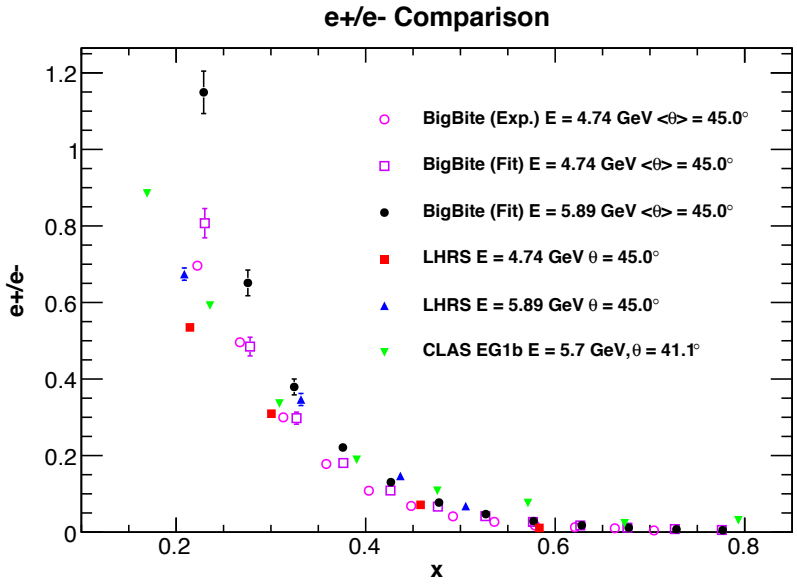

Figure 5.38: World e^+/e^- data, including measurements on BigBite for $E = 4.74$ GeV and measurements on the LHRS at $E = 4.74$ GeV and 5.89 GeV. The derived ratio for BigBite at 5.89 GeV is also shown (black markers). Figure reproduced from [169].

positron asymmetries for $E = 4.74$ and 5.89 GeV were found to be $\approx 2\%$ for $E = 4.74$ GeV and $\approx 1\%$ for $E = 5.89$ GeV [169]. These constant values were applied as a correction to the electron asymmetries, scaled by the e^+/e^- ratio.

5.5.3.2.3 Monte Carlo Simulation

The contamination studies concerning the pions and pair-produced electrons were checked using a Geant4 [218] Monte Carlo simulation of the BigBite detector*, which focused on studying the energy deposition in the BigBite calorimeter. The event generator was defined so that different particle types (e^-, π^-) were thrown at random weighted by their cross section as a function of scattering angle and momentum, modeled by F1F209 [200] and Wiser [219] fits, respectively. The simulation was found to be in good agreement with the real data, where various cuts used on the real data set were mimicked in analyzing the simulated data, so as to obtain an accurate comparison [169].

5.5.3.3 Correcting for Contamination

The contamination due to the asymmetries of charged pions and the pair-produced electrons may be removed from the measured electron asymmetry $A_m^{e^-}$ to obtain the corrected

*developed by V. Mamyan

electron asymmetry A^{e^-} by computing:

$$A^{e^-} = \frac{A_m^{e^-} - f_1 A^{\pi^-} - f_3 A_m^{e^+} + f_2 f_3 A^{\pi^+}}{1 - f_1 - f_3 + f_2 f_3}, \tag{5.35}$$

where $f_1 = \pi^-/e^-$; $f_2 = \pi^+/e^+$; $f_3 = e^+/e^-$; $A^{\pi^\pm}$ are the $\pi^\pm$ asymmetries, and $A_m^{e^+}$ is the measured positron asymmetry. Considering the fact that the corrections for the pion asymmetries are very small, Equation 5.35 can be simplified to be:

$$A^{e^-} \approx \frac{A_m^{e^-} - f_3 A_m^{e^+}}{1 - f_1 - f_3 + f_2 f_3} \equiv A^{\text{cor}}. \tag{5.36}$$

At this point, the bins for which $x > 0.90$ were removed from the analysis, so as to avoid the quasi-elastic and resonance contributions, which start at $x \approx 0.90$.

The physics asymmetries, corrected for contamination due to pions and pair-produced electrons, are shown in Figure 5.39 and are tabulated in Appendix E.2. The red (blue) markers indicate the $E = 4.74\,\text{GeV}$ (5.89 GeV) data. The left panel shows $A_\parallel$ and the right panel shows $A_\perp$. The error bars indicate the statistical errors only.

The statistical error for $A_\parallel$ is computed as:

$$\delta A = \sqrt{(\delta A)^2 + \left(\frac{\partial A}{\partial D_{\text{N}_2}}\right)^2 (\delta D_{\text{N}_2})^2}, \tag{5.37}$$

where δA is the statistical error on the asymmetry*; δD_{N_2} is the statistical error on the dilution factor D_{N_2}. The statistical error for $A_\perp$ ($S = 90^\circ$ or 270°), is:

$$\delta A^j = \sqrt{(\delta A^j)^2 + \left(\frac{\partial A^j}{\partial D_{\text{N}_2}}\right)^2 (\delta D_{\text{N}_2})^2 + \left(\frac{\partial A^j}{\partial \langle\cos\phi\rangle}\right)^2 (\delta \langle\cos\phi\rangle)^2}, \tag{5.38}$$

where $j = 90$ or 270. The errors on the effective beam and target polarizations, P_b and P_t, enter in the systematic errors. Additionally, systematic errors due to the contamination corrections are also considered (Sect. 5.5.6).

5.5.4 Radiative Corrections

To compute the radiative corrections for asymmetries, we utilized a similar approach as shown in Section 5.4.3. The main difference is that we carried out the corrections on polarized cross section differences, $\Delta\sigma$, related to asymmetries by:

*this includes the statistical errors on the measured pion and positron asymmetries

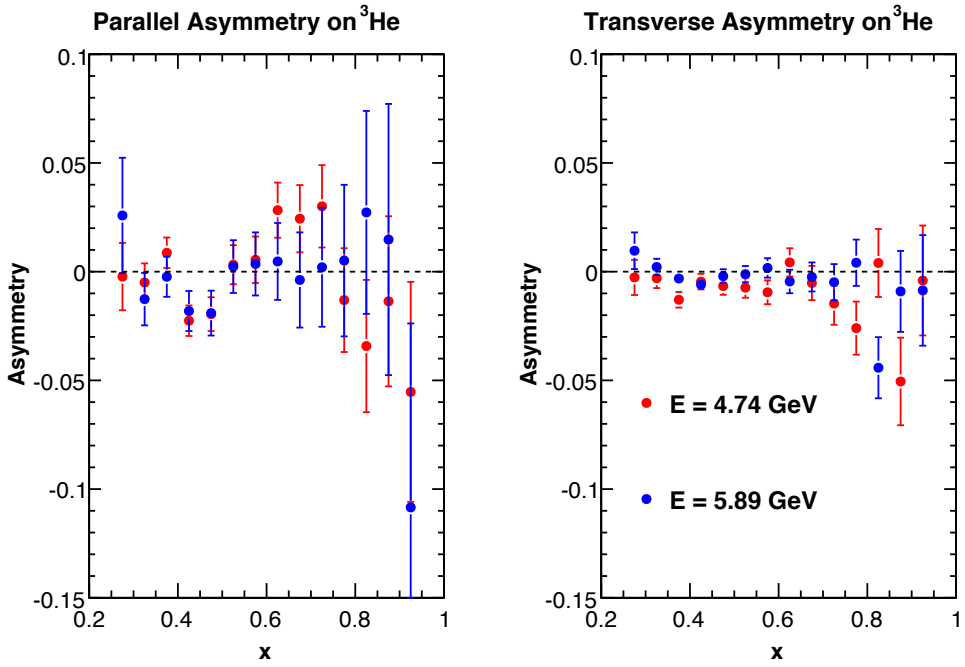

Figure 5.39: The background-corrected physics asymmetries for $E = 4.74\,\text{GeV}$ (red) and $5.89\,\text{GeV}$ (blue). The left panel shows the parallel asymmetries and the right panel shows the perpendicular asymmetries. The error bars indicate the statistical errors only. Figure reproduced from [169].

$$\Delta\sigma^r_{\parallel,\perp} = 2\sigma^r_0 A^r_{\parallel,\perp}, \tag{5.39}$$

where $A_{\parallel,\perp}$ indicates a radiated asymmetry where the target is polarized either longitudinal $(\parallel)$ or transverse $(\perp)$ with respect to the incident electron beam momentum. The unpolarized cross section is σ^r_0, where the r indicates that radiative effects have been applied. We used the F1F209 [200] model for the unpolarized cross section. The model used to fill out the integration phase space needed in the calculations was composed of components that describe three different kinematic regions: the DIS, the quasi-elastic region, and the resonance region. The model used for the DIS region was the DSSV [220] global analysis PDF model; for the quasi-elastic region, we utilized P. Bosted's nucleon form factors [221], smeared by a quasi-elastic scaling function [222] to simulate the nuclear effects of ^{3}He. To model the resonance region, we used the MAID [141] model.

Putting the DIS, quasi-elastic and resonance contributions together [*], we built up $\Delta\sigma$. In the radiative correction procedure, the quasi-elastic tail was not subtracted first, but rather was included in the integration. The elastic tail was found to be negligible and was not subtracted.

[*]The details of how all three regions were constructed is documented in Appendix C.3.

To minimize statistical fluctuations in the radiative corrections, the corrections were performed on a model of our data set. After obtaining the Born $\Delta\sigma$, the corresponding asymmetry was obtained by inverting Equation 5.39 (but using the *Born* σ_0) to find A. Then, the size of the radiative correction at the asymmetry level was determined as:

$$\Delta A = A_b - A_r, \tag{5.40}$$

where A_b is the Born asymmetry and A_r is the radiated asymmetry. This ΔA was applied to our data for both the parallel and perpendicular cases as an additive correction. The size of the radiative correction was found to be at most on the order of 10^{-3} in the lowest x bin.

The radiative corrections in the DIS region were checked against results obtained from following the formalism of Akushevich *et al.* [223]. The results from our method agreed with those found using their method to the 10^{-4} level in the asymmetry. This check was performed in DIS kinematics only, since the calculations of [223] do not treat the resonance region, and approximates the quasi-elastic peak as a delta function.

5.5.5 Born Asymmetries

The Born asymmetries with their systematic errors are shown in Figure 5.40 and are tabulated in Appendix E.2. The systematic errors are discussed in Section 5.5.6.

5.5.6 Systematic Errors

The systematic errors were obtained by varying all of the inputs to the asymmetry extraction to reasonable levels and observing the change in the Born asymmetry. The quantities varied consisted of the electron cuts, nitrogen dilution factor, beam and target polarizations, pion and pair-production contamination factors, and radiative corrections. The systematic uncertainties due to all contributions were smaller than the statistical errors for all bins for $E = 4.74$ and 5.89 GeV data, at the level of $\lesssim 7 \times 10^{-3}$ for most bins, where the errors due to the cuts tends to dominate. These studies, except for the radiative correction errors, were done by M. Posik and a more detailed discussion may be found in [169]. Appendix E.2.2 gives tables of the various contributions to the systematic errors on the asymmetries. The total systematic uncertainty is computed as an in quadrature sum of all contributing terms.

For the systematic errors due to the radiative corrections, the input models were varied at random by up to $\pm 10\%$ for 30 runs, and the size of the radiative correction was determined for each run set. It was found that the size of the radiative correction changed by less than 5%. Additionally, the radiation thicknesses seen by the incident and scattered electrons were varied by up to 10%; it was found that the resulting Born asymmetry changed by

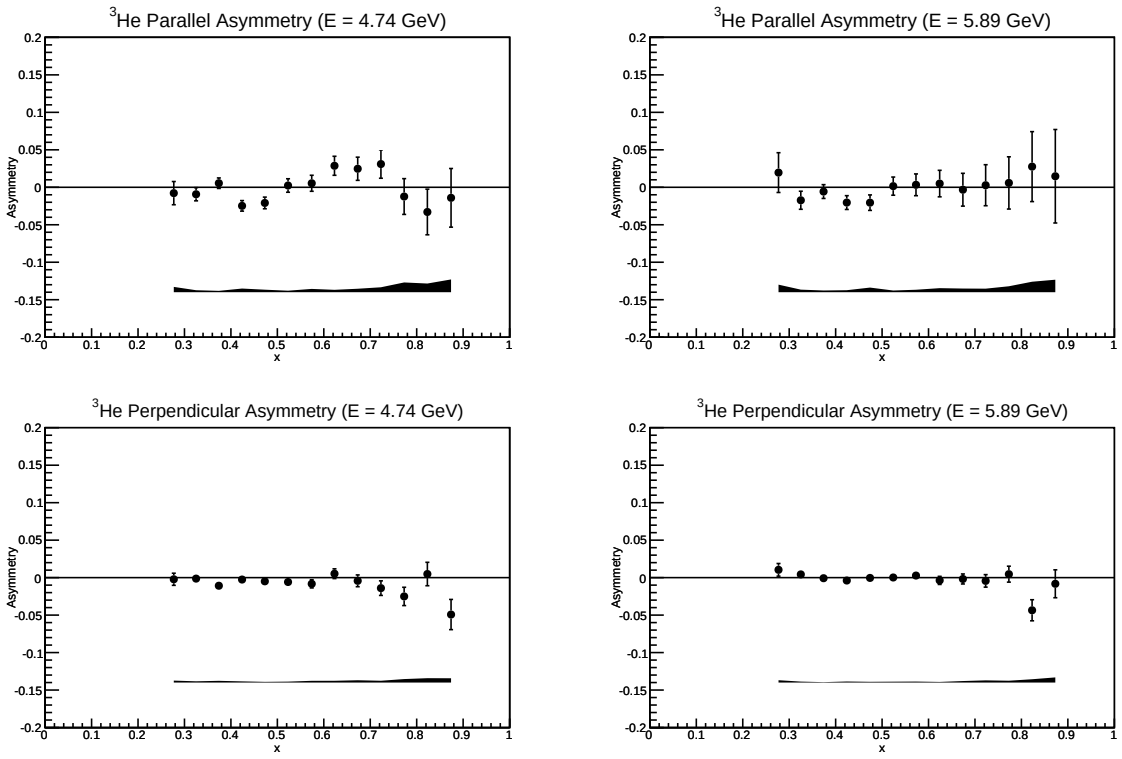

Figure 5.40: The Born asymmetries for $E = 4.74\,\text{GeV}$ and $5.89\,\text{GeV}$, shown on the left and right columns, respectively. The top row shows $A_{\parallel}$ while the bottom row shows $A_{\perp}$. The error bars indicate the statistical errors, while the bands represent the systematic errors.

less than 1.5%. These two errors added in quadrature gives the error on the Born asymmetry due to radiative corrections, at $< 10^{-3}$ ($\sim 5.2\%$). The error on the size of the radiative correction is given in Figure 5.41.

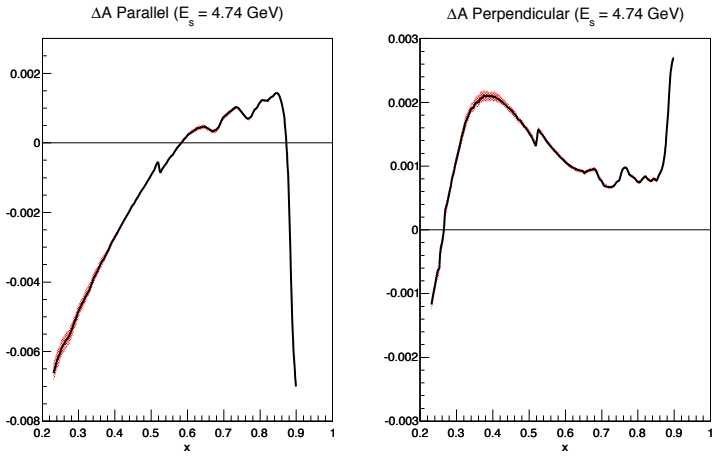

(a) E = 4.74 GeV

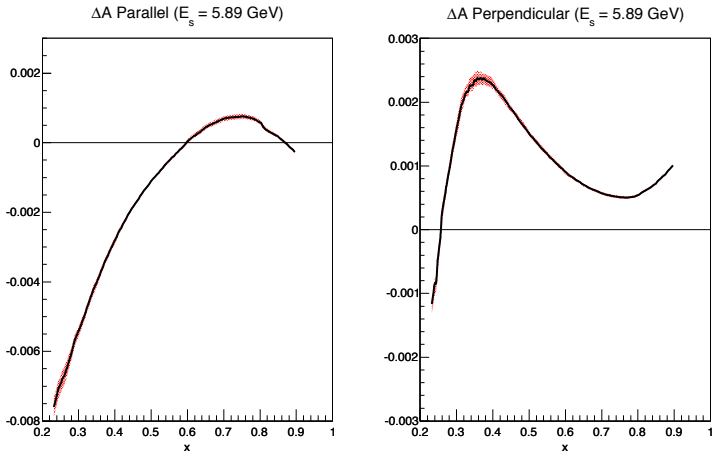

(b) E = 5.89 GeV

Figure 5.41: The size of the radiative corrections for the parallel (left column) and the perpendicular (right column) asymmetries. The top row shows the $E = 4.74$ GeV result, while the bottom column shows the 5.89 GeV result. The red band indicates the error on the correction size, due to the varying the input models and radiation thicknesses.

5.6 A_1 and g_1/F_1

In this section, we describe the procedure used to compute $g_1^{^3\mathrm{He}}/F_1^{^3\mathrm{He}}$ and $A_1^{^3\mathrm{He}}$ from the born asymmetries $A_\parallel$ and $A_\perp$ (Sect. 5.6.1); the discussion continues with the nuclear corrections leading to g_1^n/F_1^n and A_1^n (Sect. 5.6.2); in Section 5.6.3, the systematic errors associated with the ^{3}He and neutron results are discussed.

5.6.1 Extraction From Data

To extract $g_1^{^3\mathrm{He}}/F_1^{^3\mathrm{He}}$ and $A_1^{^3\mathrm{He}}$ from the Born asymmetries, we follow Equations 2.16 and 2.21. For these asymmetries, the kinematic factors given in those equations were binned as a function of x. The mean of a given kinematic factor was used as the central value, while its root mean square (RMS) was used as its statistical uncertainty. The low-level kinematic variables are shown in Figures 5.42–5.45, and the high-level kinematic variables, which show up in Equations 2.16 and 2.21, are shown in Figures 5.46 and 5.47. The parameterization of $R \equiv \sigma_L/\sigma_T$ from [224] is shown in Figure 5.48. The kinematic variable d' needed in the g_1/F_1 extraction is shown in Figure 5.49. The systematic errors for these variables and how they contribute to the errors on the measured g_1/F_1 and A_1 will be discussed in Section 5.6.3.

The measured $g_1^{^3\mathrm{He}}/F_1^{^3\mathrm{He}}$ and $A_1^{^3\mathrm{He}}$ will be presented in Section 6.1. The results and systematic errors for A_1 are tabulated in Appendix E.3, while Appendix E.5 gives tables of the results and the systematic errors for g_1/F_1. The quantities $g_2^{^3\mathrm{He}}/F_1^{^3\mathrm{He}}$ and $A_2^{^3\mathrm{He}}$ were also extracted according to Equations 2.17 and 2.22, and are tabulated in Appendix E.6 and E.4, respectively.

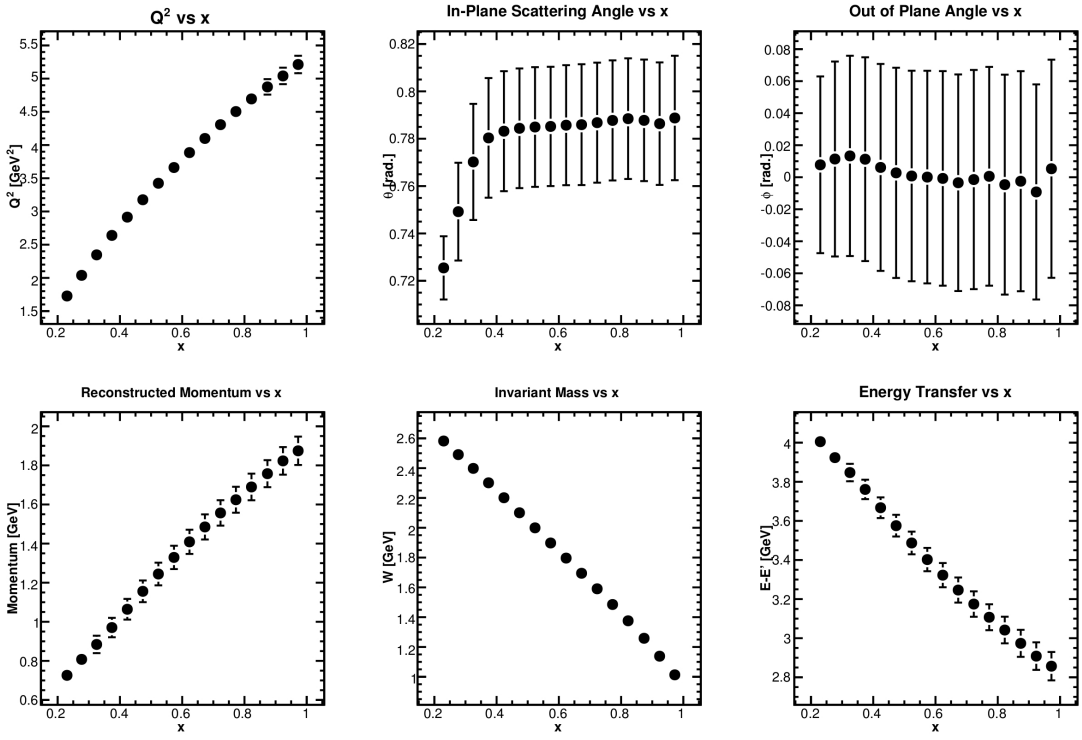

Figure 5.42: Low-level kinematic variables for $E = 4.74\,\text{GeV}$. These variables go into the calculation of d, D, η and ξ, needed for the A_1 extraction. The errors indicated are statistical only. Plots reproduced from [169].

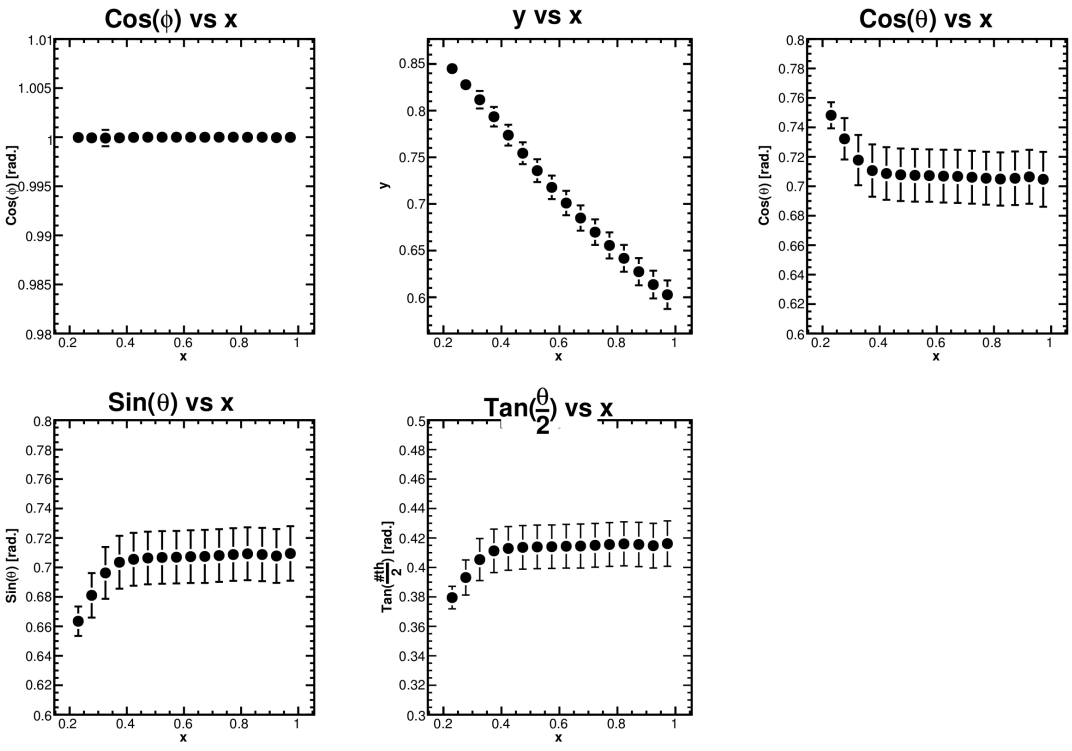

Figure 5.43: Low-level angular kinematic variables for $E = 4.74$ GeV. These variables go into the calculation of d, D, η, ξ and d', needed for the A_1 and g_1/F_1 extraction. The errors indicated are statistical only. Plots reproduced from [169].

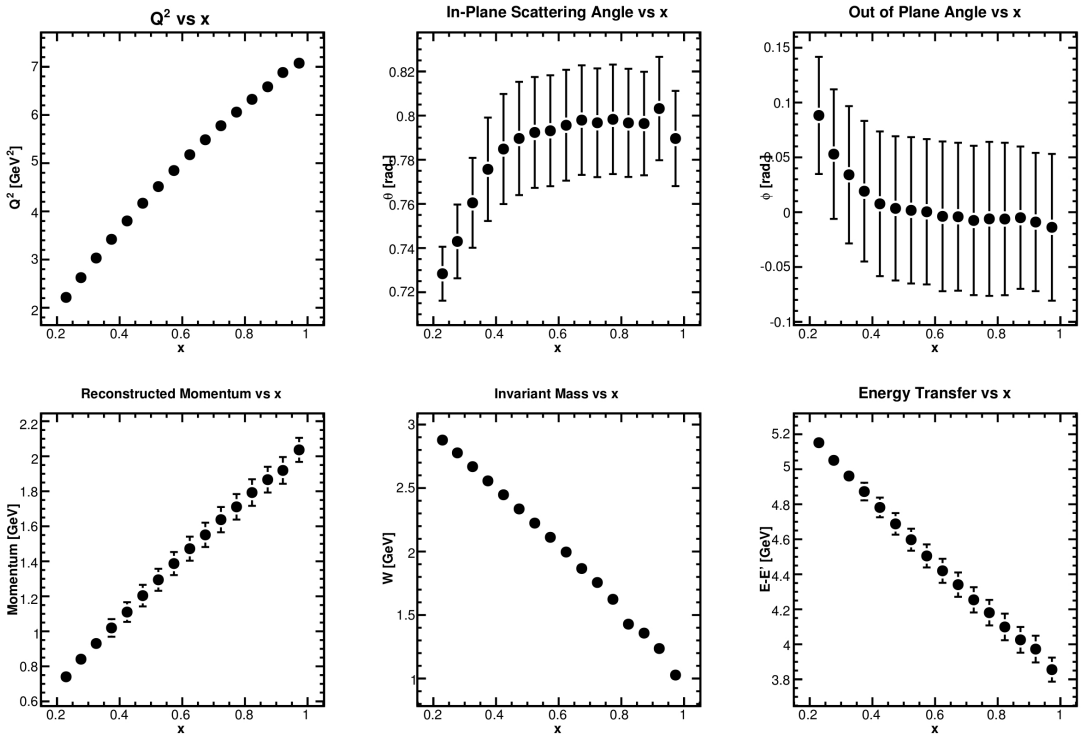

Figure 5.44: Low-level kinematic variables for $E = 5.89\,\text{GeV}$. These variables go into the calculation of d, D, η and ξ, needed for the A_1 extraction. The errors indicated are statistical only. Plots reproduced from [169].

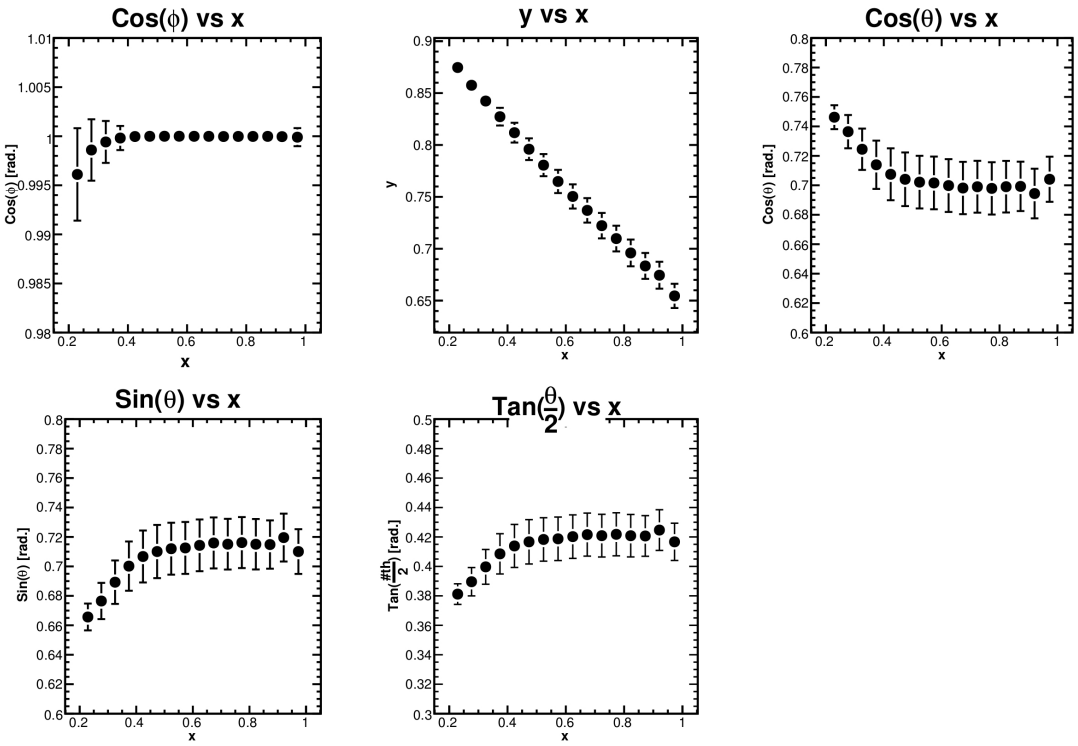

Figure 5.45: Low-level angular kinematic variables for $E = 5.89$ GeV. These variables go into the calculation of d, D, η, ξ and d', needed for the A_1 and g_1/F_1 extraction. The errors indicated are statistical only. Plots reproduced from [169].

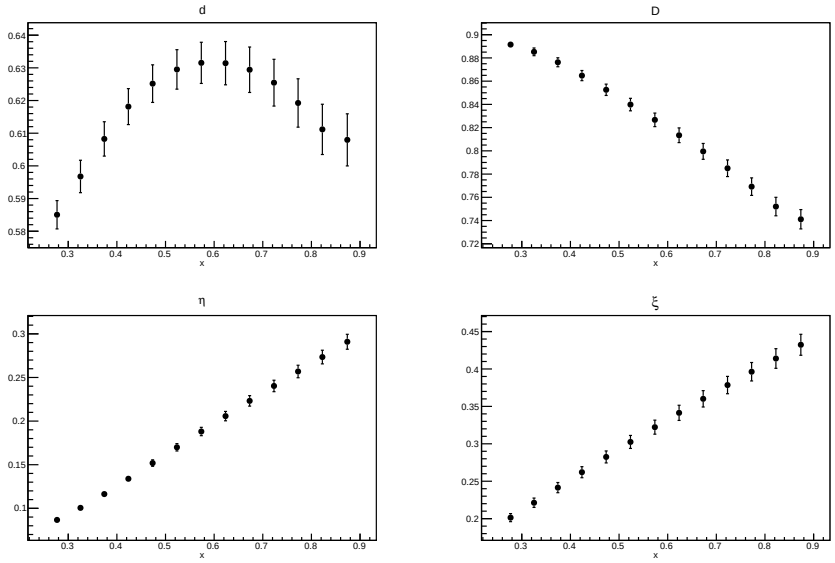

Figure 5.46: Kinematic variables that directly contribute to the A_1 extraction for $E = 4.74$ GeV. The errors indicated are statistical only.

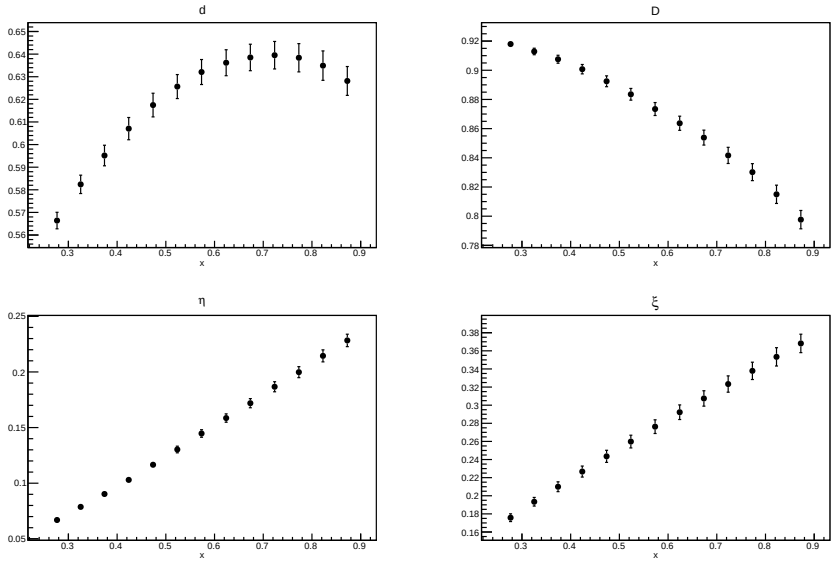

Figure 5.47: Kinematic variables that directly contribute to the A_1 extraction for $E = 5.89\,\text{GeV}$. The errors indicated are statistical only.

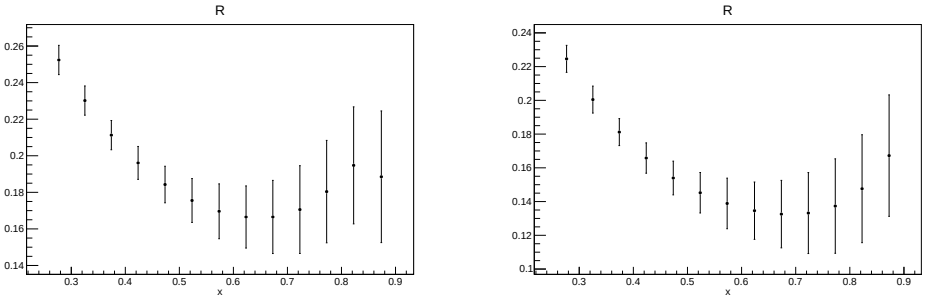

(a) E_s = 4.74 GeV (b) E_s = 5.89 GeV

Figure 5.48: The function $R \equiv \sigma_L/\sigma_T$, from the R1998 fit [224] (a): $E = 4.74\,\text{GeV}$ data; (b): $E = 5.89\,\text{GeV}$ data. The errors indicated are systematic only.

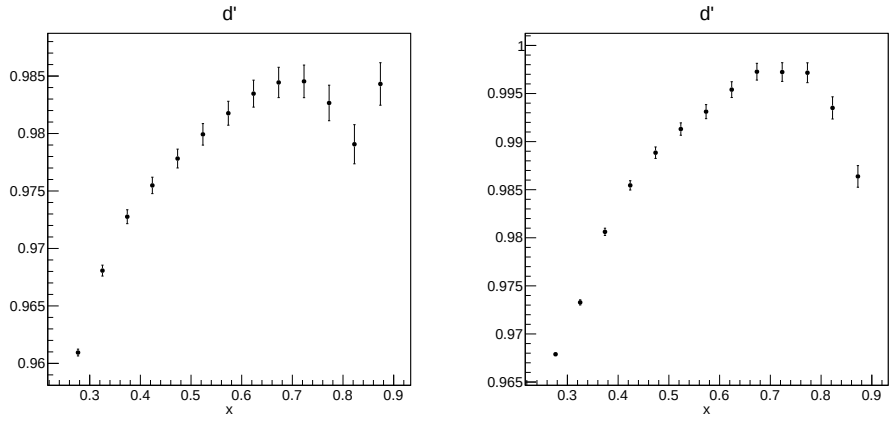

(a) E_s = 4.74 GeV (b) E_s = 5.89 GeV

Figure 5.49: The kinematic variable d' needed in the g_1/F_1 extraction. (a): $E = 4.74$ GeV data; (b): $E = 5.89$ GeV data. The errors indicated are statistical only.

5.6.2 Nuclear Corrections

Nucleons bound in nuclei behave differently than those in free space, primarily due to nuclear effects such as spin depolarization, Fermi motion, nuclear binding, and nuclear shadowing and anti-shadowing effects. Additionally, the presence of non-nucleonic degrees of freedom and the off-shellness of nucleons can alter the characteristics of bound nucleons. Such effects need to be removed in order to obtain the nucleon quantities from measurements on nuclear targets; in our case, this corresponds to obtaining neutron data from ^{3}He measurements. In particular, we want to obtain g_1^n/F_1^n and A_1^n from $g_1^{^3\mathrm{He}}/F_1^{^3\mathrm{He}}$ and $A_1^{^3\mathrm{He}}$, respectively.

5.6.2.1 DIS Data

The complete description of the g_1 spin structure function on ^{3}He in terms of its nuclear components over the range $10^{-4} \leq x \leq 0.8$ was originally given by Bissey *et al.* [225], where $g_1^{^3\mathrm{He}}$ can be represented as the convolution of the off-shell neutron $\tilde{g}_1^n$ and off-shell proton $\tilde{g}_1^p$ spin structure functions with the spin-dependent light-cone momentum distributions $\Delta f_{N/^3\mathrm{He}}(y)$, where y is the ratio of the struck nucleon's light-cone-plus component of the momentum to that of the nucleus:

$$\begin{aligned} g_1^{^3\mathrm{He}}\left(x,Q^2\right) &= \int_x^3 \frac{dy}{y}\Delta f_{n/^3\mathrm{He}}(y)\tilde{g}_1^n\left(x/y,Q^2\right) + \int_x^3 \frac{dy}{y}\Delta f_{p/^3\mathrm{He}}(y)\tilde{g}_1^p\left(x/y,Q^2\right) \\ &- 0.014\left[g_1^p\left(x,Q^2\right) - 4g_1^n\left(x,Q^2\right)\right] \\ &+ a(x)g_1^n\left(x,Q^2\right) + b(x)g_1^p\left(x,Q^2\right). \end{aligned} \tag{5.41}$$

The motion of the nucleons inside the nucleus (i.e., Fermi motion) and their binding is parameterized by $\Delta f_{N/^3\mathrm{He}}(y)$, which can be calculated by using ground state wave functions of ^{3}He. The function $\Delta f_{N/^3\mathrm{He}}(y)$ is sharply peaked at $y \approx 1$ due to the small separation energy per nucleon. Combining this with the assumption that the off-shell nucleon structure functions $\tilde{g}_1^N$ can be replaced with their on-shell counterparts g_1^N, leads to the approximation:

$$g_1^{^3\mathrm{He}}(x) \approx P_n g_1^n(x) + P_p g_1^p(x) - 0.014\left[g_1^p(x) - 4g_1^n(x)\right] + a(x)g_1^n(x) + b(x)g_1^p(x), \tag{5.42}$$

where we have suppressed the Q^2-dependence in the equation for simplicity. The quantities $P_{p,n}$ are the effective polarizations of the proton and neutron in ^{3}He [226], respectively. The third term in Equations 5.41 and 5.42 arises due to the $\Delta(1232)$ component in the ^{3}He

wave function [225]. The functions $a(x)$ and $b(x)$ describe nuclear shadowing and anti-shadowing effects. Nuclear shadowing occurs in the x range of $0.0035 < x < 0.03 \sim 0.07$, where the ratio of $2F_2^A/(AF_2^d) < 1$; nuclear anti-shadowing occurs in the range of $0.03 \sim 0.07 \leq x \leq 0.2$, where the F_2 ratio is greater than 1 [227, 228]. In this experiment, the x coverage does not extend below $x \sim 0.2$. Therefore, due to our kinematic coverage in this experiment, these terms were left out of the analysis and Equation 5.42 becomes:

$$g_1^{^3\mathrm{He}}(x) \approx P_n g_1^n(x) + 2P_p g_1^p(x) - 0.014\left[g_1^p(x) - 4g_1^n(x)\right]. \tag{5.43}$$

To obtain the nuclear corrections to extract g_1^n/F_1^n, we first divide Equation 5.43 by $F_1^{^3\mathrm{He}}$ and rewrite $F_1^{^3\mathrm{He}}$ in terms of $F_2^{^3\mathrm{He}}$. Solving for g_1^n/F_1^n yields [40]:

$$\frac{g_1^n}{F_1^n} = \frac{1}{\tilde{P}_n}\frac{F_2^{^3\mathrm{He}}}{F_2^n}\left(\frac{g_1^{^3\mathrm{He}}}{F_1^{^3\mathrm{He}}} - \tilde{P}_p\frac{F_2^p}{F_2^{^3\mathrm{He}}}\frac{g_1^p}{F_1^p}\right), \tag{5.44}$$

where $R \equiv \sigma_L/\sigma_T$, the ratio of longitudinal to transverse virtual photon cross sections, is considered equal for the proton and ^{3}He. The quantity $\tilde{P}_p = 2P_p - 0.014$ and $\tilde{P}_n = P_n + 0.056$. The effective polarization of the proton used was $P_p = -0.028^{+0.009}_{-0.004}$, and the neutron value used was $P_n = 0.86^{+0.036}_{-0.020}$ [71]. Using Eq. 5.44, we can extract g_1^n/F_1^n from our ^{3}He data. For the unpolarized $F_2^{^3\mathrm{He}}$ structure function, we utilized the F1F209 model [200], which incorporates Fermi motion and EMC effects. For F_2^p and F_2^n, the unpolarized PDF model CJ12 [127] was used. A fit to world g_1^p/F_1^p data [18, 19, 51, 64, 73, 229] was performed and used in the analysis*. The fit was a second-order polynomial in x with three free parameters and assumed Q^2-independence. This is a reasonable assumption as the Q^2 dependence mostly cancels in the ratio of g_1/F_1 to leading order and next-to-leading order [43].

Using the expression of A_1 in terms of the structure functions g_1, g_2 and F_1, we obtain (cf. Eq. 5.44):

$$A_1^n = \frac{1}{\tilde{P}_n}\frac{F_2^{^3\mathrm{He}}}{F_2^n}\left(A_1^{^3\mathrm{He}} - \tilde{P}_p\frac{F_2^p}{F_2^{^3\mathrm{He}}}A_1^p\right). \tag{5.45}$$

The same models for F_2 on ^{3}He, the proton and the neutron used in the g_1/F_1 analysis were used in the A_1 analysis. A Q^2-independent, second-order polynomial in x fit to world A_1^p data [18, 19, 51, 67, 68, 73, 229] was performed and used in the analysis†. The analysis for the $E = 4.74\,\mathrm{GeV}$ (5.89 GeV) data was carried out at the average Q^2 value of the data set, at $2.59\,\mathrm{GeV}^2$ $\left(3.67\ \mathrm{GeV}^2\right)$. Figures 5.50 and 5.51 show all the contributions that go

*A detailed discussion of the fitting procedure for g_1^p/F_1^p is presented in Appendix D.

†A detailed discussion of the fitting procedure for A_1^p is given in Appendix D.

into the A_1^n extraction for $E = 4.74$ GeV and 5.89 GeV data, respectively. The top left panel shows $A_1^{^3\mathrm{He}}$ and the resulting A_1^n data for both the DIS and resonance regions*. The error bars shown are statistical only. The top right panel shows the contributions due to A_1^p. The bottom left panel shows F_2^n, F_2^p and $F_2^{^3\mathrm{He}}$. The bottom right panel shows the F_2 ratio for ^{3}He to the neutron, divided by the effective neutron polarization $\tilde{P}_n$. The F_2 functions are evaluated at the appropriate Q^2 value for the $E = 4.74$ GeV or 5.89 GeV data. Similar plots follow for the g_1^n/F_1^n analysis.

The results obtained for both g_1^n/F_1^n and A_1^n will be presented in Section 6.2.

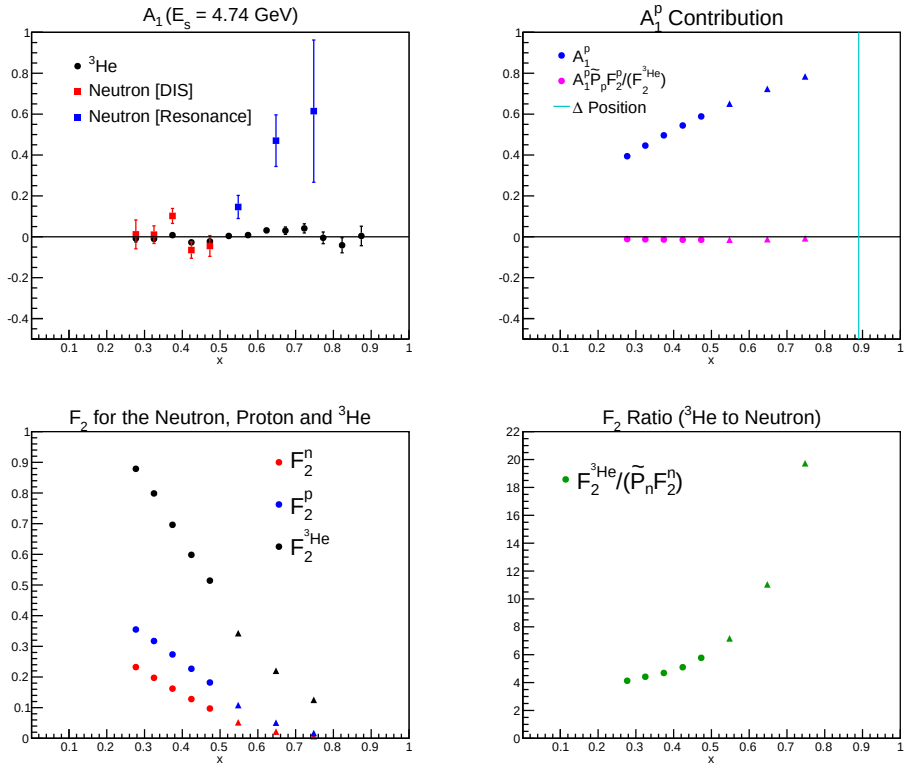

Figure 5.50: Contributions to the A_1^n extraction for $E = 4.74$ GeV data. The top left panel shows ^{3}He data and the resulting neutron data in both the DIS and resonance regions. The contribution from A_1^p is shown in the top right, where we use our fit to the world proton data. The bottom left panel shows F_2 on the neutron, proton and ^{3}He, where the nucleon F_2 is evaluated using the CJ12 model [127] and the ^{3}He model is evaluated using the F1F209 model [200]. The bottom right panel shows the ^{3}He to neutron ratio for F_2 divided by the effective neutron polarization $\tilde{P}_n$.

*See Section 5.6.2.2 for more detail about the resonance data.

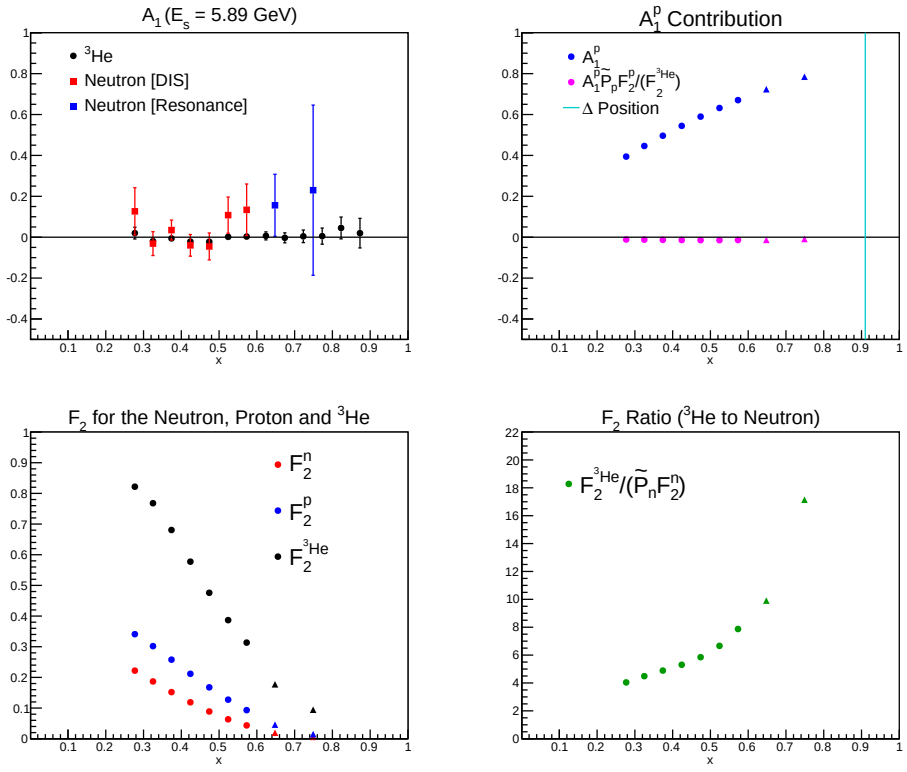

Figure 5.51: Contributions to the A_1^n extraction for $E = 5.89$ GeV data. The description of the panels is the same as that for Figure 5.50.

5.6.2.2 Resonance Data

With the intention of pushing to larger x to potentially start to discern between the various models and predictions for A_1^n, we can examine our resonance data on A_1 under the assumption of duality [72, 73, 93, 94, 97]. We have rebinned the $A_1^{^3\mathrm{He}}$ and $g_1^{^3\mathrm{He}}/F_1^{^3\mathrm{He}}$ results for E = 4.74 GeV and 5.89 GeV in the resonance region into three equally spaced x bins of 0.548, 0.648, and 0.748 for the $E = 4.74$ GeV data and $x = 0.648$ and 0.749 for $E = 5.89$ GeV, respectively. Our rebinning was restricted to a maximum central value of $x \sim 0.75$ so as to avoid the delta resonance which has its peak at $x \approx 0.90$*. The rebinning of the A_1 data is shown in Figures 5.52(a) and 5.52(b). The black data points were obtained from a statistical error-weighted average of the red data points that contribute to a given new bin, indicated by the vertical black bars. The systematic error for a new bin was obtained by an average of the errors contributing to that bin with a weight of 1. The same procedure was done for the g_1/F_1 data.

Applying nuclear corrections to our rebinned resonance data yields the results shown in Section 6.2, and are tabulated in Appendix E.3. The analysis for the $E = 4.74$ GeV

*Also, the upper bound of the last bin is $x = 0.8$, as the nuclear corrections are valid up to that x value.

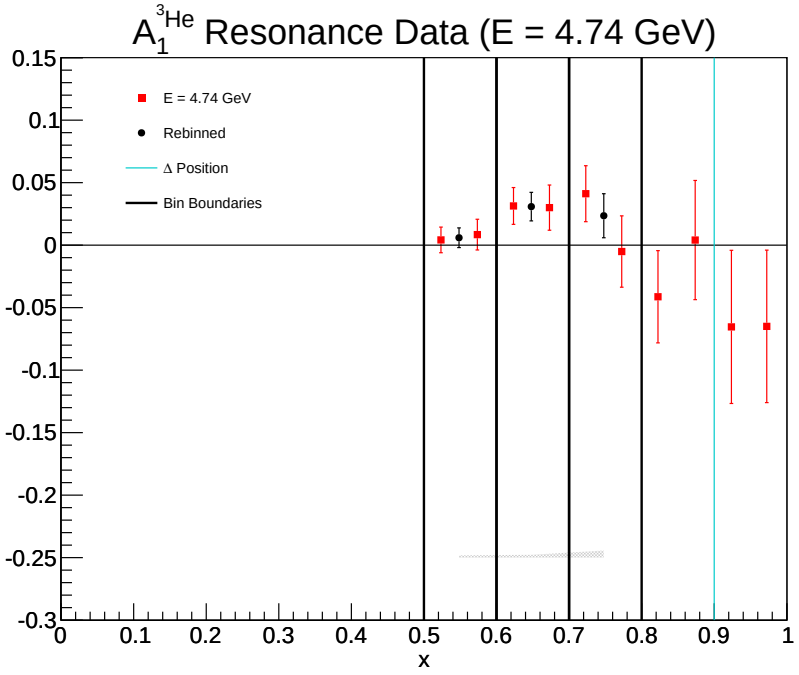

(a) $E_s = 4.74$ GeV

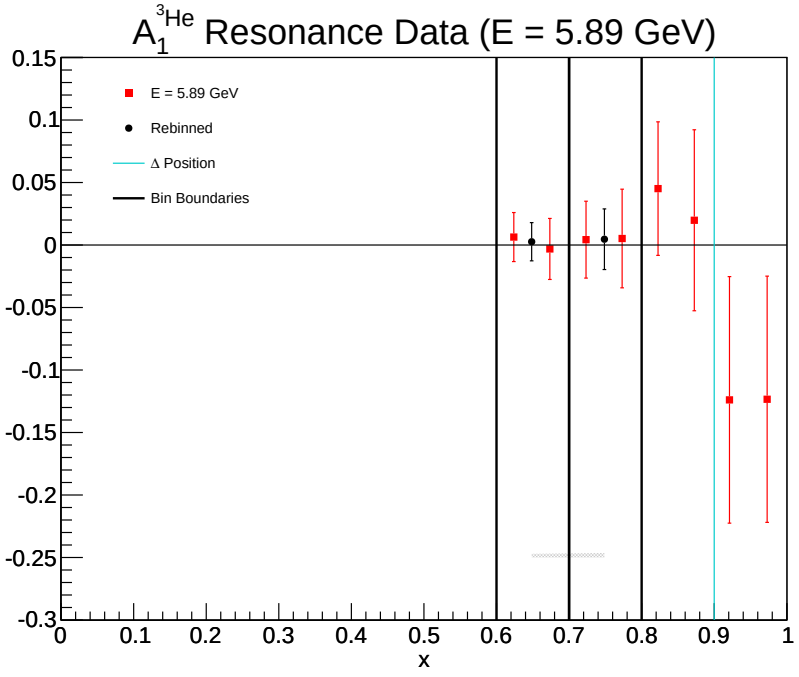

(b) $E_s = 5.89$ GeV

Figure 5.52: Rebinning of the $A_1^{^3\mathrm{He}}$ data. The rebinned data points were obtained from a statistical-error-weighted average, while the systematic error (gray band) was obtained from an average with a weight of 1 for the errors contributing to the new bin. (a): $E_s = 4.74$ GeV data; (b): $E_s = 5.89$ GeV data.

(5.89 GeV) data was carried out at the average Q^2 value of the data set, at 3.89 GeV^2 $\left(5.58\ \text{GeV}^2\right)$. The same approach was also employed for g_1/F_1; those results are presented in Section 6.2 and are tabulated in Appendix E.5.

There has been active work in computing nuclear corrections for resonance data in recent time [230]. The differences between such calculations and the prescription above are sizable only in kinematics where the Δ resonance is prominent. Additionally, accurate calculations according to [230] require particularly precise data. To estimate the strength of the Δ in our kinematics, we have computed $A_1^{^3\text{He}}$ using the MAID model [141] for $g_1^{^3\text{He}}$ and the F1F209 model [200] for $F_1^{^3\text{He}}$, as shown in Figure 5.53. We can see the large Δ peak for $Q^2 = 3\,\text{GeV}^2$ curve, shown in blue. The red curve indicates $Q^2 = 3.89\,\text{GeV}^2$, the $\langle Q^2 \rangle$ of our $E = 4.74\,\text{GeV}$ resonance data; since the MAID model is only valid up to 5 GeV^2, we show $Q^2 = 4.9\,\text{GeV}^2$ (green curve). In considering $\langle Q^2 \rangle = 5.58\,\text{GeV}^2$ for our $E = 5.89\,\text{GeV}$ data, one can see how such resonance behavior will be even smaller than what is indicated by the $Q^2 = 4.9\,\text{GeV}^2$ calculation. In Figure 5.53 we also indicate the position of the upper edge of the highest x bin of our (rebinned) resonance data. It is clear that the resonance structure in these kinematics is not very pronounced given the Q^2 range. Due to this and the large statistical errors on our resonance data relative to our DIS measurements, we take the duality approach outlined above for nuclear corrections on our resonance data.

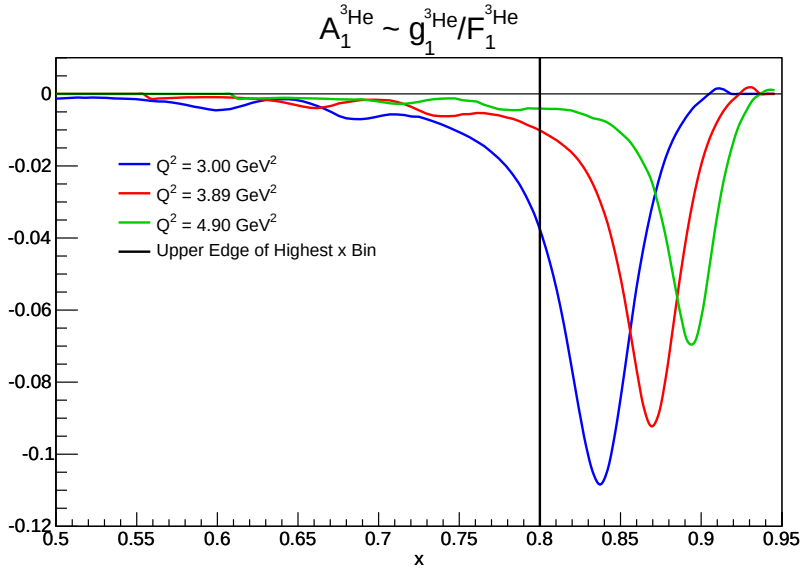

Figure 5.53: $A_1^{^3\text{He}}$ using the MAID [141] and F1F209 [200] models to illustrate the resonance behavior in our kinematics. The blue curve indicates $Q^2 = 3\,\text{GeV}^2$, the red curve is for $Q^2 = 3.89\,\text{GeV}^2$ and the green curve shows $Q^2 = 4.9\,\text{GeV}^2$. The vertical black line indicates the upper edge of the highest x bin of our (rebinned) resonance data.

5.6.3 Systematic Errors

The main factors that contribute to the errors on the ^{3}He data are the physics asymmetries $A_\parallel$ and $A_\perp$, and the kinematic factors D, η, ξ and d. Each asymmetry was varied within its error, and the change in $A_1^{^3\mathrm{He}}$ was observed. For the kinematics, the low-level variables of the electron momentum p and scattering angle θ were changed within their relative errors of 1% and 1.4% [169] respectively, and the kinematic factors were re-evaluated*, and the change in the A_1 asymmetry was observed.

For the systematic error on A_1^n, the inputs that were varied consisted of F_2^n and F_2^p, $F_2^{^3\mathrm{He}}$, A_1^p and our $A_1^{^3\mathrm{He}}$ data. For the neutron and proton F_2, various models [89, 127, 231, 232] were compared, and the largest difference in A_1^n was taken as the error. The same procedure was used for $F_2^{^3\mathrm{He}}$, where the parameterizations considered were F1F209 [200] and NMC95 [233]. The remaining quantities, $A_1^{^3\mathrm{He}}$, our fit to A_1^p data and the effective polarizations P_n and P_p were varied within their errors for 1000 trials, and the average deviation from the extracted value was taken as the error. The in quadrature sum of each component is given as the total error. The errors are given in Tables E.37 and E.38 for the DIS results, and the errors for the resonance data are presented in Tables E.39 and E.40.

The same procedures are followed for the g_1/F_1 data, and the errors are tabulated in Appendix E.5.

*The ratio $R \equiv \sigma_L/\sigma_T$, which enters into the calculation of D, was also varied within its given systematic error in this study.

5.7 Flavor Decomposition

5.7.1 Extraction From g_1/F_1 Data

Using the g_1^n/F_1^n data, we can extract the polarized-to-unpolarized quark ratios $(\Delta u + \Delta\bar{u})/(u+\bar{u})$ and $(\Delta d + \Delta\bar{d})/(d+\bar{d})$ according to Equations 2.43 and 2.44, where we need a parameterization of $(d+\bar{d})/(u+\bar{u})$ and g_1^p/F_1^p. For the former, we used the CJ12 model [127], as shown in Figure 5.54 for $Q^2 = 2.59\,\text{GeV}^2$. For g_1^p/F_1^p, we used our fit to the world data*, as discussed in Section 5.6.2. The analysis for the $E = 4.74\,\text{GeV}$ (5.89 GeV) data was carried out at the average Q^2 value of the data set, at $2.59\,\text{GeV}^2$ ($3.67\,\text{GeV}^2$).

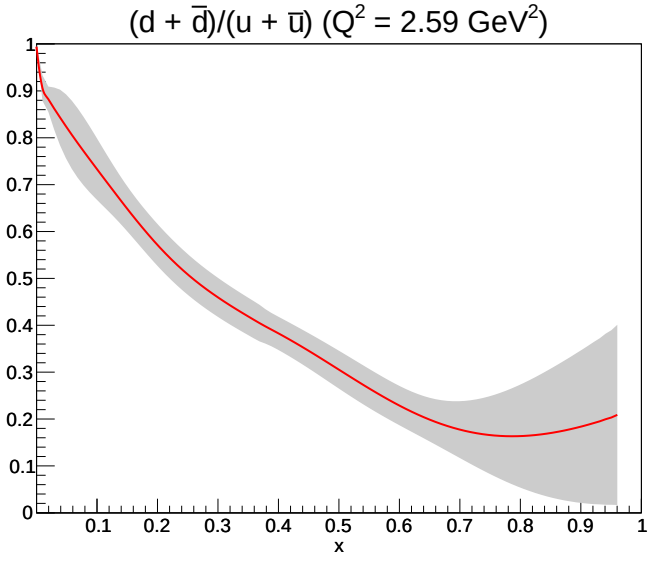

Figure 5.54: The quantity $R^{du} = (d+\bar{d})/(u+\bar{u})$ computed from the CJ12 model [127] for $Q^2 = 2.59\,\text{GeV}^2$. A similar curve is used for $\langle Q^2 \rangle = 3.67\,\text{GeV}^2$ data.

The results are tabulated in Appendix E.7, and will be presented in Section 6.3.

5.7.2 Systematic Errors

The systematic errors for the up and down quark ratios were determined by varying the inputs individually and observing the change in the result. The inputs considered were our g_1^n/F_1^n data, our g_1^p/F_1^p fit, and the $(d+\bar{d})/(u+\bar{u})$ ratio. Each quantity was varied within their respective errors for 1000 runs, and the average deviation was taken as the error.

In this leading-order analysis, the strange contribution is typically left out of the calculation and taken as an error†. We followed the same procedure, where we evaluate the

*See Appendix D for details about the g_1^p/F_1^p fit.

†This is a reasonable approach for $x \gtrsim 0.3$ where the strange quarks do not contribute much.

strange contribution as follows: we compute $(\Delta u + \Delta\bar{u})/(u+\bar{u})$ and $(\Delta d + \Delta\bar{d})/(d+\bar{d})$ with the strange component *included*:

$$\frac{\Delta u+\Delta\bar{u}}{u+\bar{u}} = \left(\frac{\Delta u+\Delta\bar{u}}{u+\bar{u}}\right)_{s,\bar{s}=0} + \frac{s+\bar{s}}{u}\left[\frac{4}{15}\frac{g_1^p}{F_1^p} - \frac{1}{15}\frac{g_1^n}{F_1^n} - \frac{1}{5}\frac{\Delta s+\Delta\bar{s}}{s+\bar{s}}\right] \quad (5.46)$$

$$\frac{\Delta d+\Delta\bar{d}}{d+\bar{d}} = \left(\frac{\Delta u+\Delta\bar{u}}{u+\bar{u}}\right)_{s,\bar{s}=0} + \frac{s+\bar{s}}{d}\left[\frac{4}{15}\frac{g_1^n}{F_1^n} - \frac{1}{15}\frac{g_1^n}{F_1^n} - \frac{1}{5}\frac{\Delta s+\Delta\bar{s}}{s+\bar{s}}\right], \quad (5.47)$$

where the terms $(\ldots)_{s,\bar{s}=0}$ are defined in Equations 2.43 and 2.44 and have no strange contributions. The second term in Equations 5.46 and 5.47 is the strange contribution for the up and down quark ratios, respectively. We compute these terms using various models [87, 89, 127, 220, 231, 234, 235], and took the largest difference between all model combinations as the error for omitting the strange contribution for the up and down quark ratios. The in quadrature sum of all contributions gives the full systematic errors, which are summarized in Appendix E.7.2.

5.8 g_1

In this section, we give an overview of the analysis to obtain $g_1^{^3\mathrm{He}}$ from the measured unpolarized cross sections and double-spin asymmetries. A more detailed discussion of the $g_1^{^3\mathrm{He}}$ analysis may be found in [169].

5.8.1 Extraction From Data

The spin structure function g_1 may be obtained from the measured unpolarized cross section σ_0 and the double-spin asymmetries $A_\parallel$ and $A_\perp$ through:

$$g_1 = \frac{MQ^2}{4\alpha^2}\frac{2y}{(1-y)(2-y)}\sigma_0\left[A_\parallel + \tan(\theta/2)A_\perp\right]. \quad (5.48)$$

The measured cross section from the LHRS data did not have the same binning as the asymmetry data measured on BigBite; to obtain a cross section value for each BigBite bin, the cross section data (Sect. 5.4.4) were interpolated and extrapolated according to the fit function:

$$f(x) = \exp\left(a+bx+cx^2\right), \quad (5.49)$$

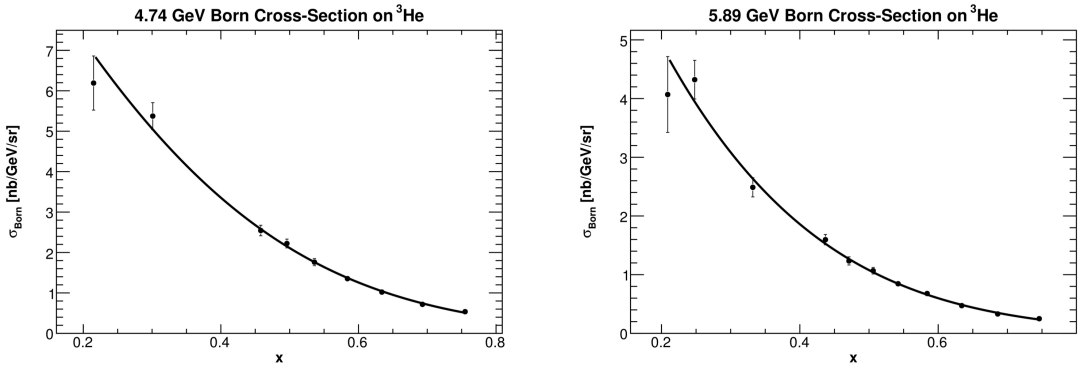

Figure 5.55: The fit function used to interpolate and extrapolate the measured cross sections (Sect. 5.4.4). The error bars shown are the in-quadrature sum of the statistical and systematic errors. Figure reproduced from [169].

where a, b and c were free parameters determined by the fitting of the data; x is the Bjorken-x variable. This analysis was done by M. Posik [169]. The fit results are shown in Figure 5.55.

Utilizing the fit for the unpolarized cross section data, the g_1 structure function for ^{3}He may be formed according to Equation 5.48, and is presented in Figure 5.56. The error bars represent our statistical errors, while the error bands represent the systematic errors*. The world data plotted are DIS data from SLAC E142 [60] and JLab E99-117 [71], and the JLab E01-012 data [72] are resonance data. The gray band represents global analyses from [87, 89, 220, 234, 235].

*The systematic errors include contributions from the double-spin asymmetries, kinematics, and the unpolarized cross section fit. See [169] for more details.

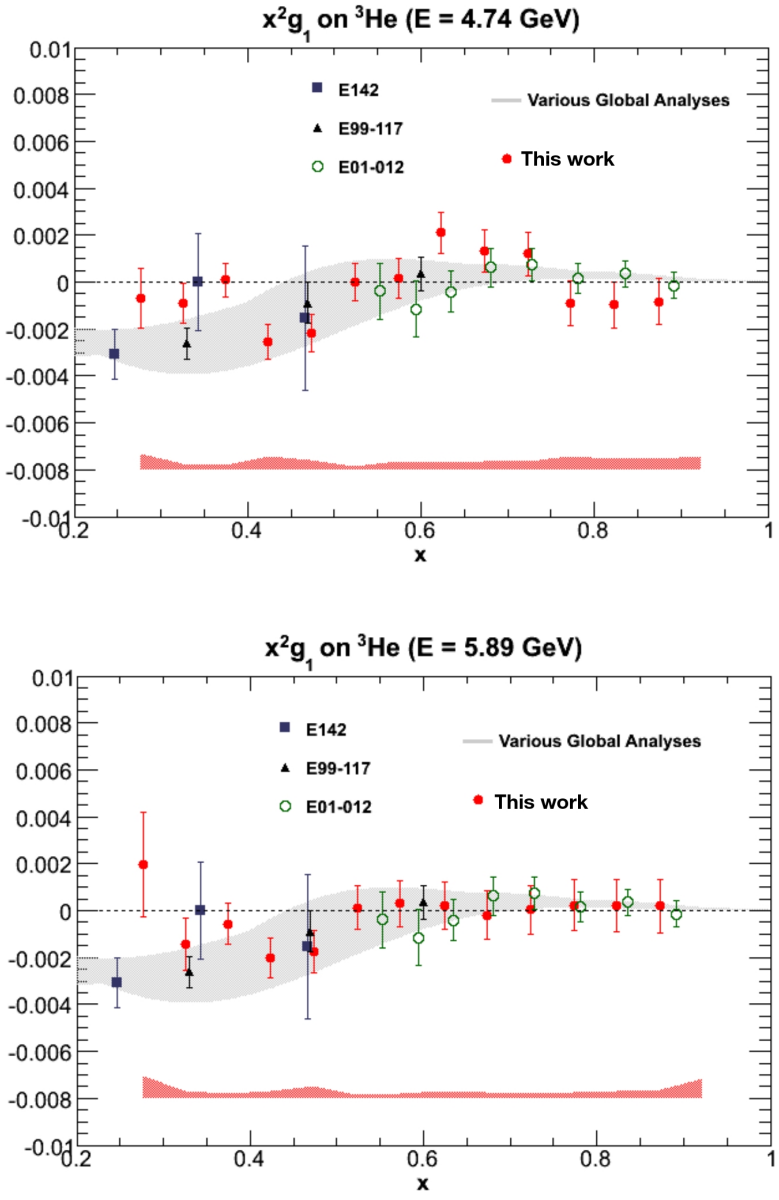

Figure 5.56: The $g_1^{^3\mathrm{He}}$ results for $E = 4.74\,\mathrm{GeV}$ (5.89 GeV) are given in the top (bottom) panel. The error bars indicate the statistical errors, while the red band indicates the systematic error. The world data are from SLAC E142 [60] and JLab E99-117 [71], both of which are DIS data; resonance data from JLab E01-012 [72] are also plotted. The gray band represents global analyses from [87, 89, 220, 234, 235]. Figure reproduced from [169].

5.9 a_2

The analysis necessary to extract a_2, the second moment of g_1, is discussed in this section. We first introduce the Cornwall-Norton Moments in Section 5.9.1, and then we present the analyses needed to complete the entire integral in Sections 5.9.2– 5.9.4.

5.9.1 The Cornwall-Norton Moments

Using the OPE, an infinite set of sum rules may be derived under a twist expansion of the spin structure functions g_1 and g_2 [43]. Such expansions of g_1 and g_2 are known as the Cornwall-Norton (CN) moments [58]:

$$\int_0^1 x^{n-1} g_1\left(x,Q^2\right) dx = \frac{1}{2} a_{n-1}, \quad n = 1,3,5,\ldots \tag{5.50}$$

$$\int_0^1 x^{n-1} g_2\left(x,Q^2\right) dx = \frac{n-1}{2n}\left(d_{n-1} - a_{n-1}\right), \quad n = 3,5,7,\ldots, \tag{5.51}$$

where only twist-2 and twist-3 contributions are considered. The quantities a_{n-1} and d_{n-1} represent the twist-2 and twist-3 matrix elements, respectively* The expansions are only over odd integers, which is a result of the symmetry of the structure functions under charge conjugation [197].

Using our results for $g_1^{^3\mathrm{He}}$ (Fig. 5.56), we can evaluate the $n = 3$ CN moment (Eqn. 5.50), known as a_2:

$$a_2\left(Q^2\right) = \int_0^1 x^2 g_1\left(x,Q^2\right) dx. \tag{5.52}$$

Since our measured x-range consists of $0.25 < x < 0.90$, we also have to consider the unmeasured regions of $x < 0.25$ (referred to as the low-x region), and $x > 0.90$ (referred to as the high-x region). In the following, we discuss the analysis associated with each region leading to the extraction of a_2^n.

5.9.2 Low-x Region

For the low-x portion of the integral to evaluate a_2^n, we consider the world data on g_1^n from SLAC E142 [60], E143 [51] E154 [82], and JLab E97-103 [236]. Plotting $x^2 g_1^n$ as a function of x, we fit a third-order polynomial in x, assuming no Q^2-dependence, see Figure 5.57. The

*The convention used by [58] is such that the matrix elements are labeled according to n as opposed to $n-1$, as defined in this work.

gray band indicates the fitting error obtained by an estimate in the spread of the data (cf. Section 5.6.2). The obtained fit parameters are:

$$\begin{aligned} p_0 &= 1.692\text{E-}04 \pm 1.829\text{E-}04 \\ p_1 &= -1.584\text{E-}02 \pm 8.093\text{E-}03 \\ p_2 &= 2.561\text{E-}02 \pm 8.886\text{E-}02 \\ p_3 &= 1.423\text{E-}02 \pm 2.755\text{E-}01 \end{aligned} \tag{5.53}$$

Integrating over this fit yields a_2^n in the low-x region given in Equation 5.54.

$$a_2^n = -3.056\text{E-}04 \quad \text{for} \quad 0.02 \leq x \leq 0.25 \tag{5.54}$$

We note here that the fit was done down to $x = 0.02$; this has a minimal effect on the a_2 calculation due to the x^2-weighting of the integral. This value for the low-x region (Eqn. 5.54) was taken as a constant for each Q^2 bin that we have data for, $\langle Q^2 \rangle = 3.21\,\text{GeV}^2$ and $4.32\,\text{GeV}^2$, corresponding to the $E = 4.74\,\text{GeV}$ and $5.89\,\text{GeV}$ data sets, respectively. The data used in the low-x region cover $0.5 < Q^2 < 10\,\text{GeV}^2$, and it can be seen in Figure 5.57 that the Q^2-dependence is minimal.

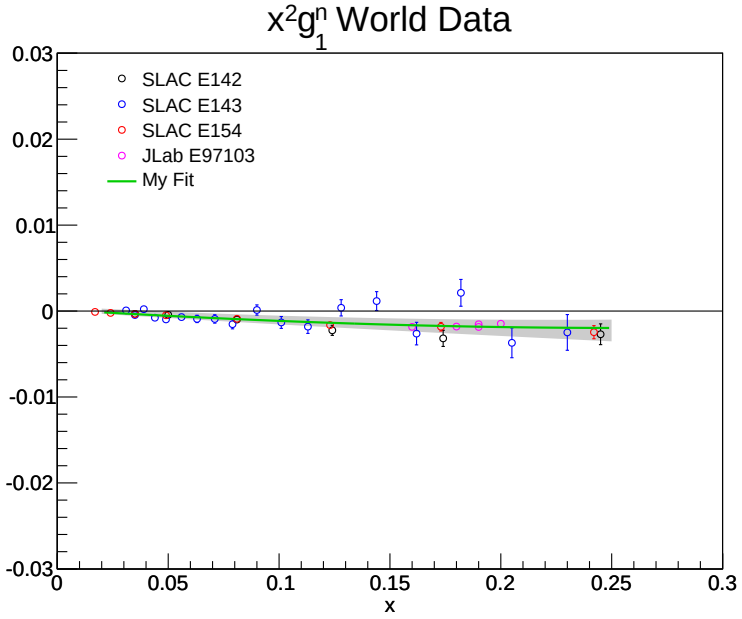

Figure 5.57: The world data [51, 60, 82, 236] on g_1^n in the range $0 < x < 0.25$. The data cover $0.5 < Q^2 < 10\,\text{GeV}^2$. It can be seen in the plot that the Q^2-dependence is minimal. Our fit is given by the green curve, and its error is given by the gray band.

Table 5.3: The extracted $a_2^{^3\mathrm{He}}$ in the measured region of $0.25 < x < 0.90$. The errors listed are statistical and systematic, respectively. All errors are absolute.

$\langle Q^2 \rangle$ (GeV^2)	$a_2^{^3\mathrm{He}}$ (measured)
3.21	-2.085E-04 $\pm$ 1.613E-04 $\pm$ 3.539E-05
4.32	-1.351E-04 $\pm$ 2.079E-04 $\pm$ 3.348E-05

5.9.3 Measured Region

5.9.3.1 ^{3}He Integration

For the measured region of x, we compute the integral using our $g_1^{^3\mathrm{He}}$ data:

$$a_2^{^3\mathrm{He}}\left(Q^2\right) = \int_{0.25}^{0.90} x^2 g_1^{^3\mathrm{He}}\left(x, Q^2\right) dx. \tag{5.55}$$

This is done for the $E = 4.74\,\mathrm{GeV}$ and $5.89\,\mathrm{GeV}$ data sets, where the average Q^2 is $3.21\,\mathrm{GeV}^2$ and $4.32\,\mathrm{GeV}^2$, respectively. The result of that integration is given in Table E.72. The systematic error given in the table is due to the varying our $g_1^{^3\mathrm{He}}$ data within their systematic errors, along with the errors coming from x and observing the change on the resulting $a_2^{^3\mathrm{He}}$ value.

5.9.3.2 Target Mass Corrections

The CN moments have been argued to only be valid when the terms corresponding to the finite mass of the nucleon can be neglected; such factors are called target mass correction (TMC) terms [237–242]. These corrections are related to twist-2 operators and are of order $\mathcal{O}\left(M^2/Q^2\right)$. The *Nachtmann* moments M_1 and M_2* incorporate target mass corrections into the integrals of interest, compared to the CN moments which do not incorporate TMCs.

The M_1 moments are are connected to the twist-2 matrix element a_2 [58, 140, 243]:

$$\begin{aligned} M_1^n\left(Q^2\right) &\equiv \frac{1}{2} a_{n-1} \\ &= \int_0^1 dx \frac{\xi^{n+1}}{x^2} \left[g_1\left(x, Q^2\right) \left(\frac{x}{\xi} - \frac{n^2}{(n+2)^2} \frac{M^2 x^2}{Q^2} \frac{\xi}{x} \right) \right. \\ &\quad \left. - g_2\left(x, Q^2\right) \left(\frac{M^2 x^2}{Q^2} \frac{4n}{n+2} \right) \right], \end{aligned} \tag{5.56}$$

*The M_2 moments correspond to the twist-3 matrix element d_2 and will not be discussed here.

Table 5.4: The extracted $a_2^{^3\mathrm{He}}$ in the measured region of $0.25 < x < 0.90$ using the CN moment and Nachtmann moment approaches. The second-to-last column is the absolute difference between the two calculations. We see that the difference between the two is smaller than the statistical errors.

$\langle Q^2 \rangle$ (GeV^2)	CN Moment	Nachtmann Moment	$\Delta a_2^{^3\mathrm{He}}$	Stat. Error (CN)
3.21	-2.09E-04	-9.09E-05	1.18E-04	1.61E-04
4.32	-1.35E-04	-1.14E-04	2.16E-05	2.08E-04

where $\xi = 2x/\left(1+\sqrt{1+4M^2x^2/Q^2}\right)$ and $n = 3, 5\ldots$. In the limit of large Q^2, one can see how these moments reduce to the CN moments. In evaluating the Nachtmann moments, we need to evaluate the $n = 3$ moment in order to compare to the CN moment (cf. Equation 5.50). Therefore, we evaluate M_1^3 to obtain a_2 in the Nachtmann formalism. We note here the dependence on g_2; because of this, we utilize the $g_2^{^3\mathrm{He}}$ data measured in this experiment*. Comparing the integrals in the two forms, we find that the difference between the two results is *smaller* than the size of our statistical errors, as shown in Table 5.4. Because of this, we decided to not include TMCs in our calculations.

5.9.3.3 Nuclear Corrections

With the $a_2^{^3\mathrm{He}}$ quantity extracted in the measured region for our two average Q^2 bins, we need to apply nuclear corrections. This is done in a similar fashion as shown in Section 5.6.2, where a_2^n is given as:

$$a_2^n = \frac{1}{\tilde{P}_n}\left(a_2^{^3\mathrm{He}} - \tilde{P}_p a_2^p\right), \tag{5.57}$$

where $\tilde{P}_n$ and $\tilde{P}_p$ are the effective polarizations of the neutron and proton in ^{3}He, respectively. They include effects due to the presence of Δ components in the ^{3}He wave function and are defined in Section 5.6.2. The proton a_2 is evaluated by considering various models [87, 89, 220, 234, 235, 244] and taking the average as the central value for a_2^p and the maximum difference between the models as the error. The values used for a_2^p are given in Table 5.5. Using these values for a_2^p, we can extract a_2^n from our ^{3}He data; the neutron results are given in Table 5.6.

*The structure function analysis for both $g_1^{^3\mathrm{He}}$ and $g_2^{^3\mathrm{He}}$ was carried out by M. Posik. We use the results from his work. For more details, see [169].

Table 5.5: a_2^p estimated by considering various global analyses [87, 89, 220, 234, 235, 244]. The average of all values is the central value given, while the maximum difference between the models is taken as the error.

$\langle Q^2 \rangle$ (GeV^2)	a_2^p
3.21	9.623E-03 $\pm$ 9.414E-04
4.32	9.126E-03 $\pm$ 8.464E-04

Table 5.6: The extracted a_2^n in the measured region of $0.25 < x < 0.90$. The error given here is statistical only.

$\langle Q^2 \rangle$ (GeV^2)	a_2^n (measured)
3.21	5.078E-04 $\pm$ 1.761E-04
4.32	5.499E-04 $\pm$ 2.270E-04

5.9.4 High-x Region

To evaluate a_2^n on the range $0.90 < x < 1$, we consider the *elastic* contribution ($x = 1$). Considering the size of our $g_1^{^3\mathrm{He}}$ data, we consider the region leading up to the elastic ($0.90 < x < 0.9\bar{9}$) to be negligible. The elastic component may be evaluated as:

$$a_2^{n,el} = \int_0^1 dx x^2 g_1^{n,el}(x, Q^2) \tag{5.58}$$

$$= \int_0^1 dx x^2 \frac{G_M^n(Q^2)}{2} \frac{G_E^n(Q^2) + \tau G_M^n(Q^2)}{1+\tau} \delta(x-1) \tag{5.59}$$

$$= \frac{G_M^n(Q^2)}{2} \frac{G_E^n(Q^2) + \tau G_M^n(Q^2)}{1+\tau}, \tag{5.60}$$

where $\tau \equiv Q^2/(4M^2)$, and M is the nucleon mass; the elastic electric form factor for the neutron is G_E^n, while the elastic magnetic form factor is G_M^n. We evaluate the elastic a_2^n using the Riordan [245] parameterization for G_E^n and the Kelly [246] parameterization for G_M^n. The elastic a_2 on the neutron is shown as a function of Q^2 in Figure 5.58.

5.9.5 Full Neutron Extraction

To extract the full a_2^n, we add the contributions from all three x regions:

$$a_2^n = a_2^n(\text{low-}x) + a_2^n(\text{measured}) + a_2^n(\text{high-}x). \tag{5.61}$$

The results will be presented in Section 6.4 and are tabulated in Appendix E.8.

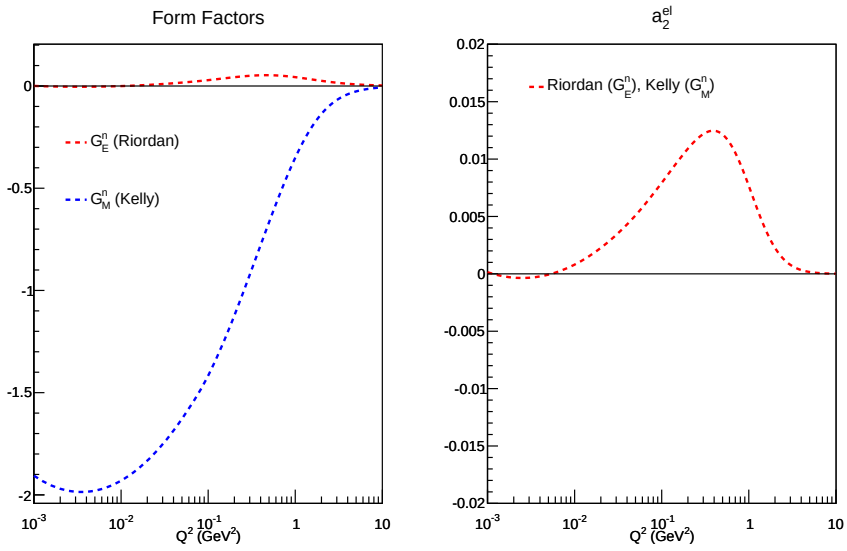

Figure 5.58: The left panel shows the G_E^n (red) and G_M^n (blue) elastic form factors, using the Riordan [245] and Kelly [246] parameterizations, respectively. The right panel shows the elastic contribution to a_2^n.

5.9.6 Systematic Errors

To obtain the systematic error on our a_2^n result, we vary the inputs for a given region, and compute the resulting a_2 while keeping the other inputs constant; for instance, when computing the systematic error due to the low-x region, we vary our fit within its error and compute the low-x integral. From there, we extract a_2^n using the already-extracted measured and high-x a_2^n values. This is done for 1000 trials for each x region, and the average deviation from our extracted result is taken as the error. In the measured region, our $a_2^{^3\mathrm{He}}$ is varied within its systematic error, as are the effective neutron and proton polarizations; the a_2^p value is also varied within its error. For the elastic component, we also utilize the Galster [211] and dipole parameterizations for G_E^n and G_M^n; the difference between the resulting a_2^n and the one obtained when using the Riordan [245] and Kelly [246] parameterizations for G_E^n and G_M^n is taken as the error. The in quadrature sum of all errors gives the total error. The error analysis results are tabulated in Appendix E.8.

CHAPTER 6

RESULTS

In this chapter, we present the results extracted for $A_1^{^3\mathrm{He}}$ and $g_1^{^3\mathrm{He}}/F_1^{^3\mathrm{He}}$ in Section 6.1, and in Section 6.2 we present the results for A_1^n and g_1^n/F_1^n. In Section 6.3, we show the results for the flavor decomposition analysis to obtain $(\Delta u+\Delta\bar{u})/(u+\bar{u})$ and $(\Delta d+\Delta\bar{d})/(d+\bar{d})$. The results for a_2^n are presented in Section 6.4. Tables of all results are given in Appendix E.

6.1 $A_1^{^3\mathrm{He}}$ and $g_1^{^3\mathrm{He}}/F_1^{^3\mathrm{He}}$

The ^{3}He results for A_1 are presented in Figure 6.1(a), where our results for $E = 4.74\,\mathrm{GeV}$ ($5.89\,\mathrm{GeV}$) are given by the red (blue) points. The error bars on our data indicate the statistical error and the red (blue) band represents the systematic error for $E = 4.74\,\mathrm{GeV}$ ($5.89\,\mathrm{GeV}$). Also plotted is the world DIS data from SLAC E142 [60], HERMES [66] and JLab E99-117 [71]. Also plotted is resonance data from JLab E01-012 [72] at their two highest $\langle Q^2 \rangle$ bins of $2.6\,\mathrm{GeV}^2$ and $3.6\,\mathrm{GeV}^2$. The data are compared to selected models, including the statistical quark model from Bourrely *et al.* [89] given by the orange curve, the pQCD with orbital angular momentum parameterization from Avakian *al.* [88] (magenta) and the global analysis from Leader *et al.* [86] given by the cyan curve. Our results are in good agreement with the current world data, and are consistent with the trend displayed by the statistical quark model. The E06-014 experiment was a dedicated measurement of the quantity d_2^n, not A_1^n, so the statistical precision of the A_1 results are not as competitive with those of JLab E99-117, an A_1-dedicated measurement. Despite this, we do have more complete kinematic coverage in that our measurement covers the DIS and resonance regions, where the resonance data starts at $x > 0.519$ (0.623) for $E = 4.74\,\mathrm{GeV}$ ($5.89\,\mathrm{GeV}$).

The results for $g_1^{^3\mathrm{He}}/F_1^{^3\mathrm{He}}$ are shown in Figure 6.1(b), where our data are given by the red and blue points for $E = 4.74\,\mathrm{GeV}$ and $5.89\,\mathrm{GeV}$ data, respectively. The world DIS data

presented in the plot is from JLab E99-117, while the $g_1^{^3\mathrm{He}}/F_1^{^3\mathrm{He}}$ models displayed correspond to the same groups used in the $A_1^{^3\mathrm{He}}$ plot. Similar to the $A_1^{^3\mathrm{He}}$ results, our statistical errors are not quite as competitive with those of JLab E99-117, but we do provide a more complete kinematic coverage, with results for the DIS and resonance regions. Our results are also in good agreement with the statistical quark model of Bourrely *et al.*

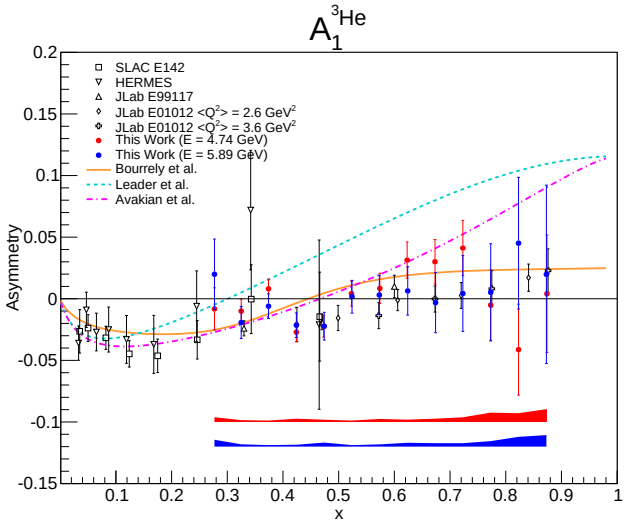

(a) $A_1^{^3\mathrm{He}}$ Results

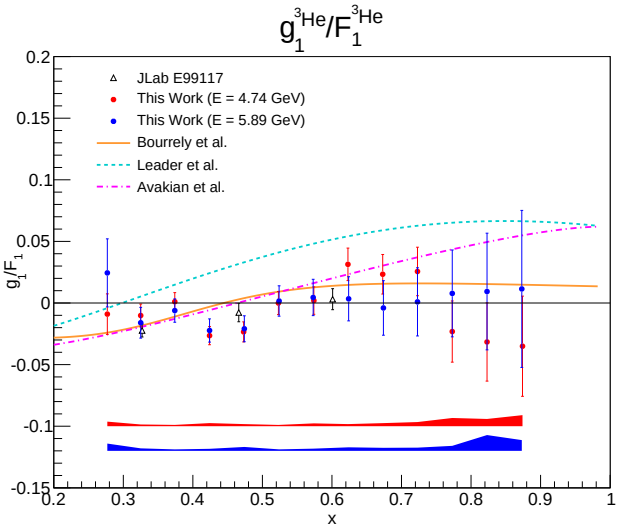

(b) $g_1^{^3\mathrm{He}}/F_1^{^3\mathrm{He}}$ Results

Figure 6.1: $A_1^{^3\mathrm{He}}$ and $g_1^{^3\mathrm{He}}/F_1^{^3\mathrm{He}}$ results for $E = 4.74\,\mathrm{GeV}$ (5.89 GeV) shown in red (blue). The statistical errors are indicated by the error bars, while the colored bands show the systematic errors. The models displayed are from Bourrely *et al.* (orange) [89], Avakian *et al.* (magenta) [88], and Leader *et al.* (cyan) [86]. (a): $A_1^{^3\mathrm{He}}$ data, compared to world DIS data from SLAC E142 [60], JLab E99-117 [71], and resonance data from JLab E01-012 [72]. (b): $g_1^{^3\mathrm{He}}/F_1^{^3\mathrm{He}}$ data, compared to world DIS data from JLab E99-117.

6.2 A_1^n and g_1^n/F_1^n

6.2.1 DIS Results

Results for A_1^n are given in Figure 6.2, where our data are indicated by the red (blue) points for $E = 4.74$ GeV (5.89 GeV), and the colored bands indicate their systematic errors. World DIS data presented are SLAC E142 [60] and E154 [61], JLab E99-117 [71] and HERMES [64]. The models shown are the relativistic CQM model from Isgur [81] (gray band), a statistical quark model [89, 90] (orange), and pQCD models from Leader *et. al* [86] (cyan), and Avakian *et al.* [88] (magenta), where the latter model explicitly includes orbital angular momentum Fock states into their calculations. A modified NJL model from Cloët *et al.* [114] (green) is also plotted. The predictions from Roberts *et al.* [126] are plotted at $x = 1$, which follow from Dyson-Schwinger Equation treatments, where non-pointlike diquark correlations arise naturally as a consequence of dynamical chiral symmetry breaking. Our results are consistent with the world data, in particular the results from JLab E99-117, which shows a zero-crossing at $x \approx 0.5$. Our results tend to exclude the pQCD calculation from Leader *et al.*, which is formulated under the notion of hadron helicity conservation, where orbital angular momentum of quarks is assumed to be zero; this points perhaps to an importance of orbital angular momentum of quarks in the nucleon.

Our extracted results for g_1^n/F_1^n are shown in Figure 6.3, where our data are indicated by the red (blue) points for $E = 4.74$ GeV (5.89 GeV), and the colored bands indicate their systematic errors. The world DIS data presented here corresponds to SLAC E143 [51] and E155 [229] and JLab E99-117 [71]. The models shown are the same as shown in Figure 6.2, without the the modified NJL model. Our data are consistent with the data from JLab E99-117 and the plotted models. Our results also provide much better precision relative to the SLAC measurements.

6.2.2 Resonance Results

By invoking duality [72, 73, 93, 94, 97], we have extracted A_1^n in the resonance region, as shown in Section 5.6.2.2. Our results are presented in Figure 6.4(a), which shows our DIS results along with the resonance points (solid squares). Also displayed are resonance data from JLab E01-012 [72] (yellow and purple crosses), where we have applied the nuclear corrections according to the procedure outlined in Section 5.6.2.2. To get a clearer picture, we have combined our results from $E = 4.74$ GeV and 5.89 GeV, due to the lack of Q^2-dependence, shown in Figure 6.4(b). Despite the large statistical errors of our data, it appears that the trend of the A_1^n data becomes somewhat constant beyond $x = 0.6$ and

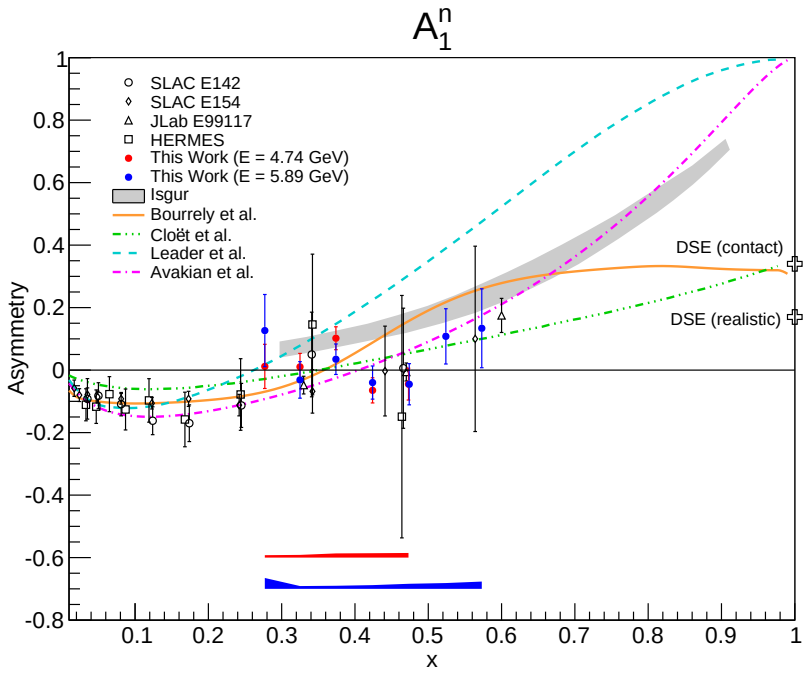

Figure 6.2: A_1^n results compared to world data and models. Our data for $E = 4.74$ GeV (5.89 GeV) are given by the red (blue) data points; the error bars indicate the statistical errors, while the bands give the systematic errors. Also plotted are the world data from SLAC E142 [60] and E154 [61], JLab E99-117 [71] and HERMES [64]. The models shown are from Isgur [81] (gray band), Bourrely *et al.* [89, 90] (orange), Leader *et. al* [86] (cyan), Avakian *et al.* [88] (magenta), and Cloët *et al.* (green) [114].

appears to be in reasonable agreement with the predictions of the statistical quark model of Bourrely *et al.*; our resonance data provide a first glimpse into the large x region that will be probed in the upcoming 12 GeV era at JLab [91, 92].

Similar to what was done for the A_1 data, we obtained g_1^n/F_1^n in the resonance region, indicated by the solid squares in Figure 6.5(a), where the same world data and models as Figure 6.3 are plotted. Averaging our results over $E = 4.74$ GeV and 5.89 GeV together, we obtain the data shown in Figure 6.5(b). Overall, it is seen that our experiment agrees well with the models, and provides higher precision data compared to what is currently available. Our resonance results provide a good benchmark for future experiments in the upcoming 12 GeV era at JLab.

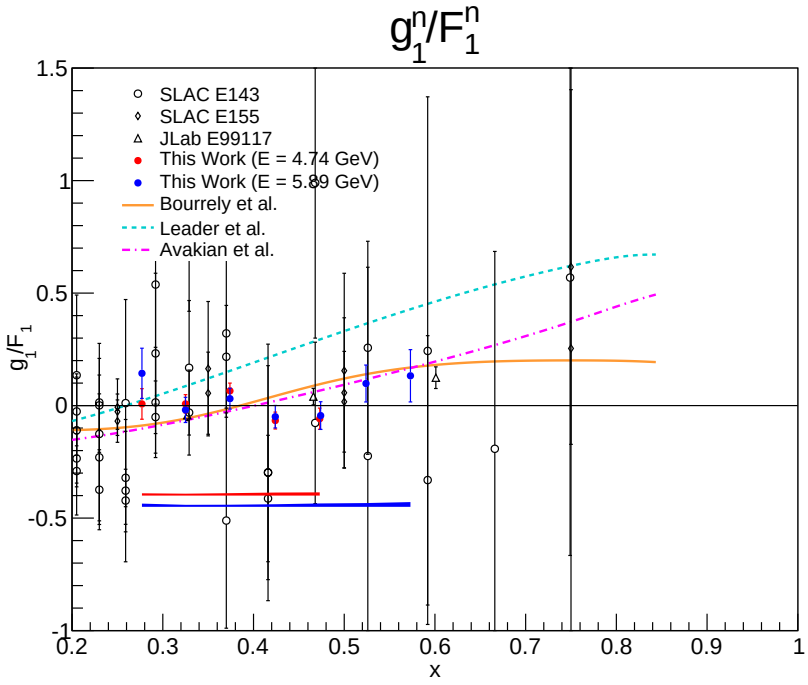

Figure 6.3: g_1^n/F_1^n results compared to world data and models. Our data for $E = 4.74\,\text{GeV}$ (5.89 GeV) are given by the red (blue) data points; the error bars indicate the statistical errors, while the bands give the systematic errors. Also plotted are the world data from SLAC E143 [51] and E155 [229] and JLab E99-117 [71]. The models shown are those from Bourrely *et al.* [89] (solid), Avakian *et al.* [88] (magenta), and Leader *et al.* [86] (cyan).

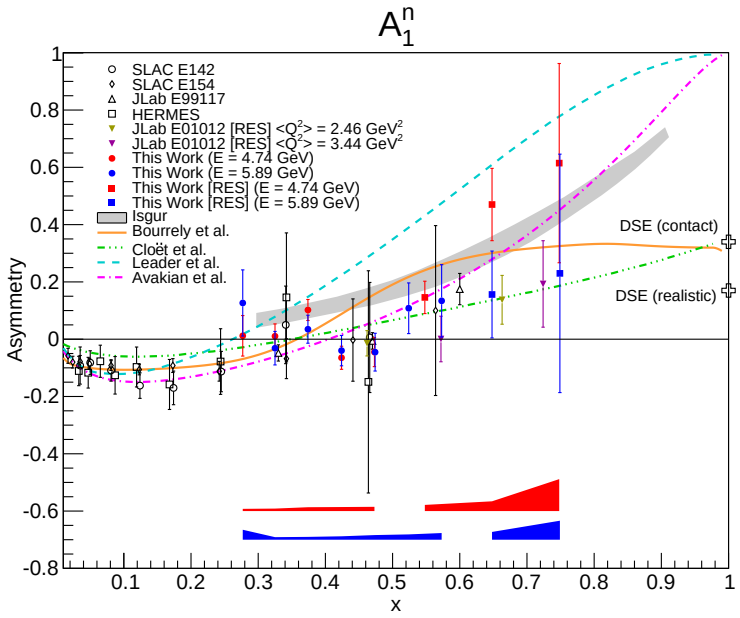

(a) A_1^n DIS and resonance results

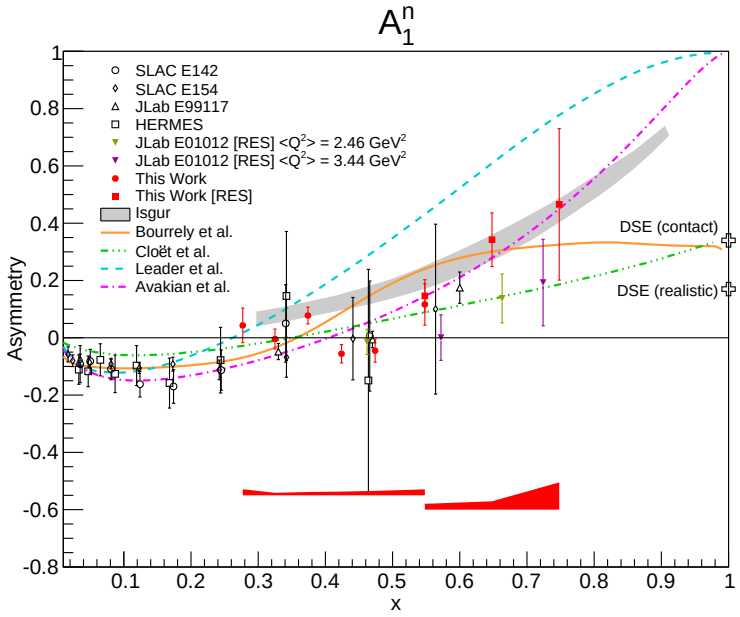

(b) A_1^n DIS and resonance results, averaged over $E = 4.74$ GeV and 5.89 GeV.

Figure 6.4: A_1^n results for the DIS and resonance regions, compared to world data and models. (a): Our data for $E = 4.74$ GeV (5.89 GeV) are given by the red (blue) data points; the error bars indicate the statistical errors, while the bands give the systematic errors. The same world data and models are plotted as seen in Figure 6.2, but now includes resonance data from JLab E01-012 [72], where we have applied the nuclear corrections, see text. (b): Same plot as the top panel, but now our data are averaged over the two beam energies of $E = 4.74$ GeV and 5.89 GeV.

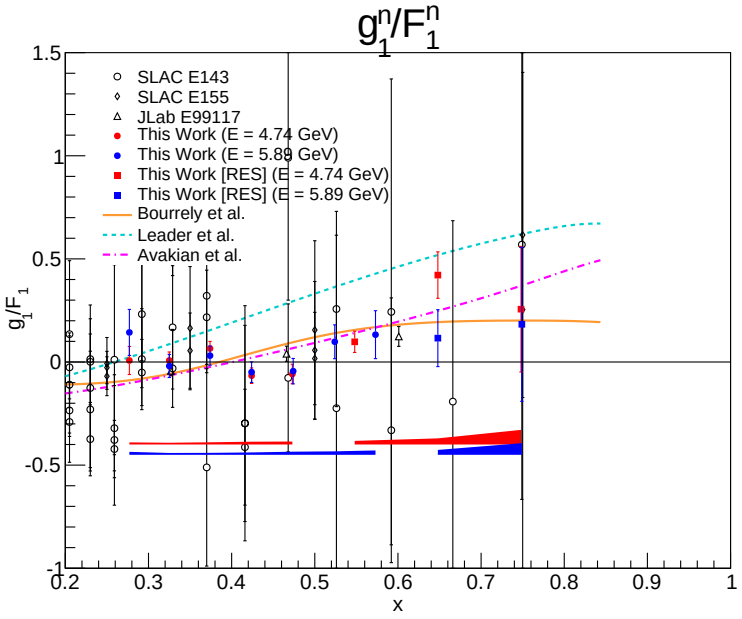

(a) g_1^n/F_1^n DIS and resonance results

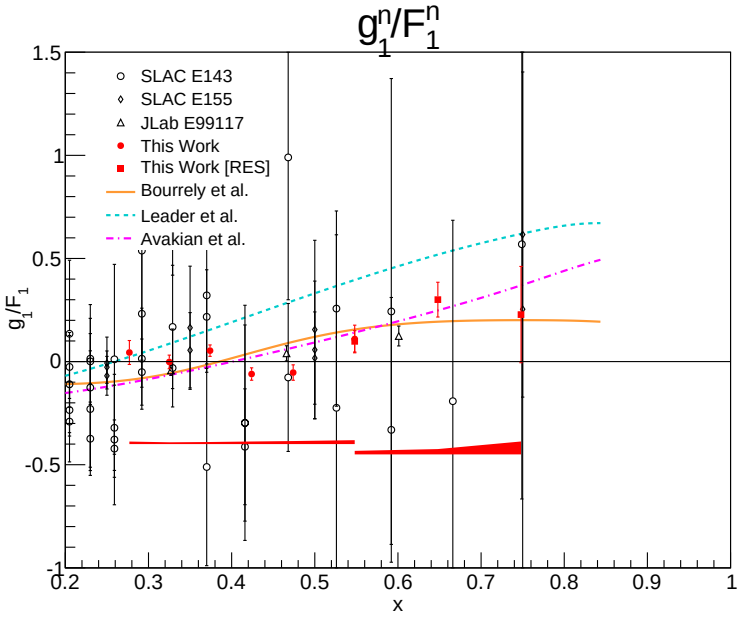

(b) g_1^n/F_1^n DIS and resonance results, averaged over $E = 4.74\,\text{GeV}$ and $5.89\,\text{GeV}$.

Figure 6.5: g_1^n/F_1^n results for the DIS and resonance regions, compared to world data and models. (a): Our data for $E = 4.74\,\text{GeV}$ ($5.89\,\text{GeV}$) are given by the red (blue) data points; the error bars indicate the statistical errors, while the bands give the systematic errors. The same world data and models are plotted as seen in Figure 6.3. (b): Same plot as the top panel, but now our data are averaged over the two beam energies of $E = 4.74\,\text{GeV}$ and $5.89\,\text{GeV}$.

6.3 Flavor Decomposition

Using our results for g_1^n/F_1^n, we have extracted the polarized-to-unpolarized quark ratios $(\Delta u + \Delta\bar{u})/(u + \bar{u})$ and $(\Delta d + \Delta\bar{d})/(d + \bar{d})$. Our results are displayed in Figure 6.6(a), where the red (blue) points represent the $E = 4.74\,\text{GeV}$ (5.89 GeV) data. The error bars indicate the statistical and systematic errors added in quadrature. The gray band indicates the uncertainty from leaving out the strange quark contribution, which is also included in our error bars. The world data plotted includes DIS results from JLab E99-117 [71] and CLAS EG1b [73]. The HERMES data [66] are from a semi-inclusive DIS measurement. The models plotted are two types of pQCD calculations: Leader *et al.* [86] (cyan), which requires hadron helicity conservation, under the assumption of zero quark orbital angular momentum; the other is from Avakian *et al.* [88], which includes orbital angular momentum explicitly into their calculations (magneta). The statistical quark model from Bourrely *et al.* [89, 90] is also plotted (orange curve) along with a modified NJL model from Cloët *et al.* [114] (green). The points plotted at $x = 1$ are Dyson-Schwinger Equation treatments from Roberts *et al.* [126]. We have also computed a statistical error-weighted average over our results at $E = 4.74\,\text{GeV}$ and 5.89, given in Figure 6.6(b). For the up quark, our results hint towards a flattening of the trend of the ratio in the large-x region, pointing towards the DSE calculations of Roberts *et al.* [126]. Higher-precision g_1^p/F_1^p data are required to be able to discern between the various models; at the current precision, we do not have this capability. On the down quark, our results confirm the negative trend of the existing data, with no indication of a change in the trend towards positive values, as would be expected from the pQCD calculations. However, our results rule out the pQCD parameterization that requires hadron helicity conservation [86]. This again indicates the potential importance of orbital angular momentum in the spin structure of the nucleon.

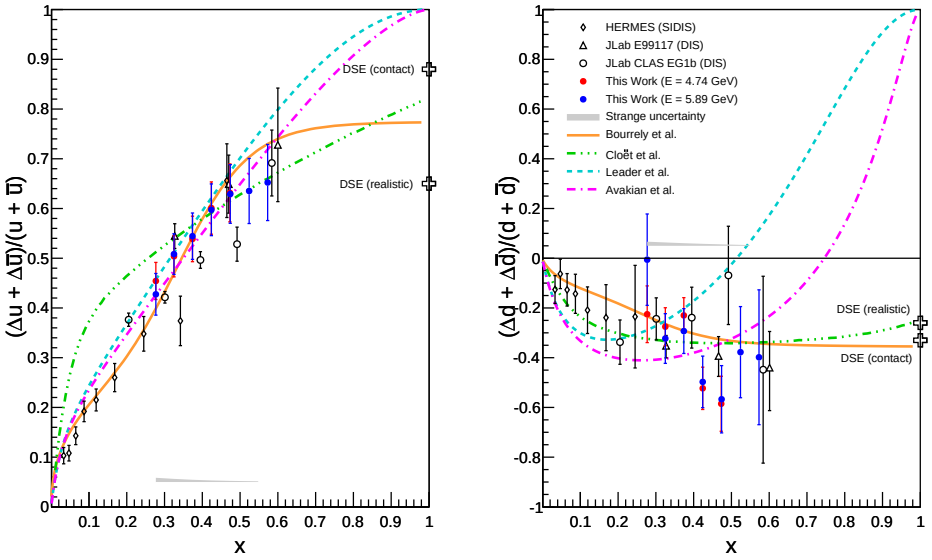

(a) Flavor decomposition results.

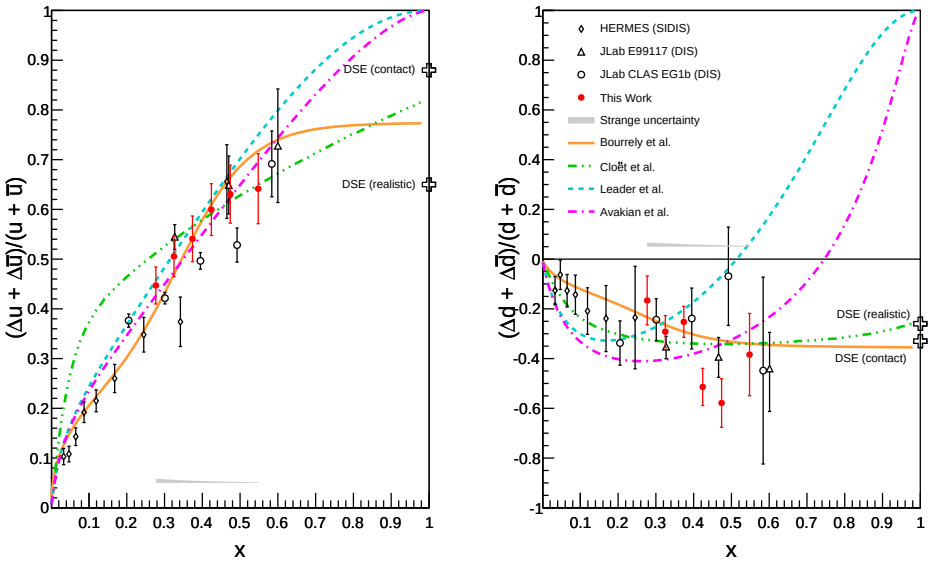

(b) Flavor decomposition results, averaged over $E = 4.74$ GeV and 5.89 GeV.

Figure 6.6: Flavor decomposition DIS results compared to world data and models. (a): Our data for $E = 4.74$ GeV (5.89 GeV) are given by the red (blue) data points; the error bars indicate the statistical errors, while the bands give the systematic errors. The world data plotted are from inclusive DIS experiments JLab E99-117 [71], JLab CLAS EG1b [73] and a semi-inclusive DIS experiment at HERMES [66]. The models plotted correspond to a statistical quark model [89, 90] (orange), a pQCD calculation requiring HHC [86] (cyan), and a pQCD calculation that allows quark orbital angular momentum to be non-zero [88] (magenta). A modified NJL model [114] (green) is also plotted. The predictions at $x = 1$ are from DSE treatments [126]. (b): Same plot as the top panel, but now our data are averaged over the two beam energies of $E = 4.74$ GeV and 5.89 GeV.

6.4 a_2^n

The extracted a_2^n is presented as the red points in Figure 6.7; the inner error bar for our data is statistical only, while the outer error bar shows the in quadrature sum of the statistical and systematic errors. The top panel shows the result *without* the elastic contribution and is compared to data from SLAC E143 [51] and a Lattice QCD calculation from Göckeler *et al.* [135]. It is important to note here that the Lattice calculation has the elastic *included* already and that the error bar includes a 15% systematic error estimate from extrapolating their calculation to the chiral limit [135]. The bottom panel of the plot shows the a_2 data including the elastic contribution, which is given as the dashed curve and is computed by using the Riordan [245] and Kelly [246] parameterizations for G_E^n and G_M^n, respectively. We see that our results have excellent errors relative to what is currently available from the world data and model calculations, albeit their $Q^2 = 5\,\mathrm{GeV}^2$ for both SLAC E143 and the Lattice calculation.

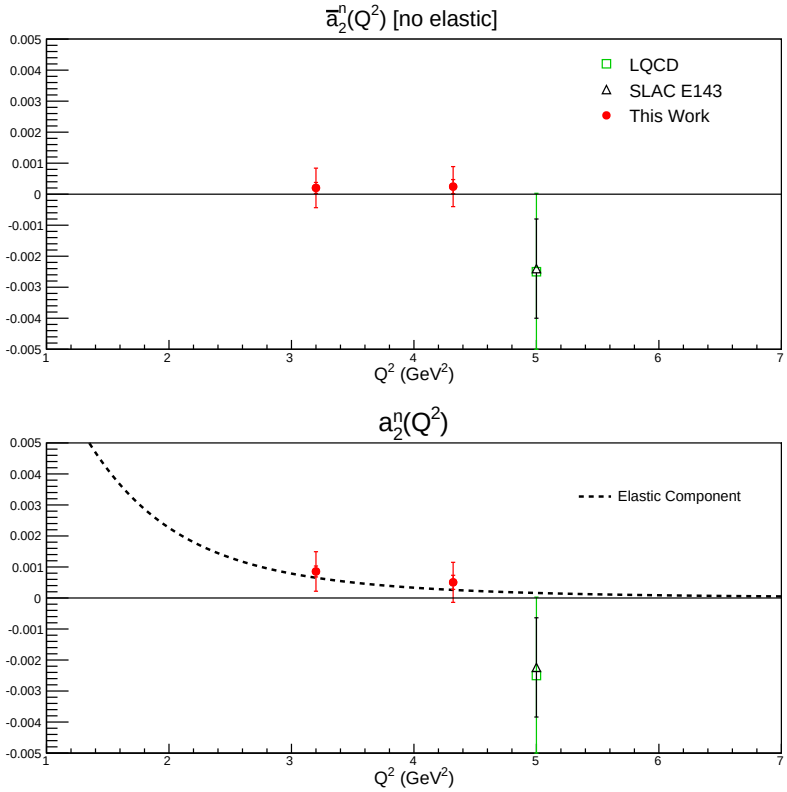

Figure 6.7: Our extracted a_2^n measurement compared to SLAC E143 [51] and a Lattice QCD calculation [135], both of which are at $Q^2 = 5\,\mathrm{GeV}^2$. The top panel shows the data *without* the elastic contribution, while the bottom panel shows the data *with* the elastic contribution. The Lattice calculation includes the elastic contribution in both panels. The elastic contribution is computed by using the Riordan [245] and Kelly [246] parameterizations for G_E^n and G_M^n, respectively.

CHAPTER 7

CONCLUSION

We have presented the analysis of the E06-014 experiment, where we have extracted the unpolarized cross section σ_0, that was used in the analysis to obtain a_2^n. Also, we have presented the work necessary to extract double-spin asymmetries $A_\parallel$ and $A_\perp$ leading to the calculation of the virtual photon-nucleon asymmetry $A_1^{^3\mathrm{He}}$. From there, we obtained A_1^n by applying nuclear corrections. We have also evaluated the structure function ratio g_1/F_1 on both ^{3}He and the neutron. Using our g_1^n/F_1^n data, we obtained the polarized-to-unpolarized quark ratios $(\Delta u + \Delta\bar{u})/(u+\bar{u})$ and $(\Delta d + \Delta\bar{d})/(d+\bar{d})$. Utilizing our measured $g_1^{^3\mathrm{He}}$ data, we extracted the twist-2 matrix element $a_2^{^3\mathrm{He}}$; applying nuclear corrections, we obtained a_2^n.

Our results for $A_1^{^3\mathrm{He}}$ are in good agreement with the existing world data, providing a more complete kinematic coverage relative to the other experiments which yielded either DIS or resonance measurements. Our results are consistent with the trend displayed by the statistical quark model [89]. Similar results follow for $g_1^{^3\mathrm{He}}/F_1^{^3\mathrm{He}}$.

The measurements of A_1^n in the DIS region are in good agreement with current data, and explicitly rules out the pQCD calculation requiring hadron helicity conservation by Leader *et al.* [86] towards $x \sim 0.57$. The relativistic constituent quark model [81], statistical quark model [89, 90] and the pQCD calculation with orbital angular momentum included [88] remain as good descriptions of the physics given the precision of the current data including our results. Our resonance extraction under the assumption of duality [72, 93, 94], combined with our analysis on the JLab E01-012 [72] data, reveals interesting behavior of A_1^n at larger x ($x > 0.6$), where the data suggests that the asymmetry starts to become constant, and perhaps in line with the DSE predictions at $x = 1$ of 0.34 (0.17) in a contact (realistic) framework from Roberts *et al.* [126]. These resonance results will provide a benchmark for the upcoming experiments at JLab in the 12 GeV era [91, 92].

Our results on g_1^n/F_1^n show improved precision relative to the existing SLAC data [51, 229], and are in agreement with the JLab E99-117 [71] data. Our data are also consistent

with the trend indicated by the statistical quark model [89] and the pQCD calculation with orbital angular momentum included [88].

The extracted polarized-to-unpolarized quark ratio for the down quark reveals a negative trend of the ratio, confirming what has been seen previously in inclusive DIS measurements at JLab [71, 73] and semi-inclusive DIS measurements at HERMES [66]. The lack of evidence of the down quark ratio turning positive towards larger $x \sim 0.6$ indicates that the pQCD with HHC calculation [86] does not describe the physics adequately, and that orbital angular momentum may be playing a more prominent role; however, the slope of our data does not necessarily agree with the trend of the Avakian *et al.* calculation [88], and it appears that the statistical quark model [89, 90] agrees best with our data set. The results on the up quark are driven by our fit to existing world g_1^p/F_1^p data, and hence at the current precision, we cannot discern between the various models; though it does appear that the ratio tends to flatten out towards the highest x bins we have data for, and appears to trend towards the DSE calculations of Roberts *et al.* [126].

The twist-2 matrix element a_2^n shows increased precision relative to the available data from SLAC E143 [51] and the Lattice QCD calculation from Göckeler *et al.* [135].

Our measurements of A_1^n in the DIS regime confirm the trend seen in previous measurements, and also points to the importance of orbital angular momentum in spin structure of the nucleon. The resonance results give a point of reference to check against in the next-generation experiments planned at JLab. The ratio $(\Delta d + \Delta\bar{d})/(d + \bar{d})$ provides further evidence that the quark orbital angular momentum plays an important role in nucleon spin structure.

REFERENCES

[1] R. W. Mcallister and R. Hofstadter, Phys. Rev. **102**, 851 (1956).

[2] M. Gell-Mann, Phys. Lett. **8**, 214 (1964).

[3] G. Zweig, Tech. Rep., CERN (1964), 8182/TH 401.

[4] E. D. Bloom, D. Coward, H. DeStaebler, J. Drees, G. Miller, et al., Phys. Rev. Lett. **23**, 930 (1969).

[5] M. Breidenbach, J. I. Friedman, H. W. Kendall, E. D. Bloom, D. Coward, et al., Phys. Rev. Lett. **23**, 935 (1969).

[6] J. D. Bjorken, Phys. Rev. **179**, 1547 (1969).

[7] K. G. Wilson, Phys. Rev. D **10**, 2445 (1974).

[8] G. S. Bali, Phys. Rep. **343**, 1 (2001).

[9] A. Pich (1995), `hep-ph/9505231`.

[10] Y. Nambu and A. Shalit, *Precludes in Theoretical Physics* (North Holland, Amsterdam, 1966).

[11] Y. Nambu and M. Han, Phys. Rev. D **10**, 674 (1974).

[12] S. Bethke, Eur. Phys. J. C **64**, 689 (2009).

[13] J. R. Ellis and R. L. Jaffe, Phys. Rev. D **9**, 1444 (1974).

[14] M. Alguard, W. Ash, G. Baum, J. Clendenin, P. Cooper, et al., Phys. Rev. Lett. **37**, 1261 (1976).

[15] M. Alguard, W. Ash, G. Baum, M. Bergstrom, J. Clendenin, et al., Phys. Rev. Lett. **41**, 70 (1978).

[16] G. Baum, M. Bergstrom, J. Clendenin, R. Ehrlich, V. Hughes, et al., Phys. Rev. Lett. **45**, 2000 (1980).

[17] G. Baum, M. Bergstrom, P. Bolton, J. Clendenin, N. de Botton, et al., Phys. Rev. Lett. **51**, 1135 (1983).

[18] J. Ashman et al. (European Muon Collaboration), Phys. Lett. B **206**, 364 (1988).

[19] J. Ashman et al. (European Muon Collaboration), Nucl. Phys. B **328**, 1 (1989).

[20] R. Jaffe and A. Manohar, Nucl. Phys. B **337**, 509 (1990).

[21] X.-D. Ji, Phys. Rev. Lett. **78**, 610 (1997).

[22] S. Kuhn, J.-P. Chen, and E. Leader, Prog. Part. Nucl. Phys. **63**, 1 (2009).

[23] M. Burkardt, Int. J. Mod. Phys. Conf. Ser. **25**, 1460029 (2014).

[24] C. A. Aidala, S. D. Bass, D. Hasch, and G. K. Mallot, Rev. Mod. Phys. **85**, 655 (2013).

[25] D. de Florian, R. Sassot, M. Stratmann, and W. Vogelsang (2014).

[26] G. M. Shore and B. E. White, Nucl. Phys. B **581**, 409 (2000).

[27] B. L. G. Bakker, E. Leader, and T. L. Trueman, Phys. Rev. D **70**, 114001 (2004).

[28] S. D. Bass, Rev. Mod. Phys. **77**, 1257 (2005).

[29] X.-S. Chen, X.-F. Lu, W.-M. Sun, F. Wang, and T. Goldman, Phys. Rev. Lett. **100**, 232002 (2008).

[30] M. Wakamatsu, Phys. Rev. D **81**, 114010 (2010).

[31] E. Leader, Phys. Rev. D **83**, 096012 (2011).

[32] X. Ji, X. Xiong, and F. Yuan, Phys. Rev. D **88**, 014041 (2013).

[33] C. Lorce, Phys. Rev. D **87**, 034031 (2013).

[34] Y. Hatta, Phys. Lett. B **708**, 186 (2012).

[35] K. Nakamura et al. (Particle Data Group), J. Phys. G **37**, 075021 (2010).

[36] S. Drell and T.-M. Yan, Phys. Rev. Lett. **25**, 316 (1970).

[37] G. Bunce, N. Saito, J. Soffer, et al., Annu. Rev. Nucl. Part. Sci. **50**, 525 (2000).

[38] C. Aidala, M. Bai, L. Bland, et al., *Research Plan for Spin Physics at RHIC. Report for DOE* (2005), `http://spin.riken.bnl.gov/rsc/report/masterspin.pdf`.

[39] F. Halzen and A. D. Martin, *Quarks and Leptons* (John Wiley and Sons, Inc., 1984).

[40] X. Zheng, Ph.D. thesis, Massachusetts Institute of Technology (2002).

[41] A. deShalit and H. Feshbach, *Theoretical Nuclear Physics Volume I: Nuclear Structure* (Wiley Classics Library Edition, 1990).

[42] B. Povh, K. Rith, C. Scholz, et al., *Particles and Nuclei* (Springer, 2004), 4th ed.

[43] M. Anselmino, A. Efremov, and E. Leader, Phys. Rep. **261**, 1 (1995).

[44] J. Bjorken and E. A. Paschos, Phys. Rev. **185**, 1975 (1969).

[45] J. Callan, Curtis G. and D. J. Gross, Phys. Rev. Lett. **22**, 156 (1969).

[46] A. V. Manohar (1992), `hep-ph/9204208`.

[47] D. Parno, Ph.D. thesis, Carnegie Mellon University (2011).

[48] K. G. Wilson, Phys. Rev. **179**, 1499 (1969).

[49] S. Wandzura and F. Wilczek, Phys. Lett. B **72**, 195 (1977).

[50] L. N. Hand, Phys. Rev. **129**, 1834 (1963).

[51] K. Abe et al. (E143 collaboration), Phys. Rev. D **58**, 112003 (1998).

[52] D. Drechsel, S. S. Kamalov, and L. Tiator, Phys. Rev. D **63**, 114010 (2001).

[53] J. Soffer and O. V. Teryaev, Phys. Lett. B **490**, 106 (2000).

[54] G. Altarelli and G. Parisi, Nucl. Phys. B **126**, 298 (1977).

[55] Y. L. Dokshitzer, Sov. Phys. JETP **46**, 641 (1977).

[56] V. N. Gribov and L. N. Lipatov, Sov. J. Nucl. Phys. **15**, 438 (1972).

[57] P. L. Anthony et al., Phys. Lett. B **493**, 19 (2000).

[58] W. Melnitchouk, R. Ent, and C. Keppel, Phys. Rep. **406**, 127 (2005).

[59] W. Melnitchouk, R. Ent, and C. E. Keppel, Phys. Rep. **406**, 127 (2005).

[60] P. Anthony et al. (E142 Collaboration), Phys. Rev. D **54**, 6620 (1996).

[61] K. Abe et al. (E154 Collaboration), Phys. Rev. Lett. **79**, 26 (1997).

[62] P. Anthony et al. (E155 Collaboration), Phys. Lett. B **463**, 339 (1999).

[63] P. Anthony et al. (E155 Collaboration), Phys. Lett. B **493**, 19 (2000).

[64] K. Ackerstaff et al. (HERMES Collaboration), Phys. Lett. B **404**, 383 (1997).

[65] A. Airapetian et al. (HERMES Collaboration), Phys. Lett. B **442**, 484 (1998).

[66] K. Ackerstaff et al. (HERMES Collaboration), Phys. Lett. B **464**, 123 (1999).

[67] A. Airapetian et al. (HERMES Collaboration), Phys. Rev. D **75**, 012007 (2007).

[68] B. Adeva et al. (Spin Muon Collaboration), Phys. Rev. D **58**, 112001 (1998).

[69] M. Alekseev et al. (COMPASS Collaboration), Phys. Lett. B **690**, 466 (2010).

[70] E. Ageev et al. (COMPASS Collaboration), Phys. Lett. B **647**, 330 (2007).

[71] X. Zheng et al. (Jefferson Lab Hall A Collaboration), Phys. Rev. C **70**, 065207 (2004).

[72] P. Solvignon et al. (Jefferson Lab E01-012 Collaboration), Phys. Rev. Lett. **101**, 182502 (2008).

[73] K. Dharmawardane et al. (CLAS Collaboration), Phys. Lett. B **641**, 11 (2006).

[74] L. Y. Glozman and D. Riska, Phys. Rep. **268**, 263 (1996).

[75] F. E. Close, Nucl. Phys. B **80**, 269 (1974).

[76] F. E. Close, Phys. Lett. B **43**, 422 (1973).

[77] J. Poucher, M. Breidenbach, W. Ditzler, J. I. Friedman, H. W. Kendall, et al., Phys. Rev. Lett. **32**, 118 (1974).

[78] E. Riordan, A. Bodek, M. Breidenbach, D. Dubin, J. Elias, et al., Phys. Rev. Lett. **33**, 561 (1974).

[79] A. Bodek, M. Breidenbach, D. Dubin, J. Elias, J. Friedman, et al., Phys. Rev. Lett. **30**, 1087 (1973).

[80] R. D. Carlitz, Phys. Lett. B **58**, 345 (1975).

[81] N. Isgur, Phys. Rev. D **59**, 034013 (1999).

[82] K. Abe et al. (E154 Collaboration), Phys. Lett. B **404**, 377 (1997).

[83] G. Farrar and D. R. Jackson, Phys. Rev. Lett. **35**, 1416 (1975).

[84] Phys. Lett. B **70**, 346 (1977).

[85] S. J. Brodsky, M. Burkardt, and I. Schmidt, Nucl. Phys. B **441**, 197 (1995).

[86] E. Leader, A. V. Siderov, and D. B. Stamenov, Int. J. Mod. Phys. A **13**, 5573 (1998).

[87] E. Leader, A. V. Sidorov, and D. B. Stamenov, Phys. Rev. D **75**, 074027 (2007).

[88] H. Avakian, S. J. Brodsky, A. Deur, and F. Yuan, Phys. Rev. Lett. **99**, 082001 (2007).

[89] C. Bourrely, J. Soffer, and F. Buccella, Eur. Phys. J. C **23**, 487 (2002).

[90] C. Bourrely and J. Soffer, in preparation.

[91] G. G. Franklin, S. Riordan, D. Seymour, et al., *Measurement of Neutron Spin Asymmetry A_1^n in the Valence Quark Region Using an 8.8 GeV and 6.6 GeV Beam Energies and BigBite Spectrometer in Hall A* (2006), Proposal for Jefferson Lab PAC 30, spokespersons: J. Annand, T. Averett, G. Cates, N. Liyanage, Z.-E. Meziani, G. Rosner, B. Wojtsekhowski, X. Zheng.

[92] S. Zhou, X. Li, H. Gao, et al., *Measurement of Neutron Spin Asymmetry A_1^n in the Valence Quark Region Using an 11 GeV Beam and a Polarized ^{3}He Target in Hall C* (2010), Proposal for Jefferson Lab PAC 36, spokespersons: G. Cates, J.-P Chen, Z.-E Meziani and X. Zheng.

[93] E. D. Bloom and F. J. Gilman, Phys. Rev. Lett. **25**, 1140 (1970).

[94] E. D. Bloom and F. J. Gilman, Phys. Rev. D **4**, 2901 (1971).

[95] I. Niculescu, C. Armstrong, J. Arrington, K. Assamagan, O. Baker, et al., Phys. Rev. Lett. **85**, 1182 (2000).

[96] A. Airapetian et al. (HERMES Collaboration), Phys. Rev. Lett. **90**, 092002 (2003).

[97] P. Bosted et al. (CLAS Collaboration), Phys. Rev. C **75**, 035203 (2007).

[98] W. Melnitchouk, Phys. Rev. Lett. **86**, 35 (2001), see erratum in Phys. Rev. Lett. **93**, 199901 (2001).

[99] A. De Rujula, H. Georgi, and H. D. Politzer, Annals Phys. **103**, 315 (1977).

[100] D. Diakonov (1995), `hep-ph/9602375`.

[101] E. Witten, Nucl. Phys. B **160**, 57 (1979).

[102] R. F. Dashen and A. V. Manohar, Phys. Lett. B **315**, 425 (1993).

[103] R. F. Dashen and A. V. Manohar, Phys. Lett. B **315**, 438 (1993).

[104] E. Guadagnini, Nucl. Phys. B **236**, 35 (1984).

[105] H. Weigel, L. Gamberg, and H. Reinhardt, Phys. Lett. B **399**, 287 (1997).

[106] H. Weigel, L. Gamberg, and H. Reinhardt, Phys. Rev. D **55**, 6910 (1997).

[107] R. Alkofer, H. Reinhardt, and H. Weigel, Phys. Rep. **265**, 139 (1996).

[108] O. Schroeder, H. Reinhardt, and H. Weigel, Nucl. Phys. A **651**, 174 (1999).

[109] Y. Nambu and G. Jona-Lasinio, Phys. Rev. **122**, 345 (1961).

[110] Y. Nambu and G. Jona-Lasinio, Phys. Rev. **124**, 246 (1961).

[111] D. Diakonov and V. Y. Petrov (2000).

[112] M. Wakamatsu, Phys. Rev. D **67**, 034006 (2003).

[113] M. Wakamatsu, Phys. Rev. D **67**, 034005 (2003).

[114] I. Cloët, W. Bentz, and A. W. Thomas, Phys. Lett. B **621**, 246 (2005).

[115] N. Kochelev, Phys. Rev. D **57**, 5539 (1998).

[116] A. Chodos, R. Jaffe, K. Johnson, C. B. Thorn, and V. Weisskopf, Phys. Rev. D **9**, 3471 (1974).

[117] A. W. Schreiber, A. Signal, and A. W. Thomas, Phys. Rev. D **44**, 2653 (1991).

[118] X. Song and J. McCarthy, Phys. Rev. D **49**, 3169 (1994).

[119] S. Theberge, A. W. Thomas, and G. A. Miller, Phys. Rev. D **22**, 2838 (1980).

[120] A. W. Thomas, Adv. Nucl. Phys. **13**, 1 (1984).

[121] A. W. Schreiber, P. J. Mulders, A. Signal, and A. W. Thomas, Phys. Rev. D **45**, 3069 (1992).

[122] A. Thomas, Prog. Part. Nucl. Phys. **61**, 219 (2008).

[123] C. Boros and A. W. Thomas, Phys. Rev. D **60**, 074017 (1999).

[124] F. E. Close and A. W. Thomas, Phys. Lett. B **212**, 227 (1988).

[125] F. M. Steffens, H. Holtmann, and A. W. Thomas, Phys. Lett. B **358**, 139 (1995).

[126] C. D. Roberts, R. J. Holt, and S. M. Schmidt, Phys. Lett. B **727**, 249 (2013).

[127] J. Owens, A. Accardi, and W. Melnitchouk, Phys. Rev. D **87**, 094012 (2013).

[128] H. Abramowicz, T. Hansl-Kozanecka, J. May, P. Palazzi, A. Para, et al., Z. Phys. C **25**, 29 (1984).

[129] W. Melnitchouk and A. W. Thomas, Phys. Lett. B **377**, 11 (1996).

[130] R. Jaffe, Comments Nucl. Part. Phys. **19**, 239 (1990).

[131] B. W. Filippone and X.-D. Ji, Adv. Nucl. Phys. **26**, 1 (2001).

[132] M. Burkardt, *The g_2 Spin Structure Function* (2009), arXiv:0905.4079v1 [hep-ph].

[133] M. Burkardt, Phys. Rev. D **88**, 114502 (2013).

[134] S. Choi et al., *Measurement of the neutron d_2: Towards the electric χ_e and magnetic χ_b color polarizabilities*, proposal for Jefferson Lab PAC 29 (2005).

[135] M. Göckeler, R. Horsley, D. Pleiter, P. E. Rakow, A. Schafer, et al., Phys. Rev. D **72**, 054507 (2005).

[136] P. Solvignon (2011), private communication.

[137] E. V. Shuryak and A. Vainshtein, Nucl. Phys. B **201**, 141 (1982).

[138] X.-D. Ji and C.-h. Chou, Phys. Rev. D **42**, 3637 (1990).

[139] M. Amarian, L. Auerbach, T. Averett, J. Berthot, P. Bertin, et al., Phys. Rev. Lett. **89**, 242301 (2002).

[140] K. Slifer et al. (Resonance Spin Structure Collaboration), Phys. Rev. Lett. **105**, 101601 (2010).

[141] D. Drechsel, S. Kamalov, and L. Tiator, Eur. Phys. J. A **34**, 69 (2007).

[142] P. Anthony et al. (E155 Collaboration), Phys. Lett. B **553**, 18 (2003).

[143] J. Friar et al., Phys. Rev. C **42**, 6 (1990).

[144] F. Bissey, A. Thomas, and I. Afnan, Phys. Rev. C **64**, 024004 (2001).

[145] R. L. Sutherland, *Handbook of Non-Linear Optics* (CRC Press, 2003), 2nd ed.

[146] J. Hansknect and M. Poelker, Phys. Rev. Spec. Top. Accel. Beams **9**, 063501 (2006).

[147] C. Leemann, D. Douglas, and G. Krafft, Ann. Rev. Nucl. Part. Sci. **51**, 413 (2001).

[148] M. Friend, D. Parno, F. Benmokhtar, A. Camsonne, M. Dalton, et al., Nucl. Instrum. Meth. A **676**, 96 (2012).

[149] C. Sinclair, P. Adderley, B. Dunham, J. Hansknecht, P. Hartmann, et al., Phys. Rev. ST Accel. Beams **10**, 023501 (2007).

[150] J. M. Grames, C. K. Sinclair, J. Mitchell, et al., Phys. Rev. Spec. Top. Accel. Beams **7**, 042802 (2004).

[151] K. Allada, Ph.D. thesis, University of Kentucky (2010).

[152] J. Alcorn et al., Nucl. Instrum. Meth. A **522**, 294 (2004).

[153] I. L. Gennari, ed., *Precision intercomparison of beam current monitors at CEBAF* , vol. 4 (IEE Operations Center, 1995).

[154] C. K. Sinclair, Tech. Rep., Jefferson Lab (1998), JLAB-ACC 98-04.

[155] F. Lipps and H. A. Tolheck, Physica **20**, 85 (1954).

[156] F. Lipps and H. A. Tolheck, Physica **20**, 395 (1954).

[157] M. Tiefenback and D. Douglas, Tech. Rep., Jefferson Lab (1992), jLab-TN92-061.

[158] D. Marchand, Ph.D. thesis, Université Blaise Pascal (1998).

[159] J. Huang, Ph.D. thesis, Massachusetts Institute of Technology (2012).

[160] W. Happer, Rev. Mod. Phys. **44**, 169 (1972).

[161] A. S. Kolarkar, Ph.D. thesis, University of Kentucky (2008).

[162] E. Babcock, I. Nelson, S. Kadlecek, B. Driehuys, L. W. Anderson, F. W. Hersman, and T. G. Walker, Phys. Rev. Lett. **91**, 123003 (2003).

[163] T. G. Walker and W. Happer, Rev. Mod. Phys. **69**, 629 (1997).

[164] N. R. Newbury, A. S. Barton, P. Bogorad, et al., Phys. Rev. A **48**, 558 (1993).

[165] T. G. Walker, J. H. Thywissen, and W. Happer, Phys. Rev. A **56**, 2090 (1997).

[166] A. B. Baranga, S. Appelt, M. .V.Romalis, et al., Phys. Rev. Lett. **80**, 2801 (1998).

[167] T. E. Chupp, R. A. Loveman, A. K. Thompson, et al., Phys. Rev. C **45**, 915 (1992).

[168] C. Dutta, Ph.D. thesis, University of Kentucky (2010).

[169] M. Posik, Ph.D. thesis, Temple University (2013).

[170] W. Lorenzon, T. Gentile, and R. McKeown, Phys. Rev. A. **47**, 468 (1993).

[171] Y. Zheng (2012), private communication.

[172] *GIMP: The GNU Image Manipulation Program*, `http://www.gimp.org`.

[173] I. Kominis, Ph.D. thesis, Princeton University (2001).

[174] Y. Qiang, Ph.D. thesis, Massachusettes Institute of Technology (2007).

[175] K. Fissum et al., Tech. Rep., Jefferson Laboratory (2000), jLab-TN-00-016.

[176] W. Leo, *Techniques for Nuclear and Particle Physics Experiments: A How To Approach* (Springer-Verlag, 1994), 2nd ed.

[177] C. Grupen and B. Shwartz, *Particle Detectors* (Cambridge University Press, 2008), 2nd ed.

[178] P. H. Solvignon, Ph.D. thesis, Temple University (2006).

[179] H. Bach and N. Neuroth, *The Properties of Optical Glass* (Springer, 1995), 2nd ed.

[180] D. Green, *The Physics of Particle Detectors* (Cambridge University Press, 2000).

[181] X. Qian, Ph.D. thesis, Duke University (2010).

[182] R. Winston, J. Opt. Soc. Am. **60**, 245 (1970).

[183] B. Sawatzky, Tech. Rep., Temple University (2007), http://www.jlab.org/~brads/d2n/cerenkov/review_cerenkov_d2.pdf.

[184] R. Michaels, *Hall A HRS Trigger* (2003), http://hallaweb.jlab.org/equipment/daq/strig.pdf.

[185] B. Sawatzky, *Private communication*.

[186] K. Allada, *Private communication*.

[187] S. Lewis, Tech. Rep., Lawrence Berkeley National Laboratory (????).

[188] R. Michaels, R. Feuerbach, and B. Reitz, *Trigger Programming for Hall A Spectrometers* (2004), Notes on Trigger Programming for E94-107, http://hallaweb.jlab.org/equipment/daq/trigger_coinc.html.

[189] *ROOT: C++ Data Analysis Framework*, http://root.cern.ch/drupal/.

[190] *ROOT/C++ Analyzer for Hall A*, http://hallaweb.jlab.org/podd/.

[191] X. Qian et al., Phys. Rev. Lett. **107**, 072003 (2011).

[192] J. Huang, *Private communication* (2011).

[193] N. Liyanage, Tech. Rep., Jefferson Lab (2002), JLAB-TN-02-012.

[194] C. Curtis et al., jefferson Lab Alignment Group Data Transmittal, **A1189**, **A1197**, **A1198**, **A1208**.

[195] A. Orsborn, *Assessment of the Hall A Vertical Drift Chamber Analysis Software Performance Through Monte Carlo Simulation* (2005), SULI Program Report.

[196] D. Flay, *LHRS Analysis Update for d_2^n* (2012), E06-014 progress report. https://hallaweb.jlab.org/wiki/images/4/4d/DF_LHRS_update_5_23_12.pdf.

[197] K. Slifer, Ph.D. thesis, Temple University (2004).

[198] D. Flay, *LHRS Analysis for d_2^n: Kinematics, BCM Zeroes and Scintillator Checks* (2011), E06-014 progress report. https://hallaweb.jlab.org/wiki/images/b/b1/DF_LHRS_1_28_11.pdf.

[199] J. LeRose, *Snake transfer functions*, https://hallaweb.jlab.org/news/minutes/tranferfuncs.html.

[200] P. Bosted and V. Mamyan, *Empirical Fit to electron-nucleus scattering* (2012), arXiv:1203.2262v2 [nucl-th].

[201] L. Mo and Y. Tsai, Rev. Mod. Phys. **41**, 205 (1969).

[202] Amroun et al., Nucl. Phys. A **579**, 596 (1994).

[203] J. W. Lightbody and J. S. O'Connell, Comp. in Phys. p. 57 (1988).

[204] S. Stein et al., Phys. Rev. D **12**, 1884 (1975).

[205] R. Whitney, *radcor.f*, fortran analysis code.

[206] Y.-S. Tsai (1971), SLAC-PUB-0848.

[207] D. Parno, *Private communication* (2012).

[208] Y. Zhang, *Private communication* (2012).

[209] D. Flay, *LHRS Analysis for d_2^n: Systematic Error Studies for Target Variables* (2011), E06-014 Progress Report, `https://hallaweb.jlab.org/wiki/images/7/7b/DF_LHRS_8_17_11.pdf`.

[210] J. Mccarthy, I. Sick, and R. Whitney, Phys. Rev. C **15**, 1396 (1977).

[211] S. Galster, H. Klein, J. Moritz, K. Schmidt, D. Wegener, et al., Nucl.Phys. **B32**, 221 (1971).

[212] G. Franklin, private communication.

[213] R. Michaels and B. Moffit, *Parity daq for charge asymmetry feedback*, `http://hallaweb.jlab.org/experiment/HAPPEX/HAPPEXII/paritydaq/partiy_daq.html`.

[214] S. Riordan, Ph.D. thesis, Carnegie Mellon University (2008).

[215] G. W. Miller, Ph.D. thesis, Princeton University (2001).

[216] Y. Qiang, private communication.

[217] P. Bosted, Tech. Rep. (2004), CLASNOTE 2004-005.

[218] S. Agostinelli et al., Nucl. Instrum. Meth. **A505**, 250 (2003).

[219] D. E. Wiser, Ph.D. thesis, University of Wisconsin (1977).

[220] D. de Florian, R. Sassot, M. Stratmann, and W. Vogelsang, Phys. Rev. Lett. **101**, 072001 (2008).

[221] P. E. Bosted, Phys. Rev. C **51**, 409 (1995).

[222] J. E. Amaro, M. Barbaro, J. Caballero, T. Donnelly, A. Molinari, et al., Phys. Rev. C **71**, 015501 (2005).

[223] I. Akushevich, A. Ilyichev, N. Shumeiko, A. Soroko, and A. Tolkachev, Comput. Phys. Commun. **104**, 201 (1997).

[224] K. Abe et al. (E143 Collaboration), Phys. Lett. B **452**, 194 (1999).

[225] F. R. P. Bissey, V. A. Guzey, M. Strikman, and A. W. Thomas, Phys. Rev. C **65**, 064317 (2002).

[226] J. L. Friar, B. Gibson, G. Payne, A. Bernstein, and T. Chupp, Phys. Rev. C **42**, 2310 (1990).

[227] P. Amaudruz, Nucl. Phys. B **144**, 3 (1995).

[228] Arneodo et al., Nucl. Phys. B **144**, 12 (1995).

[229] P. Anthony et al. (E155 Collaboration), Phys. Lett. B **458**, 529 (1999).

[230] J. J. Ethier and W. Melnitchouk, Phys. Rev. C **88**, 054001 (2013).

[231] J. Pumplin, D. R. Stump, J. Huston, et al., J. High Energy Phys. **07**, 012 (2002).

[232] C. Bourrely, J. Soffer, and F. Buccella, Phys. Lett. B **648**, 39 (2007).

[233] M. Arneodo et al. (New Muon Collaboration.), Phys. Lett. B **364**, 107 (1995).

[234] T. Gehrmann and W. J. Stirling, Phys. Rev. D **53**, 6100 (1996).

[235] D. de Florian, G. Navarro, and R. Sassot, Phys. Rev. D **71**, 094018 (2005).

[236] K. Kramer, D. Armstrong, T. Averett, W. Bertozzi, S. Binet, et al., Phys. Rev. Lett. **95**, 142002 (2005).

[237] O. Nachtmann, Nucl. Phys. B **63**, 237 (1973).

[238] S. Wandzura, Nucl. Phys. B **122**, 412 (1977).

[239] H. Georgi and H. D. Politzer, Phys. Rev. D **14**, 1829 (1976).

[240] S. Matsuda and T. Uematsu, Nucl. Phys. B **168**, 181 (1980).

[241] A. V. Sidorov and D. B. Stamenov, Mod. Phys. Lett. A **21**, 1991 (2006).

[242] A. Accardi and W. Melnitchouk, Phys. Lett. B **670**, 114 (2008).

[243] A. Piccione and G. Ridolfi, Nucl. Phys. B **513**, 301 (1998).

[244] J. Blumlein and H. Bottcher, Nucl. Phys. B **636**, 225 (2002).

[245] S. Riordan, S. Abrahamyan, B. Craver, A. Kelleher, A. Kolarkar, et al., Phys. Rev. Lett. **105**, 262302 (2010).

[246] J. Kelly, Phys. Rev. C **70**, 068202 (2004).

[247] D. Parno, *Yellow Cover Material Study* (2011), `https://hallaweb.jlab.org/wiki/index.php/Energy_Loss_%28d2n%29`.

APPENDIX A

ELECTRON EFFICIENCIES

Presented in Table A.1 are the electron cut efficiencies binned by the LHRS momentum setting and beam energy for the gas Čerenkov, pion rejector, one-track and β cuts. Additionally, the trigger efficiencies are given.

p (GeV)	E (GeV)	ε_{cer} (%)	ε_{pr} (%)	ε_{1} (%)	ε_{β} (%)	$\varepsilon_{\text{trig}}$ (%)
0.60	4.74	96.33 ± 1.37	98.70 ± 0.79	99.28 ± 0.59	99.96 ± 0.46	99.96
0.60	5.89	95.57 ± 1.42	98.49 ± 0.56	99.34 ± 0.43	99.96 ± 0.32	99.96
0.70	5.89	96.20 ± 0.84	99.24 ± 0.61	99.28 ± 0.56	99.96 ± 0.47	99.95
0.80	4.74	97.14 ± 3.07	99.57 ± 1.09	99.21 ± 0.84	99.94 ± 0.71	99.94
0.90	5.89	96.32 ± 1.55	99.52 ± 1.07	99.29 ± 0.79	99.95 ± 0.68	99.95
1.12	4.74	97.08 ± 1.52	99.54 ± 1.11	99.16 ± 0.82	99.95 ± 0.86	99.95
1.13	5.89	96.08 ± 2.01	99.48 ± 1.37	99.23 ± 1.04	99.92 ± 0.83	99.93
1.19	4.74	97.67 ± 1.50	99.74 ± 1.06	99.04 ± 0.79	99.97 ± 0.82	99.94
1.20	5.89	97.48 ± 2.04	99.18 ± 1.77	99.21 ± 1.31	99.91 ± 1.27	99.97
1.26	4.74	97.92 ± 1.25	99.64 ± 1.16	99.08 ± 0.92	99.93 ± 0.90	99.98
1.27	5.89	97.93 ± 1.82	99.64 ± 1.39	99.17 ± 0.97	99.93 ± 0.89	99.94
1.34	4.74	97.53 ± 1.69	99.56 ± 1.53	99.02 ± 0.99	99.96 ± 1.05	99.96
1.34	5.89	97.54 ± 2.06	99.11 ± 1.99	98.98 ± 1.19	99.96 ± 1.27	99.96
1.42	4.74	97.53 ± 1.63	99.32 ± 1.91	99.19 ± 1.24	99.95 ± 0.99	99.95
1.42	5.89	97.75 ± 1.69	99.35 ± 1.60	98.81 ± 1.18	99.95 ± 1.03	99.94
1.51	4.74	98.36 ± 1.61	99.47 ± 1.71	99.10 ± 1.15	99.95 ± 1.04	99.95
1.51	5.89	98.07 ± 1.85	99.33 ± 1.85	99.17 ± 1.33	99.85 ± 1.14	99.94
1.60	4.74	98.16 ± 2.07	99.40 ± 2.06	98.95 ± 1.42	99.89 ± 1.29	99.96
1.60	5.89	97.59 ± 2.98	99.33 ± 2.20	98.83 ± 1.41	99.88 ± 1.31	99.95
1.70	5.89	98.12 ± 3.28	99.11 ± 3.21	98.62 ± 1.92	99.85 ± 1.75	99.94

Table A.1: The electron efficiencies at each kinematic setting of the LHRS for the gas Čerenkov, pion rejector, one-track, β cut efficiencies and trigger efficiencies. The large (statistical) error bars are seen on some of the kinematic settings as there were significantly reduced statistics at these momentum bins. There are no statistical errors indicated on the trigger efficiencies since their errors were negligible.

APPENDIX B

THE EFFECTIVE TARGET LENGTH

The effective target length seen by the spectrometer, ΔZ, is illustrated in Figure B.1. The spectrometer views the target, depicted by the dark black rectangle, at an angle θ; therefore, the *effective* length that the spectrometer sees is *longer* than what the actual length is. From the diagram, it can be seen that the effective length ΔZ is related to the y-coordinate (in the target coordinate system):

$$\cos\alpha = \sin\theta \tag{B.1}$$

$$\sin\theta = \frac{L}{2\Delta y} \tag{B.2}$$

$$\Rightarrow \Delta Z = 2\Delta y = \frac{L}{\sin\theta}. \tag{B.3}$$

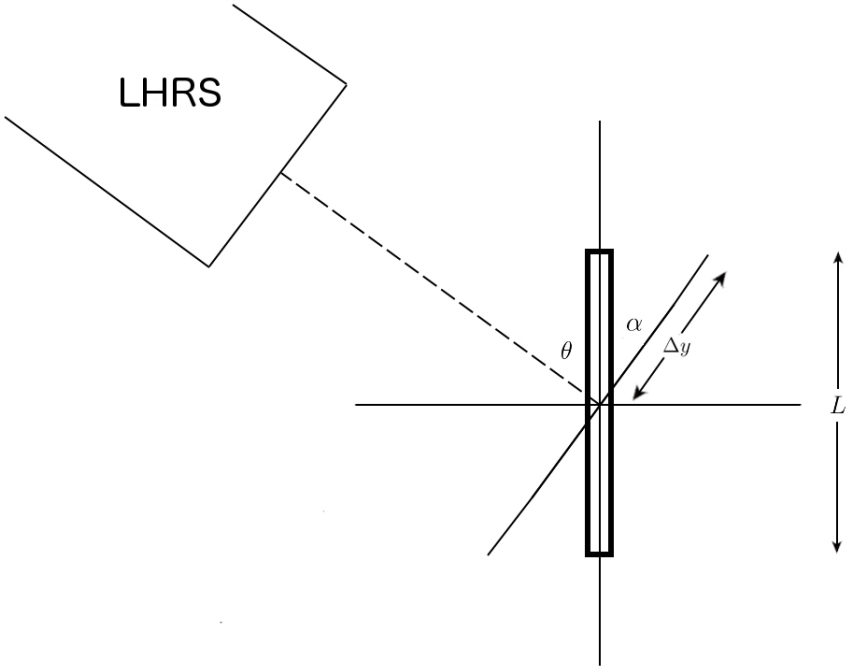

Figure B.1: A diagram illustrating how ΔZ is computed from the y-coordinate seen by the spectrometer. The electron beam enters from the bottom of the diagram.

APPENDIX C

RADIATIVE CORRECTIONS

This chapter contains extra details concerning the radiative correction analysis. In particular, the radiation lengths are presented in Section C.1 and the cross section model is discussed in detail in Section C.2. The models used in the radiative corrections for the asymmetries are presented in Section C.3.

C.1 Radiation Lengths

The material thicknesses in the path of the incoming electron for the LHRS and BigBite are listed in Table C.1. Electrons measured on the LHRS and BigBite share the same incident path along the beamline, and hence have the same radiation length before the interaction occurs at the target. The materials include the beryllium endcap of the beam pipe, followed by ^{4}He in the target enclosure up to the glass endcap of the target cell, followed by half of the ^{3}He target material.

For the scattered electron measured by the LHRS, the material thicknesses are given by Table C.2. The materials in the path of the scattered electron are ^{3}He, the target cell wall, ^{4}He, air and kapton. The thicknesses of ^{3}He and the target cell wall are calculated as the amount of material seen at an angle of 45° with respect to the beamline, see Figure C.1. The BigBite spectrometer path is not drawn here, as it is the same as the LHRS, placed symmetrically on the other side of the beamline, at 45° to the right.

The radiation lengths seen by the scattered electrons measured by the BigBite spectrometer are listed in Table C.3, which are similar to what is seen by the LHRS. The thickness of ^{3}He, glass and ^{4}He seen by the two spectrometers are the same because they are both positioned at 45° with respect to the beamline. The main difference with BigBite is that there is a larger region of air before entering the spectrometer and there is no kapton.

Radiation Lengths: Before Scattering				
Material	ρ (g/cm^3)	X_0 (g/cm^2)	L (cm)	T (#X_0)
Be	1.85	65.19	0.025	7.20E-04
^{4}He	1.66E-03	876.66	22.86	4.33E-05
Glass (GE-180)	2.77	19.42	0.012	1.73E-03
^{3}He	1.25E-03	54.28	19.05	4.39E-04
Total	–	–	–	**2.93E-03**

Table C.1: The radiation lengths of the materials in the path of the incoming electron.

LHRS Radiation Lengths: After Scattering				
Material	ρ (g/cm^3)	X_0 (g/cm^2)	L (cm)	T (#X_0)
^{3}He	1.25E-03	54.28	1.34	3.08E-05
Glass (GE-180)	2.77	19.42	0.24	3.35E-02
^{4}He	1.66E-03	876.66	79.05	1.49E-04
Air	1.20E-03	36.81	51.23	1.67E-03
Kapton	1.42	40.61	0.025	8.88E-04
Total	–	–	–	**3.62E-02**

Table C.2: The radiation lengths of the materials in the path of the scattered electron in the LHRS.

BigBite Radiation Lengths: After Scattering				
Material	ρ (g/cm^3)	X_0 (g/cm^2)	L (cm)	T (#X_0)
^{3}He	1.25E-03	54.28	1.34	3.08E-05
Glass (GE-180)	2.77	19.42	0.23	3.35E-02
^{4}He	1.66E-03	876.66	79.05	1.49E-04
Air	1.20E-03	36.81	101.95	3.32E-03
Total	–	–	–	**3.70E-02**

Table C.3: The radiation lengths of the materials in the path of the scattered electron for the BigBite spectrometer.

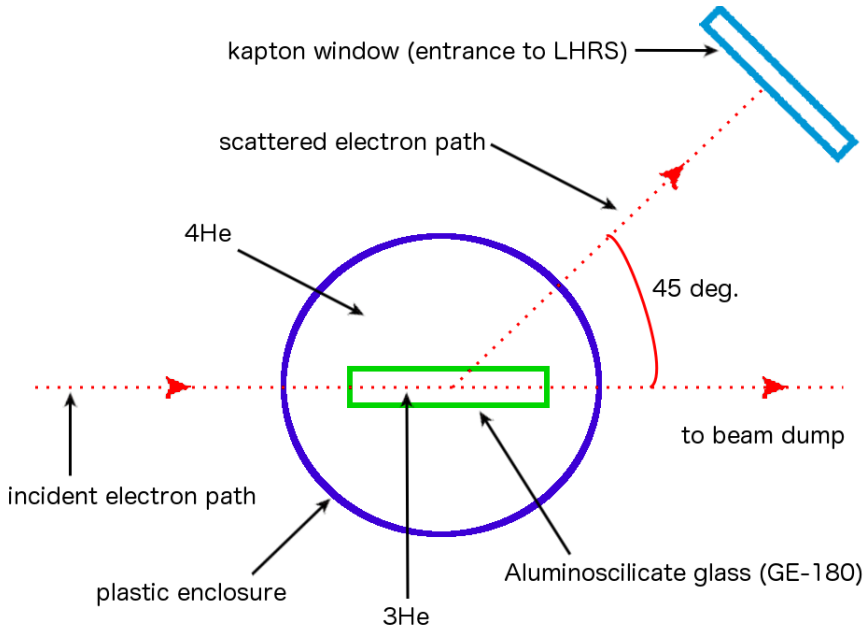

Figure C.1: A top-view of Hall A showing the electron's path before entering the LHRS. Unfortunately, the plastic target enclosure thickness was not known. Various material types of the enclosure's thickness were tested and found to be negligible relative to the other materials [247]. The electron path to the BigBite spectrometer is similar, but is not shown; it would be on the right side of the beamline, at an angle of 45°.

C.2 Cross Sections

C.2.1 F1F209 Model

In order to carry out the radiative corrections on the data of interest, one needs data *at the same scattering angle* to fill out the phase space that is indicated by the limits of the integrals in Equation 5.24. It turns out that we did not take enough data, as the experiment only covered two beam energies of 4.74 and 5.89 GeV. However, we can use a model to generate the needed input spectra to carry out our radiative corrections.

The model we used was F1F209, by P. Bosted and V. Mamyan [200]. It is a phenomenological model fit to various Born cross section data for various targets and is valid for $A > 2$. The kinematic coverage is $0 < W < 3.2\,\text{GeV}$ and $0.2 < Q^2 < 5\,\text{GeV}^2$. F1F209 is fortran code that calculates the unpolarized structure functions F_1 and F_2, each of which is a sum of a quasi-elastic and an inelastic term. These may be in turn used to calculate the Born cross section according to:

$$\frac{d^2\sigma}{d\Omega dE_p} = \frac{\alpha^2\cos^2(\theta/2)}{\left[2E_s\sin^2(\theta/2)\right]^2}\left[\frac{1}{\nu}F_2\left(W^2,Q^2\right) + 2\tan^2(\theta/2)\,\frac{1}{M}F_1\left(W^2,Q^2\right)\right], \qquad \text{(C.1)}$$

where $\alpha = 1/137$ is the fine structure constant; $\nu = E_s - E_p$ is the energy transferred to the target; M is the nucleon mass; W is the invariant mass of the virtual photon-nucleon system and Q^2 is the momentum transferred to the target squared.

C.2.2 Scaling and Testing the Model

To ensure the accuracy of the spectra predicted by the model in our particular range of W and Q^2, we tested the model against various world data. In particular, we tested it against data from JLab experiments E94-010 and E01-012, since despite these two experiments being at different scattering angles (15 and 25, 32° respectively), they do fall in our phase space, see Figure C.2. Therefore, these data provide a good calibration for the model.

The model needed some moderate tweaking to be in good agreement with the aforementioned experimental data. To bring F1F209 into agreement with the data, we noticed a weak E_s dependence in the inelastic region of the data. Therefore, we fit the ratio of data to model as a function of E_s to a line. The "scaling functon" is:

$$f(E_s) = 0.906 - 0.00699E_s. \qquad \text{(C.2)}$$

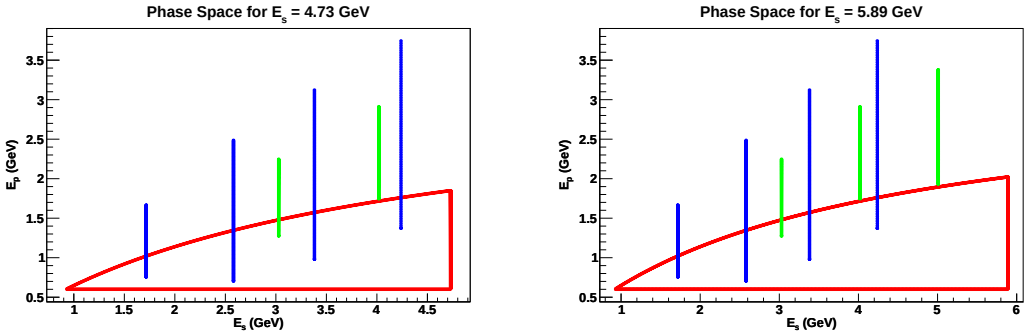

(a) $E_s = 4.74\,\text{GeV}$ (b) $E_s = 5.89\,\text{GeV}$

Figure C.2: Phase space coverage for $E_s = 4.74$ and 5.89 GeV. The vertical blue lines indicate a cross section spectrum for a given E_s from the E94-010 experiment, while the green lines indicate spectra for E01-012.

This function was applied to the inelastic component of the structure functions $F_{1,2}$. The resulting fit as compared to the data is shown in Figures C.3 and C.4. To be sure that the angular dependence was in good shape, we also compared the new scaled F1F209 fit to quasi-elastic data at larger scattering angles, shown in Figure C.5. We can see the agreement is reasonable.

C.2.3 Utilizing the Model

This optimized fit was used to generate spectra at E_s values ranging from 1.5 to 5.8 GeV in steps of 100 MeV in order to cover the full range of the phase space required at both $E_s =$ 4.74 and 5.89 GeV. The real data at 4.74 GeV was used in the unfolding of the 5.89 GeV data set.

The elastic tail and quasi-elastic tail were subtracted from our data prior to carrying out the radiative corrections as discussed in Section 5.4.3. As a result, the phase space considered in the integration starts at the pion production threshold, indicated by the upper curved boundary in Figure C.2. The elastic boundary would be at larger E_p values, and thus higher on the plot.

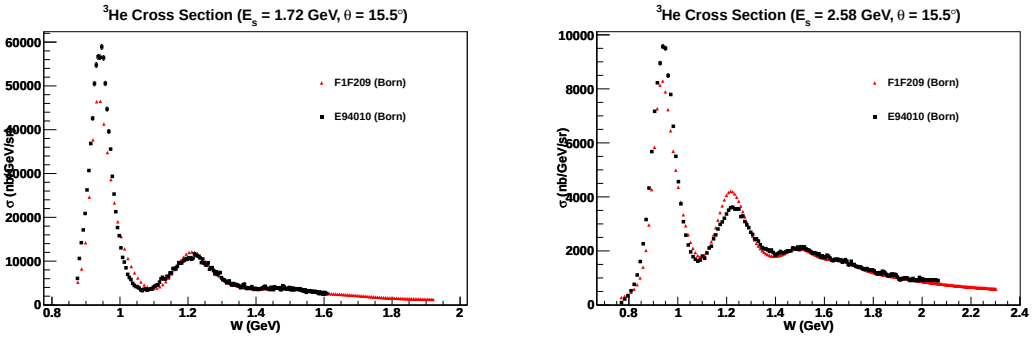

(a) $E_s = 1.72\,\text{GeV}$

(b) $E_s = 2.58\,\text{GeV}$

(c) $E_s = 3.38\,\text{GeV}$

(d) $E_s = 4.24\,\text{GeV}$

Figure C.3: F1F209 fits compared to E94-010 data.

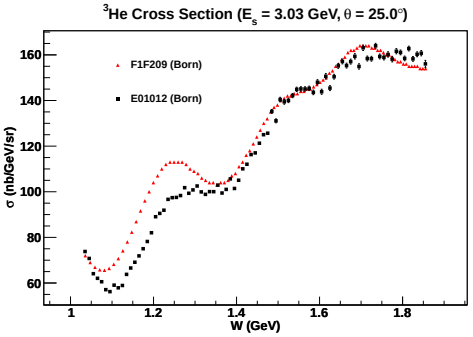

(a) $E_s = 3.02\,\text{GeV}$, $\theta = 25^\circ$

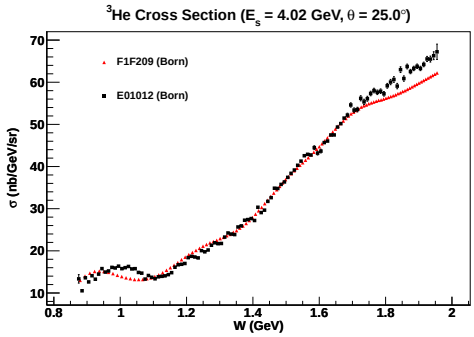

(b) $E_s = 4.02\,\text{GeV}$, $\theta = 25^\circ$

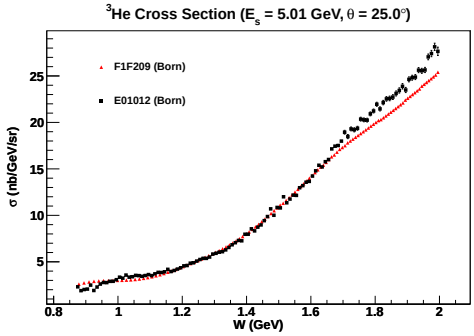

(c) $E_s = 5.01\,\text{GeV}$, $\theta = 25^\circ$

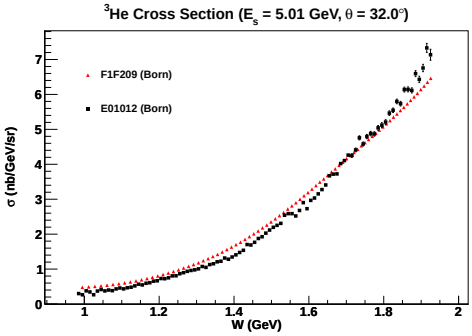

(d) $E_s = 5.01\,\text{GeV}$, $\theta = 32^\circ$

Figure C.4: F1F209 fits compared to E01-012 data.

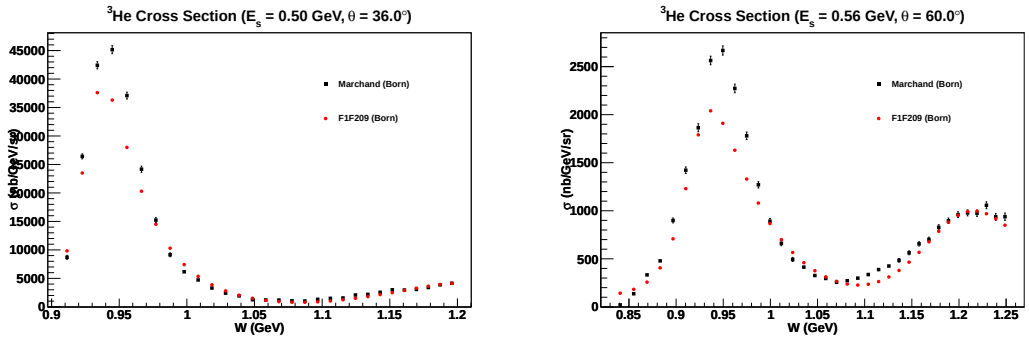

(a) $E_s = 0.50\,\text{GeV}$, $\theta = 36^\circ$ (b) $E_s = 0.56\,\text{GeV}$, $\theta = 60^\circ$

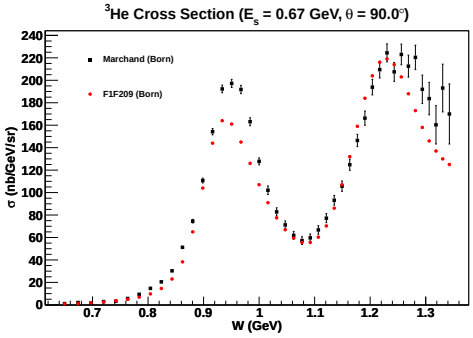

(c) $E_s = 0.67\,\text{GeV}$, $\theta = 90^\circ$

Figure C.5: F1F209 fits compared to Marchand *et. al.* data.

C.3 Double-Spin Asymmetries

To carry out the radiative corrections for the asymmetries, we determined the correction first on *polarized cross section differences*, and then converted the Born $\Delta\sigma$ back to an asymmetry. From here, the correction on the asymmetry level was determined as $\Delta A = A_b - A_r$. Since we only had data for two beam energies, a polarized cross section difference model was needed to fill out the rest of the integration phase space, which was characterized by three distinct regions of physics: the DIS, quasi-elastic, and resonance regions. Here, we discuss each component in detail.

C.3.1 Integration Phase Space

The integration phase space for the asymmetries was different from that seen in the cross sections (Fig. C.2) because the integration was carried out from the *elastic* threshold minus 5 MeV (to avoid the elastic peak and the three-body breakup threshold). This was done because we treated the quasi-elastic, resonance and DIS regions together as one. The integration phase space is now given in Figure C.6. We also show the overlap with JLab E94-010, which was used as a reference for our input model, discussed in Section C.3.2.

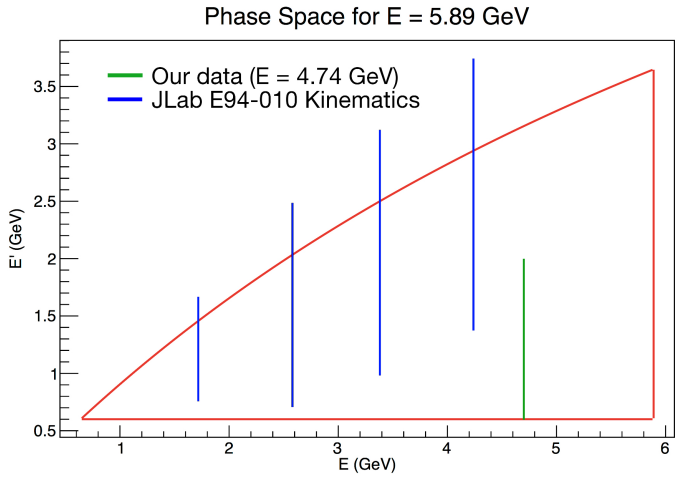

Figure C.6: Integration phase space needed for the radiative corrections for the asymmetries. Also shown are the kinematics of JLab E94-010, which served as a reference for our polarized cross section difference model, needed to fill out the integration phase space. Our kinematic coverage at $E = 4.74$ GeV is shown by the green line.

C.3.2 Polarized Cross Section Difference Model

C.3.2.1 DIS Region

The DIS region was modeled using the DSSV [220] model for the spin structure functions g_1 and g_2. The polarized cross section differences in the parallel and perpendicular cases were computed according to Equations 1.32 and 1.33.

C.3.2.2 Quasi-Elastic Region

To construct the quasi-elastic $\Delta\sigma$ for ^{3}He, we combine the nucleon form factors of P. Bosted [221] and the smearing function [222] in the following way: we use the nucleon form factors G_E and G_M from [221] and the smearing function from [222]:

$$G_E = \sqrt{CF f_{ps}\left[ZG_{E,p}^2 + (A-Z)G_{E,n}^2\right]} \tag{C.3}$$

$$G_M = \sqrt{CF f_{ps}\left[ZG_{M,p}^2 + (A-Z)G_{M,n}^2\right]}, \tag{C.4}$$

where f_{ps} is the Pauli Suppression factor, given as:

$$f_{ps}(\vec{q}) = \begin{cases} \frac{3}{4}\left(\frac{|\vec{q}|}{k_F}\right)\left[1 - \frac{1}{12}\left(\frac{\vec{q}}{k_F}\right)^2\right] & |\vec{q}| < 2k_F \\ 1 & |\vec{q}| \geq 2k_F, \end{cases} \tag{C.5}$$

where k_F is the Fermi momentum. The function $C = C(x, Q^2)$ and is written as:

$$C\left(x, Q^2\right) = x^{\alpha} \exp\left(p_0 + p_1 Q^2 + p_2 Q^4 + p_3 Q^6\right). \tag{C.6}$$

It was needed to get the normalization of the unpolarized σ_0 correct when comparing against the F1F209 model, as shown in Figure C.7. This comparison was done because the F1F209 model does well in describing the world data for the quasi-elastic region (Fig. C.5). The function F is the scaling function, written as [222]:

$$F(\psi') = \frac{1.5576}{k_F\left[1 + 1.7720^2(\psi' + 0.3014)^2\right]\left(1 + e^{-2.4291\psi'}\right)}. \tag{C.7}$$

The dimensionless scaling variable is ψ:

$$\psi \equiv \frac{1}{\sqrt{\xi_F}} \frac{\lambda - \tau}{\sqrt{(1+\lambda)\tau + \kappa\sqrt{\tau(1+\tau)}}}, \tag{C.8}$$

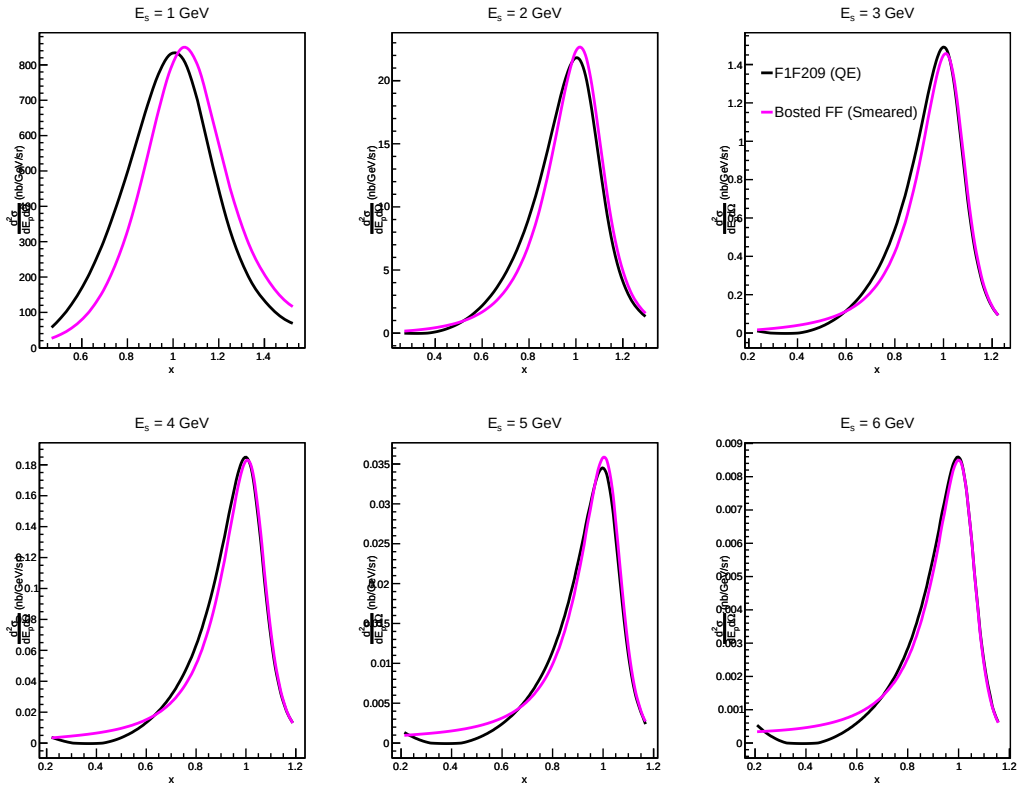

Figure C.7: A comparison of our quasi-elastic cross section model (P. Bosted nucleon form factors smeared by a quasi-elastic scaling function) to the quasi-elastic component of the F1F209 model. The scattering angle used in these plots is $\theta = 45^{\circ}$.

where the variables ξ_F, λ, κ and τ are defined as:

$$\xi_F = \sqrt{1+\eta_F^2} - 1 \tag{C.9}$$

$$\eta_F = k_F / M \tag{C.10}$$

$$\lambda = \frac{\nu}{2M} \tag{C.11}$$

$$\kappa = \frac{|\vec{q}|}{2M} \tag{C.12}$$

$$\tau = \kappa^2 - \lambda^2. \tag{C.13}$$

To obtain the dimensionless variable ψ', $\lambda \rightarrow \lambda' = \lambda - \lambda_{\text{shift}}$, where an energy shift E_{shift} is introduced, such that $\lambda_{\text{shift}} = E_{\text{shift}}/(2M)$ and $\tau \rightarrow \tau' = \kappa^2 - \lambda'^2$. One can see how $\psi' = \psi'\left(x, Q^2\right)$; with this in mind, we have evaluated ψ' at $\left(x + x_0, Q^2\right)$, which centered the quasi-elastic peak properly in our calculations. This was done because when checking the model against world data, our calculated quasi-elastic peak needed to be shifted to agree

with the data. The parameters α, x_0 and p_i were determined to be:

$$\begin{aligned}
\alpha &= 1.7 \\
x_0 &= 0.05 \\
p_0 &= 0.4461 \\
p_1 &= -0.7607 \\
p_2 &= 0.1207 \\
p_3 &= -0.0075,
\end{aligned}$$

and the Fermi momentum used was $k_F = 115\,\text{MeV}$ and $E_{\text{shift}} = 1\,\text{MeV}$. Utilizing Equations 1.32 and 1.33, we construct the polarized cross section differences $\Delta\sigma_{\parallel}$ and $\Delta\sigma_{\perp}$, with the *quasi-elastic* spin structure functions g_1 and g_2 given in terms of our quasi-elastic form factors G_E^{QE} and G_M^{QE}:

$$g_1^{\text{QE}}\left(x,Q^2\right) = \frac{G_M^{\text{QE}}\left(x,Q^2\right)}{2}\frac{G_E^{\text{QE}}\left(x,Q^2\right)+\tau G_M^{\text{QE}}\left(x,Q^2\right)}{1+\tau} \tag{C.14}$$

$$g_2^{\text{QE}}\left(x,Q^2\right) = \frac{\tau G_M^{\text{QE}}\left(x,Q^2\right)}{2}\frac{G_E^{\text{QE}}\left(x,Q^2\right)-G_M^{\text{QE}}\left(x,Q^2\right)}{1+\tau}. \tag{C.15}$$

C.3.2.3 Resonance Region

For the resonance region, we used the MAID model [141]. In particular, for a given electron helicity h and target polarization P, the polarized cross section is formed as:

$$\sigma^{h,P} = \tilde{P}_p\left\{\sigma^{h,P}\left[p\left(e,e'p\right)\pi^0\right]+\sigma^{h,P}\left[p\left(e,e'n\right)\pi^+\right]\right\} \tag{C.16}$$

$$+ \tilde{P}_n\left\{\sigma^{h,P}\left[n\left(e,e'n\right)\pi^0\right]+\sigma^{h,P}\left[n\left(e,e'p\right)\pi^-\right]\right\} \tag{C.17}$$

where each pion electroproduction channel is included. The effective polarization of the neutron is $\tilde{P}_n = P_n + 0.056$, with $P_n = 0.86^{+0.036}_{-0.020}$; the effective polarization of the proton is $\tilde{P}_p = P_p - 0.014$, with $P_p = -0.028^{+0.009}_{-0.004}$ [40]. The $\tilde{P}_{n,p}$ terms indicate that contributions from the $\Delta(1232)$ component of the ^{3}He wave function are included [144]. Each reaction channel is constructed from the virtual photon cross sections in pion electroproduction:

$$\frac{d^2\sigma}{d\Omega dE'} = \Gamma\sigma_v = \Gamma\Big[\sigma_T + \varepsilon\sigma_L + P_y\sqrt{2\varepsilon(1+\varepsilon)}\sigma_{LT} \tag{C.18}$$

$$+ \; hP_x\sqrt{2\varepsilon(1-\varepsilon)}\sigma_{LT'} + hP_z\sqrt{1-\varepsilon^2}\sigma_{TT'}\Big] \tag{C.19}$$

$$\Gamma = \frac{\alpha}{2\pi^2}\frac{E'}{E}\frac{K}{Q^2}\frac{1}{1-\varepsilon} \tag{C.20}$$

where the virtual photon flux is Γ, and $K = \nu - \left[Q^2/(2M)\right]$ in the Hand convention [50]; the target polarization along the i^{th} axis is P_i in pion scattering plane coordinates. The polarized cross section difference $\Delta\sigma$ for the parallel and perpendicular cases is formed by computing the differences of helicity-dependent cross sections:

$$\Delta\sigma_{\parallel} = \sigma^{\downarrow\Uparrow} - \sigma^{\uparrow\Uparrow} \tag{C.21}$$

$$\Delta\sigma_{\perp} = \sigma^{\downarrow\Rightarrow} - \sigma^{\uparrow\Rightarrow}. \tag{C.22}$$

C.3.2.4 Testing the Model

Our polarized cross section difference model was compared to the JLab E94-010 data set, as its kinematics coincided with our integration phase space. Figures C.8 and C.9 show E94-010 data compared to our model (dashed curves). The left panel shows the comparison to polarized cross section differences, while the right panel shows a comparison to the unpolarized quasi-elastic peak. To get the normalization correct at low x for the polarized cross section differences, the MAID model was scaled down by a factor of 3. While the model may not do as well describing the width of the resonance peak, it does better in describing the quasi-elastic peak in both the polarized and unpolarized cases. In the systematic error studies, the model was varied up to $\pm 10\%$ at random bin-by-bin and it was found that the resulting radiative correction changed by less than 5% (Sect. 5.5.4). Because of this, we believe that this model performs adequately in describing the physics in the integration phase space.

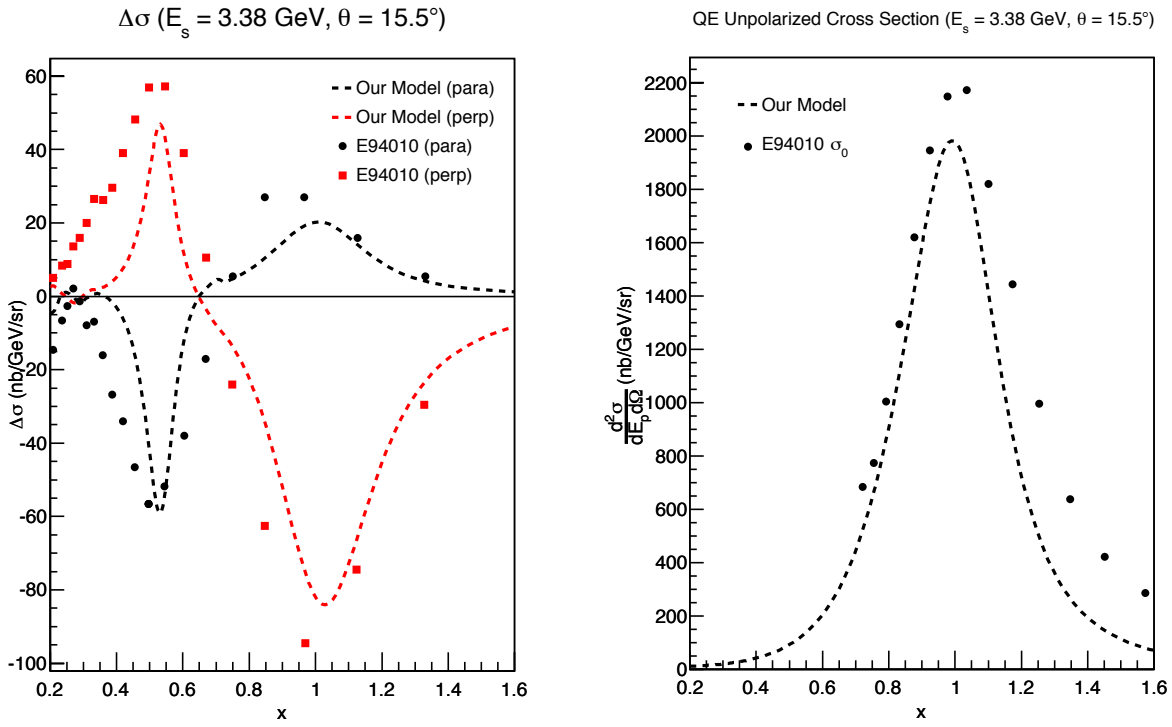

Figure C.8: The left panel shows our polarized cross section difference model (dashed) compared to JLab E94-010 data for $E_s = 3.38\,\text{GeV}$. The right panel shows the our quasi-elastic unpolarized cross section model compared to JLab E94-010 data.

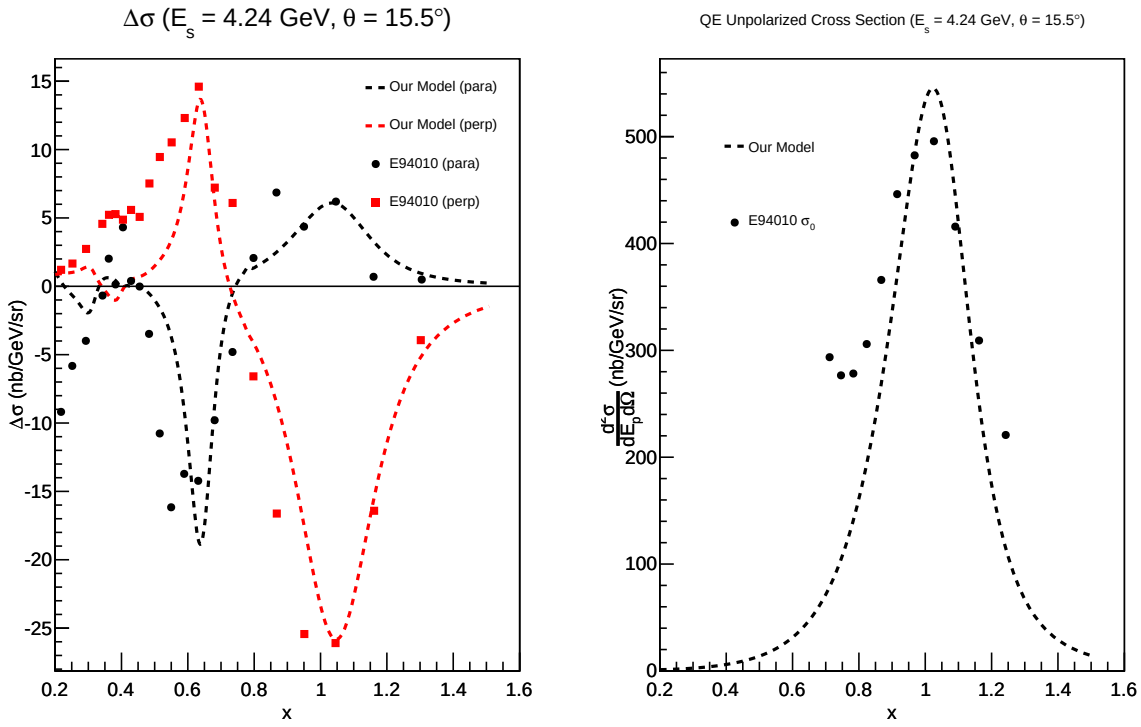

Figure C.9: The left panel shows our polarized cross section difference model (dashed) compared to JLab E94-010 data for $E_s = 4.24\,\text{GeV}$. The right panel shows the our quasi-elastic unpolarized cross section model compared to JLab E94-010 data.

APPENDIX D

FITS TO DATA

D.1 Cross Section Fits

As discussed in Section 5.4.2, due to time constraints not all kinematics were accounted for in terms of measuring the positron and nitrogen cross sections. To alleviate the issue, we fit the measured data to a function of the form:

$$f(E_p) = \frac{1}{E_p^2} e^{(a_0 + a_1 E_p)}, \tag{D.1}$$

where the scattered electron energy E_p is in GeV. This was done for each measured background signal. The fit parameters and their errors are listed in Tables D.1 and D.2.

Table D.1: Fit parameters for the nitrogen cross section (negative and positive polarity) and the positron cross section for $E = 4.74$ GeV. All errors are absolute.

Parameter	Nitrogen (Neg. Pol.)	Nitrogen (Pos. Pol.)	Positron
a_0	1.465E+01 $\pm$ 4.919E-02	1.559E+01 $\pm$ 1.604E-01	1.887E+01 $\pm$ 7.998E-02
a_1	-1.825E-03 $\pm$ 4.770E-05	-4.699E-03 $\pm$ 2.255E-04	-5.620E-03 $\pm$ 1.194E-04

Table D.2: Fit parameters for the nitrogen cross section (negative and positive polarity) and the positron cross section for $E = 5.89$ GeV. All errors are absolute.

Parameter	Nitrogen (Neg. Pol.)	Nitrogen (Pos. Pol.)	Positron
a_0	1.480E+01 $\pm$ 5.647E-02	1.614E+01 $\pm$ 2.120E-01	1.896E+01 $\pm$ 6.89949E-02
a_1	-2.123E-03 $\pm$ 5.607E-05	-5.232E-03 $\pm$ 3.126E-04	-5.421E-03 $\pm$ 9.28580E-05

D.2 A_1^p Fit

To carry out the analysis to obtain A_1^n from our $A_1^{^3\mathrm{He}}$ data, we need a fit to parameterize the A_1^p data. We fit the world data to a three-parameter, Q^2-independent fit*. This assumption is a reasonable one, in that the Q^2 dependence is not very strong, given that the world data, which are at differing Q^2, are showing roughly the same behavior; furthermore, since $A_1 \sim g_1/F_1$, the Q^2 evolution in g_1 and F_1 cancel in the ratio to leading order and next-to-leading order in Q^2 [43]. The data used in the fit includes measurements from SMC [68], HERMES [67], EMC [18, 19], SLAC E143 [51] and E155 [229], along with CLAS EG1b [73]. Before plotting the data, each experiment's results were rebinned, where new bins were formed based on a statistical error-weighted average; the systematic error for a given bin was the average of the errors contributing to that bin with a weight of 1. The fit is shown in Figure D.1, where we obtained a $\chi^2/\mathrm{ndf} = 1.00$. The fit takes the form:

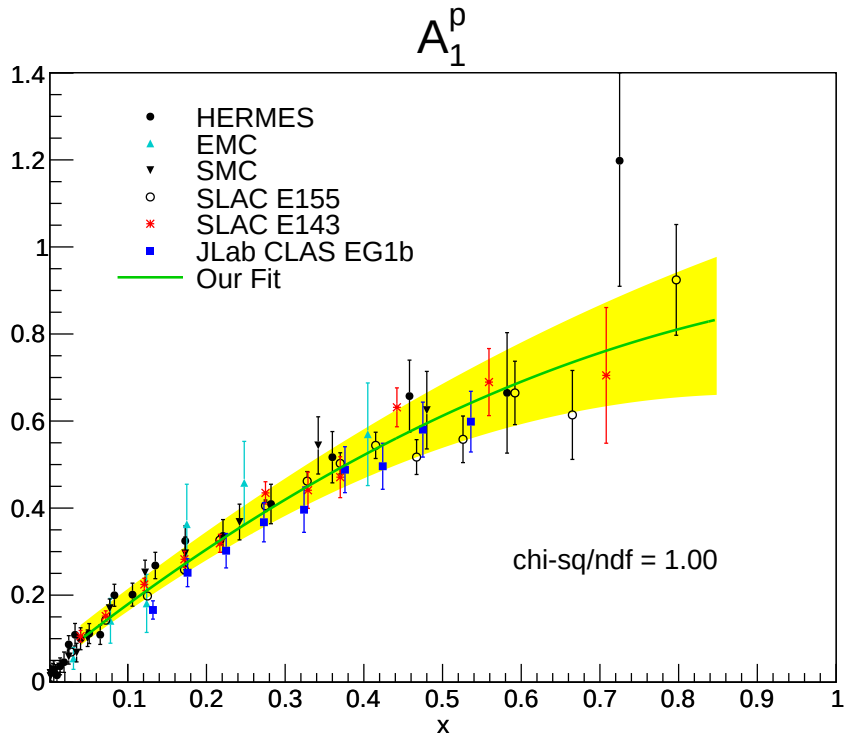

Figure D.1: Our fit to world A_1^p data. The error bars on the data are the in-quadrature sum of their statistical and systematic errors. The yellow band indicates the error on the fit.

$$f(x) = p_0 + p_1 x + p_2 x^2. \tag{D.2}$$

*The fit was done using the ROOT [189] software package.

The yellow band indicates the error on the fit, and is computed by fitting the upper and lower error bars of the data, which gives a conservative estimate on the error of the fit and reflects the spread of the A_1^p data. The fit parameters were found to be:

$$\begin{aligned} p_0 &= 0.041 \pm 0.008 \\ p_1 &= 1.442 \pm 0.081 \\ p_2 &= -0.599 \pm 0.163 \end{aligned} \tag{D.3}$$

D.3 g_1^p/F_1^p Fit

A similar analysis was carried out for extracting g_1^n/F_1^n from $g_1^{^3\mathrm{He}}/F_1^{^3\mathrm{He}}$, where we need a parameterization of the world g_1^p/F_1^p data. The world data considered was HERMES [64], SLAC E143 [51] and E155 [229], along with CLAS EG1b [73]. The fit result is shown in Figure D.2, with $\chi^2/\mathrm{ndf} = 0.87$. The fit function was similar to the A_1^p fit, in that it is a second-order polynomial in x with no Q^2dependence (Eq. D.2). The fit parameters were found to be:

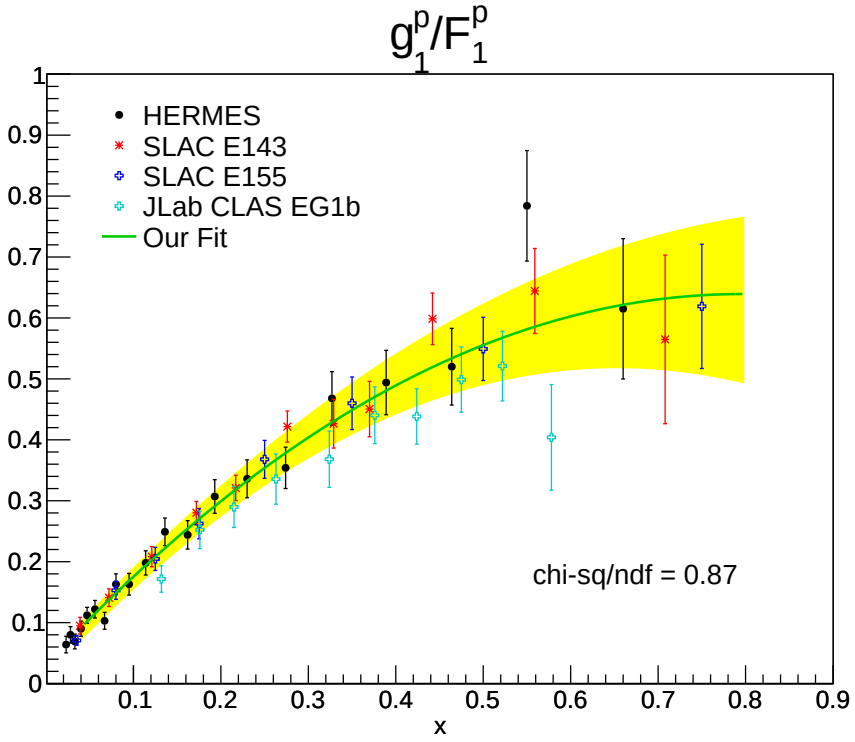

Figure D.2: Our fit to world g_1^p/F_1^p data. The error bars on the data are the in-quadrature sum of their statistical and systematic errors. The yellow band indicates the error on the fit.

$$\begin{aligned} p_0 &= 0.032 \pm 0.009 \\ p_1 &= 1.525 \pm 0.099 \\ p_2 &= -0.958 \pm 0.194. \end{aligned} \tag{D.4}$$

The yellow band in Figure D.2 gives the fit error, computed in the same fashion as was done for the A_1^p fit.

APPENDIX E

TABULATED RESULTS

This appendix contains tables of all results for unpolarized cross sections, double-spin asymmetries, and the virtual photon asymmetry A_1 on ^{3}He and the neutron. Also included are tables of results for the structure function ratio g_1/F_1 on ^{3}He and the neutron, along with the polarized-to-unpolarized quark ratios for the up and down quarks, respectively. The results and systematic errors for a_2 are presented in the last section.

E.1 Cross Sections

E.1.1 Raw Cross Sections

The measured raw cross sections for $E = 4.74$ and $5.89\,\text{GeV}$ are tabulated in Tables E.1 and E.2. The positron cross sections are tabulated in Tables E.3 and E.4. The nitrogen cross sections, including their diluted forms due to the small amount of nitrogen in the ^{3}He production cell, are tabulated in Tables E.5 and E.6 for the negative polarity runs. For positive polarity, they are given in Tables E.7 and E.8. Note that not all bins were accounted for when measuring the backgrounds. To correct for this, fits to the data were done, see Section 5.4.2 and Appendix D.1. The positron to electron ratios are tabulated in Tables E.9 and E.10. All errors listed are statistical only.

Table E.1: The raw electron cross section data for $E_s = 4.74$ GeV. The errors listed are statistical only. All errors are absolute.

$\langle E_p \rangle$ (GeV)	$\frac{d^2\sigma_{\text{raw}}}{d\Omega dE_p}$ $\left(\frac{\text{nb}}{\text{sr}\cdot\text{GeV}}\right)$
0.599	26.345 ± 0.233
0.798	10.064 ± 0.138
1.118	3.134 ± 0.040
1.188	2.534 ± 0.033
1.257	1.949 ± 0.026
1.336	1.442 ± 0.024
1.416	1.048 ± 0.018
1.504	0.703 ± 0.011
1.593	0.441 ± 0.008

Table E.2: The raw electron cross section data for $E_s = 5.89$ GeV. The errors listed are statistical only. All errors are absolute.

$\langle E_p \rangle$ (GeV)	$\frac{d^2\sigma_{\text{raw}}}{d\Omega dE_p}$ $\left(\frac{\text{nb}}{\text{sr}\cdot\text{GeV}}\right)$
0.599	26.039 ± 0.133
0.699	14.416 ± 0.107
0.898	5.158 ± 0.056
1.128	2.176 ± 0.028
1.198	1.639 ± 0.029
1.268	1.304 ± 0.017
1.338	0.997 ± 0.016
1.416	0.748 ± 0.011
1.504	0.506 ± 0.010
1.594	0.339 ± 0.007
1.693	0.209 ± 0.006

Table E.3: The positron cross section data for $E_s = 4.74$ GeV. The errors listed are statistical only. All errors are absolute.

$\langle E_p \rangle$ (GeV)	$\frac{d^2\sigma_{\text{pos}}}{d\Omega dE_p}$ $\left(\frac{\text{nb}}{\text{sr}\cdot\text{GeV}}\right)$
0.599	14.093 ± 0.273
0.798	3.113 ± 0.111
1.118	0.223 ± 0.023
1.336	0.016 ± 0.007

Table E.4: The positron cross section data for $E_s = 5.89$ GeV. The errors listed are statistical only. All errors are absolute.

$\langle E_p \rangle$ (GeV)	$\frac{d^2\sigma_{\text{pos}}}{d\Omega dE_p}$ $\left(\frac{\text{nb}}{\text{sr}\cdot\text{GeV}}\right)$
0.599	17.552 ± 0.410
0.898	1.787 ± 0.079
1.128	0.319 ± 0.023
1.268	0.075 ± 0.009

Table E.5: The negative polarity nitrogen cross section data for E_s = 4.74 GeV. The second column gives the diluted nitrogen cross section, due to the nitrogen content of the production cell being $\approx 1\%$ of the ^{3}He volume. The errors listed are statistical only. All errors are absolute.

$\langle E_p \rangle$ (GeV)	$\frac{d^2\sigma_N}{d\Omega dE_p}$ $\left(\frac{\text{nb}}{\text{sr}\cdot\text{GeV}}\right)$	$\frac{d^2\sigma_{N,dil}}{d\Omega dE_p}$ $\left(\frac{\text{nb}}{\text{sr}\cdot\text{GeV}}\right)$
0.599	192.290 ± 5.026	2.009 ± 0.052
1.118	24.344 ± 1.106	0.254 ± 0.011
1.188	18.710 ± 0.816	0.196 ± 0.009
1.336	10.379 ± 0.783	0.108 ± 0.008
1.416	8.012 ± 0.424	0.084 ± 0.004
1.504	4.855 ± 0.362	0.050 ± 0.004
1.593	2.631 ± 0.800	0.027 ± 0.008

Table E.6: The negative polarity nitrogen cross section data for E_s = 5.89 GeV. The second column gives the diluted nitrogen cross section, due to the nitrogen content of the production cell being $\approx 1\%$ of the ^{3}He volume. The errors listed are statistical only. All errors are absolute.

$\langle E_p \rangle$ (GeV)	$\frac{d^2\sigma_N}{d\Omega dE_p}$ $\left(\frac{\text{nb}}{\text{sr}\cdot\text{GeV}}\right)$	$\frac{d^2\sigma_{N,dil}}{d\Omega dE_p}$ $\left(\frac{\text{nb}}{\text{sr}\cdot\text{GeV}}\right)$
0.599	194.900 ± 7.520	2.042 ± 0.079
0.699	112.240 ± 4.262	1.168 ± 0.044
0.898	43.723 ± 1.669	0.459 ± 0.018
1.128	18.191 ± 0.962	0.190 ± 0.010
1.198	13.077 ± 0.519	0.137 ± 0.005
1.268	12.238 ± 0.639	0.128 ± 0.007
1.416	7.735 ± 0.498	0.081 ± 0.005
1.594	2.223 ± 0.244	0.023 ± 0.002

Table E.7: The positive polarity nitrogen cross section data for E_s = 4.74 GeV. The second column gives the diluted nitrogen cross section, due to the nitrogen content of the production cell being $\approx 1\%$ of the ^{3}He volume. The errors listed are statistical only. All errors are absolute.

$\langle E_p \rangle$ (GeV)	$\frac{d^2\sigma_{N,pos}}{d\Omega dE_p}$ $\left(\frac{\text{nb}}{\text{sr}\cdot\text{GeV}}\right)$	$\frac{d^2\sigma_{N,dil}}{d\Omega dE_p}$ $\left(\frac{\text{nb}}{\text{sr}\cdot\text{GeV}}\right)$
0.599	87.945 ± 4.145	0.916 ± 0.043
0.798	21.696 ± 1.485	0.226 ± 0.015
1.118	2.254 ± 0.358	0.023 ± 0.004
1.336	0.331 ± 0.166	0.004 ± 0.002

Table E.8: The positive polarity nitrogen cross section data for E_s = 5.89 GeV. The second column gives the diluted nitrogen cross section, due to the nitrogen content of the production cell being $\approx 1\%$ of the ^{3}He volume. The errors listed are statistical only. All errors are absolute.

$\langle E_p \rangle$ (GeV)	$\frac{d^2\sigma_{N,pos}}{d\Omega dE_p}$ $\left(\frac{\text{nb}}{\text{sr}\cdot\text{GeV}}\right)$	$\frac{d^2\sigma_{N,dil}}{d\Omega dE_p}$ $\left(\frac{\text{nb}}{\text{sr}\cdot\text{GeV}}\right)$
0.599	112.960 ± 5.490	1.180 ± 0.057
0.898	10.853 ± 1.197	0.113 ± 0.012
1.128	1.830 ± 0.461	0.019 ± 0.005

Table E.9: The positron to electron ratio data for $E_s = 4.74$ GeV. The errors listed are statistical only. All errors are absolute.

$\langle E_p \rangle$ (GeV)	N_{e^+}/N_{e^-}
0.599	0.535 ± 0.011
0.798	0.309 ± 0.012
1.118	0.071 ± 0.008
1.336	0.011 ± 0.005

Table E.10: The positron to electron ratio data for $E_s = 5.89$ GeV. The errors listed are statistical only. All errors are absolute.

$\langle E_p \rangle$ (GeV)	N_{e^+}/N_{e^-}
0.599	0.674 ± 0.016
0.898	0.346 ± 0.016
1.128	0.147 ± 0.011
1.268	0.058 ± 0.007

E.1.2 Experimental and Born Cross Sections

Presented in Tables E.11 and E.12 are the experimental cross sections for E_s = 4.74 and 5.89 GeV as a function of E_p, x and Q^2. These bin values are the average values measured during the experiment. Tables E.13 and E.14 show the Born cross sections.

Table E.11: The experimental (radiated) cross section data for E_s = 4.74 GeV. The errors listed are statistical and systematic, respectively. All errors are absolute.

$\langle E_p \rangle$ (GeV)	$\langle x \rangle$	$\langle Q^2 \rangle$ (GeV^2)	$\frac{d^2\sigma_{\rm rad}}{d\Omega dE_p}$ $\left(\frac{\rm nb}{\rm sr\cdot GeV}\right)$
0.599	0.214	1.659	$11.470 \pm 0.365 \pm 0.894$
0.798	0.299	2.209	$6.961 \pm 0.178 \pm 0.362$
1.118	0.456	3.094	$2.722 \pm 0.048 \pm 0.129$
1.188	0.494	3.285	$2.250 \pm 0.034 \pm 0.104$
1.257	0.533	3.472	$1.747 \pm 0.026 \pm 0.084$
1.336	0.579	3.694	$1.301 \pm 0.027 \pm 0.062$
1.416	0.629	3.909	$0.948 \pm 0.018 \pm 0.046$
1.504	0.686	4.149	$0.633 \pm 0.012 \pm 0.030$
1.593	0.745	4.387	$0.390 \pm 0.012 \pm 0.019$

Table E.12: The experimental (radiated) cross section data for E_s = 5.89 GeV. The errors listed are statistical and systematic, respectively. All errors are absolute.

$\langle E_p \rangle$ (GeV)	$\langle x \rangle$	$\langle Q^2 \rangle$ (GeV^2)	$\frac{d^2\sigma_{\rm rad}}{d\Omega dE_p}$ $\left(\frac{\rm nb}{\rm sr\cdot GeV}\right)$
0.599	0.208	2.064	$8.221 \pm 0.440 \pm 0.844$
0.699	0.247	2.409	$6.486 \pm 0.116 \pm 0.460$
0.898	0.330	3.095	$3.318 \pm 0.099 \pm 0.171$
1.128	0.434	3.882	$1.749 \pm 0.038 \pm 0.086$
1.198	0.468	4.124	$1.352 \pm 0.030 \pm 0.068$
1.268	0.503	4.360	$1.107 \pm 0.020 \pm 0.054$
1.338	0.539	4.603	$0.860 \pm 0.016 \pm 0.043$
1.416	0.580	4.873	$0.655 \pm 0.012 \pm 0.032$
1.504	0.629	5.173	$0.444 \pm 0.010 \pm 0.021$
1.594	0.679	5.478	$0.297 \pm 0.007 \pm 0.014$
1.693	0.738	5.811	$0.180 \pm 0.006 \pm 0.009$

Table E.13: The Born cross section data for $E_s = 4.74\,\text{GeV}$. The errors listed are statistical and systematic, respectively. All errors are absolute.

$\langle E_p \rangle$ (GeV)	$\langle x \rangle$	$\langle Q^2 \rangle$ (GeV^2)	$\frac{d^2\sigma_{\text{Born}}}{d\Omega dE_p}$ $\left(\frac{\text{nb}}{\text{sr}\cdot\text{GeV}}\right)$
0.599	0.214	1.659	$6.191 \pm 0.365 \pm 0.561$
0.798	0.299	2.209	$5.374 \pm 0.178 \pm 0.281$
1.118	0.456	3.094	$2.544 \pm 0.048 \pm 0.121$
1.188	0.494	3.285	$2.223 \pm 0.034 \pm 0.103$
1.257	0.533	3.472	$1.762 \pm 0.026 \pm 0.084$
1.336	0.579	3.694	$1.353 \pm 0.027 \pm 0.065$
1.416	0.629	3.909	$1.021 \pm 0.018 \pm 0.050$
1.504	0.686	4.149	$0.718 \pm 0.012 \pm 0.035$
1.593	0.745	4.387	$0.536 \pm 0.012 \pm 0.028$

Table E.14: The Born cross section data for $E_s = 5.89\,\text{GeV}$. The errors listed are statistical and systematic, respectively. All errors are absolute.

$\langle E_p \rangle$ (GeV)	$\langle x \rangle$	$\langle Q^2 \rangle$ (GeV^2)	$\frac{d^2\sigma_{\text{Born}}}{d\Omega dE_p}$ $\left(\frac{\text{nb}}{\text{sr}\cdot\text{GeV}}\right)$
0.599	0.208	2.064	$4.069 \pm 0.440 \pm 0.492$
0.699	0.247	2.409	$4.322 \pm 0.116 \pm 0.310$
0.898	0.330	3.095	$2.488 \pm 0.099 \pm 0.130$
1.128	0.434	3.882	$1.596 \pm 0.038 \pm 0.079$
1.198	0.468	4.124	$1.234 \pm 0.030 \pm 0.063$
1.268	0.503	4.360	$1.067 \pm 0.020 \pm 0.052$
1.338	0.539	4.603	$0.846 \pm 0.016 \pm 0.042$
1.416	0.580	4.873	$0.679 \pm 0.012 \pm 0.033$
1.504	0.629	5.173	$0.472 \pm 0.010 \pm 0.022$
1.594	0.679	5.478	$0.331 \pm 0.007 \pm 0.016$
1.693	0.738	5.811	$0.250 \pm 0.006 \pm 0.013$

E.1.3 Systematic Errors

The breakdown of the systematic errors on the unpolarized cross sections are listed in Tables E.15 and E.16. The column "Cuts" indicates errors due to electron cuts, which includes the gas Čerenkov, E/p, and target cuts to remove the target windows; "Background" corresponds to errors related to the positron and nitrogen background subtractions; "Misc." refers to the errors incurred from the beam charge calibration, nitrogen dilution in the target and ^{3}He density; "RC" is the error due to the radiative corrections. "Total" is the in-quadrature sum of each column.

Table E.15: Systematic error breakdown for the unpolarized ^{3}He cross section at E = 4.74 GeV. All errors are in nb/GeV/sr. The E_p bin indicated is the central momentum setting of the spectrometer.

$\langle E_p \rangle$ (GeV)	Cuts	Background	Misc.	RC	Total
0.599	0.17000	0.37960	0.24460	0.28690	0.56140
0.798	0.13940	0.11690	0.21240	0.02383	0.28070
1.118	0.06456	0.01689	0.10050	0.00478	0.12080
1.188	0.05302	0.01169	0.08784	0.00085	0.10330
1.257	0.04675	0.00827	0.06963	0.00058	0.08427
1.336	0.03596	0.00573	0.05347	0.00248	0.06474
1.416	0.02809	0.00417	0.04035	0.00409	0.04951
1.504	0.01972	0.00324	0.02835	0.00520	0.03507
1.593	0.01518	0.00289	0.02119	0.00898	0.02772

Table E.16: Systematic error breakdown for the unpolarized ^{3}He cross section at E = 5.89 GeV. All errors are in nb/GeV/sr. The E_p bin indicated is the central momentum setting of the spectrometer.

$\langle E_p \rangle$ (GeV)	Cuts	Background	Misc.	RC	Total
0.599	0.10600	0.37100	0.16080	0.26040	0.49240
0.699	0.11220	0.22810	0.17080	0.04725	0.30990
0.898	0.05578	0.06123	0.09832	0.01720	0.12970
1.128	0.04424	0.01685	0.06307	0.00413	0.07897
1.198	0.03754	0.01113	0.04876	0.00383	0.06265
1.268	0.02944	0.00796	0.04216	0.00141	0.05206
1.338	0.02569	0.00565	0.03341	0.00058	0.04253
1.416	0.01819	0.00401	0.02684	0.00110	0.03268
1.504	0.01114	0.00279	0.01867	0.00152	0.02197
1.594	0.00884	0.00209	0.01306	0.00199	0.01603
1.693	0.00697	0.00181	0.00987	0.00414	0.01290

E.2 Double-Spin Asymmetries

E.2.1 Physics and Born Asymmetries

The physics asymmetries (that is, without radiative corrections) $A_{\parallel}$ and $A_{\perp}$ on ^{3}He are listed in Tables E.17 and E.18. Presented in Tables E.19 and E.20 are the Born asymmetries. The errors given are the statistical and systematic errors, respectively. All errors are absolute.

Table E.17: Physics asymmetries for $A_{\parallel}$ and $A_{\perp}$ on ^{3}He at $E = 4.74$ GeV. The errors are statistical and systematic, respectively. All errors are absolute.

$< x >$	$A_{\parallel}^{^3\mathrm{He}}$	$A_{\perp}^{^3\mathrm{He}}$
0.277	-0.002 $\pm$ 0.016 $\pm$ 0.007	-0.002 $\pm$ 0.008 $\pm$ 0.002
0.325	-0.005 $\pm$ 0.009 $\pm$ 0.002	-0.003 $\pm$ 0.004 $\pm$ 0.002
0.374	0.009 $\pm$ 0.007 $\pm$ 0.002	-0.013 $\pm$ 0.004 $\pm$ 0.002
0.424	-0.022 $\pm$ 0.007 $\pm$ 0.005	-0.004 $\pm$ 0.004 $\pm$ 0.002
0.473	-0.020 $\pm$ 0.008 $\pm$ 0.003	-0.006 $\pm$ 0.004 $\pm$ 0.001
0.523	0.003 $\pm$ 0.009 $\pm$ 0.002	-0.007 $\pm$ 0.004 $\pm$ 0.001
0.574	0.006 $\pm$ 0.011 $\pm$ 0.004	-0.010 $\pm$ 0.006 $\pm$ 0.002
0.623	0.028 $\pm$ 0.013 $\pm$ 0.003	0.004 $\pm$ 0.006 $\pm$ 0.002
0.673	0.024 $\pm$ 0.016 $\pm$ 0.004	-0.005 $\pm$ 0.008 $\pm$ 0.003
0.723	0.030 $\pm$ 0.019 $\pm$ 0.006	-0.015 $\pm$ 0.010 $\pm$ 0.002
0.773	-0.013 $\pm$ 0.024 $\pm$ 0.013	-0.026 $\pm$ 0.012 $\pm$ 0.004
0.823	-0.034 $\pm$ 0.030 $\pm$ 0.012	0.004 $\pm$ 0.016 $\pm$ 0.006
0.874	-0.014 $\pm$ 0.039 $\pm$ 0.017	-0.050 $\pm$ 0.020 $\pm$ 0.006

Table E.18: Physics asymmetries for $A_\parallel$ and $A_\perp$ on ^{3}He at $E = 5.89$ GeV. The errors are statistical and systematic, respectively. All errors are absolute.

$< x >$	$A_\parallel^{^3\mathrm{He}}$	$A_\perp^{^3\mathrm{He}}$
0.277	$0.026 \pm 0.026 \pm 0.010$	$0.010 \pm 0.008 \pm 0.003$
0.325	$-0.012 \pm 0.012 \pm 0.003$	$0.002 \pm 0.004 \pm 0.001$
0.374	$-0.002 \pm 0.009 \pm 0.002$	$-0.003 \pm 0.003 \pm 0.000$
0.424	$-0.018 \pm 0.009 \pm 0.003$	$-0.006 \pm 0.003 \pm 0.001$
0.474	$-0.019 \pm 0.010 \pm 0.006$	$-0.002 \pm 0.003 \pm 0.001$
0.524	$0.002 \pm 0.012 \pm 0.002$	$-0.001 \pm 0.004 \pm 0.001$
0.573	$0.004 \pm 0.014 \pm 0.003$	$0.002 \pm 0.004 \pm 0.001$
0.624	$0.005 \pm 0.018 \pm 0.005$	$-0.004 \pm 0.005 \pm 0.001$
0.674	$-0.004 \pm 0.022 \pm 0.005$	$-0.002 \pm 0.007 \pm 0.002$
0.723	$0.002 \pm 0.027 \pm 0.005$	$-0.005 \pm 0.008 \pm 0.003$
0.773	$0.005 \pm 0.035 \pm 0.008$	$0.004 \pm 0.010 \pm 0.002$
0.823	$0.027 \pm 0.047 \pm 0.014$	$-0.044 \pm 0.014 \pm 0.004$
0.873	$0.015 \pm 0.062 \pm 0.017$	$-0.009 \pm 0.018 \pm 0.007$

Table E.19: Born asymmetry results for $A_\parallel^{^3\mathrm{He}}$ and $A_\perp^{^3\mathrm{He}}$ for E = 4.74 GeV. The two uncertainties represent the statistical and systematic uncertainties, respectively.

$< x >$	$A_\parallel^{^3\mathrm{He}}$	$A_\perp^{^3\mathrm{He}}$
0.277	$-0.008 \pm 0.015 \pm 0.007$	$-0.002 \pm 0.008 \pm 0.003$
0.325	$-0.009 \pm 0.009 \pm 0.003$	$-0.001 \pm 0.005 \pm 0.002$
0.374	$0.005 \pm 0.007 \pm 0.002$	$-0.011 \pm 0.004 \pm 0.002$
0.424	$-0.025 \pm 0.007 \pm 0.005$	$-0.003 \pm 0.004 \pm 0.002$
0.473	$-0.021 \pm 0.008 \pm 0.003$	$-0.005 \pm 0.004 \pm 0.001$
0.523	$0.002 \pm 0.009 \pm 0.002$	$-0.006 \pm 0.005 \pm 0.001$
0.574	$0.005 \pm 0.010 \pm 0.004$	$-0.008 \pm 0.005 \pm 0.002$
0.623	$0.029 \pm 0.013 \pm 0.003$	$0.005 \pm 0.007 \pm 0.002$
0.673	$0.025 \pm 0.015 \pm 0.005$	$-0.004 \pm 0.009 \pm 0.003$
0.723	$0.031 \pm 0.019 \pm 0.007$	$-0.014 \pm 0.009 \pm 0.002$
0.773	$-0.012 \pm 0.024 \pm 0.013$	$-0.025 \pm 0.012 \pm 0.005$
0.823	$-0.033 \pm 0.030 \pm 0.012$	$0.005 \pm 0.016 \pm 0.006$
0.874	$-0.014 \pm 0.039 \pm 0.017$	$-0.049 \pm 0.020 \pm 0.006$

Table E.20: Born asymmetry results for $A_{\parallel}^{^3\mathrm{He}}$ and $A_{\perp}^{^3\mathrm{He}}$ for E = 5.89 GeV. The two uncertainties represent the statistical and systematic uncertainties, respectively.

$< x >$	$A_{\parallel}^{^3\mathrm{He}}$	$A_{\perp}^{^3\mathrm{He}}$
0.277	$0.019 \pm 0.027 \pm 0.010$	$0.010 \pm 0.008 \pm 0.003$
0.325	$-0.017 \pm 0.012 \pm 0.003$	$0.004 \pm 0.004 \pm 0.001$
0.374	$-0.006 \pm 0.009 \pm 0.002$	$-0.001 \pm 0.003 \pm 0.001$
0.424	$-0.020 \pm 0.009 \pm 0.003$	$-0.004 \pm 0.003 \pm 0.001$
0.474	$-0.021 \pm 0.010 \pm 0.006$	$0.000 \pm 0.003 \pm 0.001$
0.524	$0.002 \pm 0.012 \pm 0.002$	$0.000 \pm 0.004 \pm 0.001$
0.573	$0.003 \pm 0.015 \pm 0.003$	$0.003 \pm 0.004 \pm 0.001$
0.624	$0.005 \pm 0.018 \pm 0.005$	$-0.004 \pm 0.005 \pm 0.001$
0.674	$-0.003 \pm 0.022 \pm 0.005$	$-0.002 \pm 0.007 \pm 0.002$
0.723	$0.003 \pm 0.027 \pm 0.005$	$-0.004 \pm 0.008 \pm 0.003$
0.773	$0.006 \pm 0.035 \pm 0.008$	$0.005 \pm 0.010 \pm 0.002$
0.823	$0.028 \pm 0.047 \pm 0.014$	$-0.044 \pm 0.014 \pm 0.004$
0.873	$0.015 \pm 0.062 \pm 0.017$	$-0.008 \pm 0.019 \pm 0.007$

E.2.2 Systematic Errors

This section lists the systematic uncertainties assigned to the double-spin asymmetries $A_{\parallel}$ and $A_{\perp}$ on ^{3}He. The systematic error depends upon the electron beam polarization P_b, the target polarization P_b, the nitrogen dilution factor D_{N_2}, and contaminations in the BigBite analysis due to π^- (f_1), π^+ (f_2), and e^+ (f_3). Also given are errors due to the electron selection cuts (Cuts) and the radiative corrections (RC). Each quantity was varied to within their uncertainties and the observed change in the asymmetry was taken as the error reported here. The final column (Total) is the in-quadrature sum of each column. All errors listed are absolute. A more detailed discussion of the systematic errors may be found in [169].

Table E.21: Systematic uncertainties assigned to $A_{\parallel}^{^3\mathrm{He}}$ at an incident beam energy of 4.74 GeV.

$< x >$	P_b	P_t	D_{N_2}	f_1	f_2	f_3	Cuts	RC	Total
0.277	0.00100	0.00170	0.00010	0.00000	0.000000	0.00110	0.00671	0.00025	0.00708
0.325	0.00060	0.00100	0.00010	0.00000	0.000000	0.00050	0.00231	0.00022	0.00265
0.374	0.00010	0.00020	0.00000	0.00000	0.000000	0.00040	0.00175	0.00013	0.00181
0.424	0.00100	0.00170	0.00010	0.00000	0.000000	0.00000	0.00444	0.00037	0.00487
0.473	0.00080	0.00140	0.00010	0.00000	0.000000	0.00000	0.00292	0.00031	0.00335
0.523	0.00010	0.00010	0.00000	0.00000	0.000000	0.00010	0.00201	0.00005	0.00202
0.574	0.00020	0.00030	0.00000	0.00000	0.000000	0.00010	0.00438	0.00009	0.00440
0.623	0.00110	0.00180	0.00010	0.00000	0.000000	0.00010	0.00233	0.00043	0.00318
0.673	0.00090	0.00160	0.00010	0.00000	0.000000	0.00000	0.00423	0.00038	0.00463
0.723	0.00120	0.00190	0.00010	0.00000	0.000000	0.00000	0.00617	0.00047	0.00658
0.773	0.00050	0.00090	0.00000	0.00000	0.000000	0.00000	0.01298	0.00019	0.01302
0.823	0.00130	0.00220	0.00010	0.00000	0.000000	0.00000	0.01128	0.00050	0.01158
0.874	0.00050	0.00080	0.00000	0.00000	0.000000	0.00000	0.01702	0.00022	0.01704

Table E.22: Systematic uncertainties assigned to $A_{\perp}^{^3\mathrm{He}}$ at an incident beam energy of 4.74 GeV.

$< x >$	P_b	P_t	D_{N_2}	f_1	f_2	f_3	Cuts	RC	Total
0.277	0.00030	0.00050	0.00010	0.00000	0.000000	0.00020	0.00252	0.00010	0.00259
0.325	0.00020	0.00040	0.00000	0.00000	0.000000	0.00010	0.00161	0.00011	0.00167
0.374	0.00060	0.00100	0.00010	0.00000	0.000000	0.00010	0.00197	0.00018	0.00230
0.424	0.00020	0.00040	0.00000	0.00000	0.000000	0.00000	0.00150	0.00007	0.00157
0.473	0.00030	0.00050	0.00000	0.00000	0.000000	0.00000	0.00072	0.00009	0.00093
0.523	0.00030	0.00050	0.00000	0.00000	0.000000	0.00000	0.00108	0.00010	0.00123
0.574	0.00040	0.00060	0.00000	0.00000	0.000000	0.00000	0.00220	0.00013	0.00231
0.623	0.00020	0.00030	0.00000	0.00000	0.000000	0.00000	0.00233	0.00008	0.00236
0.673	0.00020	0.00030	0.00000	0.00000	0.000000	0.00000	0.00304	0.00007	0.00307
0.723	0.00060	0.00100	0.00010	0.00000	0.000000	0.00000	0.00208	0.00021	0.00240
0.773	0.00100	0.00180	0.00010	0.00000	0.000000	0.00000	0.00415	0.00038	0.00466
0.823	0.00020	0.00030	0.00000	0.00000	0.000000	0.00000	0.00581	0.00008	0.00583
0.874	0.00200	0.00350	0.00020	0.00000	0.000000	0.00000	0.00398	0.00074	0.00572

Table E.23: Systematic uncertainties assigned to $A_{\parallel}^{^3\mathrm{He}}$ at an incident beam energy of 5.89 GeV.

$< x >$	P_b	P_t	D_{N_2}	f_1	f_2	f_3	Cuts	RC	Total
0.277	0.00020	0.00060	0.00010	0.00000	0.000100	0.00350	0.00943	0.00036	0.01009
0.325	0.00050	0.00120	0.00010	0.00000	0.000000	0.00010	0.00316	0.00028	0.00343
0.374	0.00020	0.00040	0.00000	0.00000	0.000000	0.00010	0.00225	0.00012	0.00229
0.424	0.00060	0.00130	0.00010	0.00000	0.000000	0.00010	0.00224	0.00031	0.00268
0.474	0.00060	0.00130	0.00010	0.00000	0.000000	0.00000	0.00600	0.00031	0.00618
0.524	0.00010	0.00020	0.00000	0.00000	0.000000	0.00000	0.00225	0.00004	0.00226
0.573	0.00010	0.00030	0.00000	0.00000	0.000000	0.00000	0.00327	0.00007	0.00329
0.624	0.00010	0.00030	0.00000	0.00000	0.000000	0.00000	0.00540	0.00010	0.00541
0.674	0.00010	0.00020	0.00000	0.00000	0.000000	0.00000	0.00488	0.00009	0.00489
0.723	0.00010	0.00030	0.00000	0.00000	0.000000	0.00000	0.00472	0.00008	0.00473
0.773	0.00020	0.00010	0.00000	0.00000	0.000000	0.00000	0.00793	0.00011	0.00793
0.823	0.00080	0.00200	0.00010	0.00000	0.000000	0.00000	0.01382	0.00042	0.01400
0.873	0.00040	0.00140	0.00000	0.00000	0.000000	0.00000	0.01662	0.00022	0.01668

Table E.24: Systematic uncertainties assigned to $A_{\perp}^{^3\mathrm{He}}$ at an incident beam energy of 5.89 GeV.

$< x >$	P_b	P_t	D_{N_2}	f_1	f_2	f_3	Cuts	RC	Total
0.277	0.00030	0.00070	0.00000	0.00000	0.000000	0.00200	0.00226	0.00018	0.00313
0.325	0.00010	0.00030	0.00000	0.00000	0.000000	0.00040	0.00117	0.00011	0.00127
0.374	0.00020	0.00040	0.00000	0.00000	0.000000	0.00010	0.00026	0.00008	0.00054
0.424	0.00020	0.00050	0.00000	0.00000	0.000000	0.00000	0.00130	0.00009	0.00140
0.474	0.00010	0.00020	0.00000	0.00000	0.000000	0.00000	0.00096	0.00004	0.00098
0.524	0.00000	0.00010	0.00000	0.00000	0.000000	0.00000	0.00117	0.00004	0.00117
0.573	0.00000	0.00010	0.00000	0.00000	0.000000	0.00000	0.00131	0.00005	0.00132
0.624	0.00010	0.00030	0.00000	0.00000	0.000000	0.00000	0.00077	0.00006	0.00083
0.674	0.00010	0.00020	0.00000	0.00000	0.000000	0.00000	0.00200	0.00003	0.00202
0.723	0.00010	0.00030	0.00000	0.00000	0.000000	0.00000	0.00290	0.00007	0.00292
0.773	0.00010	0.00030	0.00000	0.00000	0.000000	0.00000	0.00242	0.00007	0.00244
0.823	0.00120	0.00300	0.00020	0.00000	0.000000	0.00000	0.00293	0.00065	0.00441
0.873	0.00020	0.00060	0.00000	0.00000	0.000000	0.00000	0.00683	0.00012	0.00686

E.3 A_1

E.3.1 ^{3}He and the Neutron

The results for $A_1^{^3\mathrm{He}}$ for $E = 4.74\,\mathrm{GeV}$ and $5.89\,\mathrm{GeV}$ are given in Tables E.25 and E.26, respectively. The rebinned resonance results for each beam energy are given in Tables E.27 and E.28. The errors listed are statistical and systematic, respectively. All errors are absolute.

The neutron results in the DIS region are given in Tables E.29 and E.30 for the $E = 4.74\,\mathrm{GeV}$ and $5.89\,\mathrm{GeV}$ data, respectively. The average Q^2 for the $E = 4.74\,\mathrm{GeV}$ and $5.89\,\mathrm{GeV}$ DIS data are $\langle Q^2 \rangle = 2.59\,\mathrm{GeV}^2$ and $3.67\,\mathrm{GeV}^2$, respectively. The averaged DIS results are given in Table E.31, where $\langle Q^2 \rangle = 3.08\,\mathrm{GeV}^2$. The neutron results in the resonance region are given in Tables E.32 and E.33 for $E = 4.74\,\mathrm{GeV}$ with $\langle Q^2 \rangle = 3.89\,\mathrm{GeV}^2$ and $E = 5.89\,\mathrm{GeV}$ and $\langle Q^2 \rangle = 5.58\,\mathrm{GeV}^2$, respectively. The averaged resonance results are given in Table E.34, where $\langle Q^2 \rangle = 4.76\,\mathrm{GeV}^2$. The errors listed are statistical and systematic, respectively. All errors are absolute.

Table E.25: Results for $A_1^{^3\mathrm{He}}$ $E = 4.74\,\mathrm{GeV}$. The two uncertainties represent the statistical and systematic uncertainties, respectively.

$< x >$	$A_1^{^3\mathrm{He}}$
0.277	-0.008 $\pm$ 0.017 $\pm$ 0.004
0.325	-0.010 $\pm$ 0.010 $\pm$ 0.001
0.374	0.008 $\pm$ 0.008 $\pm$ 0.001
0.424	-0.027 $\pm$ 0.008 $\pm$ 0.003
0.473	-0.022 $\pm$ 0.009 $\pm$ 0.002
0.523	0.004 $\pm$ 0.010 $\pm$ 0.001
0.574	0.008 $\pm$ 0.012 $\pm$ 0.002
0.623	0.031 $\pm$ 0.015 $\pm$ 0.002
0.673	0.030 $\pm$ 0.018 $\pm$ 0.003
0.723	0.041 $\pm$ 0.022 $\pm$ 0.004
0.773	-0.005 $\pm$ 0.028 $\pm$ 0.008
0.823	-0.041 $\pm$ 0.037 $\pm$ 0.007
0.874	0.004 $\pm$ 0.048 $\pm$ 0.010

Table E.26: Results for $A_1^{^3\mathrm{He}}$ for $E = 5.89$ GeV. The two uncertainties represent the statistical and systematic uncertainties, respectively.

$< x >$	$A_1^{^3\mathrm{He}}$
0.277	$0.020 \pm 0.029 \pm 0.006$
0.325	$-0.019 \pm 0.013 \pm 0.002$
0.374	$-0.006 \pm 0.010 \pm 0.001$
0.424	$-0.021 \pm 0.010 \pm 0.002$
0.474	$-0.022 \pm 0.011 \pm 0.003$
0.524	$0.002 \pm 0.013 \pm 0.001$
0.573	$0.003 \pm 0.016 \pm 0.002$
0.624	$0.006 \pm 0.020 \pm 0.003$
0.674	$-0.003 \pm 0.024 \pm 0.003$
0.723	$0.004 \pm 0.031 \pm 0.003$
0.773	$0.005 \pm 0.039 \pm 0.004$
0.823	$0.045 \pm 0.053 \pm 0.008$
0.873	$0.020 \pm 0.072 \pm 0.009$

Table E.27: Rebinned resonance results for $A_1^{^3\mathrm{He}}$ at $E = 4.74$ GeV. The two uncertainties represent the statistical and systematic uncertainties, respectively.

$< x >$	$A_1^{^3\mathrm{He}}$
0.548	$0.006 \pm 0.008 \pm 0.002$
0.648	$0.031 \pm 0.011 \pm 0.002$
0.748	$0.024 \pm 0.018 \pm 0.006$

Table E.28: Rebinned resonance results for $A_1^{^3\mathrm{He}}$ at $E = 5.89$ GeV. The two uncertainties represent the statistical and systematic uncertainties, respectively.

$< x >$	$A_1^{^3\mathrm{He}}$
0.648	$0.003 \pm 0.015 \pm 0.003$
0.749	$0.005 \pm 0.024 \pm 0.004$

Table E.29: DIS results for A_1^n at $E = 4.74$ GeV. The two uncertainties represent the statistical and systematic uncertainties, respectively.

$< x >$	A_1^n
0.277	$0.012 \pm 0.071 \pm 0.008$
0.325	$0.010 \pm 0.043 \pm 0.009$
0.374	$0.102 \pm 0.037 \pm 0.013$
0.424	$-0.065 \pm 0.040 \pm 0.014$
0.473	$-0.045 \pm 0.051 \pm 0.015$

Table E.30: DIS results for A_1^n at $E = 5.89$ GeV. The two uncertainties represent the statistical and systematic uncertainties, respectively.

$< x >$	A_1^n
0.277	$0.126 \pm 0.116 \pm 0.035$
0.325	$-0.031 \pm 0.058 \pm 0.009$
0.374	$0.035 \pm 0.049 \pm 0.010$
0.424	$-0.040 \pm 0.053 \pm 0.012$
0.474	$-0.045 \pm 0.066 \pm 0.016$
0.524	$0.108 \pm 0.088 \pm 0.018$
0.573	$0.134 \pm 0.126 \pm 0.023$

Table E.31: DIS results for A_1^n averaged over the two beam energies, where $\langle Q^2 \rangle = 3.08\,\text{GeV}^2$. The two uncertainties represent the statistical and systematic uncertainties, respectively.

$< x >$	A_1^n
0.277	$0.043 \pm 0.060 \pm 0.021$
0.325	$-0.004 \pm 0.035 \pm 0.009$
0.374	$0.078 \pm 0.029 \pm 0.012$
0.424	$-0.056 \pm 0.032 \pm 0.013$
0.474	$-0.045 \pm 0.040 \pm 0.016$
0.548	$0.116 \pm 0.072 \pm 0.021$

Table E.32: Resonance results for A_1^n at $E = 4.74$ GeV. The two uncertainties represent the statistical and systematic uncertainties, respectively.

$< x >$	A_1^n
0.548	$0.146 \pm 0.056 \pm 0.021$
0.648	$0.470 \pm 0.126 \pm 0.034$
0.748	$0.615 \pm 0.348 \pm 0.112$

Table E.33: Resonance results for A_1^n at $E = 5.89$ GeV. The two uncertainties represent the statistical and systematic uncertainties, respectively.

$< x >$	A_1^n
0.648	$0.156 \pm 0.152 \pm 0.027$
0.749	$0.230 \pm 0.416 \pm 0.066$

Table E.34: Resonance results for A_1^n averaged over the two beam energies, where $\langle Q^2 \rangle = 4.76\,\text{GeV}^2$. The two uncertainties represent the statistical and systematic uncertainties, respectively.

$< x >$	A_1^n
0.548	$0.146 \pm 0.057 \pm 0.020$
0.648	$0.342 \pm 0.094 \pm 0.029$
0.748	$0.466 \pm 0.264 \pm 0.095$

E.3.2 Systematic Errors

The systematic errors, broken down into their components, for the ^{3}He results are given in Tables E.35 and E.36. for the $E = 4.74\,\text{GeV}$ and $5.89\,\text{GeV}$ data, respectively. The column labeled $A_\parallel$ ($A_\perp$) gives the errors due to the parallel (perpendicular) asymmetry, and the column labeled "Kin." gives the errors due to the kinematic variables, including the uncertainty on the function R. The final column labeled "Total" gives the in-quadrature sum of these errors.

The neutron systematic errors in the DIS region are given in Tables E.37 and E.38; the errors for the resonance data are given in Tables E.39 and E.40 for the $E = 4.74\,\text{GeV}$ and $5.89\,\text{GeV}$ data, respectively. The column labeled $F_2^{n,p}$ gives the errors due to the F_2^n and F_2^p structure function, and the column labeled $F_2^{^3\text{He}}$ gives the errors due to the $F_2^{^3\text{He}}$ structure function. The column labeled P_p (P_n) gives the error due to the effective polarization of the proton (neutron). The columns labeled A_1^p and $A_1^{^3\text{He}}$ give the errors due to our fit to the A_1^p data, and our measured $A_1^{^3\text{He}}$ data, respectively. The in-quadrature sum of all components gives the last column, labeled "Total."

Table E.35: Systematic errors for $A_1^{^3\text{He}}$ data at $E = 4.74\,\text{GeV}$.

$< x >$	$A_\parallel$	$A_\perp$	Kin.	Total
0.277	0.00385	0.00019	0.00012	0.00386
0.325	0.00148	0.00014	0.00007	0.00148
0.374	0.00099	0.00021	0.00054	0.00115
0.424	0.00265	0.00017	0.00012	0.00266
0.473	0.00184	0.00011	0.00019	0.00185
0.523	0.00110	0.00016	0.00019	0.00113
0.574	0.00243	0.00033	0.00020	0.00246
0.623	0.00184	0.00036	0.00014	0.00188
0.673	0.00262	0.00050	0.00013	0.00267
0.723	0.00377	0.00044	0.00020	0.00380
0.773	0.00751	0.00089	0.00039	0.00757
0.823	0.00700	0.00118	0.00032	0.00710
0.874	0.01019	0.00125	0.00196	0.01045

Table E.36: Systematic errors for $A_1^{^3\mathrm{He}}$ data at $E = 5.89$ GeV.

$< x >$	$A_\parallel$	$A_\perp$	Kin.	Total
0.277	0.00552	0.00018	0.00059	0.00555
0.325	0.00185	0.00009	0.00024	0.00187
0.374	0.00123	0.00004	0.00004	0.00123
0.424	0.00151	0.00011	0.00022	0.00153
0.474	0.00327	0.00009	0.00004	0.00327
0.524	0.00120	0.00012	0.00001	0.00121
0.573	0.00180	0.00014	0.00013	0.00181
0.624	0.00312	0.00010	0.00016	0.00313
0.674	0.00277	0.00027	0.00007	0.00278
0.723	0.00274	0.00039	0.00013	0.00277
0.773	0.00443	0.00035	0.00011	0.00445
0.823	0.00787	0.00071	0.00066	0.00793
0.873	0.00927	0.00117	0.00014	0.00934

Table E.37: Systematic errors for DIS results for A_1^n at $E = 4.74$ GeV.

$< x >$	$F_2^{n,p}$	$F_2^{^3\mathrm{He}}$	P_p	P_n	A_1^p	$A_1^{^3\mathrm{He}}$	Total
0.277	0.00273	0.00070	0.00516	0.00015	0.00423	0.00268	0.00773
0.325	0.00269	0.00101	0.00616	0.00012	0.00506	0.00185	0.00867
0.374	0.00690	0.00065	0.00720	0.00169	0.00606	0.00637	0.01342
0.424	0.00598	0.00181	0.00831	0.00119	0.00689	0.00639	0.01407
0.473	0.00574	0.00171	0.00957	0.00085	0.00800	0.00528	0.01483

Table E.38: Systematic errors for DIS A_1^n results at $E = 5.89$ GeV.

$< x >$	$F_2^{n,p}$	$F_2^{^3\mathrm{He}}$	P_p	P_n	A_1^p	$A_1^{^3\mathrm{He}}$	Total
0.277	0.00450	0.00040	0.00514	0.00207	0.00464	0.03370	0.03476
0.325	0.00244	0.00131	0.00614	0.00059	0.00495	0.00306	0.00892
0.374	0.00265	0.00064	0.00719	0.00052	0.00598	0.00147	0.00986
0.424	0.00290	0.00212	0.00830	0.00074	0.00675	0.00374	0.01192
0.474	0.00394	0.00135	0.00956	0.00084	0.00766	0.00975	0.01622
0.524	0.00995	0.00000	0.01096	0.00172	0.00978	0.00505	0.01853
0.573	0.01300	0.00015	0.01247	0.00214	0.01223	0.00800	0.02330

Table E.39: Systematic errors for resonance A_1^n results at $E = 4.74$ GeV.

$< x >$	$F_2^{n,p}$	$F_2^{^3\mathrm{He}}$	P_p	P_n	A_1^p	$A_1^{^3\mathrm{He}}$	Total
0.548	0.01230	0.00005	0.01234	0.00253	0.01052	0.00642	0.02149
0.648	0.02150	0.00010	0.01546	0.00812	0.01539	0.01245	0.03405
0.748	0.09145	0.00270	0.01792	0.01062	0.02117	0.05642	0.11152

Table E.40: Systematic errors for resonance A_1^n results at $E = 5.89$ GeV.

$< x >$	$F_2^{n,p}$	$F_2^{^3\mathrm{He}}$	P_p	P_n	A_1^p	$A_1^{^3\mathrm{He}}$	Total
0.648	0.00550	0.00035	0.01469	0.00260	0.01637	0.01469	0.02714
0.749	0.05210	0.00075	0.01695	0.00379	0.02141	0.03044	0.06634

E.4 A_2

E.4.1 ^{3}He

The results for $A_2^{^3\mathrm{He}}$ for $E = 4.74\,\mathrm{GeV}$ and $5.89\,\mathrm{GeV}$ are given in Tables E.41 and E.42, respectively. The errors listed are statistical and systematic, respectively. All errors are absolute.

Table E.41: Results for $A_2^{^3\mathrm{He}}$ $E = 4.74\,\mathrm{GeV}$. The two uncertainties represent the statistical and systematic uncertainties, respectively.

$< x >$	$A_2^{^3\mathrm{He}}$
0.277	-0.005 $\pm$ 0.014 $\pm$ 0.002
0.325	-0.004 $\pm$ 0.008 $\pm$ 0.001
0.374	-0.016 $\pm$ 0.006 $\pm$ 0.005
0.424	-0.011 $\pm$ 0.006 $\pm$ 0.002
0.473	-0.014 $\pm$ 0.007 $\pm$ 0.001
0.523	-0.008 $\pm$ 0.008 $\pm$ 0.002
0.574	-0.010 $\pm$ 0.009 $\pm$ 0.002
0.623	0.019 $\pm$ 0.011 $\pm$ 0.002
0.673	0.004 $\pm$ 0.013 $\pm$ 0.002
0.723	-0.007 $\pm$ 0.016 $\pm$ 0.002
0.773	-0.042 $\pm$ 0.021 $\pm$ 0.005
0.823	-0.009 $\pm$ 0.027 $\pm$ 0.005
0.874	-0.079 $\pm$ 0.036 $\pm$ 0.010

Table E.42: Results for $A_2^{^3\mathrm{He}}$ for $E = 5.89$ GeV. The two uncertainties represent the statistical and systematic uncertainties, respectively.

$< x >$	$A_2^{^3\mathrm{He}}$
0.277	$0.022 \pm 0.016 \pm 0.010$
0.325	$0.004 \pm 0.007 \pm 0.003$
0.374	$-0.002 \pm 0.005 \pm 0.001$
0.424	$-0.011 \pm 0.005 \pm 0.002$
0.474	$-0.006 \pm 0.006 \pm 0.001$
0.524	$0.001 \pm 0.007 \pm 0.001$
0.573	$0.005 \pm 0.008 \pm 0.002$
0.624	$-0.004 \pm 0.010 \pm 0.001$
0.674	$-0.004 \pm 0.012 \pm 0.002$
0.723	$-0.005 \pm 0.016 \pm 0.002$
0.773	$0.009 \pm 0.020 \pm 0.002$
0.823	$-0.053 \pm 0.028 \pm 0.005$
0.873	$-0.006 \pm 0.038 \pm 0.006$

E.4.2 Systematic Errors

The systematic errors, broken down into their components, for the ^{3}He results are given in Tables E.43 and E.44. for the $E = 4.74\,\text{GeV}$ and $5.89\,\text{GeV}$ data, respectively. The column labeled $A_\parallel$ ($A_\perp$) gives the errors due to the parallel (perpendicular) asymmetry, and the column labeled "Kin." gives the errors due to the kinematic variables, including the uncertainty on the function R. The final column labeled "Total" gives the in-quadrature sum of these errors.

Table E.43: Systematic errors for $A_2^{^3\text{He}}$ data at $E = 4.74\,\text{GeV}$.

$< x >$	$A_\parallel$	$A_\perp$	Kin.	Total
0.277	0.00077	0.00221	0.00133	0.00269
0.325	0.00032	0.00132	0.00068	0.00152
0.374	0.00024	0.00178	0.00449	0.00483
0.424	0.00071	0.00124	0.00086	0.00167
0.473	0.00052	0.00070	0.00124	0.00152
0.523	0.00035	0.00091	0.00104	0.00142
0.574	0.00081	0.00179	0.00099	0.00220
0.623	0.00063	0.00172	0.00040	0.00188
0.673	0.00097	0.00223	0.00010	0.00244
0.723	0.00143	0.00174	0.00037	0.00228
0.773	0.00304	0.00337	0.00165	0.00483
0.823	0.00282	0.00428	0.00058	0.00517
0.874	0.00452	0.00412	0.00698	0.00928

Table E.44: Systematic errors for $A_2^{^3\text{He}}$ data at $E = 5.89\,\text{GeV}$.

$< x >$	$A_\parallel$	$A_\perp$	Kin.	Total
0.277	0.00094	0.00266	0.00893	0.00937
0.325	0.00035	0.00109	0.00317	0.00337
0.374	0.00026	0.00045	0.00049	0.00072
0.424	0.00033	0.00118	0.00208	0.00242
0.474	0.00084	0.00077	0.00021	0.00116
0.524	0.00032	0.00086	0.00008	0.00092
0.573	0.00048	0.00099	0.00086	0.00140
0.624	0.00085	0.00062	0.00093	0.00141
0.674	0.00085	0.00150	0.00037	0.00176
0.723	0.00085	0.00220	0.00067	0.00245
0.773	0.00151	0.00173	0.00053	0.00236
0.823	0.00280	0.00327	0.00275	0.00511
0.873	0.00360	0.00515	0.00013	0.00629

E.5 g_1/F_1

E.5.1 ^{3}He and the Neutron

The results for $A_1^{^3\mathrm{He}}$ for $E = 4.74$ GeV and 5.89 GeV are given in Tables E.45 and E.46, respectively. The rebinned resonance data for the two beam energies are given in Tables E.47 and E.48. The errors listed are statistical and systematic, respectively. All errors are absolute.

The neutron results in the DIS region are given in Tables E.49 and E.50 for $E = 4.74$ GeV with $\langle Q^2 \rangle = 2.59\,\mathrm{GeV}^2$ and 5.89 GeV with $\langle Q^2 \rangle = 3.67\,\mathrm{GeV}^2$, respectively; the averaged results over these two data sets is given in Table E.51, where $\langle Q^2 \rangle = 3.08\,\mathrm{GeV}^2$. The neutron results in the resonance region are given in Tables E.52 and E.53 for $E = 4.74$ GeV with $\langle Q^2 \rangle = 3.89\,\mathrm{GeV}^2$ and 5.89 GeV with $\langle Q^2 \rangle = 5.58\,\mathrm{GeV}^2$, respectively. The averaged resonance results are given in Table E.54, where $\langle Q^2 \rangle = 4.76\,\mathrm{GeV}^2$. The errors listed are statistical and systematic, respectively. All errors are absolute.

Table E.45: Results for $g_1^{^3\mathrm{He}}/F_1^{^3\mathrm{He}}$ for $E = 4.74$ GeV. The two uncertainties represent the statistical and systematic uncertainties, respectively.

$< x >$	$g_1^{^3\mathrm{He}}/F_1^{^3\mathrm{He}}$
0.277	-0.009 $\pm$ 0.016 $\pm$ 0.004
0.325	-0.010 $\pm$ 0.009 $\pm$ 0.001
0.374	0.001 $\pm$ 0.007 $\pm$ 0.001
0.424	-0.026 $\pm$ 0.007 $\pm$ 0.002
0.473	-0.023 $\pm$ 0.008 $\pm$ 0.002
0.523	0.000 $\pm$ 0.009 $\pm$ 0.001
0.574	0.002 $\pm$ 0.011 $\pm$ 0.002
0.623	0.031 $\pm$ 0.013 $\pm$ 0.002
0.673	0.023 $\pm$ 0.016 $\pm$ 0.002
0.723	0.026 $\pm$ 0.020 $\pm$ 0.003
0.773	-0.023 $\pm$ 0.025 $\pm$ 0.007
0.823	-0.032 $\pm$ 0.032 $\pm$ 0.006
0.874	-0.035 $\pm$ 0.041 $\pm$ 0.009

Table E.46: Results for $g_1^{^3\mathrm{He}}/F_1^{^3\mathrm{He}}$ for $E = 5.89$ GeV. The two uncertainties represent the statistical and systematic uncertainties, respectively.

$< x >$	$g_1^{^3\mathrm{He}}/F_1^{^3\mathrm{He}}$
0.277	$0.024 \pm 0.028 \pm 0.006$
0.325	$-0.016 \pm 0.012 \pm 0.002$
0.374	$-0.006 \pm 0.009 \pm 0.001$
0.424	$-0.022 \pm 0.009 \pm 0.002$
0.474	$-0.021 \pm 0.010 \pm 0.003$
0.524	$0.002 \pm 0.012 \pm 0.001$
0.573	$0.004 \pm 0.015 \pm 0.002$
0.624	$0.003 \pm 0.018 \pm 0.003$
0.674	$-0.004 \pm 0.022 \pm 0.002$
0.723	$0.001 \pm 0.028 \pm 0.003$
0.773	$0.008 \pm 0.035 \pm 0.004$
0.823	$0.009 \pm 0.047 \pm 0.013$
0.873	$0.011 \pm 0.064 \pm 0.009$

Table E.47: Rebinned resonance results for $g_1^{^3\mathrm{He}}/F_1^{^3\mathrm{He}}$ at $E = 4.74$ GeV. The two uncertainties represent the statistical and systematic uncertainties, respectively.

$< x >$	$g_1^{^3\mathrm{He}}/F_1^{^3\mathrm{He}}$
0.548	$0.001 \pm 0.007 \pm 0.002$
0.648	$0.028 \pm 0.010 \pm 0.002$
0.748	$0.007 \pm 0.015 \pm 0.005$

Table E.48: Rebinned resonance results for $g_1^{^3\mathrm{He}}/F_1^{^3\mathrm{He}}$ at $E = 5.89$ GeV. The two uncertainties represent the statistical and systematic uncertainties, respectively.

$< x >$	$g_1^{^3\mathrm{He}}/F_1^{^3\mathrm{He}}$
0.648	$0.000 \pm 0.014 \pm 0.003$
0.749	$0.004 \pm 0.022 \pm 0.003$

Table E.49: DIS results for g_1^n/F_1^n at $E = 4.74$ GeV. The two uncertainties represent the statistical and systematic uncertainties, respectively.

$< x >$	g_1^n/F_1^n
0.277	$0.007 \pm 0.068 \pm 0.010$
0.325	$0.008 \pm 0.041 \pm 0.008$
0.374	$0.065 \pm 0.034 \pm 0.011$
0.424	$-0.066 \pm 0.038 \pm 0.013$
0.473	$-0.058 \pm 0.047 \pm 0.014$

Table E.50: DIS results for g_1^n/F_1^n at $E = 5.89$ GeV. The two uncertainties represent the statistical and systematic uncertainties, respectively.

$< x >$	g_1^n/F_1^n
0.277	$0.143 \pm 0.112 \pm 0.014$
0.325	$-0.019 \pm 0.056 \pm 0.009$
0.374	$0.031 \pm 0.046 \pm 0.009$
0.424	$-0.049 \pm 0.050 \pm 0.012$
0.474	$-0.044 \pm 0.062 \pm 0.015$
0.524	$0.098 \pm 0.082 \pm 0.017$
0.573	$0.132 \pm 0.116 \pm 0.021$

Table E.51: DIS results for g_1^n/F_1^n averaged over the two beam energies, where $\langle Q^2 \rangle = 3.08\,\text{GeV}^2$. The two uncertainties represent the statistical and systematic uncertainties, respectively.

$< x >$	g_1^n/F_1^n
0.277	$0.044 \pm 0.058 \pm 0.012$
0.325	$-0.002 \pm 0.033 \pm 0.009$
0.374	$0.053 \pm 0.028 \pm 0.010$
0.424	$-0.060 \pm 0.030 \pm 0.012$
0.474	$-0.053 \pm 0.037 \pm 0.015$
0.548	$0.110 \pm 0.067 \pm 0.019$

Table E.52: Resonance results for g_1^n/F_1^n at $E = 4.74$ GeV. The two uncertainties represent the statistical and systematic uncertainties, respectively.

$< x >$	g_1^n/F_1^n
0.548	$0.098 \pm 0.051 \pm 0.017$
0.648	$0.422 \pm 0.113 \pm 0.030$
0.748	$0.256 \pm 0.304 \pm 0.071$

Table E.53: Resonance results for g_1^n/F_1^n at $E = 5.89$ GeV. The two uncertainties represent the statistical and systematic uncertainties, respectively.

$< x >$	g_1^n/F_1^n
0.648	$0.116 \pm 0.138 \pm 0.024$
0.749	$0.183 \pm 0.374 \pm 0.056$

Table E.54: Resonance results for g_1^n/F_1^n averaged over the two beam energies, where $\langle Q^2 \rangle = 4.76\,\text{GeV}^2$. The two uncertainties represent the statistical and systematic uncertainties, respectively.

$< x >$	g_1^n/F_1^n
0.548	$0.098 \pm 0.052 \pm 0.017$
0.648	$0.300 \pm 0.084 \pm 0.026$
0.748	$0.228 \pm 0.234 \pm 0.063$

E.5.2 Systematic Errors

The breakdown of the systematic errors for g_1/F_1 on ^{3}He are given in Tables E.55 and E.56. The errors on the DIS neutron results are given in Tables E.57 and E.58. The resonance neutron errors are given in Tables E.59 and E.60. The description of the various columns is the same as in Appendix E.3.2.

Table E.55: Systematic errors for $g_1^{^3\mathrm{He}}/F_1^{^3\mathrm{He}}$ data at E = 4.74 GeV.

$< x >$	$A_\parallel$	$A_\perp$	Kin.	Total
0.277	0.00368	0.00053	0.00004	0.00372
0.325	0.00134	0.00035	0.00004	0.00138
0.374	0.00092	0.00049	0.00004	0.00104
0.424	0.00256	0.00033	0.00013	0.00258
0.473	0.00171	0.00020	0.00011	0.00172
0.523	0.00103	0.00026	0.00002	0.00106
0.574	0.00220	0.00047	0.00003	0.00226
0.623	0.00161	0.00050	0.00017	0.00169
0.673	0.00243	0.00067	0.00014	0.00253
0.723	0.00335	0.00051	0.00020	0.00339
0.773	0.00641	0.00097	0.00016	0.00649
0.823	0.00576	0.00126	0.00028	0.00590
0.874	0.00859	0.00123	0.00032	0.00868

Table E.56: Systematic errors for $g_1^{^3\mathrm{He}}/F_1^{^3\mathrm{He}}$ data at E = 5.89 GeV.

$< x >$	$A_\parallel$	$A_\perp$	Kin.	Total
0.277	0.00532	0.00257	0.00005	0.00591
0.325	0.00172	0.00107	0.00004	0.00203
0.374	0.00117	0.00019	0.00001	0.00119
0.424	0.00135	0.00095	0.00004	0.00165
0.474	0.00316	0.00011	0.00005	0.00316
0.524	0.00120	0.00011	0.00000	0.00120
0.573	0.00164	0.00068	0.00001	0.00178
0.624	0.00272	0.00091	0.00002	0.00287
0.674	0.00242	0.00044	0.00001	0.00246
0.723	0.00237	0.00107	0.00002	0.00260
0.773	0.00390	0.00112	0.00004	0.00406
0.823	0.00709	0.01068	0.00018	0.01282
0.873	0.00848	0.00203	0.00010	0.00872

Table E.57: Systematic errors for DIS results for g_1^n/F_1^n at E = 4.74 GeV.

$< x >$	$F_2^{n,p}$	$F_2^{^3\mathrm{He}}$	P_p	P_n	g_1^p/F_1^p	$g_1^{^3\mathrm{He}}/F_1^{^3\mathrm{He}}$	Total
0.277	0.00253	0.00071	0.00532	0.00012	0.00327	0.00763	0.01021
0.325	0.00248	0.00098	0.00627	0.00013	0.00397	0.00306	0.00846
0.374	0.00564	0.00029	0.00723	0.00108	0.00492	0.00247	0.01075
0.424	0.00577	0.00173	0.00819	0.00110	0.00608	0.00636	0.01349
0.473	0.00602	0.00170	0.00924	0.00097	0.00737	0.00505	0.01433

Table E.58: Systematic errors for DIS results for g_1^n/F_1^n at E = 5.89 GeV.

$< x >$	$F_2^{n,p}$	$F_2^{^3\mathrm{He}}$	P_p	P_n	g_1^p/F_1^p	$g_1^{^3\mathrm{He}}/F_1^{^3\mathrm{He}}$	Total
0.277	0.00450	0.00045	0.00510	0.00245	0.00330	0.01193	0.01434
0.325	0.00218	0.00116	0.00603	0.00033	0.00408	0.00451	0.00892
0.374	0.00242	0.00062	0.00695	0.00053	0.00504	0.00292	0.00942
0.424	0.00311	0.00211	0.00789	0.00084	0.00608	0.00441	0.01156
0.474	0.00377	0.00126	0.00890	0.00076	0.00706	0.00917	0.01515
0.524	0.00915	0.00000	0.00998	0.00168	0.00893	0.00394	0.01678
0.573	0.01240	0.00015	0.01111	0.00228	0.01065	0.00714	0.02114

Table E.59: Systematic errors for resonance results for g_1^n/F_1^n at E = 4.74 GeV.

$< x >$	$F_2^{n,p}$	$F_2^{^3\mathrm{He}}$	P_p	P_n	g_1^p/F_1^p	$g_1^{^3\mathrm{He}}/F_1^{^3\mathrm{He}}$	Total
0.548	0.00879	0.00001	0.00954	0.00323	0.00953	0.00603	0.01749
0.648	0.01915	0.00010	0.01144	0.00676	0.01420	0.01161	0.02966
0.748	0.04305	0.00075	0.01255	0.00513	0.01881	0.05135	0.07091

Table E.60: Systematic errors for resonance results for g_1^n/F_1^n at E = 5.89 GeV.

$< x >$	$F_2^{n,p}$	$F_2^{^3\mathrm{He}}$	P_p	P_n	g_1^p/F_1^p	$g_1^{^3\mathrm{He}}/F_1^{^3\mathrm{He}}$	Total
0.648	0.00430	0.00010	0.01210	0.00437	0.01415	0.01339	0.02374
0.749	0.04170	0.00060	0.01327	0.00487	0.01999	0.02899	0.05638

E.6 g_2/F_1

E.6.1 ^{3}He

The results for $g_2^{^3\mathrm{He}}/F_1^{^3\mathrm{He}}$ for $E = 4.74$ GeV and 5.89 GeV are given in Tables E.61 and E.62, respectively. The errors listed are statistical and systematic, respectively. All errors are absolute.

Table E.61: Results for $g_2^{^3\mathrm{He}}/F_1^{^3\mathrm{He}}$ for $E = 4.74$ GeV. The two uncertainties represent the statistical and systematic uncertainties, respectively.

$< x >$	$g_2^{^3\mathrm{He}}/F_1^{^3\mathrm{He}}$
0.277	-0.006 $\pm$ 0.034 $\pm$ 0.006
0.325	-0.001 $\pm$ 0.017 $\pm$ 0.003
0.374	-0.037 $\pm$ 0.012 $\pm$ 0.004
0.424	0.002 $\pm$ 0.011 $\pm$ 0.002
0.473	-0.005 $\pm$ 0.011 $\pm$ 0.001
0.523	-0.015 $\pm$ 0.012 $\pm$ 0.002
0.574	-0.020 $\pm$ 0.013 $\pm$ 0.003
0.623	0.000 $\pm$ 0.014 $\pm$ 0.002
0.673	-0.017 $\pm$ 0.016 $\pm$ 0.003
0.723	-0.036 $\pm$ 0.019 $\pm$ 0.002
0.773	-0.039 $\pm$ 0.022 $\pm$ 0.004
0.823	0.018 $\pm$ 0.027 $\pm$ 0.005
0.874	-0.071 $\pm$ 0.033 $\pm$ 0.005

Table E.62: Results for $g_2^{^3\mathrm{He}}/F_1^{^3\mathrm{He}}$ for $E = 5.89\,\mathrm{GeV}$. The two uncertainties represent the statistical and systematic uncertainties, respectively.

$< x >$	$g_2^{^3\mathrm{He}}/F_1^{^3\mathrm{He}}$
0.277	$0.044 \pm 0.044 \pm 0.008$
0.325	$0.026 \pm 0.017 \pm 0.003$
0.374	$-0.001 \pm 0.012 \pm 0.001$
0.424	$-0.005 \pm 0.011 \pm 0.002$
0.474	$0.007 \pm 0.011 \pm 0.002$
0.524	$0.000 \pm 0.012 \pm 0.002$
0.573	$0.006 \pm 0.013 \pm 0.002$
0.624	$-0.011 \pm 0.015 \pm 0.001$
0.674	$-0.003 \pm 0.017 \pm 0.002$
0.723	$-0.010 \pm 0.021 \pm 0.003$
0.773	$0.007 \pm 0.025 \pm 0.003$
0.823	$-0.095 \pm 0.032 \pm 0.005$
0.873	$-0.020 \pm 0.041 \pm 0.007$

E.6.2 Systematic Errors

The breakdown of the systematic errors for g_2/F_1 on ^{3}He are given in Tables E.63 and E.64. The description of the various columns is the same as in Appendix E.3.2.

Table E.63: Systematic errors for $g_2^{^3\mathrm{He}}/F_1^{^3\mathrm{He}}$ data at E = 4.74 GeV.

$< x >$	$A_\parallel$	$A_\perp$	Kin.	Total
0.277	0.00154	0.00541	0.00008	0.00563
0.325	0.00056	0.00305	0.00004	0.00311
0.374	0.00038	0.00384	0.00039	0.00388
0.424	0.00093	0.00228	0.00005	0.00247
0.473	0.00064	0.00122	0.00011	0.00139
0.523	0.00037	0.00151	0.00017	0.00156
0.574	0.00082	0.00261	0.00024	0.00275
0.623	0.00055	0.00237	0.00008	0.00243
0.673	0.00083	0.00290	0.00017	0.00302
0.723	0.00111	0.00213	0.00041	0.00244
0.773	0.00220	0.00392	0.00058	0.00453
0.823	0.00189	0.00486	0.00022	0.00522
0.874	0.00268	0.00429	0.00110	0.00517

Table E.64: Systematic errors for $g_2^{^3\mathrm{He}}/F_1^{^3\mathrm{He}}$ data at E = 5.89 GeV.

$< x >$	$A_\parallel$	$A_\perp$	Kin.	Total
0.277	0.00225	0.00782	0.00044	0.00815
0.325	0.00075	0.00287	0.00017	0.00297
0.374	0.00049	0.00106	0.00002	0.00116
0.424	0.00054	0.00251	0.00010	0.00257
0.474	0.00123	0.00159	0.00001	0.00201
0.524	0.00044	0.00174	0.00000	0.00179
0.573	0.00064	0.00178	0.00007	0.00189
0.624	0.00105	0.00104	0.00010	0.00148
0.674	0.00090	0.00228	0.00004	0.00245
0.723	0.00086	0.00317	0.00011	0.00329
0.773	0.00142	0.00247	0.00010	0.00285
0.823	0.00255	0.00424	0.00112	0.00507
0.873	0.00290	0.00643	0.00023	0.00705

E.7 Flavor Separation

E.7.1 Polarized-to-Unpolarized Quark Ratios for u and d

The results for the polarized-to-unpolarized quark ratios $(\Delta u + \Delta\bar{u})/(u + \bar{u})$ and $(\Delta d + \Delta\bar{d})/(d + \bar{d})$ are given in Table E.65 for the $E = 4.74\,\text{GeV}$ data, while the results for $E = 5.89\,\text{GeV}$ are given in Table E.66. The average Q^2 of the two data sets was $2.59\,\text{GeV}^2$ and $3.67\,\text{GeV}^2$, respectively. The results averaged over the two data sets is given in Table E.67, where $\langle Q^2 \rangle = 3.08\,\text{GeV}^2$.

Table E.65: Results for $(\Delta u + \Delta\bar{u})/(u + \bar{u})$ and $(\Delta d + \Delta\bar{d})/(d + \bar{d})$ at $E = 4.74\,\text{GeV}$. The two uncertainties represent the statistical and systematic uncertainties, respectively.

$< x >$	$(\Delta u + \Delta\bar{u})/(u + \bar{u})$	$(\Delta d + \Delta\bar{d})/(d + \bar{d})$
0.277	$0.454 \pm 0.013 \pm 0.035$	$-0.225 \pm 0.110 \pm 0.029$
0.325	$0.504 \pm 0.008 \pm 0.041$	$-0.275 \pm 0.069 \pm 0.033$
0.374	$0.539 \pm 0.006 \pm 0.045$	$-0.230 \pm 0.060 \pm 0.039$
0.424	$0.601 \pm 0.006 \pm 0.052$	$-0.523 \pm 0.068 \pm 0.052$
0.473	$0.631 \pm 0.007 \pm 0.058$	$-0.585 \pm 0.088 \pm 0.066$

Table E.66: Results for $(\Delta u + \Delta\bar{u})/(u + \bar{u})$ and $(\Delta d + \Delta\bar{d})/(d + \bar{d})$ at $E = 5.89\,\text{GeV}$. The two uncertainties represent the statistical and systematic uncertainties, respectively.

$< x >$	$(\Delta u + \Delta\bar{u})/(u + \bar{u})$	$(\Delta d + \Delta\bar{d})/(d + \bar{d})$
0.277	$0.428 \pm 0.022 \pm 0.036$	$-0.006 \pm 0.182 \pm 0.028$
0.325	$0.508 \pm 0.010 \pm 0.040$	$-0.323 \pm 0.094 \pm 0.034$
0.374	$0.544 \pm 0.008 \pm 0.046$	$-0.293 \pm 0.081 \pm 0.040$
0.424	$0.597 \pm 0.008 \pm 0.051$	$-0.497 \pm 0.090 \pm 0.051$
0.474	$0.629 \pm 0.009 \pm 0.058$	$-0.567 \pm 0.116 \pm 0.068$
0.524	$0.635 \pm 0.012 \pm 0.064$	$-0.378 \pm 0.165 \pm 0.080$
0.573	$0.652 \pm 0.015 \pm 0.075$	$-0.398 \pm 0.250 \pm 0.104$

Table E.67: Results for $(\Delta u + \Delta\bar{u})/(u + \bar{u})$ and $(\Delta d + \Delta\bar{d})/(d + \bar{d})$ averaged over the two beam energies, where $\langle Q^2 \rangle = 3.08\,\mathrm{GeV}^2$. The two uncertainties represent the statistical and systematic uncertainties, respectively.

$< x >$	$(\Delta u + \Delta\bar{u})/(u + \bar{u})$	$(\Delta d + \Delta\bar{d})/(d + \bar{d})$
0.277	$0.447 \pm 0.011 \pm 0.035$	$-0.166 \pm 0.094 \pm 0.029$
0.325	$0.505 \pm 0.006 \pm 0.040$	$-0.292 \pm 0.055 \pm 0.033$
0.374	$0.541 \pm 0.005 \pm 0.046$	$-0.252 \pm 0.048 \pm 0.040$
0.424	$0.600 \pm 0.005 \pm 0.052$	$-0.514 \pm 0.054 \pm 0.051$
0.474	$0.631 \pm 0.006 \pm 0.058$	$-0.579 \pm 0.070 \pm 0.067$
0.548	$0.642 \pm 0.009 \pm 0.070$	$-0.384 \pm 0.138 \pm 0.092$

E.7.2 Systematic Errors

Tables E.68 and E.69 give a breakdown of the systematic errors at $E = 4.74\,\text{GeV}$ for the up and down quark ratios, respectively. Tables E.70 and E.71 list the errors for $E = 5.89\,\text{GeV}$. Each column of the table represents the contribution due to our g_1^n/F_1^n data, our fit to world g_1^p/F_1^p data, the $(d+\bar{d})/(u+\bar{u})$ parameterization, and the strange uncertainty, respectively. The in-quadrature sum of each quantity is displayed in the last column, labeled "Total."

Table E.68: Error table for $(\Delta u + \Delta\bar{u})/(u+\bar{u})$ at $E = 4.74\,\text{GeV}$.

$< x >$	g_1^n/F_1^n	g_1^p/F_1^p	$(d+\bar{d})/(u+\bar{u})$	s	Total
0.277	0.00098	0.03363	0.00326	0.00870	0.03490
0.325	0.00077	0.03999	0.00359	0.00645	0.04067
0.374	0.00094	0.04499	0.00361	0.00458	0.04538
0.424	0.00112	0.05190	0.00462	0.00328	0.05222
0.473	0.00108	0.05747	0.00507	0.00235	0.05775

Table E.69: Error table for $(\Delta d + \Delta\bar{d})/(d+\bar{d})$ at $E = 4.74\,\text{GeV}$.

$< x >$	g_1^n/F_1^n	g_1^p/F_1^p	$(d+\bar{d})/(u+\bar{u})$	s	Total
0.277	0.00816	0.01749	0.01455	0.01673	0.02940
0.325	0.00702	0.02280	0.01886	0.01363	0.03332
0.374	0.00943	0.02807	0.02280	0.01071	0.03888
0.424	0.01225	0.03551	0.03467	0.00814	0.05176
0.473	0.01320	0.04391	0.04754	0.00594	0.06631

Table E.70: Error table for $(\Delta u + \Delta\bar{u})/(u+\bar{u})$ at $E = 5.89\,\text{GeV}$.

$< x >$	g_1^n/F_1^n	g_1^p/F_1^p	$(d+\bar{d})/(u+\bar{u})$	s	Total
0.277	0.00136	0.03483	0.00198	0.00830	0.03589
0.325	0.00081	0.03889	0.00375	0.00619	0.03957
0.374	0.00081	0.04556	0.00380	0.00439	0.04594
0.424	0.00096	0.05109	0.00446	0.00311	0.05139
0.474	0.00119	0.05796	0.00481	0.00222	0.05821
0.524	0.00117	0.06423	0.00413	0.00160	0.06439
0.573	0.00139	0.07488	0.00386	0.00124	0.07500

Table E.71: Error table for $(\Delta d + \Delta \bar{d})/(d + \bar{d})$ at $E = 5.89\,\text{GeV}$.

$< x >$	g_1^n/F_1^n	g_1^p/F_1^p	$(d+\bar{d})/(u+\bar{u})$	s	Total
0.277	0.01141	0.01829	0.00864	0.01631	0.02838
0.325	0.00747	0.02239	0.01973	0.01339	0.03355
0.374	0.00821	0.02872	0.02503	0.01036	0.04032
0.424	0.01066	0.03539	0.03438	0.00781	0.05108
0.474	0.01480	0.04497	0.04929	0.00566	0.06858
0.524	0.01655	0.05692	0.05298	0.00358	0.07958
0.573	0.02279	0.07646	0.06641	0.00213	0.10383

E.8 a_2

E.8.1 ^{3}He and the Neutron

Table E.72 gives the $a_2^{^3\mathrm{He}}$ result in the measured region of $0.25 < x < 0.90$. The neutron result, decomposed into its low-x, measured, and high-x components, is given in Table E.73. Table E.74 displays the a_2^n result obtained over the full integration range with its statistical and systematic errors.

Table E.72: The extracted $a_2^{^3\mathrm{He}}$ in the measured region of $0.25 < x < 0.90$. The errors listed are statistical and systematic, respectively. All errors are absolute.

$\langle Q^2 \rangle$ (GeV^2)	$a_2^{^3\mathrm{He}}$ (measured)
3.21	-2.085E-04 $\pm$ 1.613E-04 $\pm$ 3.539E-05
4.32	-1.351E-04 $\pm$ 2.079E-04 $\pm$ 3.348E-05

Table E.73: The extracted a_2^n over the full x range, decomposed into the low-x, measured and high-x components. The column labeled "full" is the sum of all three regions. No errors are listed here, see Section E.8.2.

$\langle Q^2 \rangle$ (GeV^2)	low-x	measured	high-x	full
3.21	-3.056E-04	5.078E-04	6.530E-04	8.552E-04
4.32	-3.056E-04	5.499E-04	2.601E-04	5.044E-04

Table E.74: The extracted a_2^n over the full x range. The errors listed are statistical and systematic, respectively. All errors are absolute.

$\langle Q^2 \rangle$ (GeV^2)	a_2^n
3.21	8.552E-04 $\pm$ 1.761E-04 $\pm$ 6.125E-04
4.32	5.044E-04 $\pm$ 2.270E-04 $\pm$ 6.042E-04

E.8.2 Systematic Errors

The systematic errors for the measured $a_2^{^3\mathrm{He}}$ are given in Table E.75, where the column labeled $g_1^{^3\mathrm{He}}$ corresponds to the error due to our $g_1^{^3\mathrm{He}}$ data, and the column labeled x is the error due to x in the integration. The in-quadrature sum of the two contributions is given as the column labeled "Total." The systematic errors for the a_2^n extraction for the full x range are presented in Table E.76. The columns labeled low-x (high-x) correspond to the errors due to the low-x (high-x) regions. The errors due to the effective proton (neutron) polarization is given by the column labeled $\tilde{P}_p$ ($\tilde{P}_n$). The errors due to a_2^p and our measured $a_2^{^3\mathrm{He}}$ are also given. The in-quadrature sum of each contribution is labeled as "Total" in the last column.

Table E.75: The systematic errors contributing to the $a_2^{^3\mathrm{He}}$ result in the measured x range. The last column is the in-quadrature sum of all contributions.

$\langle Q^2 \rangle$ (GeV^2)	$g_1^{^3\mathrm{He}}$	x	Total
3.21	3.428E-05	8.803E-06	3.539E-05
4.32	3.281E-05	6.681E-06	3.348E-05

Table E.76: The systematic errors contributing to the a_2^n result over the full x range. The last column is the in-quadrature sum of all contributions.

$\langle Q^2 \rangle$ (GeV^2)	low-x	high-x	$\tilde{P}_p$	$\tilde{P}_n$	a_2^p	$a_2^{^3\mathrm{He}}$	Total
3.21	1.374E-04	1.373E-04	2.439E-04	3.012E-04	3.068E-04	3.052E-04	6.125E-04
4.32	8.878E-05	8.880E-05	2.518E-04	3.054E-04	3.118E-04	3.089E-04	6.042E-04